eman ta zabal zazu
Universidad del País Vasco
Euskal Herriko Unibertsitatea

Development of Lithium and Sodium ion capacitors with high energy-to-power ratios

María Arnaiz González

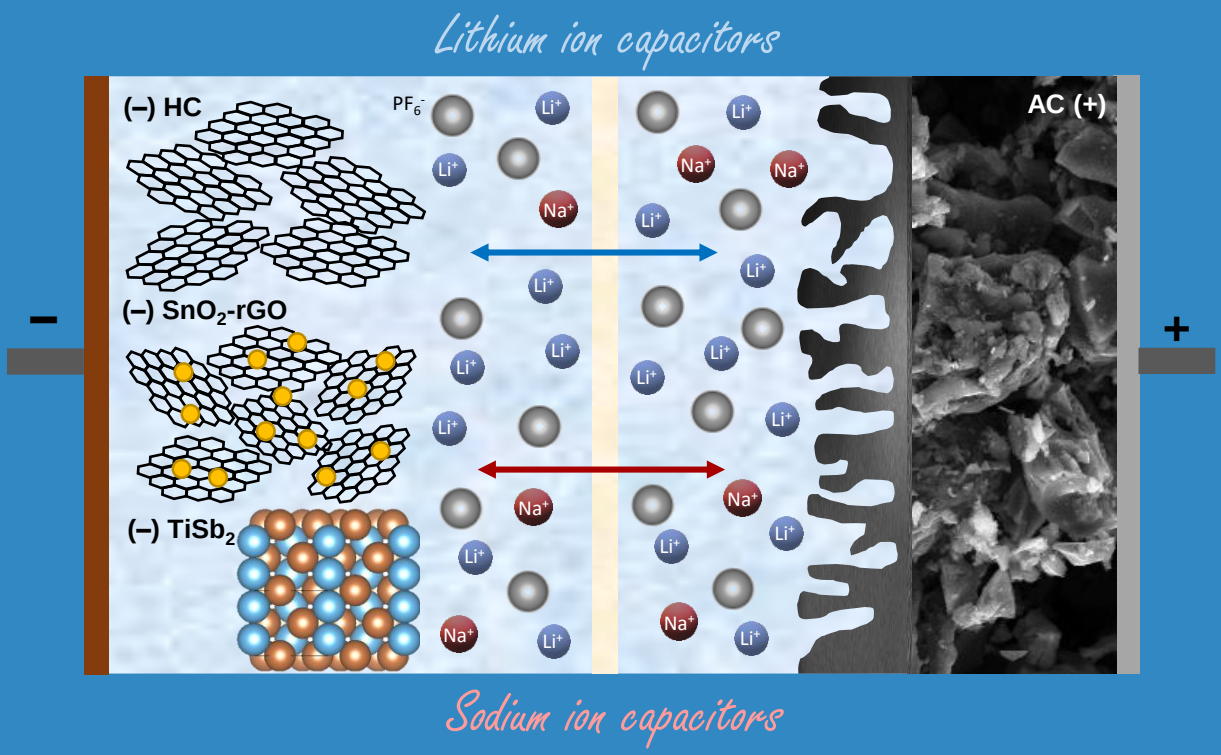

2019

EUSKAL HERRIKO UNIBERTSITATEA

ZIENTZIA ETA TEKNOLOGIA FAKULTATEA

INGENIARITZA KIMIKO SAILA

Development of Lithium and Sodium ion capacitors with high energy-to-power ratios

Doctor of Philosophy

by

María Arnaiz González

Thesis supervisors:

Prof.Teófilo Rojo

Prof. Federico Mijangos

Leioa, 2019

Nire aita eta amari,

Viure no és estar vius,

viure és l'actitud d'omplir la vida,

la vida, allò que passa quan tu rius!

~Txarango~

Acknowledgements

Tras tres años de doctorado, ha llegado el momento de cerrar una etapa, pero no sin antes dar las gracias a todas aquellas personas que han formado parte de ella.

En primer lugar, me gustaría dar las gracias a CIC energiGUNE y a mis directores Prof. Teófilo Rojo y Prof. Federico Mijangos por darme la oportunidad de iniciar mi carrera investigadora. Al igual que al Ministerio de Ciencia, Innovación y Universidades por la beca pre-doctoral (FPU15/04876) y la beca de estancia breve (EST/000151).

My warmest thanks to Dr. Gurpreet Singh for giving me the opportunity to start working at CICenergiGUNE, and especially to Dr. Eider Goikolea and Dr. Jon Ajuria for accepting me in their hybrids team. Eider, mila esker superkapen munduan murgiltzen lagundu izanagatik eta irakatsi didazun guztiagatik. Baita hainbeste lagundu nauten telefono dei luzeengatik ere. Jon, zuri esker infinituak baino ezin dizkizut eman. Mila esker uneoro egon izanagatik. Lagundu, irakatsi eta nigan konfiatu duzun guztiagatik. Eskerrik asko zure pazientziagatik eta tesi honi dedikatu diozun denboragatik. Zorionez edo zoritxarrez, baina eskaileretako kafeak amaitu dira. Mila esker bioi, nahiz eta askotan ni zoratzea lortu duzuen, “oreka lortu dugula esango nuke”. Esker onenak bihotzez! ☺

I would also like to thank Prof. Andrea Balducci for hosting me during four months in his group in the Friedlich Schiller University of Jena. Ho imparato molto sugli elettroliti e ho avuto un´esperienza molto positiva in Jena. Also thanks to Timo, Lars, Patrik, Jakob, Chris, Simon and Peihua for making my stay so nice. I also want to thank Dr. Sonia Dsoke for hosting me in the Karslruhe Institue of Technology. Lo stage è durato solo un mese, ma è stato sufficiente per scoprire e conoscere l´intrigante mondo del potassio. Senza dubbio, due stage molto utili che mi hanno permesso di creare importanti legami professionali con altrettanti rinomati gruppi di ricerca, grazie mille!

Gracias también a la Dra. Cristina Botas por ayudarme tanto en mis primeros meses de tesis y hacerme ver el lado positivo de las cosas. También dar las gracias al Dr. JL Gómez-Cámer por trasladarnos su sabiduría en aleaciones y por sus largas explicaciones.

Especial gracias a todos mis compañeros que día tras día han hecho que la tesis haya sido no sólo una experiencia enriquecedora científicamente sino también personalmente. Gracias a todos los doctorandos con los que he compartido esta etapa: a Xabi, por estos 8 años, por escucharme y entenderme; a Ane por preocuparse por mí; a Itziar por la ayuda en esta última etapa, pero también por las risas entre tanta tragedia; a JS porque nunca sabré si hablas en serio; a Jaione por ser tan terremoto; a Oier por darnos a conocer noticias extrañas; a Begoña S. por su tranquilidad; a Juanlu porque me debes un salmorejo; a Mikel por luchador and to Tandra for her kindness. Eskerrak eman ere Maiderri, beti laguntzeko prest egon izanagatik eta gure glühweine-ngatik; a MJ por los rayos…pero sobre todo por su amistad!; a María E. por su paciencia y ayuda en el microscopio; a Cristina Flores por ser la mejor compi de alemán; a Nebil por sus sabias reflexiones sobre la ciencia; a M&M por su alegría y carreras en Bologna; a Leire Tutera por las risas continuas; a Cristina (TES) por ser la más cotilla; a Uxue por su simpatía; a Marina por su eterna paciencia; a Gelines por las risas; a Guillermo por su siempre buen humor; a Giorgio por ser el mercado nuestro punto de encuentro; Ajuriari, zientziaz aparte, nutrizioan eta diseinu grafikoan oinarritutako kapitulu bat idatzi ahalko nukeelako ere; y especial gracias a Silvia, por el apoyo en estos últimos meses, y porque a pesar de hablar por los codos, también sabe escuchar. Gracias a todos, os echaré de menos!

Por último, mila esker a mi cuadrilla, por ayudarme a desconectar y disfrutar de la vida. Muchas gracias también a mi ama y aita, porque son los que en lo personal más intensamente han vivido conmigo estos tres años. Gracias por escucharme, comprenderme, aconsejarme y apoyarme en cada momento de esta etapa de mi vida.

Gracias a cada una de las personas que habeis creído y confiado en mí, ahora y siempre. Esker anitz nire irribarrea aurpegian marraztuta mantendu duzuen guztioi! ☺

Table of contents

Chapter 2: Dual carbon metal ion capacitors

Chapter 3: Looking toward alternative electrolytes for dual carbon metal ion capacitors

Chapter 4: SnO_2-rGO as negative electrode for lithium ion capacitors

Chapter 5: $TiSb_2$ as negative electrode for LICs and NICs

Chapter 6: General discussion, conclusions and future perspectives

Appendices

Table of contents

Abstract

Metal ion capacitor technology (MIC, being M = L for Li and N for Na) was first developed in the early 2000's as a novel approach based on the internal hybridization of lithium ion batteries (LIBs) and electrical double layer capacitors (EDLCs). These systems hold promise to merge the best features of each technology, achieving high energy densities, thanks to the battery-type electrode, at high power densities, owing to the capacitor-type electrode, while maintaining long cycle life. Since the first commercial lithium ion capacitor reached the market in 2008, research on this field has notoriously increased. However, most of the developed systems gain energy at the expenses of power and/or cycle life. Hence, the aim of this thesis is to develop more energetic, more powerful and more stable lithium and sodium ion capacitors (LICs and NICs).

In this scenario, the activated carbon (AC) has been the material of choice for the capacitor-type positive electrode owing to its fast response, stability and low-cost, while for the battery-type negative electrode three different faradaic materials with their own particular set of assets have been investigated. Hard carbon (HC), SnO_2 embedded in a reduce graphene oxide matrix (SnO_2-rGO) and $TiSb_2$ intermetallic compound have been the selected materials. LICs and NICs have been developed with HC and $TiSb_2$ while the use of SnO_2-rGO has been limited to Li-ion technology owing to the poor performance shown in sodium.

The selection of these specific battery-type materials has been driven by their low reduction potential and high specific capacity response. Being the energy density of a MIC described by the specific capacitance and the cell voltage of the device, the use of the selected materials allows targeting for **high energy density outputs**. In order to be able to also give response at high rates, *i.e.* at low discharge times, ensuring also **high power density outputs,** the preparation of each material as well as the electrodes have

been optimized. To this end, reduction on particle size for HC and $TiSb_2$, and carbon/graphene coating techniques for SnO_2-rGO and $TiSb_2$ materials have been followed. This way, as high as 87 Wh kg^{-1}_{AM}, 60 Wh kg^{-1}_{AM} and 90 Wh kg^{-1}_{AM} energy density values have been obtained within a discharge time of few minutes for LIC (HC:AC), LIC (SnO_2-rGO:AC) and LIC ($TiSb_2$:AC), respectively. Meanwhile, 54 Wh kg^{-1}_{AM} and 65 Wh kg^{-1}_{AM} have been obtained for NIC (HC:AC) and NIC ($TiSb_2$:AC), respectively.

Finally, in order to neutralize the large volume changes that alloying materials (*i.e.* Sn and Sb) suffer during cycling; different strategies have been followed in order to achieve **high durability devices**. In the case of SnO_2-rGO, the graphene matrix itself plays a role buffering volume expansion/contractions. In the case of $TiSb_2$, a titanium matrix only capable of mitigating the Li-based alloy volume changes (Li_3Sb, 135%) was used while for the larger Na-based alloy volume expansions (Na_3Sb, 293%) an additional study in the $TiSb_2$ electrode fabrication process has been carried out studying the effect of different binders. Following this strategies 10000 cycle life was achieved for LIC (HC:AC) and LIC ($TiSb_2$:AC), while 2000 for LIC (SnO_2-rGO:AC). With regard to Na-ion devices, the cyclability was limited to 1000-2000 cycles.

Moreover, since the cell voltage of a device can also be enlarged by electrolytes with wider electrochemical stability window, different electrolytes have also been investigated for the HC-based MICs which turned out to be the best negative electrode. As a result, the use of a novel ester-based solvent has allowed increasing the operational voltage window of a LIC, paving the way towards 5 V energy storage devices.

Overall, it is possible to say that the obtained results have satisfied the initial goal of developing more energetic, more powerful and more stable LICs and NICs.

Laburpena

Metal ioi kondentsadoreen teknologia (MIC, non M = litioa, L; edo sodioa, N den) XX. hamarkadaren hasieran sortu zen litio ioi bateria (LIB) eta geruza elektriko bikoitzeko kondentsadoreen (*electrical double layer capacitor*, EDLC) arteko barne hibridazioaren ikuspegi berria lehenengo aldiz garatu zenean. Gailu berri hauek teknologia bakoitzaren propietate onenak batzeko gaitasuna izateko esperantzarekin sortu ziren. Bateria motako elektrodoari esker energia dentsitatea altua lortzen den bitartean, kondentsadore motako elektrodoari esker potentzia altua lortuko da, ahal den heinean ziklabilitate luzea mantenduz. Lehenengo litio ioi kondentsadorea merkaturatu zenetik 2008an, alor honetan garaturiko ikerkuntza nabarmenki areagotu da. Hala ere, orain arte garaturiko sistema gehienek lorturiko energia irabaziak potentziaren edo ziklabilitatearen ordainetan izan dira. Ondorioz, tesi honen helburua energetikoagoak, azkarragoak eta egonkorragoak diren litio eta sodio ioi kondentsadoreak (LIC eta NICak) garatzea da.

Testuinguru honetan, ikatz aktibatuaren (*activated carbon*, AC) deskarga denbora laburra, egonkortasuna eta kostu baxua dela eta, kondentsadore motako elektrodo positibo moduan hautatua izan da. Bien bitartean, bateria motako elektrodo negatiboari dagokionez, hiru material faradaiko ezberdin aukeratu dira: ikatz gogorra (*hard carbon*, HC), SnO_2 grafeno erreduzituko matrize batean kapsulatua (SnO_2-rGO) eta $TiSb_2$ konposatu intermetalikoa. HC eta $TiSb_2$ materialek LIC eta NICak garatzea baimendu dute. Aldiz, SnO_2-rGOaren erabiliera sodio-ioi teknologian ezinezkoa izan da eta litiora mugatu da.

Bateria motako material hauen aukeraketa haien erredukzio potentzial baxu eta kapazitate espezifiko balio altuetan oinarritu da. MIC baten energia dentsitatea, bere kapazitantzia espezifikoak eta sistemaren boltai leihoak definitzen dute, ondorioz, aukeraturiko materialek **energia dentsitate altua** lortzea ahalbidetu dute. Bestalde, korronte altuetan erantzun azkarra emateko helburuarekin (hots, deskarga denbora

baxuetan), material eta elektrodo bakoitzaren prestaketa optimizatu behar izan da **potentzia dentsitate altua** bermatzeko. Xede honekin, HC eta $TiSb_2$ partikulen tamaina txikitu eta SnO_2-rGO eta $TiSb_2$ materialen ikatz edo grafenozko estaltzea burutu da. Modu honetan, 87 Wh kg^{-1}_{AM}, 60 Wh kg^{-1}_{AM} eta 90 Wh kg^{-1}_{AM} energia dentsitate balioak lortu dira minutu gutxiko deskarga denboretan LIC (HC:AC), LIC (SnO_2-rGO:AC) eta LIC ($TiSb_2$:AC) sistemetarako. Aldiz, NIC (HC:AC) eta NIC ($TiSb_2$:AC) sistemetarako, 54 Wh kg^{-1}_{AM} eta 65 Wh kg^{-1}_{AM} lortu dira.

Amaitzeko, aleazioetan oinarritutako materialek (hau da, Sn eta Sb) pairatzen dituzten bolumen aldaketak indargabetzeko helburuarekin eta ondorioz **ziklabilitate luzea bermatu** dezaketen gailuak garatzeko, estrategia ezberdinak jarraitu dira. SnO_2-rGOren kasuan, grafenozko matrizea bera, bolumen hedatze/konpresioak indargabetzeko eginkizuna betetzen du. Ostera, $TiSb_2$ materialaren kasuan, titanio matrizeak soilik litioan oinarritutako aleazioen bolumen aldaketak (Li_3Sb, 135%) neutralizatzeko gai izan da. Aldiz, sodiozko aleazioen bolumen aldaketak ia hirukoitzak izanik (Na_3Sb, 293%), aglutinatzaile ezberdinak aztertu behar izan dira elektrodoen fabrikazio prozesua optimizatu eta bolumen aldaketak eragindako kalteak hein batean minimizatzeko. Estrategia hauek jarraituz, LIC (HC:AC) eta LIC ($TiSb_2$:AC) sistemek 10000 ziklo gainditu dituzte, LIC (SnO_2-rGO:AC) aldiz 2000 ziklo iraun ditu. Na-ioi sistemei dagokionez, ziklabilitatea ez da 1000-2000 ziklotik pasa.

Bestalde, MICen boltai leihoa elektrokimikoki egonkorragoak diren elektrolitoen bitartez hedatu daitekeenez, elektrolito ezberdinak aztertu dira HCetan oinarritutako MICetarako. Horrela, ester motako disolbatzaile berri bat erabiliz, ikatzetan oinarritutako LICaren boltai leihoa zabaltzea lortu da, generazio berriko 5 V-ko gailuen garapenerako bidea lausotuz.

Orokorrean, doktorego tesi honetan lortutako emaitzak hasierako helburua asetu dutela esan daiteke, energetikoagoak, azkarragoak eta egonkorragoak diren LIC eta NICak garatzea lortu baita.

Resumen

La tecnología de los condensadores de metal ion (MIC, siendo M = L para Li y N para Na) se desarrolló por primera vez a principios de los años 2000 como un enfoque novedoso basado en la hibridación interna de baterías de litio-ion (LIB) y condensadores eléctricos de doble capa (EDLC). Estos sistemas prometen unir las mejores características de cada tecnología, logrando altas densidades de energía, gracias al electrodo de tipo batería; a altas densidades de potencia, gracias al electrodo de tipo condensador, manteniendo al mismo tiempo una larga ciclabilidad. Desde que el primer condensador comercial de litio ion llegó al mercado en 2008, la investigación en este campo ha aumentado notablemente. Sin embargo, la mayoría de los sistemas desarrollados ganan energía a expensas de la potencia y/o la ciclabilidad. Por lo tanto, el objetivo de esta tesis es desarrollar condensadores de litio y sodio ion (LICs y NICs) más energéticos, con más potencia y más estables.

En este escenario, el carbón activado (*activated carbon*, AC) debido a su rápida respuesta, estabilidad y bajo coste, ha sido el material escogido para ser utilizado como electrodo positivo de tipo condensador, mientras que para el electrodo negativo de tipo batería se han investigado tres materiales farádicos diferentes: carbón duro (*hard carbon*, HC), SnO_2 embebido en una matriz de óxido de grafeno reducido (SnO_2-rGO) y el compuesto intermetálico $TiSb_2$. Utilizando HC y $TiSb_2$ se han podido desarrollar tanto LICs como NICs, mientras que el SnO_2-rGO solamente se ha utilizado en la tecnología de litio ion debido a su pobre rendimiento en sodio.

La selección de estos materiales de tipo batería ha sido impulsada por su bajo potencial de reducción y su alta capacidad específica. Los materiales seleccionados permiten obtener **altos valores de densidad energética,** siendo ésta definida en los MICs por la capacitancia específica y el voltaje de celda. Además, con el objetivo de poder dar respuesta a altas corrientes, es decir, a bajos tiempos de carga/descarga, se ha optimizado la preparación de los materiales así como la de los electrodos, asegurando

de esta forma una **alta densidad de potencia**. Con este fin, se ha reducido el tamaño de partícula del HC y $TiSb_2$; y los materiales de SnO_2-rGO y $TiSb_2$ han sido embebidos en una matriz de grafeno o recubiertos con un carbón conductor. De éste modo, se han obtenido valores de energía tan altos como 87 Wh kg^{-1}_{AM}, 60 Wh kg^{-1}_{AM} y 90 Wh kg^{-1}_{AM} en tiempos de descargas de poco minutos para los LIC (HC:AC), LIC (SnO_2-rGO:AC) y LIC ($TiSb_2$:AC), respectivamente. Mientras que se han obtenido 54 Wh kg^{-1}_{AM} y 65 Wh kg^{-1}_{AM} para los NIC (HC:AC) y NIC ($TiSb_2$:AC).

Por último, para neutralizar los enormes cambios de volumen que sufren los materiales de aleación (*i.e.* Sn y Sb) durante el ciclado, se han seguido diferentes estrategias para desarrollar dispositivos de **larga ciclabilidad**. En el caso del SnO_2-rGO, la misma matriz de grafeno juega un papel importante a la hora de mitigar las expansiones/contracciones de volumen que se dan. En el caso de $TiSb_2$, la matriz de titanio tan sólo ha sido capaz de mitigar los cambios de volumen de las aleaciones de litio (Li_3Sb, 135%), mientras que para poder mitigar las expansiones de volumen de las aleaciones de sodio (Na_3Sb, 293%) se ha llevado a cabo un estudio adicional basado en el uso de diferentes aglutinantes en la preparación de los electrodos para este material. Gracias a estas estrategias, los sistemas LIC (HC:AC) y LIC ($TiSb_2$:AC) han superado los 10000 ciclos, mientras que el sistema LIC (SnO_2-rGO:AC) ha llegado a los 2000 ciclos. En cuanto a los sistemas de Na-ion, la ciclabilidad ha estado limitada a 1000-2000 ciclos.

Además, dado que la ventana de voltaje de un MIC también puede aumentarse utilizando electrolitos con mayor estabilidad electroquímica, se han estudiado diferentes electrolitos para los MICs basados en HC. Como resultado, el uso de un nuevo disolvente basado en un éster ha permitido aumentar la ventana de voltaje del LIC carbonoso, abriendo el camino hacia dispositivos de almacenamiento de energía de 5 V.

En general, se puede decir que los resultados obtenidos han conseguido el objetivo inicial de desarrollar LICs y NICs más energéticos, con más potencia y más estables.

List of Tables and Schemes

List of Figures

CHAPTER 1

Introduction

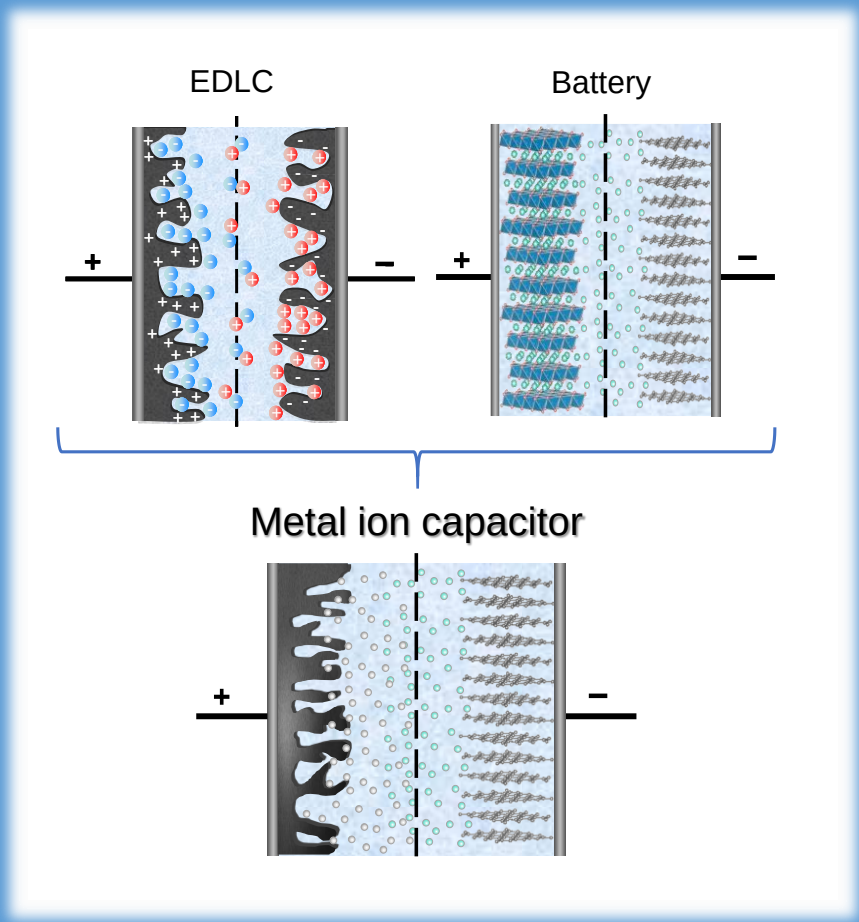

Introduction

Driven by the environmental issues caused by industrialization and the increasing demand on fossil fuels, renewable energy sources take a key role in the move from a toxic and harmful energy system to an eco-friendly one. Unfortunately, renewables are weather dependant, thus discontinuous, and the use of energy storage systems is critical for their development. In addition, the evolution to the electric vehicle (EV) is also envisaged as a key factor towards a healthier environment. To this end, the development of new energy storage systems delivering high energy and high power is also absolutely necessary. Among others, electrochemical energy storage systems hold the key for this transition.

Usually, lithium ion batteries (LIBs) or electrical double layer capacitors (EDLCs) are used when high energy or high power, respectively, is required. But, when high energy at high power is required, typically, both systems are externally hybridized by a series connection. This definitively increases the cost and the complexity of the battery management system. In the early 2000´s, a novel approach based on the internal hybridization of LIBs and EDLCs led to the development of metal ion capacitor (MIC) technology. These systems hold promise to merge the best features of each technology, achieving high energy at high power while maintaining long cyclability. In this scenario, the development of more energetic, more powerful and more stable MICs will be the backbone of this PhD thesis.

In Chapter 1, the working principles and challenges of both LIBs and EDLCs are first explained. Next MIC technology is reviewed in depth, from the working principles and challenges of this novel technology to the state-of-the-art of both lithium and sodium ion capacitors (LICs and NICs).

Table of contents:

1.1. Energy storage technologies

The first Industrial Revolution that took place during the 18th and the 19th centuries transformed that society functioning under the umbrella of an agriculture-based economy into the actual that relays on industry-based economy (**Figure 1.1**). The industrialization of many countries rapidly increased the energy demand which has been mainly satisfied by the use of fossil fuels. Although they are formed by natural processes, those take much longer than the fast consumption rate of world population, consequently, they are considered as non-renewable and finite energy sources. Since they are based on organic compounds, their combustion produces high amounts of carbon dioxide (CO_2) and other volatile compounds, all of them catalogued as greenhouse gasses (GHGs) and causing the greenhouse effect that is responsible for the climatic change. In addition, the extraction and distribution of fossil fuels from the Earth crust has a huge environmental impact and cost.

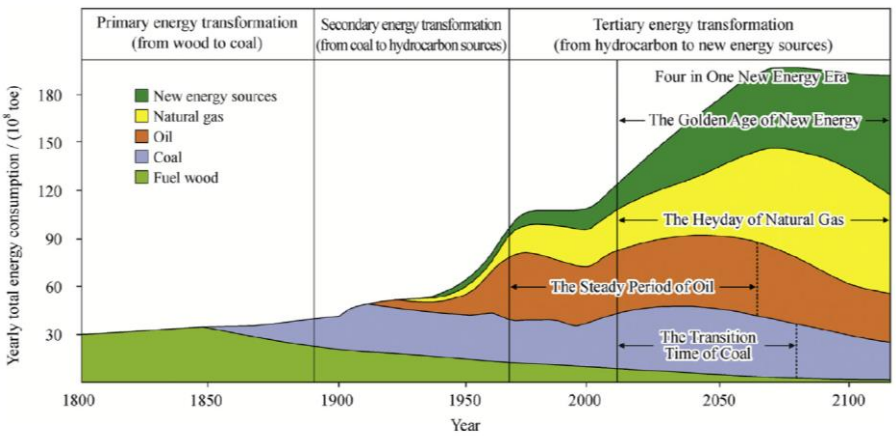

Figure 1.1. Trends and forecasts of global energy consumption [1].

In the last years, owing to new environmental policies and the population concern, society is slowly moving towards clean energy sources such as renewable energies, which do not

emit GHGs. The use of the sunlight (solar power), the wind (wind power), the heat of the Earth (geothermal) or the movement of tides (hydraulic) has become crucial to generate clean energy. The International Energy Agency reported in 2018 that renewables saw the highest rate of growth among different energy sources. It is the case for the power sector that presented the highest growth of low-carbon energy, with a renewable-based electricity generation increase of 6.3% (380 TWh) in 2017, representing a total 25% of the global electricity generation. In October 2018, The European Council agreed on a new 2030 Framework for Climate and Energy. In this framework, renewables play an important role toward a more competitive, secure and sustainable energy system with the aim of reducing GHGs by promoting low-carbon technologies [2].

Unfortunately, renewable energy sources are discontinuous. They suffer fluctuations depending on the weather forecast and different factors such as the strength of the wind, sunlight hours or the movement of tides. Thus, in order to create a non-dependent and continuous electricity source, energy storage is necessary to meet the mismatch between the generation and the consumption. To this end, new technologies are now focused on the development of efficient and reliable electrical energy storage systems.

Energy storage defines the process of converting electrical energy from a power network into a form that is stored for converting back to electricity when it is demanded. Historically, energy storage has been important for three main different reasons: i) it reduces electricity costs storing electricity at off-peak times when the price is lower, in order to use it back at peaks of higher prices, ii) improves the reliability of the power supply, *e.g.* blackouts due to natural disasters, and iii) maintains and improves power quality, frequency and voltage. **Figure 1.2** shows how during low demand periods (night period) energy is stored with the aim of using it at those high demand periods (most active hours of the day), highlighting the importance of having energy storage devices [1].

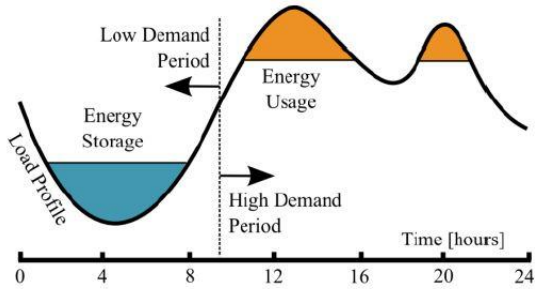

Figure 1.2. Energy storage and usage peaks during 24 hours [3].

Nowadays, the electric grid is destined to include energy storage systems as a major component in order to ensure grid stability and secure supply at peak demands. Moreover, two main emerging markets for energy storage are foreseen in on-grid and off-grid business areas respectively. First, renewable energies, where power fluctuations and weather dependency should be solved, and second, electric vehicles (EVs) or hybrid electric vehicles (HEVs), a very promising industry called to replace fossil fuel derived gasoline and diesel engines by batteries.

Among the different energy storage systems, three main technologies can be distinguished: mechanical, thermal and electrochemical energy storage systems. On the one hand, the most common mechanical storage systems are pumped hydroelectric power plants (pumped hydro storage, PHS), compressed air energy storage (CAES) and flywheel energy storage (FES). PHS plants are the most flexible and widespread choice for on-grid applications [4]. On the other hand, thermal energy storage systems store heat by different means in an insulated reservoir. This way, energy can be used later in different industrial or residential applications, such as space heating and cooling, hot water production or electricity generation. [5].

1.2. Electrochemical energy storage

Opposite to mechanical and thermal energy storage, electrochemical energy storage systems are accessible for small-scale applications and for those that need rapid electric

energy conversion and release. Electrochemical energy storage systems convert and store energy by means of chemical and/or physical mechanisms and are now the main choice for energy storage in electronic devices. Currently, they can be classified by their charge storage mechanism, from secondary batteries to electrochemical capacitors and to the newest hybrid or metal ion capacitors combining the aforementioned technologies (**Scheme 1.1**). They are commonly distinguished by their energy-to-power densities and charge/discharge time characteristics, and are usually represented in a Ragone plot (see **Figure 1.3**). In the following sections each of the technologies are introduced in depth.

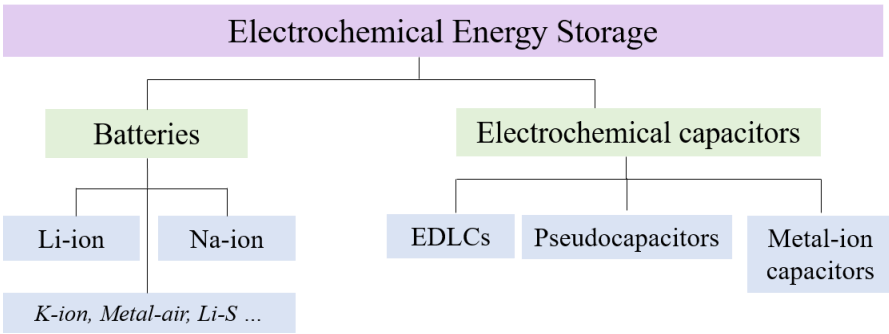

Scheme 1.1. Main electrochemical energy storage technologies.

However, it was in 1800 when Alessandro Volta invented the first battery. He was trying to demonstrate that what Luigi Galvani called “animal electricity” was not animal but only electricity. After some experiments with death frogs, Galvani believed that their bodies generate electricity and that the fluid in the nerves transported that electricity to muscles, causing muscular movement. Nevertheless, Volta found that the movement was originated by the contact of two different metals with the legs of the frog. He demonstrated that the achievement of a voltage was related to two metals necessarily connected by something humid, not certainly a frog, but a paper soaked in dilute acid would have been enough. He also found that increasing the amount of connecting metals with wet paper, higher voltage output was possible leading to higher electrical currents. He also demonstrated that metals have different electron affinities and that the potential

of different metals allowed higher voltage cells. After this pioneering discovery, research on the field increased significantly in the following years, giving rise to the development of the electrochemical energy storage technology, mainly to the battery related field.

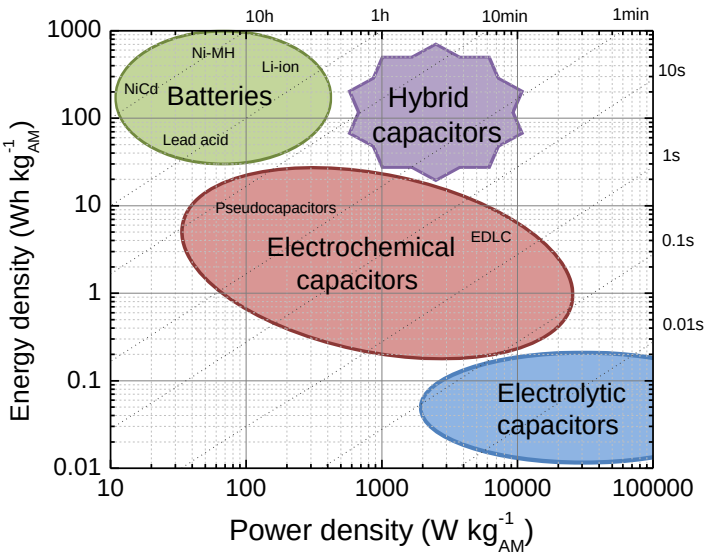

Figure 1.3. Electrochemical energy storage devices classified by the stored energy and power densities.

1.3. Batteries

Batteries are the main energy storage devices when high energy density is required. They are able to convert chemical energy into electrical energy by means of oxidation and reduction reactions, using a cathode (positive electrode) and an anode (negative electrode) separated by a membrane immersed in an electrolyte. During the charge step, ions are extracted from the positive electrode by an oxidation reaction and migrate across the electrolyte and permeate through the separator to the negative electrode where the reduction reaction occurs. Contrary, in the discharge step, electrons follow the opposite direction and the negative electrode is oxidized, while the positive electrode is reduced.

The stored energy density of a rechargeable battery is defined by the working voltage of the cell and the specific capacity that each material is able to store.

Lead-acid batteries were the first commercially available rechargeable batteries, invented in 1859 by Gaston Planté [6]. Owing to their versatility and low-cost, lead acid batteries had been widely used along the years (and still are), in a wide number of applications ranging from renewables to transportation. In 1899, nickel-cadmium batteries (NiCd) were developed by Waldemar Junger and were soon commercialized in 1910. However, being cadmium a toxic element, natural evolution toward more environmentally friendly rechargeable batteries gave rise to new nickel-hydrogen (Ni-H_2) cells started in 1970s. Later, in 1989, nickel-metal hydride batteries (NiMH) were developed at Yuasa Battery Company [7,8]. The main competitor of the latter are the alkaline manganese secondary batteries, which reached the market by the Union Carbide Company (USA) in 1946. In 1993, Rayovac Company started producing rechargeable alkaline manganese dioxide-zinc (RAM) batteries, which doubled the energy density of NiCd ones. Owing to their lower self-discharge loss, better charge-retention and environmental sustainability, RAM batteries became the brand of choice for many market applications, *e.g.* toys and games among others [9].

Nevertheless, the above-mentioned type of batteries are very sensitive to overcharging and overheating during charge. Nowadays, being portable electronics one of the most important applications for rechargeable batteries, safety left some of this batteries aside. In this context, lithium ion batteries (LIBs) first emerged on the scene in 1991 and have dominate the market ever since. Compared to previous technologies, LIBs are lightweight, present high specific energy, low self-discharge, long cycle life and high recyclability. Thereby, nowadays, they do not only dominate the portable electronic market but they are also the technology of choice for future EVs [10]. As summary, a timeline for the most relevant milestones in the battery field is shown in the upper part of **Figure 1.4**.

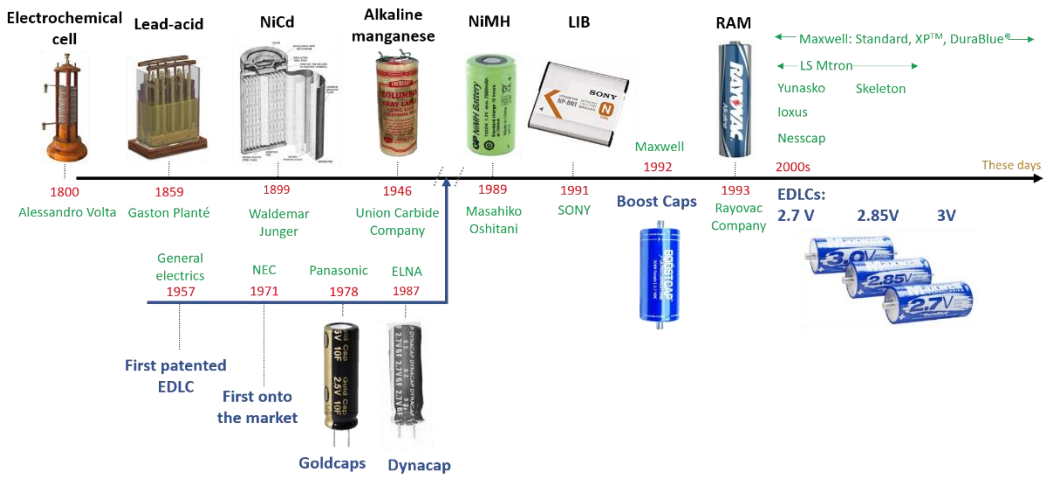

Figure 1.4. Timeline of the most relevant batteries and electrochemical capacitors.

Being LIB technology one of the origins for metal ion capacitors, its comprehension is crucial and consequently is now deeply reviewed.

1.3.1. Lithium ion batteries

LIBs are rechargeable batteries in which lithium ions migrate from the negative to the positive electrode during discharging and go back when charging. Thus, a lithium source is always necessary. The first primary LIB was introduced in the 1970s by SANYO Inc. and consisted of a lithium metal anode and a MnO_2 cathode [11]. In 1985, MOLI Energy Inc. developed a secondary LIB using the same anode and cathode materials. Although high energy density values were obtained, low cycling stability and safety problems such as thermal runaway that could lead to explosion, cell overcharging or lithium deposition promoting dendrite formation made these cells unsafe to be commercialized [12]. In parallel, research on lithium based materials able to reversibly deintercalate Li^+ led up to lithium secondary batteries. In 1980, Professor John Goodenough discovered for the first time that Li^+ from lithium cobalt oxide ($LiCoO_2$=LCO) could migrate through the battery, from one electrode to the other and be deintercalated by the electrochemical oxidation during charging and electrochemical reduction during discharging in an aprotic media

[13]. As a result, lithium metal was not necessary any more as a lithium source and LCO was consolidated as the best cathode material for the development of secondary LIBs.

After the pioneering research of Goodenough *et al.*, first secondary LIBs were commercialized by Sony in 1991 [14]. These were based on LCO as the cathode and graphite as the anode using organic lithium hexafluorophosphate ($LiPF_6$) in 1:1 vol% ethylene carbonate:diethyl carbonate (EC:DEC) as electrolyte. A scheme of those LIBs is represented in **Figure 1.5**, where LCO is casted on an aluminium current collector while graphite is on a copper current collector in order to avoid lithium alloying reaction with aluminium at low potentials. Both electrodes are electrically isolated by a separator immersed in an electrolyte that allows for ion diffusion but forces electron flow through an external circuit.

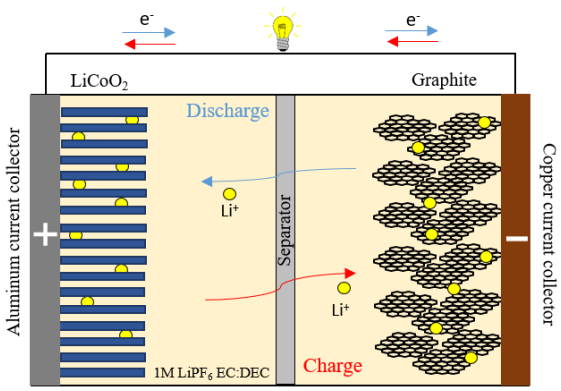

Figure 1.5. Scheme of a LIB based on LCO and graphite.

1.3.2. Working principles of LIBs

In LIBs, during the discharge step, Li^+ is released from the cathode material and migrates across the highly ion conductive electrolyte through the separator toward the negative electrode, where it is inserted into the structure of the negative electrode. Meanwhile, in the charge step, the analogous but contrary process occurs: Li^+ is deintercalated from the

anode material toward re-intercalation into the cathode material. Reactions taking place in this process are defined in **Equation 1.I** and **Equation 1.II**.

$$Li_{1-x}CoO_2 + x\ Li^+ + x\ e^- \leftrightarrow LCO \qquad \textbf{Equation 1.I}$$

$$Li_xC_6 \leftrightarrow C_6 + x\ Li^+ + x\ e^- \qquad \textbf{Equation 1.II}$$

Thus, LIBs store energy by means of redox reactions in the bulk of the materials. The charge stored is measured in coulombs and it is defined by the ions that are stored during redox reactions happen. Charge is defined by the integral of the applied constant current density and the charge/discharge time consumed (**Equation 1.III**). However, batteries are normally defined by their specific capacity value, *c*, measured in milliampere hour per gram (mAh g^{-1}) in which the charge stored per mass of active material (**Equation 1.IV**) is defined.

$$Q = \int_0^t I(t)\ dt \qquad \textbf{Equation 1.III}$$

$$c = \frac{Q}{m} \qquad \textbf{Equation 1.IV}$$

Moreover, during charge/discharge cycling, electrode-electrolyte reactions, electrode decomposition or changes in electrode volume can cause irreversible loss of capacity. This is measured by the Coulombic Efficiency (CE), defined in **Equation 1.V**.

$$CE = \frac{Q_{discharge}}{Q_{charge}} \qquad \textbf{Equation 1.V}$$

The energy density (Wh kg^{-1}_{AM}) stored in a fully charged cell is calculated by measuring the discharge time at a constant current. It is defined by the integral of the product of the current, *I*, and the voltage of the cell, V_{cell}, over the discharge time, divided by the total active mass (AM) of both electrodes (**Equation 1.VI**).

$$E = \int_0^t V_{cell}(t)\ I(t)\ dt \qquad \textbf{Equation 1.VI}$$

1.3.3. Evolution, state-of-the-art and challenges for LIBs

Currently, mostly driven by the EV industry, a new generation of batteries with higher energy densities are demanded. In order to give response to this requirement, several strategies can be followed. The energy of a battery is defined by the product of the charge and the voltage (**Equation 1.VI**), thus it is necessary to enlarge one or both of them. Research in new materials is necessary: new cathode materials able to store/deliver higher capacity values at higher potentials as well as new anode materials that can do the same but at low potentials. However, for real breakthroughs in LIBs not only innovative chemistries for electrode materials are required, but electrolyte components should also be considered. In order to exploit novel electrode materials and develop next generation 5 V batteries, new electrolytes that work beyond 4.2 V *vs.* Li^+/Li must be prepared. Parallel to the research focused on active materials and electrolytes formulation [15], electrode and cell engineering are also key success factors [16,17].

1.3.3.1. Electrode materials for LIBs

In order to increase the capacity, the first challenge is to identify materials performing better than the actual commercial LCO and graphite. A key element that limits the performance of batteries is the active element of the positive electrode; moreover, it is one of the most expensive part of a battery [18]. The search for alternative cathode materials to replace conventional LCO layered oxide in commercial LIBs has generated considerable research activity, mainly due to the problems associated with cost, safety and sustainability of Co-based materials. Due to the instability of the delithiated CoO_2 phase [19], only half of the lithium is extracted, what leads to a specific capacity of *ca.* 140 mAh g^{-1} [20]. The first step towards cobalt replacement was taken when using other transitions metals such as nickel and manganese in the structure of the layered oxide. Among others, maintaining the same structure of LCO, $LiNi_{0.80}Co_{0.15}Al_{0.05}O_2$ (NCA)

[21,22] and $LiNi_{1/3}Mn_{1/3}Co_{1/3}O_2$ (NMC) were developed [23–25]. Both NCA and NMC are currently used as positive electrodes in commercial LIBs [15].

Following the first generation of LCO alternative materials, $LiMn_2O_4$ (LMO) opened a new roadmap for cathode materials with spinel structure [26]. Contrary to the planes from previous layered oxides, in these materials the path for intercalation/deintercalation is a 3D network of channels, making them safer and lower in cost compared to LCO. However, LMO presents large capacity fading due to the Jahn-Teller distortion of Mn^{III} and dissolution of manganese into the electrolyte [27]. As in the previous layered structure, the doping with other transition metals, *i.e.* $LiM_xMn_{2-x}O_4$ (being M = transition metal), can also lead to the improvement of electrochemical properties [28,29].

Other materials such as phosphates with $LiMPO_4$ (being M = transition metal) olivine structure have also been studied as alternative cathode materials [30]. Among them, $LiFePO_4$ (LFP) is found to be the best candidate owing to its good electrochemical and thermal stability, long discharge plateau, low-cost and environmental benignity. Nowadays, LFP is a commercial material used as cathode in LIBs with a capacity approaching the theoretical one (165 out of 170 mAh g^{-1}) and showing high rate capability and safety features [31,32].

On the negative electrode, graphite is definitely the most commonly used anode material. Its excellent features such as low and flat working potential (~0.1 V *vs.* Li^+/Li) allowing for high operative voltage of the battery, low-cost and good cycle life make it the best choice among others. However, graphite only allows the intercalation of one Li^+ every six carbon atoms (LiC_6), limiting the reversible capacity to 372 mAh g^{-1}. The diffusion rate is between 10^{-9}-10^{-7} cm^2 s^{-1} [33], which also limits batteries in terms of power. Moreover, its intercalation potential is close to the lithium plating potential which could cause serious safety issues. Thus, during the last decades, research focused on the search of safer and faster Li^+ diffusion anode materials providing higher capacity that could replace graphite in commercial batteries has been followed.

Among the most studied anode materials for LIBs, four main groups comprising carbonaceous materials (*e.g.* graphite, soft carbon, hard carbon), titanium oxides ($Li_4Ti_5O_{12}$=LTO), conversion materials (oxides such as α-Fe_2O_3, Co_3O_4, phosphides, sulphides and nitrides) and alloying materials (*e.g.* Sn, Si, Sb…) can be found [34].

Carbonaceous materials are usually classified according to their graphitization degree, for instance apart from graphite, soft or graphitizable carbons, and hard or non-graphitizable carbons can be defined (**Figure 1.6**).

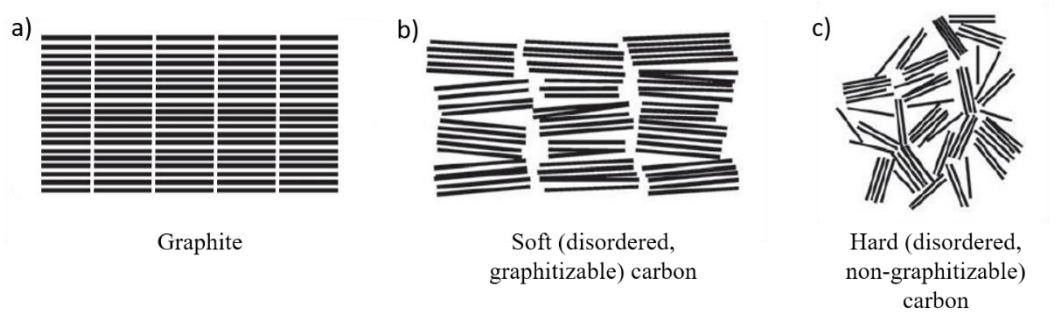

Figure 1.6. Structure of different carbonaceous materials: a) Graphite, b) Soft carbon and c) Hard carbon, adapted from [35].

The ability of the latter two (*i.e.* soft and hard carbons) to form intercalation compounds with lithium ions, the high conductivity and the electrochemical activity at low potentials make them very interesting materials to be used as negative electrodes. The most interesting feature of these carbonaceous materials relays on their disordered graphene layers which allow to insert double the amount of lithium ions into the carbonaceous structure, theoretically targeting double the capacity of graphite [36]. Moreover, their insertion potential is slightly higher than that of graphite, which makes their use as anode materials less risky. This material and its application in metal ion capacitors is studied in **Chapter 2**.

In the search for safer materials and higher capacities, LTO has been deeply studied. It shows a flat potential plateau at 1.55 V *vs.* Li^+/Li, which can suppress lithium dendrite

formation and electrolyte decomposition. LTO can accommodate three lithium ions per molecule showing an excellent cycling stability. However, it suffers from low electronic conductivity ($<10^{-13}$ S cm^{-1}) which limits its performance. Nevertheless, huge efforts such as reducing particle size and enhancing the conductivity by carbon coating have been followed to improve the properties of this material and to make it a good candidate to replace graphite in lithium ion technology [37]. In fact, several batteries based on LTO can be currently found in the market [38,39].

With regard to conversion materials -which are fully reduced by lithium to metal-, oxides (*e.g.* α-Fe_2O_3, Co_3O_4), nitrides, phosphides and sulphides can undergo conversion reactions with a theoretical capacity ranging from 500 to 1500 mAh g^{-1} [40]. Despite transition metal oxides have shown some of the most promising properties, during Li^+ insertion/deinsertion they typically break into small metal clusters that can react with lithium to form Li_2O, which causes large volume expansion and mechanical stress in the electrode upon cycling. This results in severe capacity loss and poor electrochemical conductivity. In order to improve the performance of these materials, by buffering the above-mentioned volume variations, the nanostructuring as well as the enbedment in various carbon matrixes have been investigated [41].

Alloying materials, mainly silicon, tin and antimony, have gained major attention as lithium alloying elements owing to their high capacities and low working potentials. Silicon is considered one of the most promising materials for future LIBs as it is able to store considerably more gravimetric charge with respect to other materials (*i.e.* 3000 mAh g^{-1}). In addition, its working potential is slightly higher (*i.e.* 0.4 V *vs.* Li^+/Li) than that of graphite, which allows to target for high voltage and safe batteries. Moreover, it is also abundant, cheap and enviromentally friendly. Nevertheless, it suffers from large volume variations during charge/discharge which cause mechanical failure. Alternatives to silicon such as tin that present lower gravimetric capacity of 994 mAh g^{-1} with a higher working potential at 0.5 V *vs.* Li^+/Li, or Sb with a gravimetric capacity of 660 mAh g^{-1} within a working potential of around 0.4 V *vs.* Li^+/Li have also been studied.

A reduction potential well-above zero turned out to be a desired feature for the sake of safety, avoiding any risk of metal plating. Yet, one of the major features of the alloying materials -their potential use in high power applications- has gone practically unnoticed. In this regard, their application in lithium ion capacitors have been explored by trying to overcome the large volume changes that all alloying materials suffer upon charging/discharging and causes mechanical failure. To this aim different strategies such as carbon coating or forming intermetallic compounds that should buffer those volume expansions have been followed. These materials and strategies are more in depth explained in the following **Chapters 4** and **5**.

1.3.3.2. Electrolytes for LIBs

In order to increase the cell voltage and ultimately the energy of a battery, the second challenge involves the formulation of an electrolyte with sufficiently large potential stability window. The electrochemical stability window of the electrolyte, E_g, is defined by **Equation 1.VII**, where LUMO and HOMO are the lowest unoccupied and highest occupied molecular orbitals of the electrolyte respectively.

$$E_g = E_{LUMO} - E_{HOMO} \qquad \textbf{Equation 1.VII}$$

The electrolyte is stable in a battery when the Fermi level of the anode is below E_{LUMO} ($\mu_A < E_{LUMO}$) and when the Fermi level of the cathode is higher than E_{HOMO} ($\mu_C > E_{HOMO}$) (**Figure 1.7**). Otherwise, the electrolyte is reduced by electrons from the anode, and oxidized by transferring electrons to the cathode [42]. The LUMO of almost all electrolytes is higher than the redox potential of carbonaceous materials, thus, reduction of the electrolyte in the anode is expected. This creates the well-known solid electrolyte interphase (SEI), which is an electronically insulating layer that is permeable for lithium ions.

The role of the SEI is key on the proper functioning of a battery and many research is still focused on the proper understanding of its formation and features in order to prevent battery failure [42,43]. SEI formation directly depends on the electrolyte formulation (salt, solvent, and additives), the electrode material and the formation process. The quality of the SEI is determined by its thickness and composition and will define the intercalation/deintercalation process. In the electrolyte, metal ions are solvated by solvent molecules. An effective SEI should desolvate and intercalate those pure metal ions. On the contrary, an ineffective SEI formation will lead to the intercalation of the solvated ions and thus the solvent will also be co-intercalated. If this co-intercalation is excessive, the SEI might not be completely formed and continuous exfoliation could occur [44]. Also, lithium metal deposition or dendrite formation might occur which can cause internal short circuit.

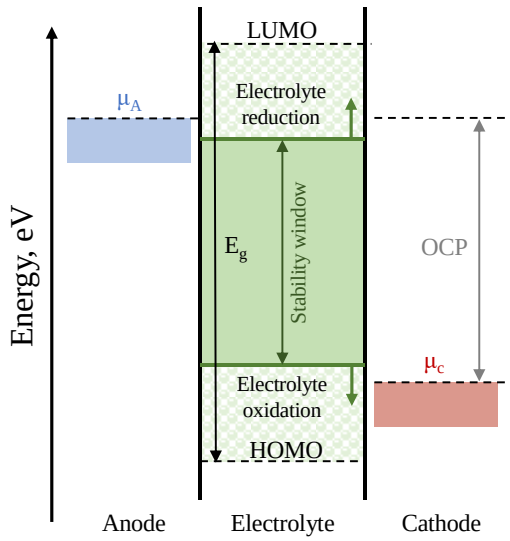

Figure 1.7. Schematic energy diagram of an electrolyte at open circuit, modified from [45].

Among the electrolytes used for LIBs, the most typical consist on lithium salts such as lithium hexafluorophosphate ($LiPF_6$), lithium tetrafluoroborate ($LiBF_4$) or lithium perchlorate ($LiCO_4$) in organic solvents such as ethylene, propylene carbonate (EC, PC),

dimethyl, diethyl carbonate (DMC, DEC) or ethyl methyl carbonate (EMC). The excellent features of PC, such as its low melting point, high boiling point and high flash point make it a safe solvent. However, considering graphite-based batteries, further investigations indicate that the SEI formed by the decomposition of EC is more appropriate for these carbonaceous material. Still, some undesirable features of EC such as a high melting point and high viscosity require the mixture of this solvent with other carbonate ones to satisfy the requirements that one unique solvent cannot meet. Thus, different mixtures of EC:DMC, EC:PC, EC:DEC, and so on can be found in literature [46]. These days, most LIBs use 1 M $LiPF_6$ dissolved in any of the aforementioned organic solvent mixtures. Non-aqueous electrolytes are necessary due to the violent reaction of lithium with water. However, safety concerns due to the high flammability and reactivity of organic solvents encouraged the search for alternative solvents.

In order to avoid the use of highly flammable organic electrolytes and with the aim of widening the electrochemical stability window and looking toward more secure and environmentally friendlier electrolytes, ionic liquids (ILs) have been investigated [47]. ILs are defined as molten salts whose fusion temperatures are at or below 100ºC. They are characterized by their high conductivity, wide electrochemical window, high thermal stability and low volatility. ILs are mostly binary systems based on anions and cations [48]. Commonly used cations are imidazolium (im^+), pyrrolidinium (Pyr_{1x}^+), pyridinium (py^+), tetraalkylammonium (NR_4^+) and tetraalkylphosphonim (PR_4^+), whereas common anions are tetrafluoroborate (BF_4^-), hexafluorophospate (PF_6^-), bis(trifluoromethansulfonyl)imide ($TFSI^-$) and bis(fluorosulfonyl)imide (FSI^-). ILs have recently been introduced in lithium ion technology not only to reduce the risk of battery failure but also to enhance their electrochemical performance [49,50]. In addition, the presence of a lithium salt is also necessary for their application in LIBs. Nevertheless, one of their main drawbacks is that high viscosity and low conductivity limit their performance at high rates. To overcome this issue, recently several works on mixtures between organic electrolytes and ILs have been successfully developed [51,52].

Moreover, next-generation electronic devices and EVs requirements need to be satisfied not only in terms of safety features but also in higher energy densities. Thus, in order to be able to use high-potential cathode materials, more stable electrolytes (>4.3 *vs.* Li^+/Li) than the typical organic ones should be investigated. Among other, sulfone-based, fluorinated, or organic nitrile solvents have been recently investigated [53–55].

1.3.4. Beyond LIBs

The fast development of portable electronic devices and EVs has increased the need of LIBs, which has had a significant impact on the lithium demand, and hence, has increased the price of raw materials (*i.e.* lithium) and is affecting worldwide reserves. Therefore, as lithium is not a naturally abundant element and is confined to few countries, alternative metals to lithium should also be considered to ensure the future of secondary batteries in case lithium supply is disrupted.

Sodium, the fourth most abundant element on earth, is unlimited in nature, is worldwide distributed and is easy to extract. Thus, it could be an interesting alternative for metal ion batteries. Sodium ion batteries (NIBs) were first studied when the development of LIBs in 1970s and 1980s began, but due to the rapid success of LIBs and their commercialization, the studies on NIBs were almost abandoned. Nonetheless, research in NIBs is now on vogue as confirmed by the increasing number of review papers covering the whole range of materials [56,57] and electrolytes [58,59] on this technology.

The configuration of NIBs and electrochemical storage mechanisms share some similarities with LIBs, however, important differences exist between both technologies. Na^+ have larger ionic radius (1.02 Å) in comparison with Li^+ (0.76 Å) and this, among others, affects transport properties. Sodium has also higher atomic weight than lithium (23 g mol^{-1} *vs.* 6.9 g mol^{-1}) and higher standard reduction potential (-2.71 V *vs.* SHE for Na^+/Na and -3.02 V *vs.* SHE for Li^+/Li), and therefore the energy density of a specific NIB will always be lower than that of its LIB counterpart.

Among cathode materials for NIBs, different oxides (*e.g.* $NaFeO_2$), polyanions such as phosphates (*e.g.* $NaFePO_4$), pyrophosphates (*e.g.* $Na_2FeP_2O_7$), fluorosulfates (*e.g.* Na_2FePO_4F), NASICON (Na^+ super ionic conductor) type compounds (*e.g.* $Na_3V_2(PO_4)_3$) and organic compounds (*e.g.* $Na_2C_6O_6$) have been investigated [58]. Instead, the selection of anode materials has been one of the major drawbacks of the technology. Due to the short interlayer distance of graphite and the thermal instability of the formed Na-based graphite intercalation compounds the insertion of Na^+ into graphene sheets is limited [60]. Hence, the well-stablished anode for LIBs was almost abandoned for NIBs until the very recent discovery of glyme-based electrolytes which enable a successful insertion/deinsertion mechanism [61]. However, in 2000 Dahn and Stevens reported for the first time on the use of hard carbon in NIBs delivering an initial reversible capacity of 300 mAh g^{-1} [62]. This fact opened new avenues in the research of hard carbons and since then, they have been extensively investigated [63–65]. Furthermore, alloy-based materials (*e.g.* Sn, P, Ge, Sb), conversion materials (*e.g.* $NiCo_2O_4$, Fe_2O_3), titanium-based compounds (*e.g.* $Li_4Ti_5O_{12}$) and organic composites have also been studied as anode materials in sodium ion technology.

Beyond lithium and sodium ion batteries, potassium ion batteries (KIBs) have recently caught major attention in the scientific community. KIBs share the working principles of LIBs and NIBs. Potassium is also cheap and abundant element, and thus, makes it an interesting alternative to lithium. Moreover, its standard reduction potential is similar to that of lithium (-2.93 V *vs.* SHE for K^+/K), allowing cell voltages similar to those of LIBs. Additionally, K^+ are much weaker Lewis acids which leads to a smaller Stoke radius or effective hydrated radius in solution. This results in a higher transport number and therefore, an increased power performance [66,67]. Thus, KIBs might also be an alternative beyond LIBs.

Among metal ion batteries, recently magnesium or aluminium ion batteries have also been investigated as well as other technologies such as metal-sulfur or metal-air batteries. The latter ones are lately catching major attention owing to the high theoretical capacity

values and abundancy of sulfur and oxygen. However, the cell chemistry is complex and there are still many key issues to be solved toward practical device development.

Hence, huge research is being done in the field of batteries regarding materials and electrolytes in order to obtain high energy devices. Nevertheless, instead or apart from energy density, high power is sometimes also required. Thus, in parallel to batteries research, high power electrochemical capacitors, also known by the product names supercapacitors and ultracapacitors, have been under development.

1.4. Electrochemical capacitors

Electrochemical capacitors are based on two electrodes (symmetric or asymmetric) with a separator between them, charged by applying a potential difference between the electrodes which causes the charge migration toward the surface of the electrode with opposite polarity and the creation of a double layer. Consequently, they adopted the name of electrical double layer capacitors (EDLCs). Compared to conventional capacitors, EDLCs utilize high specific surface area (SSA) materials as electrodes instead of metal plates and a separator soaked in an electrolyte as a dielectric medium. This configuration allows increasing the capacitance and the energy by a factor of 10000 moving from micro- and milli-farad ranges of conventional capacitors to tens, hundreds and even thousands of farads per device. Unlike batteries that store/deliver high energy density values at discharge times in the range of hours, EDLCs can operate at much higher specific power by fast charging/discharging the device (*i.e.* in the range of seconds). In addition, they outperform batteries in longevity, owing to their long cycle life (*i.e.* > 100000 cycles). Unfortunately, the charge that can be stored in a double layer is very limited compared to the charge that can be stored by chemical reactions.

Moreover, owing to the key role that batteries played towards EVs and HEVs, they grab the attention of companies devoted to the development of electrochemical energy storage devices. Consequently, this slowed the development of electrochemical capacitors and

created a huge gap between the first patented electrochemical capacitor in 1957 by General Electric [68] until the first optimized and commercialized one in 1992 (go back to **Figure 1.4**). Although they were originally used for computer memory backups, electrochemical capacitors were later also implemented in other consumer electronics, *i.e.* photo flashes in digital cameras, uninterruptible power supplies (UPS), renewables, cranes, electric buses and defibrillators among others. However, it was not until the United States Department of Energy (DOE) suggested the potential use of electrochemical capacitors in HEVs when new companies emerged to develop and optimize the technology. Maxwell Technologies launched into the market the first optimized EDLC with low internal resistance and a 2.7 V cell voltage. Later, companies like Yunasko, Ioxus or Nesscap started commercializing cells with the same rated voltage and in parallel Maxwell achieved to develop higher cell voltage devices, *i.e.* 2.85 V and 3 V, allowing to store higher energy densities without losing power [69]. Currently, Skeleton Technologies, using patented curve graphene instead of conventional activated carbon (AC) as active material, claim to possess the highest energy and power density EDLCs in the market, offering industrial cells of 2.85 V with capacitance values ranging from 500 to 3200 F [70].

Owing to the enormous progress on this technology, these days different automotive companies have implemented electrochemical capacitors in their fuel-saving start-stop systems. This way, the EDLC module is charged when the car brakes and afterwards the charge is released when the car starts. This already implemented technology by most automotive companies allows to save up to 30% of energy. Likewise, some companies devoted to urban transport have also implemented this technology in their energy optimization systems. In the case of a tram, this not only reduces the energy consumption but also the visual impact by eliminating the catenary. An example close to us is the Basque company CAF Power & Automotive, who since 2010 has implemented this energy storage technology in different city trams such as in Seville, Zaragoza, Tallinn, Luxembourg or Kaohsiung [71].

1.4.1. Working principles of EDLCs

Charge in EDLCs is stored by a physical mechanism consisting on ion adsorption/desorption on the surface of the electrodes. Owing to the non-faradaic charge storage mechanism, which does not involve any chemical reaction, these devices can stand millions of cycles. They are built using high SSA carbons with a narrow pore size distribution (PSD) both in the positive and the negative electrode and separated by a membrane as shown in **Figure 1.8a**. When an EDLC is charged (**Figure 1.8b**), electrons go from the positive electrode to the negative electrode through an external circuit. As a result, cations from the electrolyte are adsorbed on the surface of the negative electrode, while anions are on the positive electrode, forming the electrical double layer in both cases. During discharge, electrons migrate from the negative electrode to the positive electrode through an external circuit and ion desorption from the surface of the carbons occur.

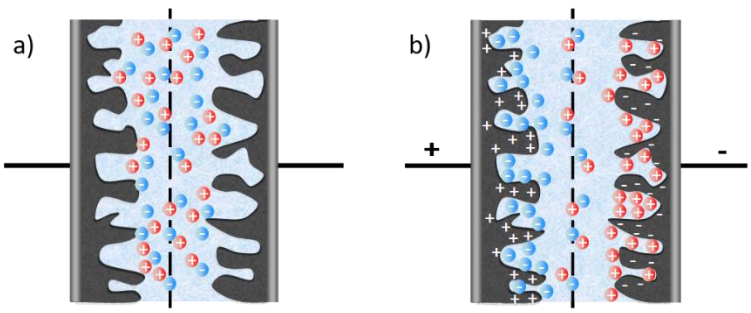

Figure 1.8. Scheme of an EDLC: a) at open potential and b) charged.

Mathematically, each electrode-electrolyte interphase represents a capacitor, thus, the complete EDLC can be considered as two capacitors connected in series, and therefore, the capacitance of the cells, C_{cell}, can be calculated by **Equation 1.VIII**, where C_+ and C_- represents the capacitance of the positive and negative electrode respectively.

$$\frac{1}{C_{cell}} = \frac{1}{C_+} + \frac{1}{C_-} \qquad \textbf{Equation 1.VIII}$$

The energy, *E*, stored in an EDLC is related to the charge at each interphase and potential difference, *V*, thus, it is directly proportional to the capacitance, *C*, as described by **Equation 1.IX**. Meanwhile the power, *P*, is the delivered energy per unit time, *t*, as stated in **Equation 1.X**.

$$E = \frac{1}{2} C V^2 \qquad \textbf{Equation 1.IX}$$

$$P = \frac{E}{t} \qquad \textbf{Equation 1.X}$$

It is necessary to minimize the overall resistance of the cell (*i.e.* current collectors, electrode materials, electrolyte and separator) if high power values want to be achieved. This resistance is normally named as the equivalent series resistance (ESR) and it defines the maximum power that is possible to achieve with an EDLC (**Equation 1.XI)**.

$$P = \frac{V_{max}^2}{4\ ESR} \qquad \textbf{Equation 1.XI}$$

Thus, in order to minimize the impact of the resistance, work must also be done in electrode engineering, hence improving the contact between material, current collector and separator.

1.4.2. Evolution, state-of-the-art and challenges for EDLCs

Since power density, cycle life and safe features of EDLCs fulfil market demands, one of the major challenges for electrochemical capacitors is to increase the energy density. Therefore, following **Equation 1.IX**, two different strategies can be followed. On one side, the capacitance could be increased, thus, research should be driven towards the development of materials with higher capacitance values. On the other side, the cell voltage could also be increased. In fact, this approach would have a major impact as energy is proportional to the square value of the voltage. Thereby, both approaches are discussed in the following sections.

1.4.2.1. Electrode materials for EDLCs

In order to obtain high capacitance values, EDLCs should be based on non-polarizable materials with high SSA that are good electrical conductors. Currently, carbons are the dominant material in EDLC technology owing to their lightweight, low-cost, abundancy, high electrical conductivity, thermal and chemical stability, high porosity and high SSA characteristics. One of their main properties is their versatility and ease of design. Since electrolyte ions are adsorbed onto the surface of the electrode, pore size of these materials needs to be tailored to fulfil the requirements of each system [72,73]. The IUPAC classified pores in three main categories, macropores (>50 nm), mesopores (2-50 nm) and micropores (<2 nm). In EDLCs micropores and mesopores are the most important ones. Micropores are responsible for the adsorption/desorption of ions and thus, of the capacitance, while the role of mesopores is to facilitate the ions and electrolyte propagation trough the carbon structure. In order to obtain high capacitance values the material should be tailored to the electrolyte that is used. Hence, pore size and ion size should be similar [74,75].

Among the most widely studied carbon materials, carbide derived carbons (CDCs), carbon nanotubes (CNTs), graphene and activated carbons (ACs) can be found. CDCs (**Figure 1.9a**) are attractive for their application in EDLCs owing to their unique nanoporous structure, high SSA (ranging from 1000 to 3000 $m^2 g^{-1}$), narrow PSD and possibility to tune the pore size and volume [76]. While, CNTs (**Figure 1.9b**) present multi-walled or single-walled nanoscale tubular morphology dominated by their mesoporous character which offers a combination of low electrical resistivity and high porosity in a very accessible structure [77]. Nevertheless, they show limited capacitance owing to their low SSA of only 120 - 500 $m^2 g^{-1}$. In the case of graphene, its 2D crystal lattice presents fast transport properties and theoretical calculation considering two side of hexagonal surface gives a 2630 $m^2 g^{-1}$ theoretical SSA. However, different techniques have been applied in order to increase the porosity and/or the SSA, such as thermal exfoliation of graphite oxide (**Figure 1.9c**) [78], activation of graphene [79,80] or

stacking small graphene sheets into a porous structure [81]. More recently, metal-organic frameworks (MOFs) have been introduced as high SSA materials (7000 $m^2 g^{-1}$) [82]. Their structural and compositional tunability and versatility have provided the potential to become a serious alternative to be used in energy storage devices [83].

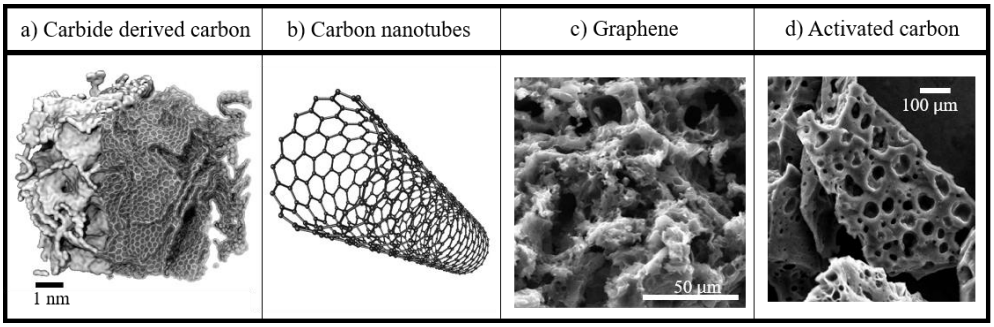

Figure 1.9. Different carbon materials for EDLCs: CNT [76], CNTs [77], graphene [84], and olive pits derived AC.

ACs are the oldest and best-known porous carbons. The use of AC in Egypt was described as early as in 1500 BC [85], whereas industrial production started in United States in 1913. Nowadays, they are the benchmark material for EDLCs owing to their high SSA, high availability, facile stablished industrial processes and low-cost. They are obtained from carbon-rich organic precursors through heat treatment (*i.e.* carbonization) and further activation. Precursors are obtained from many different sources such as renewable sources, fossil fuels or their derivative coal and coke. However, in the last years, ACs from natural precursors have attracted considerable attention owing to their great cycle stability, low-cost and attractive overall performance [86]. After the carbonization step, an amorphous carbon is obtained from the organic precursor, while activation leads to the formation of the porosity (**Figure 1.9d**). Two different activation procedures have been widely used: physical and chemical. Physical activation is followed at high temperatures under an oxidizing atmosphere (*e.g.* steam, CO_2…), whereas chemical activation is done by mixing the carbonized material with chemicals such as KOH or

K_2CO_3 followed by thermal treatment. Linares-Sólano *et al.* investigated the differences on the physicochemical characteristics of a coal tar pitch carbon fibres after physical and chemical activation separately. They concluded that the physical activation always shows wider PSD (5 - 30 nm). Moreover, to reach high porosity, higher burn-off is needed, which is not interesting from an industrial point of view. Additionally, it was demonstrated that similar SSA but with higher yield is possible to achieve when chemical instead of physical activation is utilized. Thus, it was concluded that the chemical activation is more selective and less destructive than the physical activation. Currently, most of the chemical activation are carried out using KOH [87]. One of the main advantages of ACs and its chemical activation method is that pore size can be easily controlled. Redondo *et al.* showed the textural properties of ACs prepared with different KOH/C ratios, demonstrating that SSA and PSD can be controlled changing the KOH/C ratio [73].

In **Table 1.1** different carbons derived from natural precursors and activated with KOH are summarized. It is shown that high SSA carbons and high specific capacitance values, utilizing commonly used organic electrolytes, are possible to obtain from biomass waste.

Table 1.1. ACs derived from different biomass sources: SSA and highest capacitance values in organic electrolytes.

Carbon source	**SSA ($m^2\ g^{-1}$)**	**Maximum capacitance ($F\ g^{-1}$)**	**Electrolyte**	**Ref.**
Coconut shell	1515	118	1M $TEABF_4$ (ACN)	[88]
Eucalyptus wood	2970	236	1M $TEABF_4$ (ACN)	[88]
Cellulose	2460	185	1M $TEABF_4$ (ACN)	[88]
Potato starch	2270	180	1M $TEABF_4$ (ACN)	[88]
Wheat straw	2316	251	1.2M $MeEt_3BF_4$ (ACN)	[89]
Cherry stone	1300	120	1M $(C_2H_5)_4NBF_4$ (ACN)	[90]
Olive pits	2400	150	1M $TEABF_4$ (ACN)	[72]

1.4.2.2. Electrolytes for EDLCs

The electrolyte also plays a key role in the development of high energy EDLCs. The most important features an electrolyte needs to fulfil are i) high ionic concentration, ii) small solvated ionic radius, iii) low viscosity, iv) high electrochemical stability, v) high conductivity, and vi) low cost. Electrolytes used for EDLCs are mainly classified in two different groups: aqueous and non-aqueous.

Aqueous electrolytes can be subdivided into acidic (H_2SO_4), alkaline (KOH) and neutral (KCl, $LiClO_4$, NaCl, Na_2SO_4,…). First EDLCs were based on aqueous electrolytes and high capacitance and ionic conductivity (1 S cm^{-1}) were achieved. However, they are hardly selected for commercial EDLCs because of their narrow voltage window. The latter is limited by the thermodynamic stability upper potential of just ~ 1.23 V. Despite this important drawback, they have been widely studied in literature owing to their low-cost and easy handling features [91–96]. Thus, the technology moved towards the use of organic electrolytes in order to work at higher voltages and consequently obtain higher energy devices.

Non-aqueous electrolytes can be classified in two big groups: organic electrolytes and ILs. Their ionic conductivity and specific capacitance are lower than those of aqueous electrolytes [97,98]. However, non-aqueous based supercapacitors can reach cell voltages of at least 2.7 V, which allows them to deliver higher energy density values. In the last years, many efforts have been made to increase their electrochemical stability [99].

In regard with organic electrolytes, most commercially available EDLCs systems are based on acetonitrile (ACN) or propylene carbonate (PC) solvents while the salts are usually tetraethylammonium tetrafluoroborate (TEA-NBF_4, NEt_4BF_4, Et_4NBF_4) or triethylmethylammonium tetrafluoroborate (TEMA-BF_4, NEt_3MeBF_4, Et_3MeNBF_4) [100]. Currently, research is focused on the search of alternative solvents in order to

increase the stability and widen the cell voltage [101]. Among many others, sulfones [102], nitriles [103,104] and more recently cyano esters [105–107] and butylene carbonate [108,109] have been studied.

The other main non-aqueous electrolytes are ILs, which hold promise for high voltage, safe and green electrolytes. Different cations such as pyrrolidinium (Pyr_{xx}^{+}) and imidazolium (im^{+}), and different anions such as tetrafluoroborate (BF_4^{-}), bis(tridluoromethane)sulfonylimife ($TFSI^{-}$) and bis(fluorosulfonyl)imide) (FSI^{-}) have been investigated [110]. The use of ILs has allowed EDLC cell voltages up to 3.5 - 3.7 V [111,112]. Nevertheless, due to their high viscosity and low conductivity, the charge storage efficiency of IL-based EDLCs at high power densities is quite low. Thus, with the aim of overcoming this limitation, new anions and cations or even combination of ILs with organic solvents are currently under study [113]. All the above-mentioned electrolytes are summarized in **Figure 1.10** by their operative voltage.

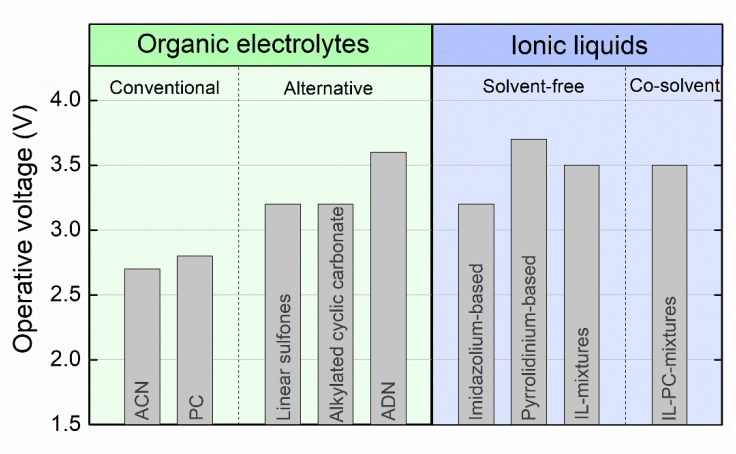

Figure 1.10. Comparison of operative voltages of different electrolytes used for EDLCs, modified from [99].

Nevertheless, the electrolyte that can meet all the ideal requirements has not yet been developed.

1.4.3. Beyond EDLCs

All efforts made in EDLC technology, going from electrode material to electrolyte research, have the ultimate goal of increasing the energy density of the overall device by either increasing the capacitance and/or the cell voltage. In the search of high energy electrochemical capacitors, a disruptive alternative was necessary, and in that context, the new metal ion capacitor technology emerged.

1.5. Metal ion capacitors

As already mentioned, EDLCs are devices able to be charged/discharged in few seconds with high efficiency and cycle life (>100000 cycles). Contrary, batteries are charged/discharged in several hours and their cycle life is significantly lower (~1000 cycles). Both electrochemical energy storage devices have attracted a great deal of attention in recent years owing to their use in EVs or HEVs. However, the power capability of batteries is significantly lower due to the slow faradaic processes that define their charge storage mechanism. Thus, in order to give response at high power demanding situations, the combination of batteries and EDLCs was envisaged. Different approaches such as external or internal hybridization have been investigated. The external hybridization consists of a series or parallel connection of EDLCs and batteries, whereas the internal hybridization is done at the electrode level in the same device [114]. In the external hybridization, where power is limited by the battery and energy by the supercapacitor due to different technology specifications, the use of converters and complex controllers is needed [115]. Hence, the development of the Battery Management System (BMS) is complex and cost of the overall system increases.

Alternatively, the internal serial hybridization of a battery and an EDLC gave birth to a new technology named as hybrid supercapacitors or metal ion capacitors (MICs, being M = L for Li or N for Na). MICs store energy combining both faradic and non-faradaic mechanisms synergistically, allowing mid energy values at high power while maintaining

a cycle life approaching that of EDLCs. In these systems one of the electrodes stores charge by means of ion insertion/deinsertion in the bulk of the material (battery-type), and the other electrode stores charge by adsorption/desorption of ions on its surface (capacitor-type) (**Figure 1.11**). Hence, given by their dual nature, MICs are able to store high energy density thanks to their battery-type electrode at high power densities owing to the capacitor-type electrode. To clarify the benefits of developing MICs, different features of batteries and EDLCs are compared in **Table 1.2.**

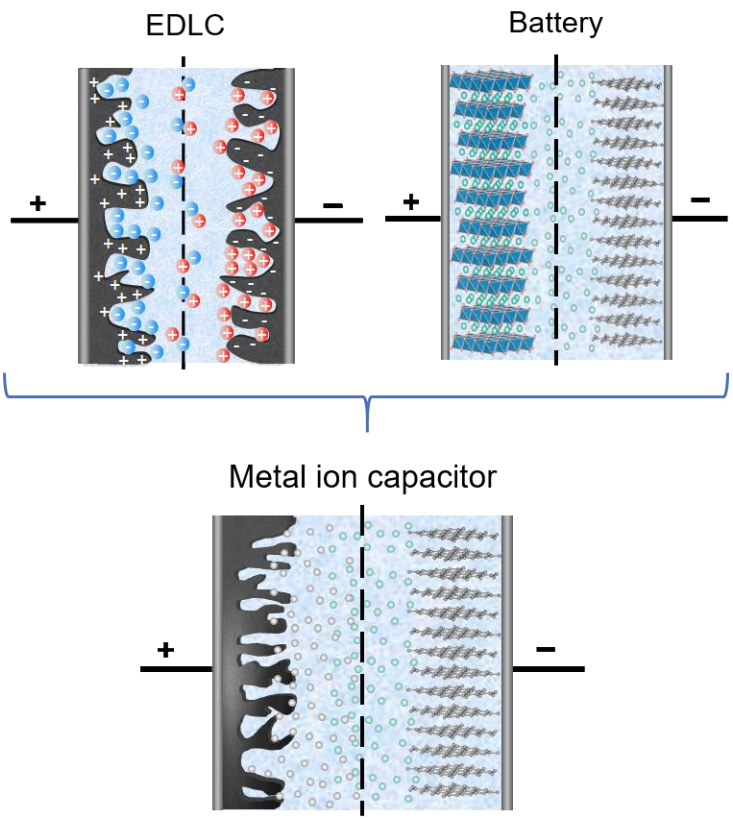

Figure 1.11. Internal serial hybridization to develop metal ion capacitors.

Among the studied MICs, lithium ion capacitors (LICs) are the most common and the only ones that are commercial. In commercialized systems, the maximum rated voltage

is 3.8 V, which is much higher than that of EDLCs, together with the higher capacitance, the energy density of LICs is approximately quadruple that of EDCLs. However, at the highest power peaks, LICs are not competitive with EDLCs yet, being limited by the slow faradaic mechanism of the battery-type electrode. Hence, the choice of the faradaic material plays a key role in the performance of the overall device and a thorough selection is necessary.

Table 1.2. Comparison of batteries, EDLCs and metal ion capacitor features.

Technology comparison	Batteries	EDLCs	Metal ion capacitors
Energy density	Very high	Low	Medium
Power density	Low	Very high	Medium-high
Discharge time	Hours	Seconds	Minutes-seconds
Internal resistance	High	Low	Low
Self discharge	Small	Big	Small
Lifetime	Relatively short	Long	Relatively long
Application	Medium power /high energy	Very high power /lower energy	High power/medium energy

Furthermore, the energy and power features of LICs enable the replacement of EDLCs in some applications such as servers, integrated circuits [116] or in kinetic energy recuperation systems [117]. Their use can result in a significant space saving and improved thermal design as the number of heat-generating components is reduced [118].

1.5.1. Working principles of metal ion capacitors

MICs are capable to deliver around 4-5 times higher energy density than EDLCs. This is obtained by modifying their configuration as schematically shown in **Figure 1.12**. In

most of these systems a battery-type material replaces the negative electrode of a typical EDLC. The former stores energy by means of faradaic reactions taking place in the bulk of the material allowing to target for higher energy densities by means of i) capacity increase owing to the higher amount of charge stored by a chemical reaction as compared to an electrosorption process and ii) widening the output cell voltage, since the potential of the negative electrode can be lowered. Furthermore, typical ACN-based electrolytes for EDLCs (which their upper potential is limited to 2.7 V) are replaced by a carbonate-based battery-type electrolyte allowing to usually increase the upper potential of the cell up to 4.2 V. Therefore, on the one hand, the low-potential battery-type electrode allows the full hybrid cell to store higher amount of charge and operate at higher cell voltage providing higher energy density. On the other hand, the capacitor-type electrode stores and releases energy rapidly providing high power density. Bringing both type of electrodes together enables the fabrication of a device with both high energy and high power densities combined with long cycle life [119].

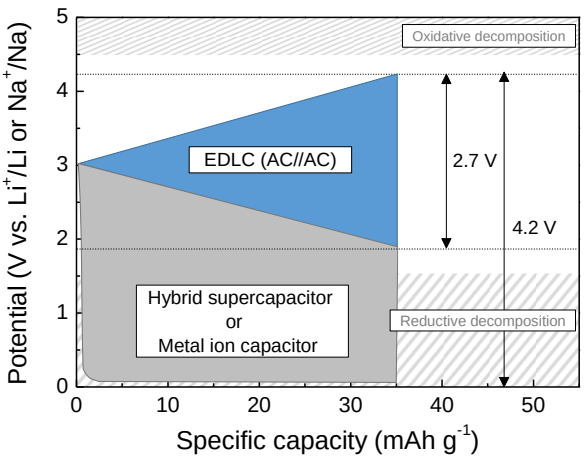

Figure 1.12. Comparison of voltage profiles of an EDLC and a hybrid supercapacitor, modified from [120].

In an ideal LIC where the cell voltage shows a linear dependence *vs.* time, *i.e.* symmetric charge/discharge, the amount of stored energy is proportional to the capacitance, *C*, and

to the square of the operating upper, V^2_{max}, and lower voltages, V^2_{min}, according to **Equation 1.XII**. Otherwise energy should be calculated by the integral of the voltage *vs.* capacity curve as in **Equation 1.VI**.

$$E = \frac{1}{2}C\left(V_{max}^2 - V_{min}^2\right) \qquad \textbf{Equation 1.XII}$$

Thus, the strategy to increase the energy density of a hybrid supercapacitor relays on increasing both the capacity and capacitance of the materials and the operative cell voltage. Those approaches have already been described in previous sections devoted to LIBs and EDLCs by material and electrolyte research.

1.5.2. State-of-the-art of LICs

The concept of asymmetric devices using a faradaic electrode was first coined at the end of the 1990s [121]. But it was not until 2001 when the first non-aqueous asymmetric electrochemical cell using nanostructured LTO (negative electrode) and AC (positive electrode) was reported in order to cover the energy-power gap existing between LIBs and EDLCs [122]. Since then, research on LICs has skyrocketed and the reported literature on this technology has raised from 52 publications in 2012 to 246 publications in 2018 (source: Web of Science) [123]. Not only the rise in publications but also the increasing number of commercial LICs from companies such as JM energy (2007), Taiyo Yuden (2010), Yunasko (2015) or Maxwell (2016) [124–127] demonstrates the potential market uptake of this technology. The possible end-user and market for LICs is focused on regenerative braking systems for energy harvesting from trains, automotive and light vehicles among others. Furthermore, Maxwell Technologies have already delivered the first commercial application of LICs which are used for rapid energy regeneration in city trams [128]. It is also very important to note that companies fabricating EDLCs have currently started producing LICs. As the president and chief executive officer of Maxwell Technologies mentioned, "*The commercial use of lithium ion capacitors represents a transformation in the energy storage industry*" [129]. This means that hybrid

supercapacitors are catching huge attention and probably will become a key technology among electrochemical energy storage systems in next years. **Figure 1.13** summarizes the state-of-the-art of some later discussed MICs together with the major market breakthroughs.

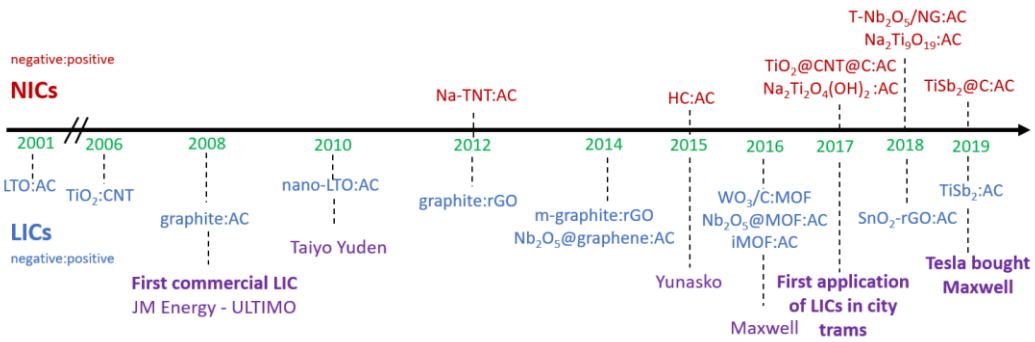

Figure 1.13. Historical evolution and present status of some later discussed LICs (blue) and NICs (red) and market breakthroughs (purple).

1.5.2.1. Positive electrodes for LICs

In order to keep the capacitor nature and provide a fast response, LIC performance needs to be governed by the capacitive positive electrode. Consequently, the best capacitor-type material should be selected for the latter. The material of choice should fulfil the following requirements: i) high SSA, ii) good electrical conductor, iii) high stability, iv) low cost, v) controllable pore size, and vi) ease of synthesis and design. Its selection is based on the research done in the field of EDLCs, thus, materials already reported for EDLCs such as ACs, CNTs [130], CDCs [131], graphene [132] and MOFs [133] have been explored in hybrid configuration. Additionally, composite materials combining both capacitive and faradaic materials have also been used to enhance the capacity stored in the positive electrode and obtain higher energy density devices [134].

Despite carbons are widely accepted as the material of choice for the positive electrode, LICs already reach a maturity degree where the next big challenge is going to be to overcome the limited charge storing nature of the positive electrode. Thus, research starts to focus on composite materials to be used in the positive electrode allowing targeting for increased capacities. Driven by the excellent features of LFP as cathode material in LIBs, such as high capacity, good rate performance and stability, Böckenfeld *et al.* reported in 2011 on a novel LFP/AC composite that exhibited large capacitance and excellent cycle stability. Rate capability tests of this blend showed 140 mAh g^{-1} capacity value at 20C with very high cycling stability [135]. Later, the same group reported on the same composite but varying the AC percentage. It was showed that a higher amount of AC has a positive impact on the electrode as it increases the conductivity and modifies the porosity around LFP particles [136]. On a further step, Shellikeri *et al.* recently reported a full hybrid laminate (pouch) cell combining LFP/AC as the positive electrode with a hard carbon (HC) as the negative electrode. This LIC displayed a specific energy density of 20 Wh kg^{-1}_{AM} which was higher in comparison with its equivalent cell configuration without LFP in the positive electrode that delivered only 14 Wh kg^{-1}_{AM} [137].

Cericola *et al.* also made an experimental analysis of the different possible approaches combining AC, LTO and LMO. Among others, they combined LTO with an AC to be used as the negative electrode and LMO with an AC to be used as the positive electrode in order to develop an internal parallel hybrid system. The obtained energy-to-power values were compared with the equivalent battery and capacitor showing that the LIC improved the capacitor in terms of energy density and the battery in terms of specific power [138].

Böckenfeld and Balducci also reported on the use of lithium vanadium phosphate ($Li_3V_2(PO_4)_3$, LVP) as a positive faradaic material using an AC as the negative electrode to develop a hybrid device. Nevertheless, due to the reduced voltage window of the system, the energy output was very limited. However, inverting the configuration by

using LVP as the negative and AC as the positive electrode the resulting LIC provided an average energy and power densities of 76.3 Wh kg^{-1}_{AM} and 3.2 kW kg^{-1}_{AM} respectively [139].

Nonetheless, ACs continue to be the material of choice for the positive electrode owing to their fast response, stability and low-cost. Driven by the environmental awareness, the use of natural waste precursors for the AC synthesis has been lately boosted. Several biomass sources such as coconut-shell [140], rice husk [141], pomelo peel [142] or olive pits [143] have already been used to prepare microporous ACs to be used as capacitor-type positive electrode in MICs technology.

1.5.2.2. Negative electrodes for LICs

Since it is widely accepted that carbonaceous materials are the best choice for the positive electrode, the faradaic negative electrode material has been the major focus of research toward high energy and high power density LICs [144]. On the contrary, within the large portfolio of battery-type materials, many materials with their own particular set of assets have been studied for LICs without discerning the best candidate amongst them. Even so, LTO and graphite were the first materials to be adapted to LIC technology.

Nanostructured LTO was the first battery-type material to be selected as negative electrode for a hybrid supercapacitor configuration owing to its 90% capacity utilization at 10C rate and 85 - 90% capacitance retention after 5000 cycles [122]. The authors showed the importance of particle size at high C-rates, and combining nanostructured LTO with an AC as the positive electrode the newly developed hybrid supercapacitor was able to provide up to a 5-fold increase in energy density with respect to its EDLC counterpart, preserving 90% of the capacity at a charge/discharge rate of 10C.

Later, in 2010, Naoi *et al.* prepared a unique nano-crystalline LTO grafted onto carbon nano-fibre anchors (nc-LTO/CNF) that improved the Li^+ diffusivity and electronic

conductivity in comparison with the bare LTO and showing an impressive rate capability performance going from 1C to 300C losing only 10% of the initial capacity. A LIC was developed using nc-LTO/CNF as the negative electrode and an AC as the positive electrode and a high energy density of 40 Wh L^{-1} at 1000 W L^{-1} (per electrode volume) was achieved [145]. In **Figure 1.14** Naoi *et al.* reviewed and compared different LTO materials in terms of charge/discharge time with their ultrafast nano-sized and carbon-grafted one, showing its excellent ability to perform at very low discharge time when combined with an AC.

Several strategies were adopted in order to get the best electrochemical performance of LTO for LIC technology. Using a novel atomic layer deposition seeded process nanosized LTO was wrapped with graphene nanosheets and a reversible capacity of 121 mAh g^{-1} at 100C with a 90% of capacity retention at 20C after 2500 cycles were obtained [146]. Nano-sized LTO was also prepared by high-energy milling at 3500 rpm and then post-calcined at 700ºC in order to improve the crystallinity, being able to obtain a good capacity retention of 99.9% after 1500 cycles [147]. In general, particle size reduction and crystallinity degree improvement are key parameters to obtain high rate capability and good capacity retention.

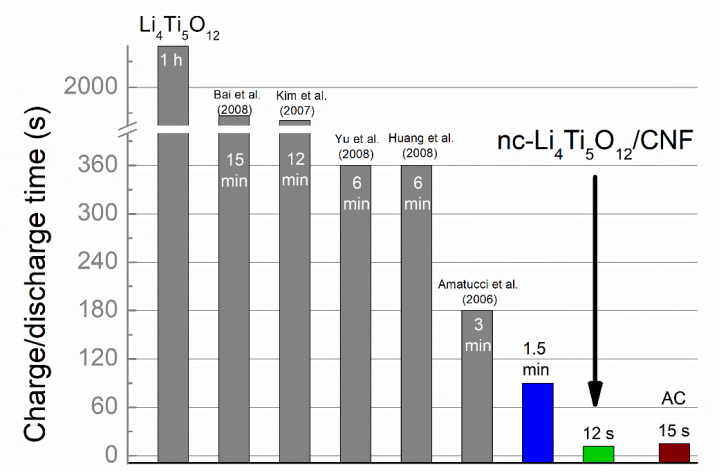

Figure 1.14. Charge/discharge time for different LTO materials, modified from [119].

Despite the fast response of LTO-based LICs, Li^+ intercalation/deintercalation into LTO takes place at 1.5 V *vs.* Li^+/Li. Therefore, there is no SEI formation on the surface of LTO and thus, the electrolyte choice is not dependent on the SEI forming ability. Nonetheless, the relatively high potential of LTO limits the cell voltage of the system. Therefore, alternative materials able to intercalate Li^+ in their structure at lower potentials should be considered to increase the energy density of the overall device.

Graphite, owing to its low intercalation potential (~0.1 V *vs*. Li^+/Li), low-cost and good cycle life, was studied as a potential negative electrode candidate in this technology. In this material as Li^+ intercalation occurs outside the stability window of common organic electrolytes a SEI is formed and thus, the choice of the electrolyte becomes very important. In 2007, Khomenko *et al.* developed a LIC in organic electrolyte (1 M $LiPF_6$ in EC:DMC) using graphite as the negative electrode and AC as the positive electrode. The cell voltage swept from 1.5 up to 4.5 V and the obtained energy density within a discharge time of 10 s was 50 Wh kg^{-1}_{AM} [148]. Later, Sivakkumar *et al.* focused on the optimization of graphite, investigating different types of graphite and evaluating the performance at high rates. It was found out that the thickness of the graphite electrode had a huge impact at high C-rates, since a 24 µm thick graphite electrode delivered 87 mAh g^{-1}, whereas a 100 µm thick electrode suffered a notorious decay, delivering only 64 mAh g^{-1} [149].

In 2012, Lee *et al.* developed a graphite-based LIC but this time the focus was set on the positive electrode. In order to overcome the capacitance limitation of standard ACs, an alternative urea-reduced graphene oxide (rGO) was used as the positive electrode. The reported specific energy density of 100 Wh kg^{-1}_{AM} at 1000 W kg^{-1}_{AM} represented an increase of 37.5% with respect to the benchmark LIC (graphite:AC) [150]. In order to also address the slow intercalation/deintercalation kinetic of graphite, the same group developed a simple treatment to modify the morphology and surface characteristics of graphite by engaging hydrogen peroxide to it, thus, increasing the edge planes of graphite. This enabled the formation of a more stable SEI that in the end enhanced the performance

of graphite. Finally, combining the urea-rGO together with the modified graphite, the new LIC reached 118 Wh kg^{-1}_{AM} at 1000 W kg^{-1}_{AM}. The cycle life of the reported system at 0.14 A g^{-1} in the 2.2 - 3.8 V cell voltage was of almost 97% after 3500 cycles [151].

The low operating potential of graphite allows increasing the cell voltage to its maximum. However, it can also lead to safety issues associated to lithium plating at high rates, moderate cycling stability and limited power response. Thus, although commercially available LICs are mostly based on graphite, other materials could offer improved features. Thereby, alternative carbonaceous materials with better kinetics that could improve safety, such as soft carbons or HCs, have been considered in the last years. The latter material and its application in MICs is studied in **Chapter 2** and **3**.

Beyond carbons, different type of insertion, alloy or conversion materials have also been studied in literature as negative electrodes. Shortly after the first reported LIC, in 2006, Wang *et al.* reported a LIC based on TiO_2 nanowires as the negative electrode and CNT as the positive electrode. However, low energy density values of 12 Wh kg^{-1}_{AM} at 300 W kg^{-1}_{AM} were obtained [130]. Despite the limited energy density, TiO_2 became of interest and new works have been reported in the last years [152,153].

Alternative transition metal oxides such as Nb_2O_5@graphene with large specific capacity and cycling stability also showed promising performance for high power applications [154]. Wang *et al.* reported a LIC based on AC and Nb_2O_5@graphene delivering an energy density of 29 Wh kg^{-1}_{AM} at 200 W kg^{-1}_{AM} [155]. Later, Liu *et al.* developed Nb_2O_5 quantum dots embedded in MOF derived nitrogen-doped porous carbon (Nb_2O_5-NC) matrix. Half-cell electrochemical results showed that 105 mAh g^{-1} specific capacity at 5 A g^{-1} (equal to 25C) was possible to obtain and maintain quite stable after 1000 cycles. The long-term cycling stability and the excellent high-rate capability boosted the use of Nb_2O_5-NC as negative electrode for LIC technology. Combined with an AC and in the voltage window of 0.5 - 4 V, 76.9 Wh kg^{-1}_{AM} at 400 W kg^{-1} and 20 Wh kg^{-1}_{AM} at

10 kW kg^{-1}_{AM} were achieved. Moreover, almost 85% capacitance was retained after 4500 cycles at 5 A g^{-1} [156].

Other transition metal oxides such as WO_3 were also reported. For instance, Xu *et al.* reported a hierarchical carbon coated WO_3 (WO_3/C) which showed a unique mesoporous structure to be used as anode material. The good rate performance of WO_3/C showing a capacity of 152.7 mAh g^{-1} at 10C, storing most of its charge in the sloping region below 0.5 V *vs.* Li^+/Li, made it very interesting to be used in LIC technology. Combined with a MOF derived nitrogen-doped carbon hollow polyhedral (MOF-NC) that delivered 100 F g^{-1} at 6 A g^{-1} and was able to maintain the capacitance in a 92.4% after 2000 cycles, a high performance LIC was possible to develop. The latter delivered a high energy density of 160 Wh kg^{-1}_{AM} at 174 W kg^{-1}_{AM}. Furthermore, this LIC showed 88% capacitance retention after 3000 cycles at 5 A g^{-1} [157].

Later, Ogihara *et al.* reported also on MOF materials but in this case to be used as negative electrode. Unlike other reported MOFs, their synthesized 2,6-naphthalene dicarboxylate dilithium (2,6-Naph$(COOLi)_2$, named as iMOF) showed a lithium intercalation reaction with two electron transfer of π-conjugated dicarboxylate operating at 0.8 V *vs.* Li^+/Li. Interestingly, it was shown that the self-assembled iMOF electrode was able to maintain a high reversible specific capacity (*i.e.* ~180 mAh g^{-1}) and small polarization at a high mass loading of *ca.* 14 mg cm^{-2}. Moreover, the areal capacity of the material increased linearly with the mass loading and reached an outstanding 2.66 mAh cm^{-2} value. A LIC based on a lithium pre-doped iMOF as the negative electrode and an AC as the positive electrode was characterized in the voltage range of 1.5 - 3.8 V and excellent volumetric energy-to-power values were reported, *i.e.* 60 Wh L^{-1} at 40 W L^{-1} and 30 Wh L^{-1} at 2.3 kW L^{-1} [158]. **Table 1.3** summarizes the most important specifications of above-discussed LICs.

Table 1.3. Summary of the above-mentioned LICs. *N. A. = not available

Negative electrode	**Positive electrode**	**Energy (Wh kg^{-1}_{AM})**	**Power (W kg^{-1}_{AM})**	**Stability**	**Ref.**
LTO	AC	N. A.	N. A.	95% after 5000 cycles at N. A.	[122]
Nc-LTO/CNF	AC	40 Wh L^{-1}	1000 W L^{-1}	90% after 9000 cycles at N. A.	[145]
Graphite	AC	100 50	2000 9000	85% after 10000 cycles at N. A.	[148]
Modified graphite	urea-rGO	118	1000	97% after 3500 cycles at 0.14 A g^{-1}	[151]
TiO_2	CNT	12	300	86% after 100 cycles at 0.2 A g^{-1}	[130]
N_2O_5@graphene	AC	29	200	N. A.	[156]
N_2O_5-NC	AC	76.9 20	400 10000	85% after 4500 cycles at 5 A g^{-1}	[156]
WO_3/C	MOF-NC	160	174	88% after 3000 cycles at 5 A g^{-1}	[157]
iMOF	AC	60 Wh L^{-1} 30 Wh L^{-1}	40 W L^{-1} 2300 W L^{-1}	85% after 1000 cycles at 10C	[158]

Going toward higher energy density and higher power density LICs, faradaic negative electrodes able to provide higher capacity values at high rates are still required. Up to day, the use of alloying materials such as tin, silicon or antimony have shown excellent potential to be used for high energy and high power LICs. The use of these materials will be deeply discussed in **Chapter 4** and **5**.

1.5.3. State-of-the-art of NICs

Although the viability of LIC technology is out of any doubt, with commercially available products in the market and LIC based solutions implemented in many fields, especially in the transportation industry, NICs are still in an earlier research stage. Motivated by the lithium scarcity, NIBs are considered an alternative to LIBs, and so, NICs could also be a future alternative to LICs. Nevertheless, currently both sodium technologies are unable to compete with their lithium counterparts and much research is still necessary in order to reach the market in the near future [159,160].

Moreover, contrary to LIC technology, where research has been focused in both positive and negative electrodes, in NIC technology, AC has been the most commonly used positive electrode and the research has been mainly focused on the search of different negative electrodes.

1.5.3.1. Negative electrodes for NICs

Given the dual battery-supercapacitor nature of MICs, NIC technology takes also advantage of the research already done in anode materials for NIBs. Research on NICs began in 2012 when Yin *et al.* reported a NIC based on porous carbon as the positive electrode and Na_4TiO_4 nanotubes (Na-TNT) as the negative electrode. Na-TNTs were synthesized by a hydrothermal treatment and then heat-treated at different temperatures. The best sample showed *ca.* 150 mAh g^{-1} at 0.17 A g^{-1} and a sloping region below 0.6 V *vs.* Na^+/Na. The full NIC device, cycled between 0 - 3 V, exhibited a maximum energy density of 34 Wh kg^{-1}_{AM} at a power density of 120 W kg^{-1}_{AM}, while at 800 W kg^{-1}_{AM} the energy density was 12 Wh kg^{-1}_{AM}. Moreover, after 1000 cycles at 0.25 A g^{-1} the capacitance retention was around 80% [161].

In 2015, the first dual carbon NIC using in both electrodes carbonaceous materials prepared from the same precursor (*i.e.* peanut shell), was reported by Mitlin's group

[162]. On one side, the AC used as the positive electrode displayed a hierarchical porous architecture with a thickness below 15 nm, a high SSA of 2396 $m^2\ g^{-1}$ and a high oxygen doping of 13.51 wt%. This material showed a specific capacity of 161 mAh g^{-1} at 0.1 A g^{1} and 73 mA g^{-1} at 25.6 A g^{-1}. On the other side, peanut shell derived HC was used as the ion intercalation negative electrode, delivering a specific capacity of 315 mAh g^{-1} combining a sloping region and a flat plateau below 0.1 V *vs.* Na^+/Na. The NIC built with the above-mentioned materials, showed the best energy-to-power density values find in literature for NICs up to day, delivering energy densities of 201 Wh kg^{-1}_{AM} at 285 W kg^{-1}_{AM} and 76 Wh kg^{-1}_{AM} at 8500 W kg^{-1}_{AM} in the cell voltage of 1.5 - 4.2 V. Moreover, it showed promising capacity retention values of 72% and 88% between 1.5 - 3.5 V cell voltage after 10000 cycles at 6.4 A g^{-1} and 51.2 A g^{-1} respectively [162].

Similar materials to the ones used in LICs have also been studied for NICs. For instance, Zhu *et al.* incorporated CNTs in carbon coated TiO_2 nanorods in order to develop the anodic TiO_2@CNT@C material. In this work the influence of adding CNTs was studied. TiO_2@CNT@C showed superior specific capacity and lower charge transfer resistance than TiO_2@C, owing to the higher electrical conductivity of CNTs. The rate performance of the latter displayed a reversible capacity of 142 mAh g^{-1} and 115 mAh g^{-1} at 2 A g^{-1} and 4 A g^{-1}, respectively. The performance of a biomass derived AC was also measured, showing a specific capacity of 40 mAh g^{-1} at 12 A g^{-1}, going for 2000 cycles with a minor capacity loss. The full NIC was assembled using TiO_2@CNT@C as the negative electrode and an AC as the positive electrode. In order to get the maximum capacity output a 1:3 mass ratio (TiO_2@CNT@C:AC) was set. This NIC presented a maximum energy density of 81.2 Wh kg^{-1}_{AM} at 126 W kg^{-1}_{AM} power density and at the high power density of 12.4 kW kg^{-1}_{AM} still delivered 37.9 Wh kg^{-1}_{AM} within a 1 - 4 V cell voltage. In addition, the NIC maintained 85% capacitance retention after 5000 cycles at 1 A g^{-1} [163].

Nb_2O_5, previously studied in LICs, has also been implemented in NICs. In this case, She *et al.* reported Nb_2O_5 nanoparticles anchored on a nitrogen-doped graphene

(T-Nb_2O_5/NG) as the negative electrode for Na-ion technology. Nb_2O_5 particles had and average size of 17 nm and were homogeneously anchored on the surface of the nitrogen-doped graphene which hindered particle growth and aggregation, as well as improving the electronic conductivity of the electrode. This material showed good rate capability (*i.e.* 101 mAh g^{-1} at 0.5 A g^{-1} and 68 mAh g^{-1} at 2 A g^{-1}) and good cycle life. Nevertheless, the assembly of T-Nb_2O_5/NG with an AC to develop a NIC did not show higher energy density than 40.5 Wh kg^{-1}_{AM} at 100 W kg^{-1}_{AM}. However, the authors highlighted the achievement of superior energy density values than other similar reported works [164].

Among the many different materials used as negative electrodes, intercalation compounds such as nanostructured $Na_2Ti_2O_4(OH)_2$ and $Na_2Ti_9O_{19}$ have also been investigated. On one side, Babu and Shaijumon reported on $Na_2Ti_2O_4(OH)_2$ as an intercalation pseudocapacitive material. It delivered *ca.* 40 mAh g^{-1} at 5 A g^{-1}, and in combination with a rice-husk derived AC the system achieved an energy density of 65 Wh kg^{-1}_{AM} at a power density of 500 W kg^{-1}_{AM} and 20 Wh kg^{-1}_{AM} at 5 kW kg^{-1}_{AM}. The capacitance retention after 3000 cycles at 1 A g^{-1} was 93% [165]. On the other side, Shaijumon's group reported on nanostructured $Na_2Ti_9O_{19}$ as Na^+ insertion material. Using this material as the negative electrode and an AC as the positive electrode, within an optimum mass ratio of 1:2.25 and in a cell voltage of 1 - 4.5 V, a NIC that exhibited a maximum energy density of 54 Wh kg^{-1}_{AM} at 687 W kg^{-1}_{AM} and a maximum power density of 5 kW kg^{-1}_{AM} delivering 20 Wh kg^{-1}_{AM} was developed. The NIC retained 75% of the initial capacity after 2000 cycles [166]. **Table 1.4** summarizes the most important specifications of the above-discussed NICs.

Table 1.4. Summary of the above-mentioned NICs. *N. A. = not available

Negative electrode	**Positive electrode**	**Energy (Wh kg^{-1}_{AM})**	**Power (W kg^{-1}_{AM})**	**Stability**	**Ref.**
Na-TNT	Porous carbon	34 12	120 800	80% after 1000 cycles at 0.25 A g^{-1}	[161]
Peanut shell derived HC	AC	201 76	285 8500	72% after 10000 cycles at 6.4 A g^{-1}	[162]
TiO_2@CNT@C	AC	81.2 37.9	126 12400	85% after 5000 cycles at 1 A g^{-1}	[163]
T-Nb_2O_5/NG	AC	40.5	100	63% after 5000 cycles at 1 A g^{-1}	[164]
$Na_2Ti_2O_4(OH)_2$	AC	65 20	500 5000	93% after 3000 cycles at 1 A g^{-1}	[165]
$Na_2Ti_9O_9$	AC	54	687	75% after 2000 cycles at N. A.	[166]

Although NICs are still an immature technology, it has been seen by this brief state-of-the-art that the research on this field is increasing notoriously as well as results are improving. However, there is still room for research and hence this thesis is focused on the development and optimization of new and promising NICs.

1.6. Scope and target of this thesis

The brief overview through the state-of-the-art of MICs has demonstrated that there is still research to be done in order to enhance the energy, power and durability of current devices. Hence, in this thesis, with the aim of overcoming those existing hybrid capacitors, while an olive pits derived AC has been the material of choice for the capacitor-type positive electrode, different battery-type negative electrodes have been

prepared and optimized in order to develop more energetic, more powerful and more stable LICs and NICs than existing ones.

In **Chapter 1**, this thesis is contextualized. Being LIBs and EDLCs pillar technologies for MICs, their comprehension is crucial and consequently they have been deeply reviewed. Later, MIC technology has been introduced in depth, from the working principles and challenges of this novel technology to the state-of-the-art of different existing LICs and NICs.

In **Chapter 2**, individual physicochemical and electrochemical characterization of biomass waste olive pits derived HC and AC has been followed. Then, using the HC as battery-type negative electrode and the AC as capacitor-type positive electrode, dual carbon LICs and NICs have been developed and optimized with the aim of getting the maximum energy-to-power outputs.

In **Chapter 3**, in order to try to widen the operative cell voltage of dual carbon MICs, the performance of these carbonaceous materials in pyrrolidonium-based ionic liquids and in a new electrolyte using an alternative solvent such as 3-cyanopropionic acid methyl ester has been investigated.

In **Chapter 4**, a self-standing, binder-free SnO_2 embedded in a reduce graphene oxide matrix (SnO_2-rGO) has been prepared by an *in-situ* synthetic approach. In this case, the rGO matrix helps to mitigate the volume changes that Sn-based alloy suffers during cycling. Physicochemical and electrochemical characterization have confirmed the optimum nano-structuring of the composite showing fast response at high current densities. Coupled with a highly porous olive pits waste derived AC as the capacitor-type positive electrode a LIC with an excellent energy density output has been fabricated.

In **Chapter 5**, $TiSb_2$ intermetallic compound has been selected as the battery-type negative electrode. The inactive phase, *i.e.* Ti, allows a fine dispersion of the active element, *i.e.* Sb, during cycling. This not only avoids the agglomeration of particles while

volume changes are given during cycling, but it also provides better conductivity to the material and longer cycle life. Thus, novel LICs using $TiSb_2$ as the negative electrode and olive pits derived AC as the positive electrode were developed. The effect of the electrode mass ratio in the energy delivery was studied. In the case of Na-ion technology, in order to enhance the Na^+ diffusion through $TiSb_2$, an additional carbon coating step was necessary. Moreover, as a result of the larger volume expansion of Na_3Sb (293%) with respect to its Li_3Sb (135%) counterpart, the final NIC lacks of stability. Hence, in order to increase the durability of these devices a detailed study in the $TiSb_2$ electrode fabrication process was carried out studying the effect of different binders.

In **Chapter 6**, a general discussion is followed, conclusions of this thesis are summarized and future perspectives are examined.

1.7. Bibliography

[1] C. Zou, Q. Zhao, G. Zhang, B. Xiong, Energy revolution: From a fossil energy era to a new energy era, Nat. Gas Ind. B. 3 (2016) 1–11. doi:10.1016/j.ngib.2016.02.001.

[2] 2030 Energy Strategy - Energy - European Commission, Energy. (n.d.). /energy/en/topics/energy-strategy-and-energy-union/2030-energy-strategy (accessed January 2, 2019).

[3] S. Sabihuddin, A.E. Kiprakis, M. Mueller, A Numerical and Graphical Review of Energy Storage Technologies, Energies. 8 (2015) 172–216. doi:10.3390/en8010172.

[4] EUROPA - Europe to experience pumped storage boom | SETIS - European Commission, (n.d.). https://setis.ec.europa.eu/setis-reports/setis-magazine/power-storage/europe-experience-pumped-storage-boom (accessed January 31, 2019).

[5] G. Alva, Y. Lin, G. Fang, An overview of thermal energy storage systems, Energy. 144 (2018) 341–378. doi:10.1016/j.energy.2017.12.037.

[6] P. Kurzweil, Gaston Planté and his invention of the lead–acid battery—The genesis of the first practical rechargeable battery, J. Power Sources. 195 (2010) 4424–4434. doi:10.1016/j.jpowsour.2009.12.126.

[7] P. Bernard, M. Lippert, Chapter 14 - Nickel–Cadmium and Nickel–Metal Hydride Battery Energy Storage, in: P.T. Moseley, J. Garche (Eds.), Electrochem. Energy Storage Renew. Sources Grid Balanc., Elsevier, Amsterdam, 2015: pp. 223–251. doi:10.1016/B978-0-444-62616-5.00014-0.

[8] P. Ruetschi, F. Meli, J. Desilvestro, Nickel-metal hydride batteries. The preferred batteries of the future?, J. Power Sources. 57 (1995) 85–91. doi:10.1016/0378-7753(95)02248-1.

[9] K.E. Aifantis, S.A. Hackney, R.V. Kumar, High Energy Density Lithium Batteries: Materials, Engineering, Applications, John Wiley & Sons, 2010.

[10] J. Kim, J. Oh, H. Lee, Review on battery thermal management system for electric vehicles, Appl. Therm. Eng. 149 (2019) 192–212. doi:10.1016/j.applthermaleng.2018.12.020.

[11] M. Yoshio, R.J. Brodd, A. Kozawa, eds., Lithium-ion batteries: science and technologies, Springer, New York, 2009.

[12] K. Ozawa, Lithium Ion Rechargeable Batteries: Materials, Technology, and New Applications, John Wiley & Sons, 2012.

[13] K. Mizushima, P.C. Jones, P.J. Wiseman, J.B. Goodenough, LixCoO2 (0<x<-1): A new cathode material for batteries of high energy density, Mater. Res. Bull. 15 (1980) 783–789. doi:10.1016/0025-5408(80)90012-4.

[14] Sony Energy Devices Corporation, (n.d.). https://www.sonyenergy-devices.co.jp/en/index.html (accessed January 2, 2019).

[15] N. Nitta, F. Wu, J.T. Lee, G. Yushin, Li-ion battery materials: present and future, Mater. Today. 18 (2015) 252–264. doi:10.1016/j.mattod.2014.10.040.

[16] K.-X. Wang, X.-H. Li, J.-S. Chen, Surface and Interface Engineering of Electrode Materials for Lithium-Ion Batteries, Adv. Mater. 27 (2015) 527–545. doi:10.1002/adma.201402962.

[17] L. Shui, F. Chen, A. Garg, X. Peng, N. Bao, J. Zhang, Design optimization of battery pack enclosure for electric vehicle, Struct. Multidiscip. Optim. 58 (2018) 331–347. doi:10.1007/s00158-018-1901-y.

[18] T. Ioannis, Li-ion batteries for mobility and stationary storage applications, (n.d.) 72.

[19] G.G. Amatucci, J.M. Tarascon, L.C. Klein, CoO2, The End Member of the Li x CoO2 Solid Solution, J. Electrochem. Soc. 143 (1996) 1114–1123. doi:10.1149/1.1836594.

[20] C. Liu, Z.G. Neale, G. Cao, Understanding electrochemical potentials of cathode materials in rechargeable batteries, Mater. Today. 19 (2016) 109–123. doi:10.1016/j.mattod.2015.10.009.

[21] J.W. Fergus, Recent developments in cathode materials for lithium ion batteries, J. Power Sources. 195 (2010) 939–954. doi:10.1016/j.jpowsour.2009.08.089.

[22] A.R. Armstrong, P.G. Bruce, Synthesis of layered LiMnO 2 as an electrode for rechargeable lithium batteries, Nature. 381 (1996) 499. doi:10.1038/381499a0.

[23] J.-M. Kim, H.-T. Chung, Role of transition metals in layered Li[Ni,Co,Mn]O2 under electrochemical operation, Electrochimica Acta. 49 (2004) 3573–3580. doi:10.1016/j.electacta.2004.03.025.

[24] C.S. Yoon, H.-H. Ryu, G.-T. Park, J.-H. Kim, K.-H. Kim, Y.-K. Sun, Extracting maximum capacity from Ni-rich Li[Ni0.95Co0.025Mn0.025]O2 cathodes for high-energy-density lithium-ion batteries, J. Mater. Chem. A. 6 (2018) 4126–4132. doi:10.1039/C7TA11346C.

[25] N.V. Kosova, E.T. Devyatkina, V.V. Kaichev, Optimization of Ni2+/Ni3+ ratio in layered Li(Ni,Mn,Co)O2 cathodes for better electrochemistry, J. Power Sources. 174 (2007) 965–969. doi:10.1016/j.jpowsour.2007.06.051.

[26] T. Ohzuku, M. Kitagawa, T. Hirai, Electrochemistry of Manganese Dioxide in Lithium Nonaqueous Cell III . X-Ray Diffractional Study on the Reduction of Spinel-Related Manganese Dioxide, J. Electrochem. Soc. 137 (1990) 769–775. doi:10.1149/1.2086552.

[27] H.M. Wu, J.P. Tu, Y.F. Yuan, Y. Li, X.B. Zhao, G.S. Cao, Electrochemical and ex situ XRD studies of a LiMn1.5Ni0.5O4 high-voltage cathode material, Electrochimica Acta. 50 (2005) 4104–4108. doi:10.1016/j.electacta.2005.01.026.

[28] K. Amine, H. Tukamoto, H. Yasuda, Y. Fujita, Preparation and electrochemical investigation of LiMn2 − xMexO4 (Me: Ni, Fe, and x = 0.5, 1) cathode materials for secondary lithium batteries, J. Power Sources. 68 (1997) 604–608. doi:10.1016/S0378-7753(96)02590-6.

[29] T.A. Arunkumar, A. Manthiram, Influence of Lattice Parameter Differences on the Electrochemical Performance of the 5 V Spinel LiMn1.5 − y Ni0.5 − z M y + z O4 (M = Li , Mg, Fe, Co, and Zn), Electrochem. Solid-State Lett. 8 (2005) A403–A405. doi:10.1149/1.1945369.

[30] S. Okada, S. Sawa, M. Egashira, J. Yamaki, M. Tabuchi, H. Kageyama, T. Konishi, A. Yoshino, Cathode properties of phospho-olivine LiMPO4 for lithium secondary batteries, J. Power Sources. 97–98 (2001) 430–432. doi:10.1016/S0378-7753(01)00631-0.

[31] L.-X. Yuan, Z.-H. Wang, W.-X. Zhang, X.-L. Hu, J.-T. Chen, Y.-H. Huang, J. B. Goodenough, Development and challenges of LiFePO 4 cathode material for lithium-ion batteries, Energy Environ. Sci. 4 (2011) 269–284. doi:10.1039/C0EE00029A.

[32] V. Etacheri, R. Marom, R. Elazari, G. Salitra, D. Aurbach, Challenges in the development of advanced Li-ion batteries: a review, Energy Environ. Sci. 4 (2011) 3243–3262. doi:10.1039/C1EE01598B.

[33] K. Persson, V.A. Sethuraman, L.J. Hardwick, Y. Hinuma, Y.S. Meng, A. van der Ven, V. Srinivasan, R. Kostecki, G. Ceder, Lithium Diffusion in Graphitic Carbon, J. Phys. Chem. Lett. 1 (2010) 1176–1180. doi:10.1021/jz100188d.

[34] S. Goriparti, E. Miele, F. De Angelis, E. Di Fabrizio, R. Proietti Zaccaria, C. Capiglia, Review on recent progress of nanostructured anode materials for Li-ion batteries, J. Power Sources. 257 (2014) 421–443. doi:10.1016/j.jpowsour.2013.11.103.

[35] G. Crabtree, E. Kócs, L. Trahey, The energy-storage frontier: Lithium-ion batteries and beyond, MRS Bull. 40 (2015) 1067–1078. doi:10.1557/mrs.2015.259.

[36] Y.P. Wu, E. Rahm, R. Holze, Carbon anode materials for lithium ion batteries, J. Power Sources. 114 (2003) 228–236. doi:10.1016/S0378-7753(02)00596-7.

[37] L. Shen, X. Zhang, E. Uchaker, C. Yuan, G. Cao, Li4Ti5O12 Nanoparticles Embedded in a Mesoporous Carbon Matrix as a Superior Anode Material for High Rate Lithium Ion Batteries, Adv. Energy Mater. 2 (2012) 691–698. doi:10.1002/aenm.201100720.

[38] Super Charge Ion Battery modules | Toshiba International Corporation - Oceania, (n.d.). https://www.tic.toshiba.com.au/super_charge_ion_battery_modules/ (accessed April 6, 2019).

[39] Lithium Ion Polymer Cells - High Energy High Power | Kokam, (n.d.). http://kokam.com/cell/ (accessed April 6, 2019).

[40] L. Ji, Z. Lin, M. Alcoutlabi, X. Zhang, Recent developments in nanostructured anode materials for rechargeable lithium-ion batteries, Energy Environ. Sci. 4 (2011) 2682–2699. doi:10.1039/C0EE00699H.

[41] X. Zhu, Y. Zhu, S. Murali, M.D. Stoller, R.S. Ruoff, Nanostructured Reduced Graphene Oxide/Fe2O3 Composite As a High-Performance Anode Material for Lithium Ion Batteries, ACS Nano. 5 (2011) 3333–3338. doi:10.1021/nn200493r.

[42] A. Wang, S. Kadam, H. Li, S. Shi, Y. Qi, Review on modeling of the anode solid electrolyte interphase (SEI) for lithium-ion batteries, Npj Comput. Mater. 4 (2018) 15. doi:10.1038/s41524-018-0064-0.

[43] O.A. Drozhzhin, V.A. Shevchenko, M.V. Zakharkin, P.I. Gamzyukov, L.V. Yashina, A.M. Abakumov, K.J. Stevenson, E.V. Antipov, Improving salt-to-solvent ratio to enable high-voltage electrolyte stability for advanced Li-ion batteries, Electrochimica Acta. 263 (2018) 127–133. doi:10.1016/j.electacta.2018.01.037.

[44] S.J. An, J. Li, C. Daniel, D. Mohanty, S. Nagpure, D.L. Wood III, The state of understanding of the lithium-ion-battery graphite solid electrolyte interphase (SEI) and its relationship to formation cycling, Carbon. 105 (2016) 52–76. doi:10.1016/j.carbon.2016.04.008.

[45] O. Borodin, X. Ren, J. Vatamanu, A. von Wald Cresce, J. Knap, K. Xu, Modeling Insight into Battery Electrolyte Electrochemical Stability and Interfacial Structure, Acc. Chem. Res. 50 (2017) 2886–2894. doi:10.1021/acs.accounts.7b00486.

[46] G. Gebresilassie Eshetu, S. Grugeon, S. Laruelle, S. Boyanov, A. Lecocq, J.-P. Bertrand, G. Marlair, In-depth safety-focused analysis of solvents used in electrolytes for large scale lithium ion batteries, Phys. Chem. Chem. Phys. 15 (2013) 9145–9155. doi:10.1039/C3CP51315G.

[47] A. Balducci, Ionic Liquids in Lithium-Ion Batteries, Top. Curr. Chem. 375 (2017) 20. doi:10.1007/s41061-017-0109-8.

[48] J. F. Wishart, Energy applications of ionic liquids, Energy Environ. Sci. 2 (2009) 956–961. doi:10.1039/B906273D.

[49] T. Vogl, C. Vaalma, D. Buchholz, M. Secchiaroli, R. Marassi, S. Passerini, A. Balducci, The use of protic ionic liquids with cathodes for sodium-ion batteries, J. Mater. Chem. A. 4 (2016) 10472–10478. doi:10.1039/C6TA02277D.

[50] L.G. Chagas, D. Buchholz, L. Wu, B. Vortmann, S. Passerini, Unexpected performance of layered sodium-ion cathode material in ionic liquid-based electrolyte, J. Power Sources. 247 (2014) 377–383. doi:10.1016/j.jpowsour.2013.08.118.

[51] L.T.M. Le, T.D. Vo, K.H.P. Ngo, S. Okada, F. Alloin, A. Garg, P.M.L. Le, Mixing ionic liquids and ethylene carbonate as safe electrolytes for lithium-ion batteries, J. Mol. Liq. 271 (2018) 769–777. doi:10.1016/j.molliq.2018.09.068.

[52] A. Guerfi, M. Dontigny, P. Charest, M. Petitclerc, M. Lagacé, A. Vijh, K. Zaghib, Improved electrolytes for Li-ion batteries: Mixtures of ionic liquid and organic electrolyte with enhanced safety and electrochemical performance, J. Power Sources. 195 (2010) 845–852. doi:10.1016/j.jpowsour.2009.08.056.

[53] A. Abouimrane, I. Belharouak, K. Amine, Sulfone-based electrolytes for high-voltage Li-ion batteries, Electrochem. Commun. 11 (2009) 1073–1076. doi:10.1016/j.elecom.2009.03.020.

[54] J. Alvarado, M.A. Schroeder, M. Zhang, O. Borodin, E. Gobrogge, M. Olguin, M.S. Ding, M. Gobet, S. Greenbaum, Y.S. Meng, K. Xu, A carbonate-free, sulfone-based electrolyte for high-voltage Li-ion batteries, Mater. Today. 21 (2018) 341–353. doi:10.1016/j.mattod.2018.02.005.

[55] D. Farhat, J. Maibach, H. Eriksson, K. Edström, D. Lemordant, F. Ghamouss, Towards high-voltage Li-ion batteries: Reversible cycling of graphite anodes and Li-ion batteries in adiponitrile-based electrolytes, Electrochimica Acta. 281 (2018) 299–311. doi:10.1016/j.electacta.2018.05.133.

[56] V. Palomares, M. Casas-Cabanas, E. Castillo-Martínez, M.H. Han, T. Rojo, Update on Na-based battery materials. A growing research path, Energy Environ. Sci. 6 (2013) 2312–2337. doi:10.1039/C3EE41031E.

[57] M. Sawicki, L.L. Shaw, Advances and challenges of sodium ion batteries as post lithium ion batteries, RSC Adv. 5 (2015) 53129–53154. doi:10.1039/C5RA08321D.

[58] N. Yabuuchi, K. Kubota, M. Dahbi, S. Komaba, Research Development on Sodium-Ion Batteries, (2014). doi:10.1021/cr500192f.

[59] W. Luo, F. Shen, C. Bommier, H. Zhu, X. Ji, L. Hu, Na-Ion Battery Anodes: Materials and Electrochemistry, (2016). doi:10.1021/acs.accounts.5b00482.

[60] M.M. Doeff, Y. Ma, S.J. Visco, L.C.D. Jonghe, Electrochemical Insertion of Sodium into Carbon, J. Electrochem. Soc. 140 (1993) L169–L170. doi:10.1149/1.2221153.

[61] B. Jache, P. Adelhelm, Use of Graphite as a Highly Reversible Electrode with Superior Cycle Life for Sodium-Ion Batteries by Making Use of Co-Intercalation Phenomena, Angew. Chem. Int. Ed. 53 (2014) 10169–10173. doi:10.1002/anie.201403734.

[62] D.A. Stevens, J.R. Dahn, High Capacity Anode Materials for Rechargeable Sodium-Ion Batteries, J. Electrochem. Soc. 147 (2000) 1271–1273. doi:10.1149/1.1393348.

[63] M.Á. Muñoz-Márquez, D. Saurel, J.L. Gómez-Cámer, M. Casas-Cabanas, E. Castillo-Martínez, T. Rojo, Na-Ion Batteries for Large Scale Applications: A Review on Anode Materials and Solid Electrolyte Interphase Formation, Adv. Energy Mater. (n.d.) n/a-n/a. doi:10.1002/aenm.201700463.

[64] Saurel Damien, Orayech Brahim, Xiao Biwei, Carriazo Daniel, Li Xiaolin, Rojo Teófilo, From Charge Storage Mechanism to Performance: A Roadmap toward High Specific Energy Sodium-Ion Batteries through Carbon Anode Optimization, Adv. Energy Mater. 0 (2018) 1703268. doi:10.1002/aenm.201703268.

[65] E. Irisarri, A. Ponrouch, M.R. Palacin, Review—Hard Carbon Negative Electrode Materials for Sodium-Ion Batteries, J. Electrochem. Soc. 162 (2015) A2476–A2482. doi:10.1149/2.0091514jes.

[66] S. Komaba, T. Hasegawa, M. Dahbi, K. Kubota, Potassium intercalation into graphite to realize high-voltage/high-power potassium-ion batteries and potassium-ion capacitors, Electrochem. Commun. 60 (2015) 172–175. doi:10.1016/j.elecom.2015.09.002.

[67] D. Stępień, Z. Zhao, S. Dsoke, Shift to Post-Li-Ion Capacitors: Electrochemical Behavior of Activated Carbon Electrodes in Li-, Na- and K-Salt Containing Organic Electrolytes, J. Electrochem. Soc. 165 (2018) A2807–A2814. doi:10.1149/2.0921811jes.

[68] H.I. Becker, Low voltage electrolytic capacitor, US2800616A, 1957. https://patents.google.com/patent/US2800616A/en (accessed January 8, 2019).

[69] Maxwell Technologies cell product lines Standard Series, XPTM Series, DuraBlue,Pseudocapacitors., Maxwell Technol. (n.d.). https://www.maxwell.com/products/ultracapacitors/cells (accessed April 5, 2019).

[70] S. Technologies, Buy the best ultracapacitors and supercapacitors online, (n.d.). https://www.skeletontech.com/ultracapacitor-webstore (accessed June 4, 2019).

[71] CAF hace del transporte público un medio de transporte sostenible, (n.d.). http://www.caf.net/es/ecocaf/ecotecnologias.php (accessed July 7, 2019).

[72] E. Redondo, J. Ségalini, J. Carretero-González, E. Goikolea, R. Mysyk, Relation between texture and high-rate capacitance of oppositely charged microporous carbons from biomass waste in acetonitrile-based supercapacitors, Electrochimica Acta. 293 (2019) 496–503. doi:10.1016/j.electacta.2018.10.031.

[73] E. Redondo, J. Carretero-González, E. Goikolea, J. Ségalini, R. Mysyk, Effect of pore texture on performance of activated carbon supercapacitor electrodes derived from olive pits, Electrochimica Acta. 160 (2015) 178–184. doi:10.1016/j.electacta.2015.02.006.

[74] J. Chmiola, G. Yushin, Y. Gogotsi, C. Portet, P. Simon, P.L. Taberna, Anomalous Increase in Carbon Capacitance at Pore Sizes Less Than 1 Nanometer, Science. 313 (2006) 1760–1763. doi:10.1126/science.1132195.

[75] C. Largeot, C. Portet, J. Chmiola, P.-L. Taberna, Y. Gogotsi, P. Simon, Relation between the Ion Size and Pore Size for an Electric Double-Layer Capacitor, J. Am. Chem. Soc. 130 (2008) 2730–2731. doi:10.1021/ja7106178.

[76] M. Oschatz, L. Borchardt, G.-P. Hao, S. Kaskel, Nanoporous Carbide-Derived Carbons as Electrode Materials in Electrochemical Double-Layer Capacitors, in: Nanocarbons Adv. Energy Storage, John Wiley & Sons, Ltd, 2015: pp. 417–453. doi:10.1002/9783527680054.ch15.

[77] A.G. Pandolfo, A.F. Hollenkamp, Carbon properties and their role in supercapacitors, J. Power Sources. 157 (2006) 11–27. doi:10.1016/j.jpowsour.2006.02.065.

[78] H.C. Schniepp, J.-L. Li, M.J. McAllister, H. Sai, M. Herrera-Alonso, D.H. Adamson, R.K. Prud'homme, R. Car, D.A. Saville, I.A. Aksay, Functionalized Single Graphene Sheets Derived from Splitting Graphite Oxide, J. Phys. Chem. B. 110 (2006) 8535–8539. doi:10.1021/jp060936f.

[79] A. Klechikov, G. Mercier, T. Sharifi, I.A. Baburin, G. Seifert, A.V. Talyzin, Hydrogen storage in high surface area graphene scaffolds, Chem. Commun. 51 (2015) 15280–15283. doi:10.1039/C5CC05474E.

[80] Y. Zhu, S. Murali, M.D. Stoller, K.J. Ganesh, W. Cai, P.J. Ferreira, A. Pirkle, R.M. Wallace, K.A. Cychosz, M. Thommes, D. Su, E.A. Stach, R.S. Ruoff, Carbon-Based Supercapacitors Produced by Activation of Graphene, Science. 332 (2011) 1537–1541. doi:10.1126/science.1200770.

[81] F. Zhang, T. Zhang, X. Yang, L. Zhang, K. Leng, Y. Huang, Y. Chen, A high-performance supercapacitor-battery hybrid energy storage device based on graphene-enhanced electrode materials with ultrahigh energy density, Energy Environ. Sci. 6 (2013) 1623–1632. doi:10.1039/C3EE40509E.

[82] O.K. Farha, I. Eryazici, N.C. Jeong, B.G. Hauser, C.E. Wilmer, A.A. Sarjeant, R.Q. Snurr, S.T. Nguyen, A.Ö. Yazaydın, J.T. Hupp, Metal–Organic Framework Materials with Ultrahigh Surface Areas: Is the Sky the Limit?, J. Am. Chem. Soc. 134 (2012) 15016–15021. doi:10.1021/ja3055639.

[83] D. Sheberla, J.C. Bachman, J.S. Elias, C.-J. Sun, Y. Shao-Horn, M. Dincă, Conductive MOF electrodes for stable supercapacitors with high areal capacitance, Nat. Mater. advance online publication (2016). doi:10.1038/nmat4766.

[84] J. Ajuria, M. Arnaiz, C. Botas, D. Carriazo, R. Mysyk, T. Rojo, A.V. Talyzin, E. Goikolea, Graphene-based lithium ion capacitor with high gravimetric energy and power densities, J. Power Sources. 363 (2017) 422–427. doi:10.1016/j.jpowsour.2017.07.096.

[85] L. Chin, Activated charcoal: Antidotal and other medical uses. By David O. Cooney. (Drugs and the Pharmaceutical Sciences, Vol. 9.) Dekker, 270 Madison Ave., New York, NY 10016. 1980. 160 pp. 15 × 23 cm. Price $23.50, J. Pharm. Sci. 69 (1980) 1361. doi:10.1002/jps.2600691138.

[86] L. Wei, G. Yushin, Nanostructured activated carbons from natural precursors for electrical double layer capacitors, Nano Energy. 1 (2012) 552–565. doi:10.1016/j.nanoen.2012.05.002.

[87] K. Kierzek, E. Frackowiak, G. Lota, G. Gryglewicz, J. Machnikowski, Electrochemical capacitors based on highly porous carbons prepared by KOH activation, Electrochimica Acta. 49 (2004) 515–523. doi:10.1016/j.electacta.2003.08.026.

[88] L. Wei, M. Sevilla, A.B. Fuertes, R. Mokaya, G. Yushin, Hydrothermal Carbonization of Abundant Renewable Natural Organic Chemicals for High-Performance Supercapacitor Electrodes, Adv. Energy Mater. 1 (2011) 356–361. doi:10.1002/aenm.201100019.

[89] X. Li, C. Han, X. Chen, C. Shi, Preparation and performance of straw based activated carbon for supercapacitor in non-aqueous electrolytes, Microporous Mesoporous Mater. 131 (2010) 303–309. doi:10.1016/j.micromeso.2010.01.007.

[90] M. Olivares-Marín, J.A. Fernández, M.J. Lázaro, C. Fernández-González, A. Macías-García, V. Gómez-Serrano, F. Stoeckli, T.A. Centeno, Cherry stones as precursor of activated carbons for supercapacitors, Mater. Chem. Phys. 114 (2009) 323–327. doi:10.1016/j.matchemphys.2008.09.010.

[91] J. Piwek, A. Platek, K. Fic, E. Frackowiak, Carbon-based electrochemical capacitors with acetate aqueous electrolytes, Electrochimica Acta. 215 (2016) 179–186. doi:10.1016/j.electacta.2016.08.061.

[92] X. Zhang, X. Wang, L. Jiang, H. Wu, C. Wu, J. Su, Effect of aqueous electrolytes on the electrochemical behaviors of supercapacitors based on hierarchically porous carbons, J. Power Sources. 216 (2012) 290–296. doi:10.1016/j.jpowsour.2012.05.090.

[93] H. Wu, K. Lian, Aqueous based asymmetrical-bipolar electrochemical capacitor with a 2.4 V operating voltage, J. Power Sources. 378 (2018) 209–215. doi:10.1016/j.jpowsour.2017.12.048.

[94] M. He, K. Fic, E. Frąckowiak, P. Novák, E.J. Berg, Influence of aqueous electrolyte concentration on parasitic reactions in high-voltage electrochemical capacitors, Energy Storage Mater. 5 (2016) 111–115. doi:10.1016/j.ensm.2016.06.001.

[95] L. García-Cruz, P. Ratajczak, J. Iniesta, V. Montiel, F. Béguin, Self-discharge of AC/AC electrochemical capacitors in salt aqueous electrolyte, Electrochimica Acta. 202 (2016) 66–72. doi:10.1016/j.electacta.2016.03.159.

[96] A. Lewandowski, A. Olejniczak, M. Galinski, I. Stepniak, Performance of carbon–carbon supercapacitors based on organic, aqueous and ionic liquid electrolytes, J. Power Sources. 195 (2010) 5814–5819. doi:10.1016/j.jpowsour.2010.03.082.

[97] J. Gamby, P.L. Taberna, P. Simon, J.F. Fauvarque, M. Chesneau, Studies and characterisations of various activated carbons used for carbon/carbon supercapacitors, J. Power Sources. 101 (2001) 109–116. doi:10.1016/S0378-7753(01)00707-8.

[98] A. Burke, Ultracapacitors: why, how, and where is the technology, J. Power Sources. 91 (2000) 37–50. doi:10.1016/S0378-7753(00)00485-7.

[99] F. Béguin, V. Presser, A. Balducci, E. Frackowiak, Carbons and Electrolytes for Advanced Supercapacitors, Adv. Mater. 26 (2014) 2219–2251. doi:10.1002/adma.201304137.

[100] E. Lust, A. Jänes, T. Pärn, P. Nigu, Influence of nanoporous carbon electrode thickness on the electrochemical characteristics of a nanoporous carbon|tetraethylammonium tetrafluoroborate in acetonitrile solution interface, J. Solid State Electrochem. 8 (2004) 224–237. doi:10.1007/s10008-003-0396-6.

[101] A. Balducci, Electrolytes for high voltage electrochemical double layer capacitors: A perspective article, J. Power Sources. 326 (2016) 534–540. doi:10.1016/j.jpowsour.2016.05.029.

[102] Electrolyte Systems for High Withstand Voltage and Durability I. Linear Sulfones for Electric Double-Layer Capacitors, (n.d.). http://jes.ecsdl.org/content/158/8/A872 (accessed February 2, 2019).

[103] C. Schütter, A.R. Neale, P. Wilde, P. Goodrich, C. Hardacre, S. Passerini, J. Jacquemin, A. Balducci, The use of binary mixtures of 1-butyl-1-methylpyrrolidinium bis{(trifluoromethyl)sulfonyl}imide and aliphatic nitrile solvents as electrolyte for supercapacitors, Electrochimica Acta. 220 (2016) 146–155. doi:10.1016/j.electacta.2016.10.088.

[104] A. Brandt, P. Isken, A. Lex-Balducci, A. Balducci, Adiponitrile-based electrochemical double layer capacitor, J. Power Sources. 204 (2012) 213–219. doi:10.1016/j.jpowsour.2011.12.025.

[105] C. Schütter, S. Passerini, M. Korth, A. Balducci, Cyano Ester as Solvent for High Voltage Electrochemical Double Layer Capacitors, Electrochimica Acta. 224 (2017) 278–284. doi:10.1016/j.electacta.2016.12.063.

[106] C. Schütter, T. Husch, V. Viswanathan, S. Passerini, A. Balducci, M. Korth, Rational design of new electrolyte materials for electrochemical double layer capacitors, J. Power Sources. 326 (2016) 541–548. doi:10.1016/j.jpowsour.2016.06.022.

[107] J. Krummacher, L.-H. Heß, Andrea. Balducci, Anodic Dissolution of Al Current Collectors in Unconventional Solvents for High Voltage Electrochemical Double-Layer Capacitors, ChemSusChem. 10 (2017) 4178–4189. doi:10.1002/cssc.201701422.

[108] K. Chiba, T. Ueda, Y. Yamaguchi, Y. Oki, F. Saiki, K. Naoi, Electrolyte Systems for High Withstand Voltage and Durability II. Alkylated Cyclic Carbonates for Electric Double-Layer Capacitors, J. Electrochem. Soc. 158 (2011) A1320–A1327. doi:10.1149/2.038112jes.

[109] L.H. Hess, A. Balducci, 1,2-butylene carbonate as solvent for EDLCs, Electrochimica Acta. 281 (2018) 437–444. doi:10.1016/j.electacta.2018.05.168.

[110] A. Brandt, S. Pohlmann, A. Varzi, A. Balducci, S. Passerini, Ionic liquids in supercapacitors, MRS Bull. 38 (2013) 554–559. doi:10.1557/mrs.2013.151.

[111] V.L. Martins, A.J.R. Rennie, N. Sanchez-Ramirez, R.M. Torresi, P.J. Hall, Improved Performance of Ionic Liquid Supercapacitors by using Tetracyanoborate Anions, ChemElectroChem. 5 (2018) 598–604. doi:10.1002/celc.201701164.

[112] R. Newell, J. Faure-Vincent, B. Iliev, T. Schubert, D. Aradilla, A new high performance ionic liquid mixture electrolyte for large temperature range supercapacitor applications (−70 °C to 80 °C) operating at 3.5V cell voltage, Electrochimica Acta. 267 (2018) 15–19. doi:10.1016/j.electacta.2018.02.067.

[113] T. Stettner, P. Huang, M. Goktas, P. Adelhelm, A. Balducci, Mixtures of glyme and aprotic-protic ionic liquids as electrolytes for energy storage devices, J. Chem. Phys. 148 (2018) 193825. doi:10.1063/1.5013117.

[114] D. Cericola, R. Kötz, Hybridization of rechargeable batteries and electrochemical capacitors: Principles and limits, Electrochimica Acta. 72 (2012) 1–17. doi:10.1016/j.electacta.2012.03.151.

[115] D. Cericola, P.W. Ruch, R. Kötz, P. Novák, A. Wokaun, Simulation of a supercapacitor/Li-ion battery hybrid for pulsed applications, J. Power Sources. 195 (2010) 2731–2736. doi:10.1016/j.jpowsour.2009.10.104.

[116] Lithium Ion Capacitors: An Effective EDLC Replacement | DigiKey, (n.d.). https://www.digikey.com/en/articles/techzone/2015/jan/lithium-ion-capacitors-an-effective-edlc-replacement (accessed March 4, 2019).

[117] M. Khodaparastan, A.A. Mohamed, W. Brandauer, Recuperation of Regenerative Braking Energy in Electric Rail Transit Systems, IEEE Trans. Intell. Transp. Syst. (2019) 1–17. doi:10.1109/TITS.2018.2886809.

[118] A. Sato, T. Yuden, TAIYO YUDEN Lithium Ion Capacitors: An Effective EDLC Replacement, (n.d.) 8.

[119] K. Naoi, 'Nanohybrid Capacitor': The Next Generation Electrochemical Capacitors, Fuel Cells. 10 (2010) 825–833. doi:10.1002/fuce.201000041.

[120] M. Lu, F. Beguin, E. Frackowiak, Supercapacitors: materials, systems and applications, John Wiley & Sons, 2013.

https://books.google.es/books?hl=es&lr=&id=uIt1kMzOduIC&oi=fnd&pg=PT7&dq=supercapacitors+materials,+systems+and+applications&ots=MlNXuVb_V-&sig=CvpUJeZxp0cOs3CEQbLJmCo3Kqo (accessed July 20, 2016).

[121] S. Razoumov, A. Klementov, S. Litvinenko, A. Beliakov, Asymmetric electrochemical capacitor and method of making, US6222723B1, 2001. https://patents.google.com/patent/US6222723B1/en (accessed June 12, 2018).

[122] G.G. Amatucci, F. Badway, A.D. Pasquier, T. Zheng, An Asymmetric Hybrid Nonaqueous Energy Storage Cell, J. Electrochem. Soc. 148 (2001) A930–A939. doi:10.1149/1.1383553.

[123] X. Wang, L. Liu, Z. Niu, Carbon-based materials for lithium-ion capacitors, Mater. Chem. Front. (2019). doi:10.1039/C9QM00062C.

[124] Lithium Ion Capacitor - LIC | JSR Micro, Inc., (n.d.). https://www.jsrmicro.com/emerging-technologies/lithium-ion-capacitor-lic (accessed December 2, 2017).

[125] Front runner of Lithium Ion Capacitor. JM Energy Corporation, (n.d.). http://www.jmenergy.co.jp/en/ (accessed November 30, 2017).

[126] Li-ion Capacitors - Yunasko is the developer and licensor of high power ultracapacitors, (n.d.). http://yunasko.com/en/products/lithium-ion-capacitors (accessed November 30, 2017).

[127] S. Technologies, Ultracapacitors and supercapacitors for energy storage, (n.d.). https://www.skeletontech.com (accessed November 30, 2017).

[128] M.T. Inc, Maxwell Technologies Delivers First Commercial Application of Lithium-Ion Capacitor Technology in China, (n.d.). https://www.prnewswire.com/news-releases/maxwell-technologies-delivers-first-commercial-application-of-lithium-ion-capacitor-technology-in-china-300354618.html (accessed December 2, 2017).

[129] Maxwell Technologies delivers first commercial application of Li-ion capacitor technology with CRRC-SRI in China, Green Car Congr. (n.d.). https://www.greencarcongress.com/2016/11/maxwell-technologies-delivers-first-commercial-application-of-li-ion-capacitor-technology-with-crrc-.html (accessed June 25, 2019).

[130] Q. Wang, Z.H. Wen, J.H. Li, A Hybrid Supercapacitor Fabricated with a Carbon Nanotube Cathode and a TiO2–B Nanowire Anode, Adv. Funct. Mater. 16 (2006) 2141–2146. doi:10.1002/adfm.200500937.

[131] T. Rauhala, J. Leis, T. Kallio, K. Vuorilehto, Lithium-ion capacitors using carbide-derived carbon as the positive electrode – A comparison of cells with graphite and Li4Ti5O12 as the negative electrode, J. Power Sources. 331 (2016) 156–166. doi:10.1016/j.jpowsour.2016.09.010.

[132] M.D. Stoller, S. Murali, N. Quarles, Y. Zhu, J.R. Potts, X. Zhu, H.-W. Ha, R.S. Ruoff, Activated graphene as a cathode material for Li-ion hybrid supercapacitors, Phys. Chem. Chem. Phys. 14 (2012) 3388–3391. doi:10.1039/C2CP00017B.

[133] J. Xu, Y. Li, L. Wang, Q. Cai, Q. Li, B. Gao, X. Zhang, K. Huo, P.K. Chu, High-energy lithium-ion hybrid supercapacitors composed of hierarchical urchin-like WO3/C anodes

and MOF-derived polyhedral hollow carbon cathodes, Nanoscale. 8 (2016) 16761–16768. doi:10.1039/c6nr05480c.

[134] A. Shellikeri, S. Yturriaga, J.S. Zheng, W. Cao, M. Hagen, J.A. Read, T.R. Jow, J.P. Zheng, Hybrid lithium-ion capacitor with LiFePO4/AC composite cathode – Long term cycle life study, rate effect and charge sharing analysis, J. Power Sources. 392 (2018) 285–295. doi:10.1016/j.jpowsour.2018.05.002.

[135] N. Böckenfeld, R.-S. Kühnel, S. Passerini, M. Winter, A. Balducci, Composite LiFePO4/AC high rate performance electrodes for Li-ion capacitors, J. Power Sources. 196 (2011) 4136–4142. doi:10.1016/j.jpowsour.2010.11.042.

[136] N. Böckenfeld, T. Placke, M. Winter, S. Passerini, A. Balducci, The influence of activated carbon on the performance of lithium iron phosphate based electrodes, Electrochimica Acta. 76 (2012) 130–136. doi:10.1016/j.electacta.2012.04.152.

[137] W.J. Cao, J.F. Luo, J. Yan, X.J. Chen, W. Brandt, M. Warfield, D. Lewis, S.R. Yturriaga, D.G. Moye, J.P. Zheng, High Performance Li-Ion Capacitor Laminate Cells Based on Hard Carbon/Lithium Stripes Negative Electrodes, J. Electrochem. Soc. 164 (2017) A93–A98. doi:10.1149/2.0351702jes.

[138] D. Cericola, P. Novák, A. Wokaun, R. Kötz, Hybridization of electrochemical capacitors and rechargeable batteries: An experimental analysis of the different possible approaches utilizing activated carbon, Li4Ti5O12 and LiMn2O4, J. Power Sources. 196 (2011) 10305–10313. doi:10.1016/j.jpowsour.2011.07.032.

[139] N. Böckenfeld, A. Balducci, On the use of lithium vanadium phosphate in high power devices, J. Power Sources. 235 (2013) 265–273. doi:10.1016/j.jpowsour.2013.02.019.

[140] S. Jayaraman, A. Jain, M. Ulaganathan, E. Edison, M.P. Srinivasan, R. Balasubramanian, V. Aravindan, S. Madhavi, Li-ion vs. Na-ion capacitors: A performance evaluation with coconut shell derived mesoporous carbon and natural plant based hard carbon, Chem. Eng. J. 316 (2017) 506–513. doi:10.1016/j.cej.2017.01.108.

[141] B. Babu, P.G. Lashmi, M.M. Shaijumon, Li-ion capacitor based on activated rice husk derived porous carbon with improved electrochemical performance, Electrochimica Acta. 211 (2016) 289–296. doi:10.1016/j.electacta.2016.06.055.

[142] F. Sun, J. Gao, Y. Zhu, X. Pi, L. Wang, X. Liu, Y. Qin, A high performance lithium ion capacitor achieved by the integration of a Sn-C anode and a biomass-derived microporous activated carbon cathode, Sci. Rep. 7 (2017) srep40990. doi:10.1038/srep40990.

[143] J. Ajuria, E. Redondo, M. Arnaiz, R. Mysyk, T. Rojo, E. Goikolea, Lithium and sodium ion capacitors with high energy and power densities based on carbons from recycled olive pits, J. Power Sources. 359 (2017) 17–26. doi:10.1016/j.jpowsour.2017.04.107.

[144] P.L. Taberna, P. Simon, J.F. Fauvarque, Electrochemical Characteristics and Impedance Spectroscopy Studies of Carbon-Carbon Supercapacitors, J. Electrochem. Soc. 150 (2003) A292–A300. doi:10.1149/1.1543948.

[145] K. Naoi, S. Ishimoto, Y. Isobe, S. Aoyagi, High-rate nano-crystalline Li4Ti5O12 attached on carbon nano-fibers for hybrid supercapacitors, J. Power Sources. 195 (2010) 6250–6254. doi:10.1016/j.jpowsour.2009.12.104.

[146] G. Wang, C. Lu, X. Zhang, B. Wan, H. Liu, M. Xia, H. Gou, G. Xin, J. Lian, Y. Zhang, Toward ultrafast lithium ion capacitors: A novel atomic layer deposition seeded preparation of Li4Ti5O12/graphene anode, Nano Energy. 36 (2017) 46–57. doi:10.1016/j.nanoen.2017.04.020.

[147] B.-G. Lee, H.-J. Ahn, J.-R. Yoon, Effects of post-calcination and mechanical pulverization on the electrochemical properties of nano-sized Li4Ti5O12 for hybrid capacitors, Curr. Appl. Phys. 17 (2017) 121–125. doi:10.1016/j.cap.2016.10.020.

[148] V. Khomenko, E. Raymundo-Piñero, F. Béguin, High-energy density graphite/AC capacitor in organic electrolyte, J. Power Sources. 177 (2008) 643–651. doi:10.1016/j.jpowsour.2007.11.101.

[149] S.R. Sivakkumar, J.Y. Nerkar, A.G. Pandolfo, Rate capability of graphite materials as negative electrodes in lithium-ion capacitors, Electrochimica Acta. 55 (2010) 3330–3335. doi:10.1016/j.electacta.2010.01.059.

[150] J.H. Lee, W.H. Shin, M.-H. Ryou, J.K. Jin, J. Kim, J.W. Choi, Functionalized Graphene for High Performance Lithium Ion Capacitors, ChemSusChem. 5 (2012) 2328–2333. doi:10.1002/cssc.201200549.

[151] J.H. Lee, W.H. Shin, S.Y. Lim, B.G. Kim, J.W. Choi, Modified graphite and graphene electrodes for high-performance lithium ion hybrid capacitors, Mater. Renew. Sustain. Energy. 3 (2014) 22. doi:10.1007/s40243-014-0022-9.

[152] H. Wang, C. Guan, X. Wang, H.J. Fan, A High Energy and Power Li-Ion Capacitor Based on a TiO2 Nanobelt Array Anode and a Graphene Hydrogel Cathode, Small. 11 (2015) 1470–1477. doi:10.1002/smll.201402620.

[153] H. Kim, M.-Y. Cho, M.-H. Kim, K.-Y. Park, H. Gwon, Y. Lee, K.C. Roh, K. Kang, A Novel High-Energy Hybrid Supercapacitor with an Anatase TiO2–Reduced Graphene Oxide Anode and an Activated Carbon Cathode, Adv. Energy Mater. 3 (2013) 1500–1506. doi:10.1002/aenm.201300467.

[154] M. Wei, K. Wei, M. Ichihara, H. Zhou, Nb2O5 nanobelts: A lithium intercalation host with large capacity and high rate capability, Electrochem. Commun. 10 (2008) 980–983. doi:10.1016/j.elecom.2008.04.031.

[155] L.P. Wang, L. Yu, R. Satish, J. Zhu, Q. Yan, M. Srinivasan, Z. Xu, High-performance hybrid electrochemical capacitor with binder-free Nb2O5@graphene, RSC Adv. 4 (2014) 37389–37394. doi:10.1039/C4RA06674J.

[156] S. Liu, J. Zhou, Z. Cai, G. Fang, Y. Cai, A. Pan, S. Liang, Nb2O5 quantum dots embedded in MOF derived nitrogen-doped porous carbon for advanced hybrid supercapacitor applications, J. Mater. Chem. A. 4 (2016) 17838–17847. doi:10.1039/C6TA07856G.

[157] J. Xu, Y. Li, L. Wang, Q. Cai, Q. Li, B. Gao, X. Zhang, K. Huo, P.K. Chu, High-energy lithium-ion hybrid supercapacitors composed of hierarchical urchin-like WO3/C anodes and MOF-derived polyhedral hollow carbon cathodes, Nanoscale. 8 (2016) 16761–16768. doi:10.1039/C6NR05480C.

[158] N. Ogihara, Y. Ozawa, O. Hiruta, A self-assembled intercalated metal–organic framework electrode with outstanding area capacity for high volumetric energy asymmetric capacitors, J. Mater. Chem. A. 4 (2016) 3398–3405. doi:10.1039/C5TA09559J.

[159] Faradion – The world leader in non-aqueous sodium-ion cell technology, (n.d.). https://www.faradion.co.uk/ (accessed September 23, 2019).

[160] Tiamat |, (n.d.). http://www.tiamat-energy.com/ (accessed September 23, 2019).

[161] J. Yin, L. Qi, H. Wang, Sodium Titanate Nanotubes as Negative Electrode Materials for Sodium-Ion Capacitors, ACS Appl. Mater. Interfaces. 4 (2012) 2762–2768. doi:10.1021/am300385r.

[162] J. Ding, H. Wang, Z. Li, K. Cui, D. Karpuzov, X. Tan, A. Kohandehghan, D. Mitlin, Peanut shell hybrid sodium ion capacitor with extreme energy–power rivals lithium ion capacitors, Energy Environ. Sci. 8 (2015) 941–955. doi:10.1039/C4EE02986K.

[163] Y.-E. Zhu, L. Yang, J. Sheng, Y. Chen, H. Gu, J. Wei, Z. Zhou, Fast Sodium Storage in TiO 2 @CNT@C Nanorods for High-Performance Na-Ion Capacitors, Adv. Energy Mater. 7 (2017) 1701222. doi:10.1002/aenm.201701222.

[164] L. She, Z. Yan, L. Kang, X. He, Z. Lei, F. Shi, H. Xu, J. Sun, Z.-H. Liu, Nb2O5 Nanoparticles Anchored on an N-Doped Graphene Hybrid Anode for a Sodium-Ion Capacitor with High Energy Density, ACS Omega. (2018). doi:10.1021/acsomega.8b02141.

[165] B. Babu, M.M. Shaijumon, High performance sodium-ion hybrid capacitor based on Na2Ti2O4(OH)2 nanostructures, J. Power Sources. 353 (2017) 85–94. doi:10.1016/j.jpowsour.2017.03.143.

[166] S.S.M. Bhat, B. Babu, M. Feygenson, J.C. Neuefeind, M.M. Shaijumon, Nanostructured Na2Ti9O19 for Hybrid Sodium-Ion Capacitors with Excellent Rate Capability, ACS Appl. Mater. Interfaces. 10 (2018) 437–447. doi:10.1021/acsami.7b13300.

CHAPTER 2

Dual carbon metal ion capacitors

Dual carbon metal ion capacitors

Nowadays, graphite is the most commonly used negative electrode for dual carbon MICs. Nevertheless, its sluggish kinetic limits the performance of MICs for applications demanding high power. Hence, it is necessary to find alternative materials that can provide an ultrafast response. Considering that electrode materials are one of the major cost increasing factors for MICs, a low-cost biomass waste (olive pits) was selected as the precursor to prepare the carbonaceous materials to be studied in dual carbon LICs and NICs. On the one hand, a disordered non-graphitizable HC was prepared to be used as the negative (battery-type) electrode. On the other hand, a high specific surface area and microporous AC was fabricated to be used as the positive (capacitor-type) electrode. Combining these two materials, long durability LICs and NICs with high energy and high power densities have been developed. The best designed LIC is able to deliver 87 Wh kg^{-1}_{AM} at 2.4 kW kg^{-1}_{AM} ($t_{discharge} \approx 3$ min) and 41 Wh kg^{-1}_{AM} at 26 kW kg^{-1}_{AM} ($t_{discharge} \approx 8$ s), whereas the best NIC is able to deliver 54 Wh kg^{-1}_{AM} at 1.4 kW kg^{-1}_{AM} ($t_{discharge} \approx 3$ min) and 24 Wh kg^{-1}_{AM} at 7.9 kW kg^{-1}_{AM} ($t_{discharge} \approx 10$ s). Showing a capacitance retention of 94% after 10000 cycles for the best LIC and 70% after 2000 cycles for the best NIC with the most appropriate constant current for each systems in order to be tested within a discharge time of 30 s.

Table of contents:

2.1. Introduction to carbonaceous materials and their application in metal ion capacitors

As introduced in **Chapter 1**, EDLCs consist normally on two ACs which store energy by means of adsorption/desorption of ions. Meanwhile LIBs are usually composed by graphite as the negative and $LiCoO_2$ or $LiFePO_4$ as the positive electrode. Hence, charge storage mechanism of each technology is described by non-faradaic and faradaic mechanisms, respectively. In the case of hybrid capacitors, a combination between both devices is followed normally replacing one AC from the EDLC by a carbonaceous (*e.g.* graphite) battery-type negative electrode. Moreover, up to day the only commercialized LIC by JM Energy is built by an AC and graphite as the positive and the negative electrode active materials, respectively. However, at laboratory scale, still some problems arise when targeting high power densities due to the sluggish kinetic of graphite. Thus, one of the major challenges of MICs is focused on the replacement of the battery-type negative electrode, since the AC is quite well-defined to be the best choice for the capacitor-type positive electrode.

Among negative electrodes, graphite has been the most commonly used one in LICs not only in academia [1–3] but also in industry [4–6]. This selection is made owing to its low reduction potential (*i.e.* ~0.1 V *vs*. Li^+/Li), low-cost and good cycle life. Moreover, since the intercalation processes take place at that low potential, the cell voltage of LICs can be widen up to 4.2 V, being the electrochemical stability of the electrolyte the only limiting factor. However, owing to their ability to form intercalation compounds with alkali metals, good conductivity and electrochemical activity at low potentials, different kind of carbonaceous materials such as soft carbons [7,8] and HCs [9,10] have also been studied.

2.1.1. Hard carbon, an alternative to graphite as negative electrode

Carbonaceous materials are usually classified according to their graphitization degree. Graphite is defined by aligned graphene layers bounded by weak van der Waals forces. Thus, as the layers are well stacked and completely ordered in parallel, the intercalation of lithium to form LiC_6 or sodium to form NaC_6 allows only the intercalation of one lithium or sodium per graphene sheet. However, it is known that NaC_6 is thermodynamically unstable in conventional carbonate ester-based electrolytes. Moriwake *et al.* showed that the stability of lithium or sodium graphite intercalation compounds (GICs) can be evaluated by calculating the formation energies through the density functional theory (DFT) calculations incorporating van der Waals functions. The formation energy is a sum of the total formation energy of the intercalated compound, the total energy of graphite, and the total energy of the pure metal. For cations larger than Na^+, the formation energy becomes more negative (more stable), owing to the greater ionicity between metal and carbon atoms as a result of the larger ionic radius. However, a negligible amount of Na^+ can be intercalated into graphite due to the thermodynamic instability of the created binary Na-GIC [11]. Contrary, even that Li^+ shows smaller ionic radius and the metal-carbon bond becomes weaker, being binding energies of GICs a dual contribution from ionic and covalent components between metal and carbon atoms and showing LiC_6 an increased covalent bond component, it overcomes the lower ionic component and becomes more stable than NaC_6 [12]. Hence, the impossibility to use graphite in ester-based electrolytes in NIBs was not only a matter of mismatch between Na^+ size and graphene structure, but also due to an energetically unfavourable formation of binary Na-GICs. Thus, in Na-ion chemistry the use of graphite was almost abandoned until the recent discovery of glyme-based electrolytes [13]. In these new electrolytes, solvated Na^+ are intercalated into graphene sheets forming a stable ternary GIC [14].

However, the low interlayer distance and consequently sluggish kinetic of graphite become the main limiting factor of this material when high rates are demanded in both Li-ion and Na-ion chemistries. Consequently, moving to disordered and non-graphitizable carbon materials, HCs are advocated in the last decades owing to their large storage capacity, low working potential and good cycling stability. Contrary to graphite, the larger interlayer distance of HCs may enhance the access of Na^+ to energetically stable sites near defects and facilitate the migration between layers [15].

HCs are easily obtained from the pyrolysis of solid-phase biomass sources or polymers at temperatures below 1500ºC and their microstructure is characterized by carbon atoms arranged in a planar hexagonal network. The high proportion of sp^3 hybridized carbon in precursors leads to a disordered microstructure with strong cross-linking that avoids any possible reorganization. This disordered orientation, with expanded interlayer distance, d_{002}, facilitates the Li^+ and Na^+ diffusion kinetic and propagation of the electrolyte into the microstructure of the material, leading to faster electrochemical responses [16,17].

2.1.1.1. Charge storage mechanism in HCs

The Li^+ or Na^+ insertion mechanism into the microstructure of the HC is similar for both technologies but rather different from graphite. In the latter, ion insertion occurs in a three-step reduction potential from 0.2 to 0.1 V *vs.* Li^+/Li, whereas in HCs, different steps can be identified depending on the chemistry. In Li-ion technology, following the "house of card" model, the charge storage mechanism was defined by single Li^+ insertion into the microstructure of the HC, and hence, a unique sloping region was defined [18]. However, recently, a two-step mechanism consisting on a first capacitive step where Li^+ are adsorbed in the edges of the HC microstructure, and a second step where ions are intercalated through the graphene sheets has been proposed [19].

Opposite to Li-ion, the use of HC was a game changer for Na-ion, enabling NIB technology. Thus, several research and many diverse Na^+ mechanisms have been proposed.

In 2000, when the use of HC in Na-ion technology was first reported [20], charge storage mechanism following the "house of cards" model was proposed. The model described a first sloping region where Na^+ is intercalated through the disordered graphene sheets (**Figure 2.1a** region Ia), followed by a second plateau region where Na^+ intercalation into micropores or pore filling occurs (**Figure 2.1a** region IIa). However, with the increasing research on HCs for NIBs, different mechanism questioning the classical model have arisen from several authors. In 2015, Bommier *et al.* demonstrated by galvanostatic intermittent titration (GITT) that in the sloping region (**Figure 2.1b** region Ib) the Na^+ diffusion (D_{Na^+}) into the HC microstructure was much faster than in the plateau region (**Figure 2.1b** region IIb), what described that first sodiation was given in easily accessible edge/defect sites. While in the plateau region, owing to a lower diffusion value, ion intercalation into graphene sheets was considered to occur, opposite to the pore filling suggested by the "house of cards" model. However, at the lowest potentials of that region, the increment on diffusion values may described that not only Na^+ intercalation but also minor pore filling was given (**Figure 2.1b** region IIIb) [21]. Later, in 2018, Saurel *et al.* described a four-step charge storage mechanism followed by i) capacitive storage in the open surface accessible to the electrolyte (**Figure 2.1c** region Ic), ii) pseudoabsorption at the internal surface, related to defects and which requires mass transport of Na^+ (**Figure 2.1c** region IIc), iii) interlayer intercalation (**Figure 2.1c** region IIIc) and iv) sodium clustering into the structure microporosity (**Figure 2.1c** region IVc) [22]. Similar mechanism based on D_{Na^+} results and *ex-situ* NMR was also proposed by Alvin *et al.* (**Figure 2.1d**). In the last case, NMR allowed confirming the formation of metallic Na-Na bonds in the micropores when the potential was below 0.1 V *vs.* Na^+/Na [23].

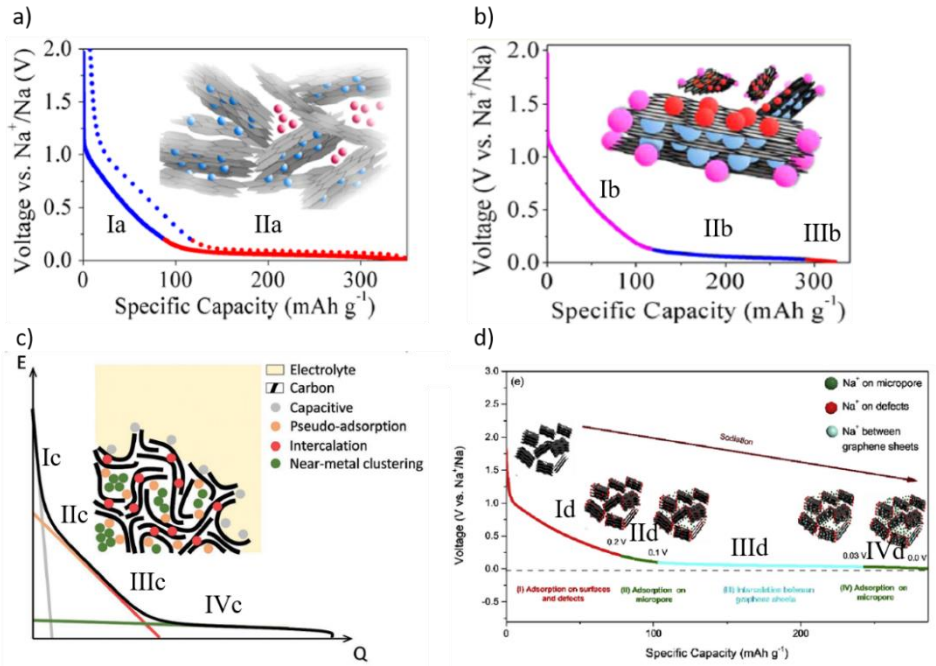

Figure 2.1. Different charge storage mechanism of Na^+ into HC proposed in literature [21–23].

The ability of HCs to store charge not only in a plateau region at low potentials –in the case of Na-ion- but also in a sloping region at higher potentials –in both technologies-, makes it a very attractive material to be used as negative electrode when fast response and safe devices are needed [24].

2.1.1.2. HCs in Li-ion technology

Among the most relevant works on HCs for LIBs, Li *et al.* reported on a HC prepared from potato starch granules which preserved the initial spherical shape. The first coulombic efficiency (CE) of this material was 73.1% and specific capacity values such as 500 mAh g^{-1} at C/10 and 430 mAh g^{-1} at 5C -maintaining an 86% of the initial capacity- were achieved [25]. Derived from another raw biomass as rice husk, Wang *et al*. reported on a HC within a fibrous network structure that was prepared using an acid

pre-treatment, hydrothermal carbonization, calcination and final SiO_2 removal. This unique microstructure material within a 98 $m^2 g^{-1}$ SSA showed a first cycle CE of 56%. The low CE was a consequence of i) the disordered nature of the HC and ii) additional SSA owing to its fibrous network. However, these features enabled to achieve a specific capacity value of 137 mAh g^{-1} at 10C, considering C to be 372 mAh g^{-1} [26]. Yang *et al.* later reported on a series of HCs with different porous structure. It was demonstrated that the porous carbons delivered higher reversible capacities than the non-porous ones. Measured at 5C, they showed as different capacity values as 330 mAh g^{-1} for the porous HC and 40 mAh g^{-1} for the non-porous one. Hence, the improved performance was ascribed to the larger SSA and suitable porous structure of the sample, which were beneficial for the accommodation of more Li^+ and electrolyte propagation [27].

Wang *et al.* used coal-tar pitch as a precursor to prepare soft carbon and phenolic resins to prepare HC. The impact of varying the amount of soft carbon from 0 wt% to 40 wt% and the heat-treatment temperature in the range from 900ºC to 1800ºC on the electrochemical performance of the as-prepared materials was studied. It was first shown that higher heat-treatment temperatures than 1200ºC reduced the rate capability performance of the material while lower temperatures (*i.e.* <900ºC) showed worst stability during constant current cycling. The most suitable amount of soft carbon was discovered to be 30 wt%, as higher soft carbon contents (*i.e.* 40 wt%) show a higher graphitic degree. Therefore, Li^+ diffusion in the layered structure became more difficult than in the disorder one and hence, lower capacity values were obtained at high rates. Thus, the HC prepared at 1200ºC within a 30 wt% content of soft carbon turned out to be the best one, showing specific capacity values of 225 mAh g^{-1} and 170 mAh g^{-1} at 2C and 10C, respectively [28]. On a different approach, Zhang *et al.* first reported on the use of an epoxy novolac resin derived HC enveloped with graphene as anode material for LIBs. As expected, owing to the outstanding conductivity of graphene, the preparation of a HC covered within a graphene network enhanced the electrochemical performance of the carbonaceous material, showing higher specific capacity values in all the studied current

densities (*i.e.* 410 *vs.* 300 mAh g^{-1} at 0.08 A g^{-1} and 240 *vs.* 120 mAh g^{-1} at 0.8 A g^{-1}) [29].

2.1.1.3. HCs in Na-ion technology

In regard with Na-ion technology, Dahn and Stevens reported for the first time on the use of HC in 2000 [20]. After this pioneering work, a huge avenue of research was opened, from the search of the best precursor to obtain the most beneficial microstructure for Na^+ diffusion to different models defining the charge storage mechanism [22]. On one side, a large amount of waste biomass, polymers derived from coal or petroleum, and polymers derived from biomass have been studied as precursors. Among carbohydrates, glucose [30], sucrose [31] and cellulose [32] have been the main sources, while as biomass waste, apple [33], cotton [34], peanut shells [35], argan [36] or rice husk [37] were some of the choices.

Among others, Väli *et al.* prepared D-glucose derived nanospheric HC by using a hydrothermal carbonization and subsequent pyrolysis at 1100ºC. Cyclic voltammogram (CV) of the material showed high Na^+ reduction/oxidation peaks revealing a good insertion/deinsertion of Na^+ into the microstructure of the material and showing a specific capacity of 160 mAh g^{-1} at 0.05 A g^{-1} over 200 cycles [30]. Cellulose, being the most abundant organic polymer on Earth, was also selected as a promising precursor to prepare HC [32]. Varying the pyrolysis temperature of this material from 700ºC to 1600ºC, it was observed that the plateau, slope, reversible and irreversible capacities were correlated. In parallel, the link between physicochemical features such as SSA, d_{002}, and pore size were also stablished. It was demonstrated that when a higher pyrolysis temperature was used, higher plateau and reversible capacities were obtained, whereas lower slope and irreversible capacity were achieved [32]. However, as it has been widely demonstrated, the optimum pyrolysis temperature changes from precursor to precursor.

In the case of using a raw biomass source like peanut shells, Lv *et al.* found 600ºC to be the most favorable pyrolysis temperature to prepare high electrochemical performance HCs for NIBs. Moreover, it was demonstrated that if the raw material was immersed into 100 ml 7% KOH dissolution before pyrolysis, a higher SSA (*i.e.* 706 $m^2 g^{-1}$) was possible to obtain and consequently a material with better electrochemical performance. Specific capacity values of 260 mAh g^{-1} at 0.05 A g^{-1} and 140 mAh g^{-1} at 1 A g^{-1} were obtained. The same material was also tested in Li-ion chemistry showing outstanding specific capacity values of 1210 mAh g^{-1} at 0.05 A g^{-1} and 380 mAh g^{-1} at 4 A g^{-1} [35]. Same authors recently reported on a similar work using orange peel precursor to get a high SSA (*i.e.* 638 $m^2 g^{-1}$) HC. In this case, also high specific capacity values such as 250 mAh g^{-1} at 0.05 A g^1 and 120 mAh g^{-1} at 1 A g^{-1} in Na-ion and 650 mAh g^{-1} at 0.05 A g^{-1} and 380 mAh g^{-1} at 1 A g^{-1} in Li-ion were obtained [38]. Similar to others, Rybarczyk *et al.* reported on the effect of the pyrolysis temperature for a rice husk derived HC, as this parameter impacts on the morphology, graphitization degree and amount of continuous channels (nanovoids). The latter significantly contributes to the Na^+ insertion and charge storage capacity. Moreover, it was found that the sample prepared at the highest temperature of 1600ºC showed higher amount of interconnected voids, which host Na^+ and contribute to the enhancement of the charge storage capacity of this material. Reversible specific capacity values of 250 mAh g^{-1} at C/5 and 100 mAh g^{-1} at 2C were obtained [37].

On the other side, plenty of research has also been carried out on HCs prepared from polymers derived from petroleum or coal such as phenolic resins [39] or polyacrilates [40], and derived from biomass such as pitches [41] or furfuryl alcohol [42]. Unlike raw biomass, where only physical parameters such as temperature, heating rate and gas flow can be controlled, in many polymers both chemical and physical parameters can be tuned enabling to obtain different carbon structures, textures and morphologies. Phenolic resins have usually been selected owing to their high carbon yield [43], nevertheless, their high toxicity, due to phenol/formaldehyde composition, and cost, advocates to replace them

by more environmentally friendly biomass derived polymers. Recently, Beda *et al.* reported on an alternative green phenolic resin. This was obtained dissolving phloroglucinol and glyoxylic acid, extracted from natural sources, in water/ethanol solvents allowing the formation of a green phenolic resin gel. Varying the experimental parameters such as solvent type, thermopolymerization and annealing temperature, the features of the HC such as yield, texture and structure were tuned. It was found that the solvent influenced on the required time to form the polymer and the cross-linking nature. In this case, water turned out to be the best solvent as only 12 h (*vs.* 3 days with ethanol) were needed to obtain a higher cross-linking nature. Whereas the carbon yield was controlled by the thermopolymerization temperature (34% at 80ºC and 22% at room temperature), the structure, d_{002}, and the disorder degree were determined by the thermal treatment temperature (*i.e.* d_{002} and SSA decreased with higher temperatures). The novel green phenolic resin was electrochemically characterized and a reversible capacity of 270 mAh g^{-1} was obtained at 37.2 mA g^{-1} current density [44]. Furfuryl alcohol provided by industrial feedstock also showed to be a good alternative to toxic phenolic resins as precursor for HCs [45]. Among others, Zhou *et al.* reported on a high-yield synthesis that showed to be highly scalable, low-cost and industrially appealing. Owing to the gas released during the high temperature pyrolysis, a HC with a SSA of 480 m^2 g^{-1} was obtained. Electrochemical characterization of the materials showed a large plateau at ~100 mV, which is representative of HCs in Na-ion, and delivered 200 mAh g^{-1} at 0.02 A g^{-1} and 50 mAh g^{-1} at 1 A g^{-1} [45].

All in all, it has been demonstrated that HCs are able to provide higher specific capacity values at higher rates in Li-ion rather than in Na-ion chemistry. Thus, while the HCs orientated to its Li-ion application have been more focused on their optimization (*i.e.* nano-structuration or addition of graphene), in Na-ion the research has been focused on the search of the best precursor and preparation method that could enhance the electrochemical performance.

In any case, motivated by the higher capacity values that HCs show at high rates and their above-mentioned better properties in comparison with graphite, looking toward high power demanding technologies such as MICs, in this thesis, an olive pits derived HC is selected for the realization of high energy and power density LICs and NICs. In the next section a brief review on the state-of-the-art of already reported dual carbon MICs is followed.

2.1.2. State-of-the-art of dual carbon MICs

After the first LTO:AC hybrid supercapacitor, plenty of efforts were focused on improving LTO properties, but its replacement by carbonaceous materials such as graphite or HC was also explored. The outstanding features of HC, not only its high specific capacities at high rates but also its normally natural source, makes it one of the most promising negative electrodes for the development of low-cost, durable and high energy and high power density MICs.

2.1.2.1. Dual carbon LICs

Recently, owing to the environmental concern, recycling and cost-effectiveness the use of inexpensive and renewable bio-sources to prepare carbonaceous materials have gained major attention. Numerous works have been reported regarding the use of biomass waste derived carbons for EDLCs, LIBs or NIBs, however, still research done in MICs is not abundant. On the one hand, among different reported dual carbon LICs derived from biomass sources, in 2016, Yang *et al*. reported on a system based on sisal fibre derived AC as the positive electrode. The nature of this biomass precursor –high crystalline cellulose and low hemicellulose and lignin content-, allowed creating high amount of defects and voids after the hydrothermal treatment. This facilitated the infiltration of KOH in its further activation, enabling the achievement of a high SSA material (*i.e.* 2111 $m^2 g^{-1}$) which delivers moderate specific capacity of 57 mAh g^{-1} at 0.1 A g^{-1} and showed 88% capacity retention after 5000 cycles at 1 A g^{-1}. Meanwhile mesocarbon

microbeds (MCMB) were used as the negative electrode. The developed 1:1 mass ratio LIC delivered an energy density per total active mass of 83 Wh kg^{-1}_{AM} at 128 W kg^{-1}_{AM} power density and 41 Wh kg^{-1}_{AM} at 5718 W kg^{-1}_{AM}, showing an energy retention of 92% after 1000 cycles at 0.5 A g^{-1} [46].

In 2017, Jayaraman *et al.* reported on the use of coconut shell derived mesoporous carbon (CS-AC) as the positive electrode and a commercial HC as the negative electrode for the realization of a LIC. The good properties of the CS-AC such as a high SSA of 1795 m^2 g^{-1} or granular morphology, together with the good behaviour of the HC showing ~350 mAh g^{-1} at 0.1 A g^{-1} encouraged them to developed a LIC. The system, assembled within a mass ratio of 1:3 (HC:CS-AC), delivered a maximum energy density of 121 Wh kg^{-1}_{AM} at 200 W kg^{-1}_{AM} [47]. More recently, in 2019, following the same biomass derived dual carbon configuration, Sennu *et al.* reported the use of wood as precursor for the development of a LIC. The high SSA of the AC and the amorphous carbon with crystalline strands which offers additional Li^+ storage sites, allowed developing a LIC delivering 216 Wh kg^{-1}_{AM} energy density at 160 W kg^{-1}_{AM}, and 70 Wh kg^{-1}_{AM} at 3000 W kg^{-1}_{AM}. Moreover, it showed a capacitance retention of ~90% after 5000 cycles at 0.5 A g^{-1} [48].

Leaving biomass waste sources aside, using glucose as precursor and MgO as a template, Li *et al.* designed a simple and controllable synthesis of holey carbon nanolayers (HCNs) which allowed controlling the microstructure and the porosity of the material. This way, the HCN used as the positive electrode (capacitive) was tailored to obtain a high SSA microporous material, while the material used as the negative electrode was not activated and hence, it was a mesoporous carbon nanolayer (CN). In the CN, two separate charge storage mechanism including diffusion control Li^+ intercalation and capacitive ion adsorption/desorption were described, being the latter about the 74% of the stored total capacity. Besides, it delivered 336, 290 and 256 mAh g^{-1} specific capacitites at 10, 15 and 20 A g^{-1} what really encouraged its use as negative electrode in LICs. Regarding the individual electrochemical characterization of the positive electrode (HCN), it was

characterized increasing the upper potential limit from 4 to 4.5 V showing no obvious distortion in CV curves. Moreover, it showed good rate capability of 103 mAh g^{-1} at 15 A g^{-1} and an initial capacity (*i.e.* 119 mAh g^{-1}) retention of 98% after 10000 cycles at 4 A g^{-1}. Motivated by the outstanding response of both electrodes, a 1:4 mass ratio (CN:HCN) LIC was developed. The latter was characterized in the cell voltage of 2 - 4.5 V delivering a maximum energy density of 181 Wh kg^{-1}_{AM} at 650 W kg^{-1}_{AM} and still 114 Wh kg^{-1}_{AM} at 65 kW kg^{-1}_{AM} [19].

Recently, Arnaiz *et al.* reported on a LIC based on an AC and a HC prepared from furfuryl alcohol-derived polymers. The polymerization technique used to make carbon from the furfuryl alcohol precursor was different from all the methods described earlier, and was flexible enough to make soft, high surface area AC, as well as a denser, low surface area HC. The HC and the HC-based negative electrode used in this study were targeted at a high-energy and high-power LIC application by specifically reducing the carbon particle size to sub-micrometric levels, using a HC with a SSA of ~300 m^2 g^{-1} and keeping the electrode mass loading below 2 mg cm^{-2}. The HC delivered a stable specific capacity of ~400 mAh g^{-1} *vs.* Li^+/Li at C/10, with excellent capacity retention of 50% at 10C (*i.e.* >200 mAh g^{-1}) and 25% at 50C (*i.e.* ~100 mAh g^{-1}). The AC used for the capacitor-type positive electrode was activated to a SSA of ~1670 m^2 g^{-1}. Overall, the LIC delivered a maximum energy density of 150 Wh kg^{-1}_{AM} at a power density of 150 W kg^{-1}_{AM}, with a 66% retention of the initial energy at the highly demanding 10000 W kg^{-1}_{AM} power peak. Additionally, long cycle life was measured, with 83% capacitance retention after 10000 cycles at 10 A g^{-1} constant current [42]. **Table 2.1** summarizes the above-mentioned state-of-the-art dual carbon LICs.

Table 2.1. Summary of the above-mentioned dual carbon LICs. *N. A. = not available

Negative electrode	Positive electrode	Energy (Wh kg^{-1})	Power (W kg^{-1})	Stability	Ref.
Mesocarbon microbeds	Sisal fibre AC	83 41	128 5718	92% after 1000 cycles at 0.5 A g^{-1}	[46]
Commercial HC	Coconut AC	121	200	N. A.	[47]
Commercial HC	Coconut AC	216 70	160 3000	90% after 5000 cycles at 0.5 A g^{-1}	[48]
Mesoporous carbon nanolayer (CN)	Holey carbon nanolayers (HCN)	181 114	650 6500	N. A.	[19]
Furfuryl alcohol HC	Furfuryl alcohol AC	150 99	150 10000	83% after 1000 cycles at 10 A g^{-1}	[42]

2.1.2.2. Dual carbon NICs

It was in 2012 when Kuratani *et al.* first developed a NIC combining HC as the negative electrode and AC as the positive one. The NIC was compared with its LIC counterpart and at low current densities (*i.e.* 0.5 mA cm^{-2}) similar capacity value of 0.2 mAh cm^{-2} was obtained. However, when increasing the current density to 50 mA cm^{-2}, whereas the LIC retained up to 30% of the initial capacity, the NIC decayed to 20% [49]. Some years later, in 2015, as previously mentioned in **Chapter 1** – **Section 1.5.3.1.**, Mitlin's group reported on the best dual carbon NIC developed up to these days. Within the cell voltage of 1.5 - 4.2 V, 201 Wh kg^{-1}_{AM}, 76 Wh kg^{-1}_{AM} and 50 Wh kg^{-1}_{AM} at 285 W kg^{-1}_{AM}, 8500 W kg^{-1}_{AM} and 16.5 kW kg^{-1}_{AM} were obtained respectively, showing 72% capacity retention after 10000 cycles at 6.4 A g^{-1} and 88% capacity retention after 10000 cycles at 51.2 A g^{-1} in a cell voltage of 1.5 - 3.5 V [50].

Later, in 2018, Li *et al.* reported on a NIC using nitrogen-doped hollow carbon nanowires (N-HCNWs) with high SSA and capacitive contribution as the negative electrode. This was combined with a commercial AC positive electrode to fabricate the final NIC. The novel N-HCNWs showed a 223.7 $m^2 g^{-1}$ SSA with both micropores and mesopores. Moreover, as other disordered carbons, a low crystalline degree and an interlayer spacing of ~0.4 nm was shown by XRD. However, in order to better understand the capacitive contribution of this material, CV tests at different scan rates were followed. This way, following the power law (from **Equation AI.IX** to **AI.XIV**), it was possible to differentiate the current coming from the capacitive and the insertion processes. Calculations demonstrated that 80% of the total stored charge was capacitive in origin. Besides, the rate capability measurement of the N-HCNWs revealed a 113 mAh g^{-1} and 90 mAh g^{-1} specific capacities at 2C and 5C, respectively. Combining this negative electrode with a commercial AC as the positive electrode, a NIC delivering 108 Wh kg^{-1}_{AM} energy density at 114 W kg^{-1}_{AM} power density and still 37.5 Wh kg^{-1}_{AM} at 9 kW kg^{-1}_{AM} working in a cell voltage of 0.5 - 4 V was developed. Furthermore, 70% of its initial capacity was retained after 2000 cycles [51].

Recently, Lee *et al.* reported on a NIC based on pyroprotein based monolithic electrodes, using pyroprotein-incorporated free-standing paper (PFP) with a SSA of ~97 $m^2 g^{-1}$ and microporous structure as the negative electrode, whereas as the positive electrode a hierarchicaly nanoporous pyroprotein (HNP) with a SSA of ~2880 $m^2 g^{-1}$ and fibrous structure was developed. The presence of pyroproteins in both materials encouraged the charge storage mechanism from oxygen and nitrogen heteroatoms, giving specific capacity values of ~228 mAh g^{-1} and ~205 mAh g^{-1} at 0.1 A g^{-1} for PFP and HNP, respectively. Combining both materials, the developed NIC delivered 150 Wh kg^{-1}_{AM} energy density at 200 W kg^{-1}_{AM} power density and 60 Wh kg^{-1}_{AM} at 12.1 kW kg^{-1}_{AM} in a cell voltage of 0.5 – 4.2 V, showing ~83% of capacitance retention after 2000 cycles at 0.5 A g^{-1} [52]. **Table 2.2** summarizes the above-mentioned state-of-the-art dual carbon NICs.

Table 2.2. Summary of the above-mentioned dual carbon NICs. *N. A. = not available

Negative electrode	Positive electrode	Energy (Wh kg^{-1})	Power (W kg^{-1})	Stability	Ref.
Peanut shell nanosheet carbon	Peanut shell ordered carbon	201 76	285 8500	72% after 10000 cycles at 6.4 A g^{-1}	[50]
Nitrogen doped hollow carbon nanowires	Commercial AC	108 37.5	114 9000	70% after 2000 cycles at N. A.	[51]
Commercial HC	coconut AC	150 60	200 12100	83% after 2000 cycles at 0.5 A g^{-1}	[52]

In this thesis, with the aim of developing dual carbon MICs, a regional waste such as olive pits biomass was used as natural source to prepare a faradaic HC and a microporous capacitive AC, which were used as the negative and the positive electrode respectively. Different to previously mentioned literature, where HC electrodes were indistinctly used for LIBs or LICs, in this work, they have been especially engineered to be implemented in LICs, a technology focused on power applications.

2.2. Olive pits derived HC as the negative electrode

It is well-known that electrode materials are one of the major contributors to the cost of supercapacitors [53]. Accordingly, the use of inexpensive electrode materials from renewable sources should be promoted [54]. In this framework, recycled olive pits have been selected. Yearly, around 1 million ton of olive pit waste is generated worldwide, of which a third originates in the Spanish olive oil industry [55,56]. Therefore, not only a low-cost precursor is used but the recycling of local bio-waste towards a more sustainable use of natural resources and the development of a more eco-friendly olive oil industry model is encouraged. Moreover, this set of natural electrode materials have been tailored to be valid for both Li- and Na-ion technologies, switching from one technology to the other by only shifting the electrolyte. This fact is not trivial since the size difference

between the ionic radius (*i.e.* 1.02 Å for Na^+ *vs.* 0.76 Å for Li^+) implies very often Li-ion and Na-ion technologies not to be interchangeable. However, their versatility enabled the fabrication of high energy and high power density LICs and NICs, with their own particular assets, suitable to cover a wide variety of different applications.

2.2.1. Material and electrode preparation: olive pits derived HC

In order to prepare the HC material, raw olive pits derived from oil industry were used as precursor. First, olive pits were crushed with a coffee grinder and then directly loaded in a stainless steel tubular furnace for the pyrolysis process by heating under an argon flow of 100 ml min^{-1} at a ramp rate of 5ºC min^{-1} to a pre-defined temperature of 900ºC and further holding it for 2 h. The pyrolysis temperature was fixed at 900ºC as it shows to be the most appropriate one in order to obtain a non-graphitizable carbon. The carbonization yield for olive pits was ~25% (**Scheme 2.1)**. Then, in order to engineer the material and reduce the particle size, a ball milling step was followed.

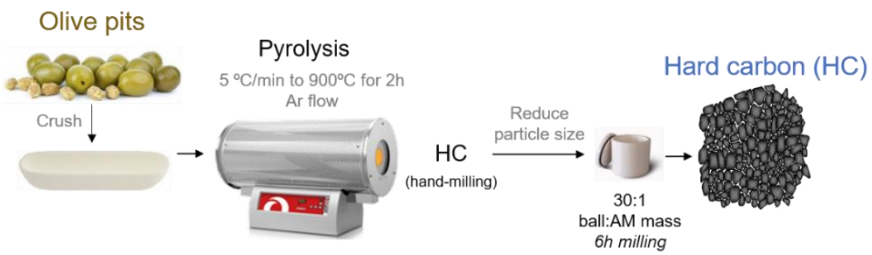

Scheme 2.1. Preparation route for olive pits derived HC.

In order to prepare laminates for further electrochemical characterization, the HC slurry was prepared by a mixture of HC, conductive carbon (Super C C65 Graphite & Carbon), and polyvinylidene fluoride (PVdF) as the binder in the mass ratio of 90:5:5 in N-methyl-2-pyrrolidone (NMP) followed by vigorous stirring for 1 h. The HC slurry was deposited onto a copper current collector sheet. Laminates were immediately transferred into a vacuum oven and dried at 80ºC under constant vacuum for 12 h before 0.95 cm^2 circular

individual electrodes were cut out. Looking toward high power applications, electrode mass loading was adjusted to obtain 1 - 2 mg cm^{-2} with a thickness of 30 – 40 µm.

2.2.2. Physicochemical characterization of the HC

Being olive pits a waste residue coming from the olive industry, the elemental analysis of the bare material shows a strong lignocellulosic character composed by 25% of α-cellulose, 35% of hemicellulose and 40% of lignin with a 51.45% of carbon content, a relatively high oxygen content of 43.28%, 6.01% of hydrogen, 0.27% of nitrogen and 0.01% of sulfur. Microstructural analysis of the HC (**Figure 2.2a**) reveals the typical lignocellulosic structure combining both cellulosic and spherical lignin moieties. Pyrolysis of lignocellulosic materials liberates most of the non-carbon elements, mainly hydrogen, oxygen and nitrogen in the form of gases and tars, leaving behind a rigid carbon skeleton formed by non-graphitic stacked graphene layers (**Figure 2.2b**) [57].

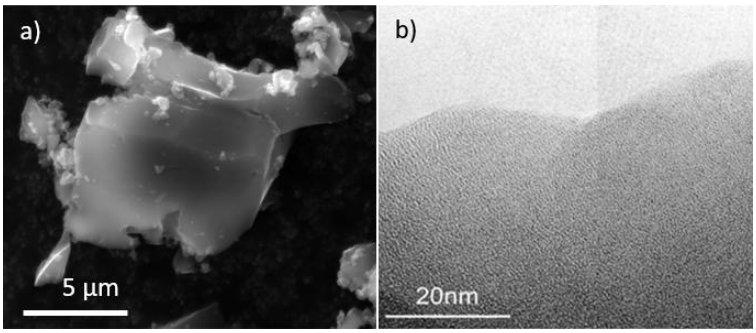

Figure 2.2. Microstrucutural analysis of the HC: a) SEM and b) TEM images.

The X-ray difraction (XRD) pattern of a commercial graphite (SFG 15L, IMERYS) and the olive pits derived HC are compared in **Figure 2.3a**. One sharpe peak corresponding to (002) plane is defined for the graphite, which shows an interlayer distance, d_{002}, of 3.36 Å calculated with Bragg's equation (**Equation AI.I**). However, two broad difraction peaks at 2θ angle of ~23º and ~43º corresponding to (002) and (100) reflexions are observed for the HC (inset **Figure 2.3a**), characteristic of a low graphitization degree. The d_{002} of the HC turns out to be *ca.* 3.9 Å, which facilitates the ion insertion into the graphene sheets in comparison with graphite. The structure of the HC was further

investigated by Raman spectroscopy. As shown in **Figure 2.3b**, while graphite exhibits a sharpe and very intese G-band (in-plane C-C vibrations), the HC exhibits a softer G-band at ~1580 cm^{-1} and a D-band at ~1340 cm^{-1} (a breathing mode only active when there is disorder in the structure). The ratio between the integral of D and G peaks from the HC was calculated by fitting the experimental curve with Gaussian and Lorentz equations and integrating them (**Equation AI.IV** to **AI.VI**). From the results obtained it is shown that the HC has a disordered morphology (I_D/I_G = 1.96). Regarding the surface characteristics, X-ray photoelectron spectroscopy (XPS) survey reveals the presence of oxygen heteroatoms (**Figure 2.3c**). The amount of oxygen is 10% which is within the typical oxygen content range found in HCs, which results from the oxidation of the surface during the synthesis and storage.

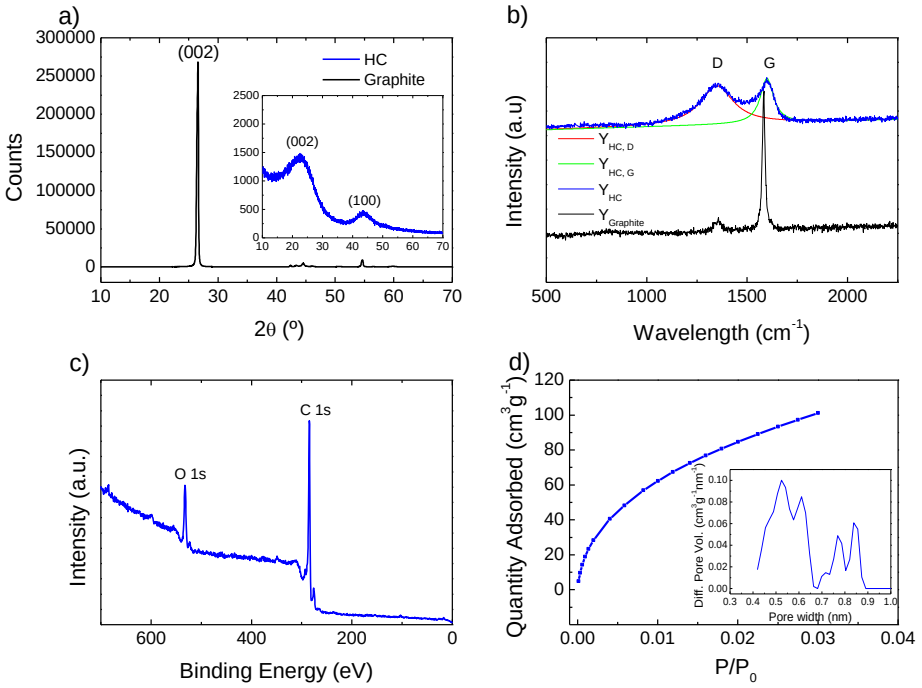

Figure 2.3. a) XRD pattern of graphite (black) and HC (blue), b) Raman spectra of graphite (black) and HC (blue), c) XPS spectra of the HC and d) CO_2 adosprtion isotherm, inset PSD.

Moreover, HCs supossed to have high ultramicroporosity [44]. Thus, in order to be able to access to pores below 1 nm, CO_2 adsorption/desorption measurement was followed.

Figure 2.3d shows the isotherm and the PSD of the olive pits derived HC. The 2D Non-Local Density Functional Theory (2D NLDFT) model used to calculate the PSD and SSA_{DFT} of the as-prepared HC describes a carbon slit pore model based on parallel circular graphene sheets as walls [58]. Thereby, using this model and the SAIEUS software, a SSA_{DFT} of 480 m^2 g^{-1} and an average PSD of 0.6 nm was obtained. Thus, even it is an insertion type material, this high SSA could also enable some capacitive behaviour.

2.2.3. Electrochemical characterization of the HC

The HC was characterized by means of CV and galvanostatic (GA) charge/discharges in 1 M $LiPF_6$ (EC:DMC) and 1 M $NaPF_6$ (EC:PC) electrolytes for Li- and Na-ion technology, respectively. **Figure 2.4a** and **2.4b** show the first three CVs recorded at 1 mV s^{-1} between 0.005 and 2 V *vs.* Li^+/Li and Na^+/Na respectively. In both cases voltammograms look similar although some differences can be inferred from the shape of the CV curves. Both voltammograms show a broad reduction peak below 1 V, which corresponds to the SEI formation. The reduction peak below 0.5 V represents the ion insertion mechanism, where most of the capacity is stored, while the oxidation peak at the same potential reveals the deinsertion of ions, showing a reversible capacity storage mechanism in both technologies.

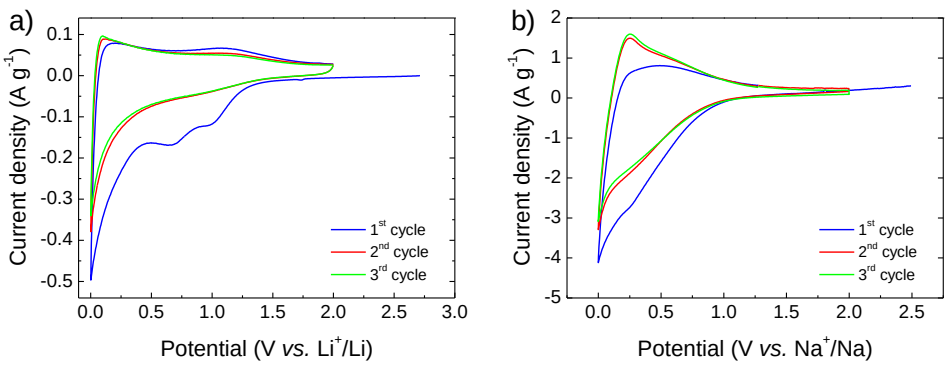

Figure 2.4. Cyclic voltammetry of the hard carbon between 0.005 – 2 V at 1 mV s^{-1} scan rate a) *vs.* Li^+/Li and b) *vs.* Na^+/Na.

GA charge/discharge profiles are shown in **Figures 2.5a** and **2.5b** and specific capacity values are calculated with **Equation AI.XV** and **AI.XVI**. The first charge step delivers a total specific capacity of 1300 mAh g^{-1} for Li-ion while it is quite lower for Na-ion, 500 mAh g^{-1}. In both cases SEI formation due to carbonate solvent decomposition starts at about ~ 1.0 - 0.8 V and then ion insertion begins [20]. However, significant differences arise in the second and posterior charge steps. The second cycle stabilizes at 390 mAh g^{-1} for Li-ion while it is considerably lower for Na-ion, set at 262 mAh g^{-1}. Analyzing the discharge profiles of HC in both technologies, as it has been reported in other works, different charge storage regions can be identified in olive pits derived HCs. Following the well-defined "house of cards" model, in Li-ion, the discharge profile of the HC shows a sloping profile below 1 V *vs.* Li^+/Li, where ions are intercalated into graphene sheets [20]. Despite in Na-ion the same sloping profile is observed, an additional plateau at 0.1 V *vs.* Na^+/Na is also visible, describing the intercalation of ions into the micropores of the material. However, the rate capability test reveals that lower capacity values are obtained in Na-ion in comparison with Li-ion chemistry. This might be mainly attributed to the larger instability of the SEI formed in Na-based systems [59] and hence leading to a more hindered insertion/deinsertion process. Nonetheless, high specific capacity values can be obtained in both technologies (**Figure 2.5c**), delivering as high as 260 mAh g^{-1} at 2C and 180 mAh g^{-1} at 20C when HC is tested in Li-ion technology and 200 mAh g^{-1} at 2C and 85 mAh g^{-1} at 20C when HC is tested in Na-ion technology. Being C the theoretical capacity of 372 mAh g^{-1} for carbonaceous materials. Moreover, outstanding capacity values such as 120 mAh g^{-1} and 70 mAh g^{-1} at 50C and 100C are achieved in Li-ion chemistry. In order to better understand the diffusion limitation of Na^+, electrochemical impedance spectroscopy (EIS) measurements before cycling at frequencies from 1 MHz to 10 mHz were followed and indicate that the charge transfer resistance is much higher for Na^+ than that for Li^+, which suggests a hindered diffusion of Na^+ throughout the electrode (**Figure 2.5d**) [60].

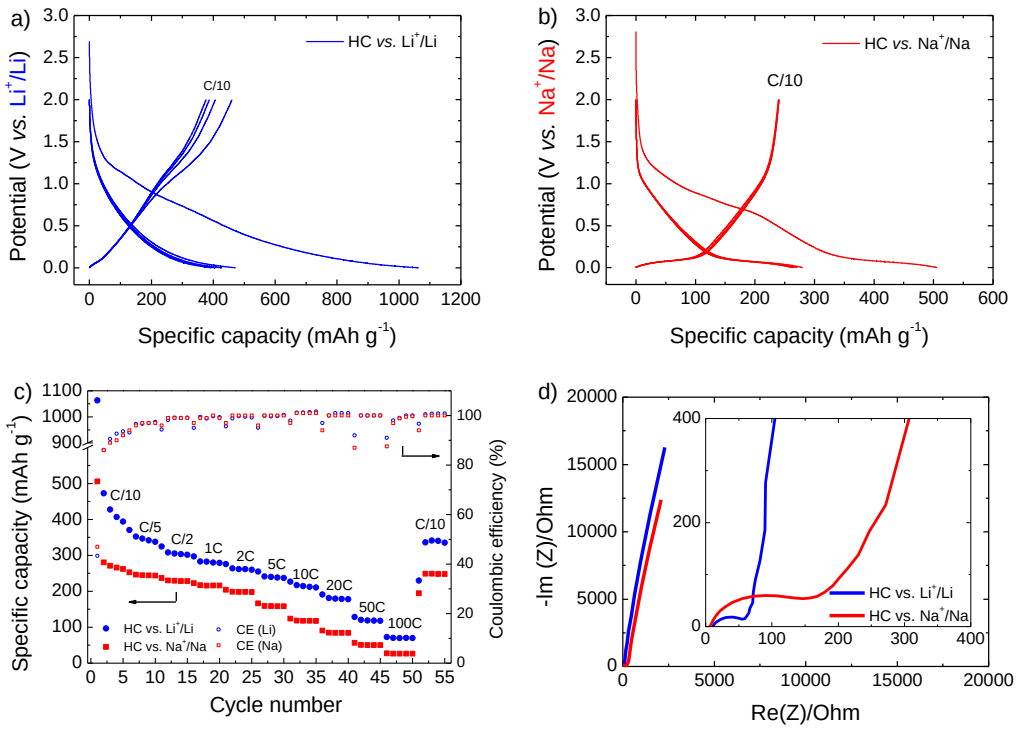

Figure 2.5. Electrochemical characterization of the HC between 0.005 and 2 V *vs.* Li^+/Li or Na^+/Na: a) Charge/discharge profiles in Li-ion, b) Charge/dishcarge profiles in Na-ion, c) Rate capability in Li- and Na-ion and d) EIS in Li- and Na-ion.

However, the high specific capacity values for the HC obtained in Li-ion chemistry might suggest that not only ion insertion/deinsertion –which is diffusion-controlled process- is taking place, but most probably also ion adsorption/desorption -capacitive controlled process- also plays a role. Hence, in order to study the diffusive and capacitive contribution of the HC in both technologies, CVs at different scan rates were followed [61]. This way, kinetic information was obtained according to the power-law (**Equation 2.I**), where i is the current and v, the scan rate. For an analytical purpose, Equation 2.I was rearranged to **Equation 2.II**.

$$i = av^b \qquad \textbf{Equation 2.I}$$

$$log\ (i) = log(a) + b \cdot log(v)$$ **Equation 2.II**

The slope of the linear curve obtained when plotting *log (i) vs. log (v)* gives the *b*-value, which will determine the nature of the current. In case *b*=0.5 the kinetic is controlled by diffusion, while if *b*=1 the capacitive charge storage mechanism is the dominant [62].

Obtained *b* values in Li-ion chemistry for anodic and cathodic processes are shown in **Figure 2.6a**. Being in Li-ion *b*=0.75 and 0.64 respectively, suggests that the kinetic is determined by both diffusion and capacitive contributions. Similar results were obtained in Na-ion chemistry (see **Figure 2.6b**), being the *b* value for the anodic and cathodic processes 0.64 and 0.52, respectively. Dunn *et al.* reported that materials with high SSA, especially at high rates, will show an elevate capacitive response [63]. Hence, having the studied HC a 480 $m^2\ g^{-1}$ SSA, some capacitive contribution was already expected [19,51].

Further calculations to determine the diffusion and capacitive contributions to the total capacity were carried out using **Equation 2.III**, where k_1v defines the capacitive- and $k_2v^{1/2}$ the diffusion-controlled currents. For an analytical purpose, Equation 2.III has been rearranged to **Equation 2.IV**, from which k_1 and k_2 values can be obtained in all the studied potential window, by the slope and the y-intercept, respectively.

$$i(V) = k_1 v + k_2 v^{1/2}$$ **Equation 2.III**

$$\frac{i(V)}{v^{1/2}} = k_1 v^{1/2} + k_2$$ **Equation 2.IV**

Figure 2.6c and **2.6d** show the capacitive contribution (shaded area) of the HC at 1 mV s^{-1}, corresponding to 78% in Li-ion and 53% in Na-ion. These results allow verifying the insertion/deinsertion mechanism previously proposed by the broad peak of the CV at ~0.5 V *vs.* Li^+/Li and Na^+/Na, where mainly a diffusion-controlled process undergoes. Instead, above 1 V, the capacitive process for Li^+ and Na^+ can be ascribed to the adsorption/desorption mechanism on the edges/defects of carbons [22]. These results

are in good agreement with recently reported HC charge storage mechanisms, where diffusive and capacitive processes take place in both Li-ion and Na-ion chemistries.

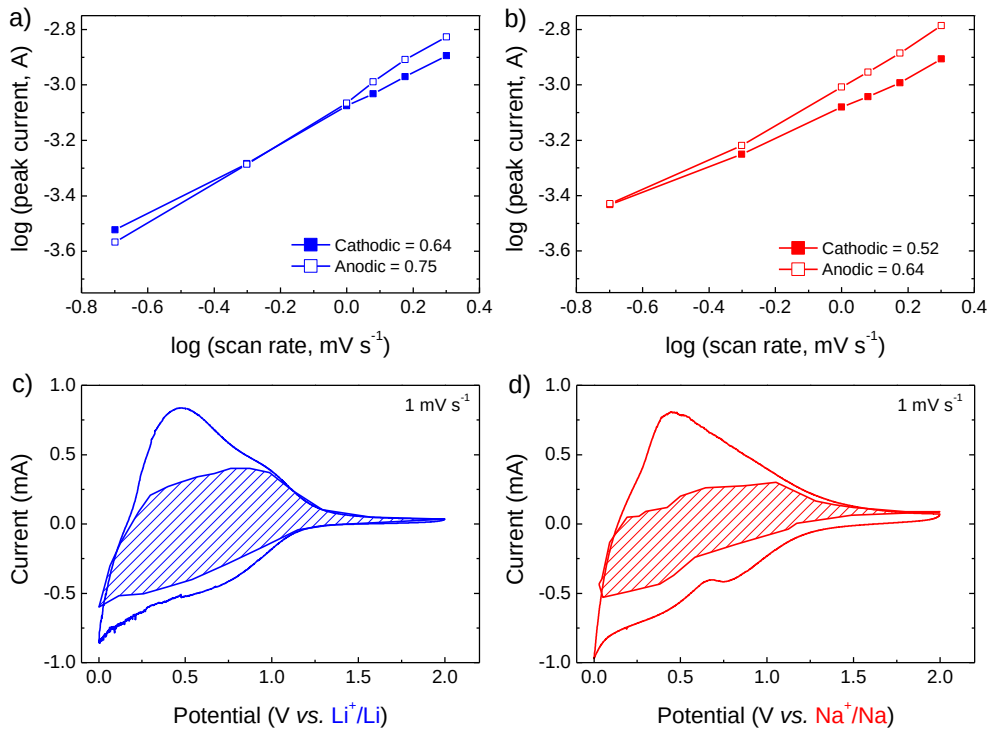

Figure 2.6. Determination of the *b* value using the relationship between peak current to sweep rate: a) HC *vs.* Li^+/Li and b) HC *vs.* Na^+/Na. CV at 0.1 mV s^{-1} separating the total current (solid line) and capacitive current (shaded regions): c) HC *vs.* Li^+/Li and d) HC *vs.* Na^+/Na.

2.3. Olive pits derived AC as the positive electrode

As it has been mentioned in **Chapter 1 - Section 1.4.2.1.**, AC is the benchmark material in EDLCs and hence also the capacitor-type material in MICs. Moreover, it has been widely reported that biomass waste derived ACs and especially those chemically activated show the best electrochemical performance. Thereby, in this thesis, using the same raw olive pit precursor a biomass waste derived AC was developed.

2.3.1. Material and electrode preparation of olive pits derived AC

In order to prepare the AC (**Scheme 2.2**), the crushed olive pits were loaded in a stainless steel tubular furnace for the pyrolysis process by heating up under an argon flow of 100 ml min^{-1} at a ramp rate of 5ºC min^{-1} to a pre-defined temperature of 700ºC and further holding it for 2 h. Then the obtained HC was physically mixed with KOH in a 1/6 mass ratio (HC/KOH) and placed in an Inconel© boat in order to activate it by heating up under an argon flow (100 ml min^{-1}) inside a horizontal stainless steel tube within a tubular furnace. The heating ramp rate was 5 ºC min^{-1} and the holding time at 700 ºC was 2 h. After activation, the microporous AC was washed off with a diluted solution of hydrochloric acid and water until neutral pH was reached and then it was dried at 120ºC under vacuum. The activation yield is ~25%. AC laminates were prepared using the same method as for HC but mixing the AC and PVdF in a mass ratio of 95:5. Contrary to HC slurry, in this case the AC slurry was laminated onto an aluminum current collector sheet.

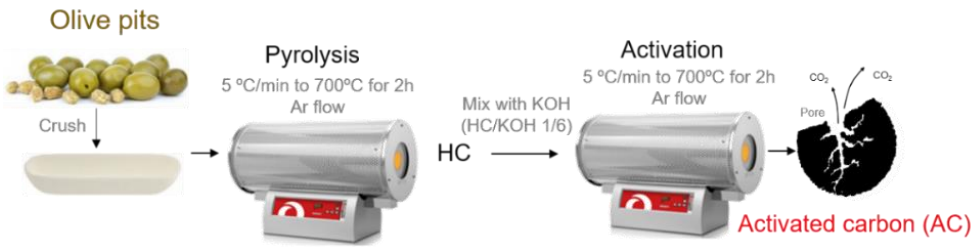

Scheme 2.2. Preparation route for olive pits derived AC.

2.3.2. Physicochemical characterization of the AC

Microstructural analysis of the AC (**Figure 2.7a**) reveals that KOH satisfactorily induced the creation of essential micropores for ion adsorption. **Figure 2.7b** shows the N_2 adsorption/desorption isotherm which saturates rapidly at low relative pressure with no noticeable sign of hysteresis. According to the IUPAC classification, this specific

isotherm exhibits a Type I profile which is related to a microporous material. A very high SSA_{DFT} of 2008 $m^2\ g^{-1}$ and an average pore size of 1 nm were calculated for the AC using previously mentioned 2D-NLDFT method, very convenient to provide fast adsorption/desorption of ions.

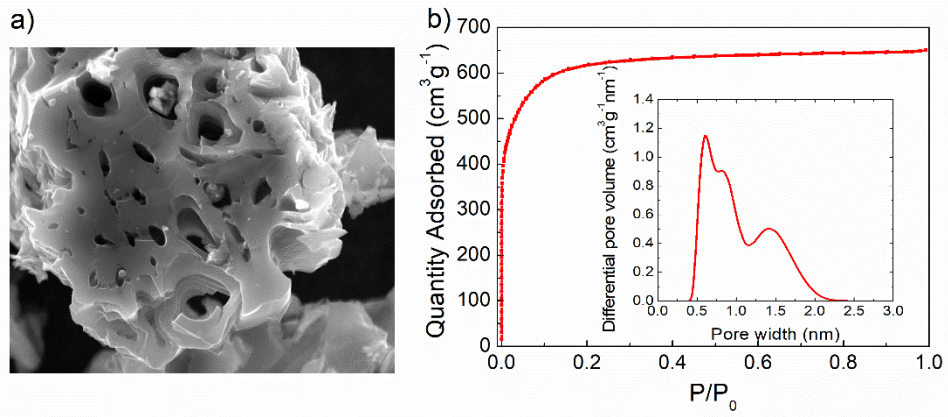

Figure 2.7. Physicochemical characterization of the AC: a) SEM image and b) N_2 adosprtion/desorption isotherm, inset: PSD.

2.3.3. Electrochemical characterization of the AC

Figure 2.8 shows the electrochemical characterization of the AC in a potential window of 2 - 4.2 V *vs.* Li^+/Li and Na^+/Na. CVs shown in **Figure 2.8a** exhibit rectangular shape indicative of a capacitive charge storage mechanism where there are not any faradaic reactions, electrolyte degradation or electrode oxidation included (**Figure AI.4**). **Figure 2.8b** shows the capacity evolution calculated by GA charge/discharges at different current densities. Although in supercapacitor technology charge storage capability is described in terms of capacitance, for the sake of a fair comparison within a consistent metric and in order to stablish the correct mass ratio in the final device ($m_+ \cdot C_+ \cdot \Delta V_+ = m_- \cdot C_- \cdot \Delta V_-$), from now on results are reported in terms of capacity [64]. Opposite to what is observed for the HC, increasing the cycling rate of the AC makes almost no difference between both technologies. **Figure 2.8c** shows the GA

charge/discharge profile of the AC in Li- and Na-based electrolytes at 5 A g^{-1}. The ohmic drop is very similar for both technologies. This trend is also confirmed by the EIS data expressed in the Nyquist Plot in **Figure 2.8d** at open circuit potential (OCP), which shows no difference between both systems neither in the de Levie porous electrode segment, nor in the almost vertical capacitive line at the lowest frequencies. This confirms that capacitive ACs can be also utilized in battery-type electrolytes.

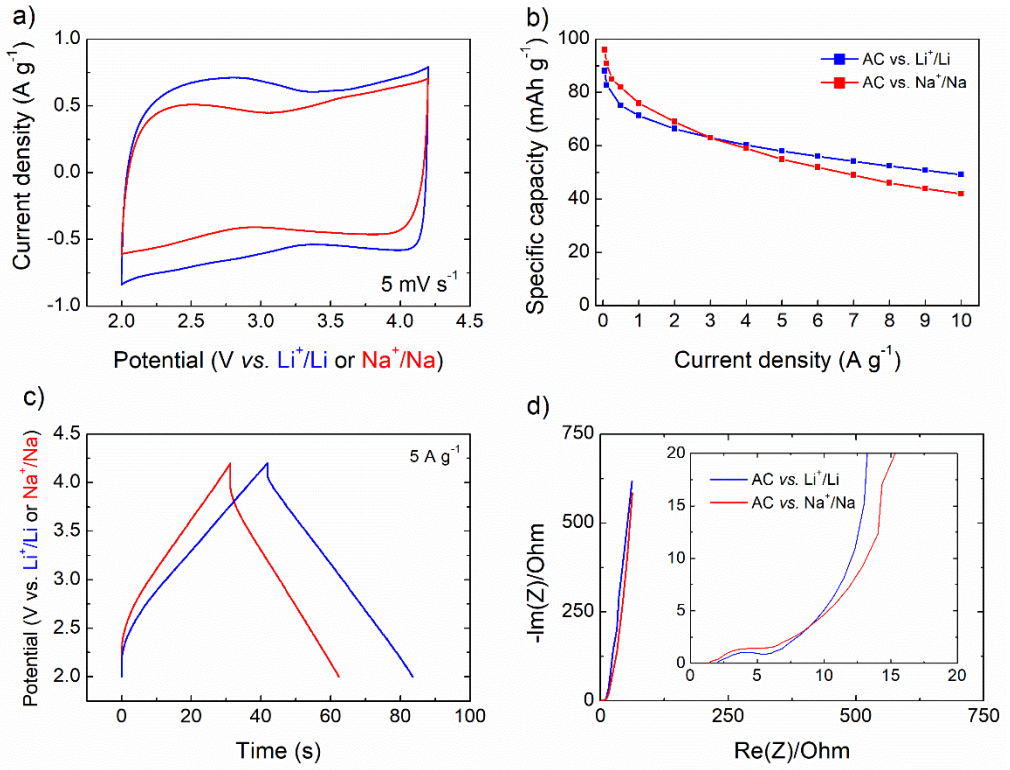

Figure 2.8. Electrochemical characterization of the AC between 2 and 4.2 V *vs.* Li^+/Li or Na^+/Na: a) CVs, b) Rate capability, c) Charge/discharge profiles at 5 A g^{-1} and d) EIS at OCP.

2.4. Development of biomass waste derived dual carbon MICs

After the individual characterization of each material, dual carbon MICs were developed. On the one hand, the HC was selected to be the battery-type negative electrode in which

the charge is stored by the insertion/deinsertion of Li^+ or Na^+ showing a faradaic charge storage mechanism. On the other hand, the AC acted as the capacitor-type positive electrode storing charge by adsorption/desorption of ions coming from the electrolyte. All MICs were assembled in three electrode airtight Swagelok® systems using glass fibre membrane (Whattman GFB) soaked in 1 M $LiPF_6$ (EC:DMC) or 1 M $NaPF_6$ (EC:PC) as separator and lithium or sodium metal disc as reference electrode, respectively.

2.4.1. Lithium ion capacitors (LICs)

In order to maximize the LIC performance, the active mass of the electrodes needs to be balanced, as charge stored in both electrodes must be equal ($Q_+=Q_-$) [65]. In **Figure 2.9a**, specific capacities of both active materials in 1 M $LiFP_6$ EC:DMC are compared at different current densities. As it is observed, the HC electrode outperforms the AC along all the studied current density range. Hence, it is not possible to get a suitable mass ratio (HC:AC) for all the current densities. Thus, as LICs are targeted for discharge times ranging from few minutes to seconds, which are normally obtained at current densities between 2 - 10 A g^{-1}, depending on the active material, the mass ratio is selected focusing at the results obtained in that region. In this case, as a first approach, a 1:1 mass ratio was selected to develop the dual carbon LIC, hereafter named as LIC (1:1). The system was assembled in a three electrode airtight Swagelok® cell using a lithium metal disc as reference electrode in order to monitor the behaviour of both positive and negative electrodes and to carry out the initial pre-conditioning step in order to maximize the output voltage and compensate for the lithium used to form the SEI in the first cycle. First, the HC was cycled 5 times from 0.005 to 2 V *vs.* Li^+/Li at C/10 and then a cut-off potential of 0.1 V *vs.* Li^+/Li was set in order to keep safety and avoid any lithium plating. Second, the AC was charged up to 4.2 V *vs.* Li^+/Li (**Figure 2.9b**).

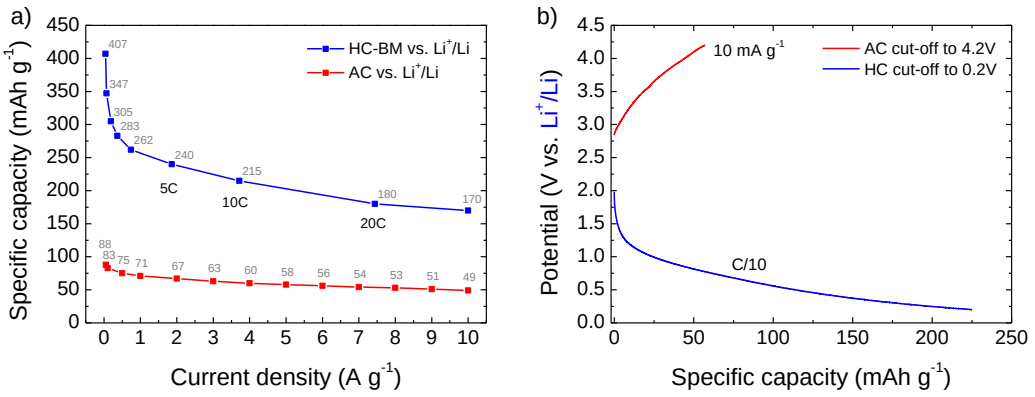

Figure 2.9. a) Specific capacity values of the HC and AC *vs.* Li^+/Li and b) Pre-conditioning step for the AC and HC with a cut-off potential set at 4.2 V and at 0.1 V *vs.* Li^+/Li respectively.

After the pre-conditioning step, the LIC (1:1) was characterized at different current densities in a voltage window of 1.5 - 4.2 V. **Figure 2.10** shows the different charge/discharge profiles of the AC (dash red line), the HC (dash-dot blue line) and the full LIC (straight black line) at different discharge times, going from the region affordable for batteries (*i.e.* 30 min) to discharge times usually restricted to EDLCs (*i.e.* 8 s). At low current densities, within a discharge time of *ca.* 20 min, the profiles corresponding to the LIC (1:1) show that the AC swings from 2 to 4 V *vs.* Li^+/Li within a symmetric ideal profile which corresponds to the capacitive storage mechanism, while the HC swings from 0.8 to 0.2 V *vs.* Li^+/Li where insertion and deinsertion of Li^+ occurs. Hence, the LIC stores charge by both faradaic and non-faradaic mechanisms. Moreover, it is shown that even the current density is increased to 1 A g^{-1} or 10 A g^{-1}, where the LIC (1:1) shows discharge times of 2 min and 6 s respectively, the potential window of each electrode remains almost constant. Nevertheless, due to the high applied current, the non-optimized cell configuration and non-holding step between charge and discharge steps, gives some ohmic resistance at the lowest discharge time of 6 s. Moreover, as it is observed, the potential window of the negative electrode is still very narrow, what means that the AC is limiting the behaviour of the LIC and it is not given its maximum capacity output.

Hence, in order to maximize the performance, the mass loading of the AC was increased, while the one of the HC was maintained constant.

This way, a 1:2 mass ratio LIC -with double the mass of AC- was developed, hereafter named as LIC (1:2). As it is observed in the profiles corresponding to LIC (1:2) in **Figure 2.10**, at low current densities, within a discharge time of *ca.* 30 min, the profiles of both AC and HC show similar shape as those from LIC (1:1). However, owing to the increase in the mass loading of the AC, the potential window of the HC is wider, going from 1 to 0.1 V *vs.* Li^+/Li. When increasing the applied current density to 1 A g^{-1}, the potential of the negative electrode goes to values very close to 0 V *vs.* Li^+/Li. Further increase up to 10 A g^{-1} shows the profile of the HC going to negative values and a limited behaviour of the AC within a very narrow potential window. This demonstrates that the HC has become the limiting electrode. Thereby, in order to develop a safe LIC, high currents where lithium plating/deposition and further short circuit can occur might be avoided when a 1:2 mass ratio is selected.

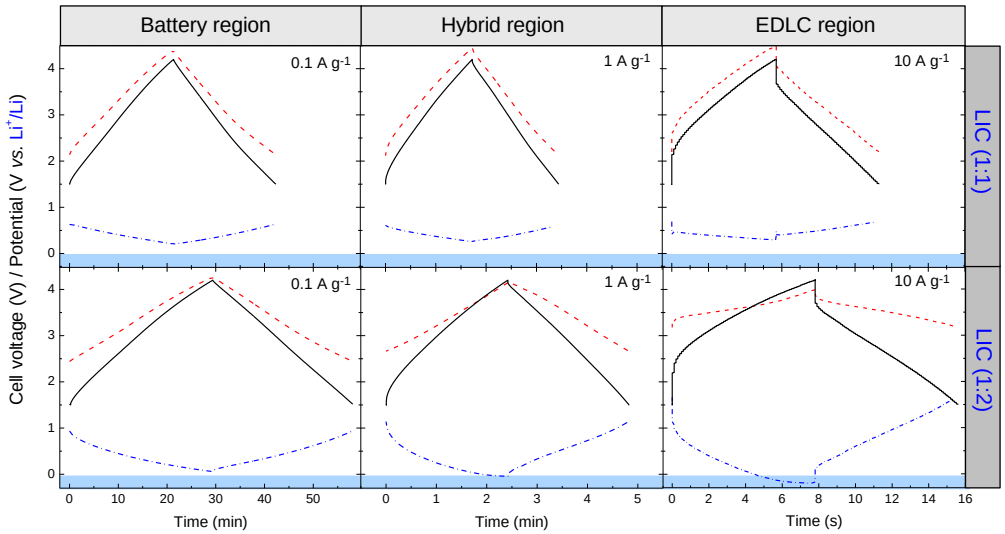

Figure 2.10. GA charge/discharge profiles for full LICs (black straight line), positive (AC, red dash line) and negative (HC, blue dash-dot line) electrodes at different discharge regions.

The energy and power density values of the studied LICs are calculated from the GA charge/discharge measurements in **Figure 2.10** using **Equation AI.XXI** and **AI.XXIV** respectively and reported in a Ragone plot in **Figure 2.11**. The active mass (AM) of both negative and positive electrodes is considered for the calculations. Grey empty rectangles show the energy-to-power points where the potential of the negative electrode goes to 0 V *vs.* Li^+/Li and thus, cannot be considered. However, as it is observed in the Ragone plot, LIC (1:2) overcomes its LIC (1:1) counterpart in the power density range of 150 – 4000 W kg^{-1}_{AM}. These higher energy density values are obtained owing to the better use of the negative electrode when the mass loading of the AC is doubled. Nevertheless, despite it allows obtaining major capacity output from the negative electrode, it also limits the behaviour of the device as at higher current densities the HC becomes the limiting electrode. Thus, the developed LIC (1:2) can only be used for those applications with discharge times in the range of 1 h - 1 min. Nevertheless, owing to the limited behaviour of the HC in the LIC (1:1) system, its energy density output is lower. However, as its potential window does not extend as much as the one from the LIC (1:2), it can afford to work at high power densities within few seconds, *i.e.* 6 s. Thereby, one or other LIC should be selected depending on the application of interest. For comparison purposes, a symmetric EDLC using the same AC and working in 1.5 M Et_4NBF_4 (acetonitrile, ACN) was also built. As it is shown in **Figure 2.11**, both developed olive pits derived LICs overcome their EDLC counterpart showing a 5-fold increase in energy density at same power densities, what confirming these devices as high energetic capacitors.

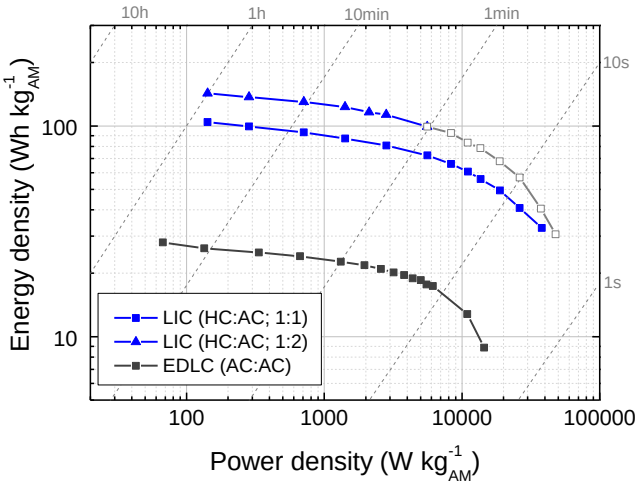

Figure 2.11. Gravimetric Ragone plot comparing LIC (1:1) and LIC (1:2) with their EDLC counterpart. Grey points show where lithium plating occurs and cannot be considered.

Energy efficiency is one of the key factors to consider for the potential application of a technology. In MICs it can be calculated by the ratio of the areas under the GA discharge/charge curves, multiplied by the current (**Equation AI.XXIII**) [66]. As a consequence of the higher equivalent series resistance (ESR), described by the ohmic drop, observed in the profiles of **Figure 2.10** when going to discharge times in the range of seconds, the energy efficiency of both LICs seems to be reduced. Both LICs show about ~91% energy efficiency in battery and hybrid regions, while going to the EDLC region, where ultrafast response is required, the energy efficiency decreases to about 76% for the LIC (1:1) and 74% for the LIC (1:2). These lower values are mostly related to the engineering of the system which is not optimized. Factors like current collectors, calendering, separator, and geometry have not been considered in this work and might be the origin of the ESR observed at high currents. In addition, the lack of a voltage hold step between the charge and discharge made the ESR be the result of both steps. Besides, the small area of lab-scale electrodes induces higher resistance. Thereby, there is plenty of room to reduce the ESR in a scale-up process.

2.4.2. Sodium ion capacitors (NICs)

Same procedure as for LICs was followed for dual carbon NICs. In **Figure 2.12a** specific capacity values of the HC and the AC in 1 M $NaPF_6$ (EC:PC) at different current densities are summarized. In this case, despite the AC shows similar specific capacity values as in Li-ion technology, the HC shows lower specific capacity values. Hence, in order to avoid any overuse of the negative electrode and sodium plating at high currents, the mass ratio was limited to 1:1. After the NIC assembly, it was pre-conditioned following the same procedure as for LICs. Once the pre-conditioning step was concluded (**Figure 2.12b**), the NIC was characterized by GA charge/discharge technique at different current densities initially within a cell voltage of 1.5 - 4.2 V.

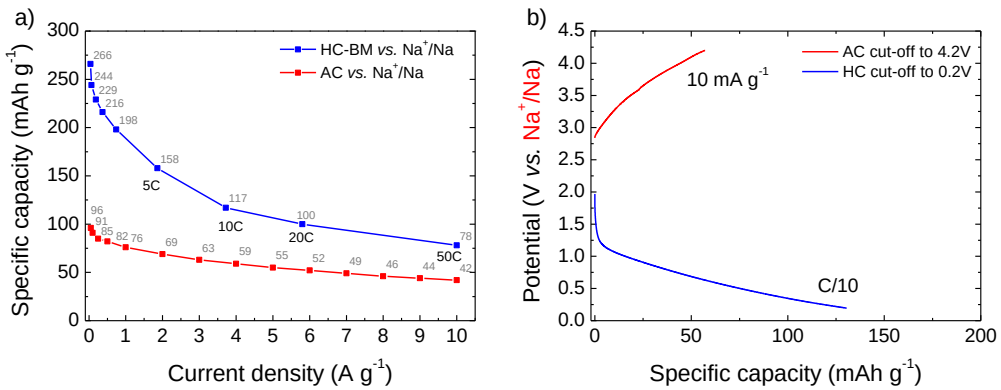

Figure 2.12. a) Specific capacity values of the HC and AC *vs.* Na^+/Na and b) Pre-conditioning step for the AC and HC with a cut-off potential set at 4.2 V and at 0.1 V *vs.* Na^+/Na respectively.

As shown in **Figure 2.13**, at low current densities, within a discharge time of ~50 min, the AC (red dash line) swings from 2.2 to 4.2 *vs.* Na^+/Na, while the HC (blue dash-dot line) does it between 0.8 - 0.1 *vs.* Na^+/Na. As it was shown in **Figure 2.5c**, the HC in Na-ion shows lower specific capacity values than in Li-ion. Hence, also its performance in a full device will be lower. Thus, at similar current densities (*i.e.* 0.1 A g^{-1}) the potential window of the HC in the NIC is wider than that of the HC in the LIC. Accordingly, the

negative electrode reaches negative potentials earlier and becomes unsafe due to the possibility of sodium plating at higher rates (*i.e.* 0.5 A g^{-1}).

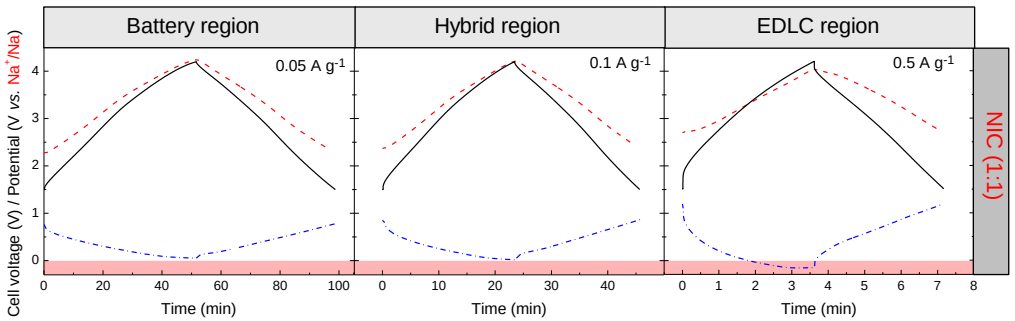

Figure 2.13. GA charge/discharge profiles for the NIC (black straight line), positive (AC, red dash line) and negative (HC, blue dash-dot line) electrodes at different discharge regions.

Nevertheless, since the HC capacity is still much higher compared to the AC, at low currents, it still allows developing a NIC able to deliver similar energy density output as its LIC (1:1) counterpart at power densities in the range of 150 – 1500 W kg^{-1}_{AM} -with an energy efficiency of 83% at lower power densities and 87% at higher ones-, obtaining even slightly higher energy density values *i.e.* 104.9 Wh kg^{-1}_{AM} at 288.3 W kg^{-1}_{AM}. However, its use over these power densities (*i.e.* $t_{discharge} \approx 3$ min) becomes dangerous as the HC potential goes to negative values and sodium plating might occur.

Hence, in order to overcome this issue, two different strategies were followed. First, the AC mass loading was decreased setting a HC:AC 1:0.8 mass ratio and second, maintaining the HC:AC 1:1 mass ratio, the cell voltage was reduced to 2 - 4 V.

As it is shown in **Figure 2.14a**, sodium plating was avoided at low discharge times, however, both strategies led to lower energy density values than the NIC (1:1) 1.5 -4.2 V system (**Figure 2.14b**). On the one hand, when reducing the mass ratio to 1:0.8 but maintaining the cell voltage at 1.5 – 4.2 V, the HC never goes to negative values and allows working at power densities up to 8000 W kg^{-1}_{AM}, within a discharge time of ~8 s

and delivering still almost double the energy density of its EDLC counterpart. On the other hand, when reducing the cell voltage to 2 - 4 V but maintaining the mass ratio at 1:1, the system delivers stable energy density values up to 2000 W kg^{-1}_{AM} power density within a discharge time of ~1 min. Grey empty points show the energy-to-power values when the potential of the negative electrode goes to 0 V *vs.* Na^+/Na and thus, cannot be considered. Overall, it can be concluded that depending on the final application of the system, one or other device should be selected.

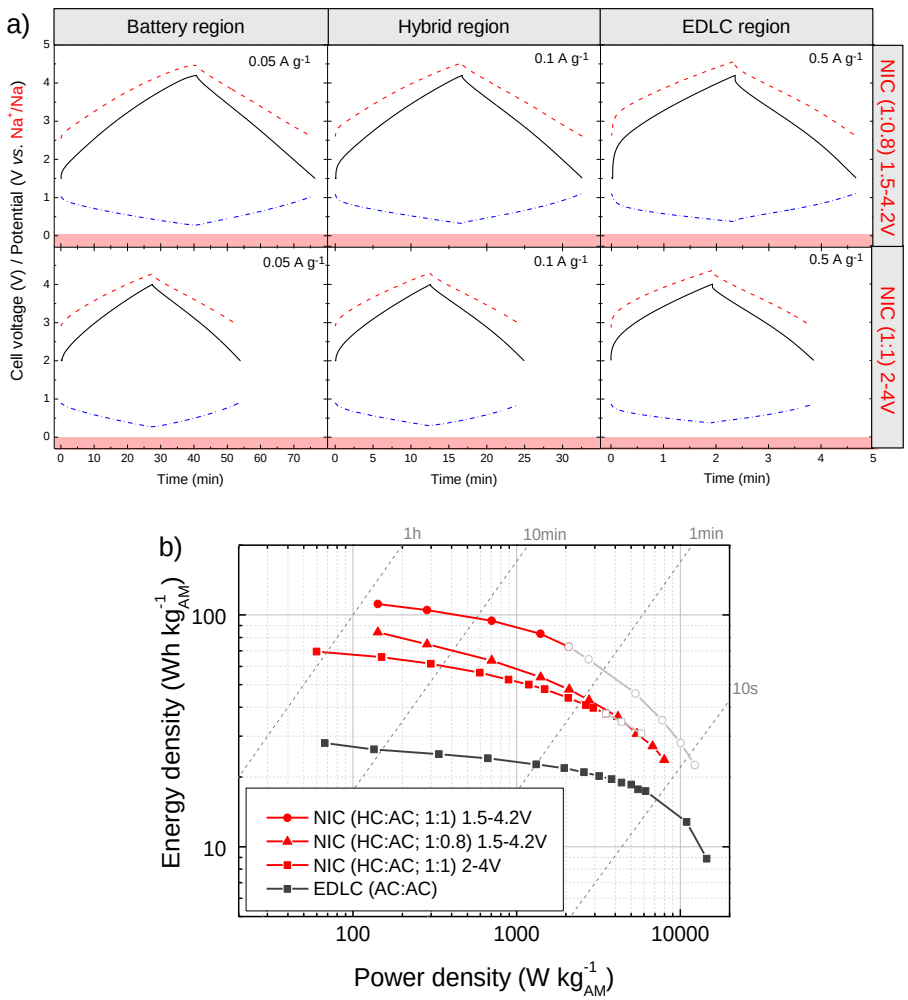

Figure 2.14. a) GA charge/discharge profiles for new NICs and b) Ragone plot of all NICs. Grey points show where sodium plating occurs and cannot be considered.

Figure 2.15a shows the Ragone plot of the studied MICs delivering the highest energy density values, while **Figure 2.15b** puts together the devices with the best balance between energy-to-power ratios. Grey empty points show the energy-to-power values when the potential of the negative electrode goes to 0 V *vs.* Li^+/Li or Na^+/Na and hence, cannot be considered. **Table 2.3** summarizes the energy-to-power density values reported in **Figure 2.15** at different discharge times. All of them showing very promising results in comparison with other dual carbon MICs reported in literature [67].

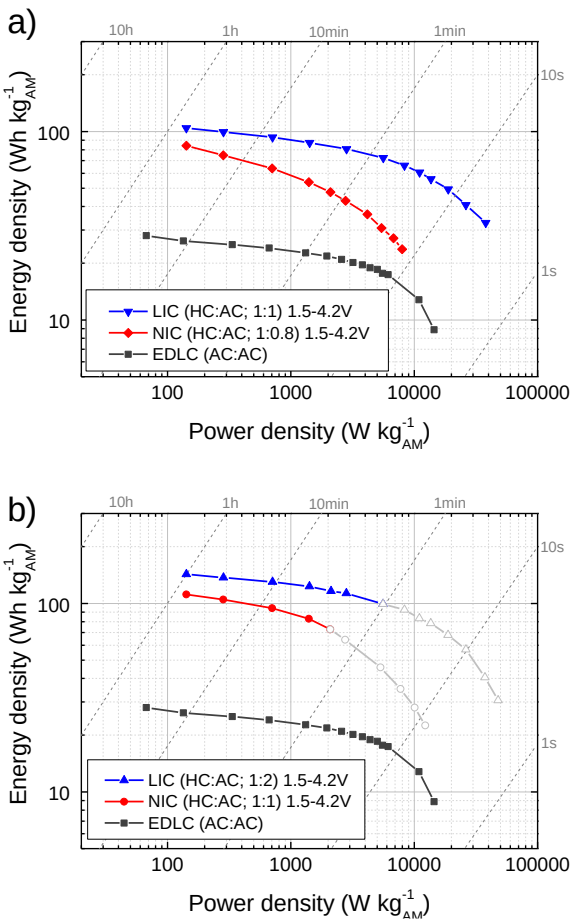

Figure 2.15. Gravimetric Ragone plots comparing the studied MICs a) at 1.5 – 4.2 V cell voltage and b) with the best balance between energy-to-power values. Grey points show where lithium or sodium plating occurs and cannot be considered.

Table 2.3. Energy-to-power density values of the studied MICs at different discharge times.

MICs (HC:AC)	$t_{dischage}$					
	~30 min		~3 min		~8 - 10 s	
	Wh kg_{AM}^{-1}	W kg_{AM}^{-1}	Wh kg_{AM}^{-1}	W kg_{AM}^{-1}	Wh kg_{AM}^{-1}	W kg_{AM}^{-1}
LIC (1:1) 1.5-4.2V	99.4	284.4	87.1	1417.3	40.8	26238.3
NIC (1:0.8) 1.5-4.2V	84.2	141.9	53.8	1401.1	23.7	7975.04
LIC (1:2) 1.5-4.2V	137	284.5	116.2	2119.8	N.A.	N.A.
NIC (1:1) 1.5-4.2V	104.9	288.3	N.A.	N.A.	N.A.	N.A.

* N.A. = not applicable

Being the cycle life of MICs another key factor to overcome EDLCs, GA charge/discharge stability tests at constant current were followed for the MICs with best energy-to-power ratios: LIC (1:1) at 1.5 - 4.2V and NIC (1:0.8) at 1.5 - 4.2V. The current was set at 2 A g^{-1} for the NIC and 5 A g^{-1} for the LIC in order to analyze the cycle life at the same discharge time, *i.e.* 30 s (**Figure 2.16**).

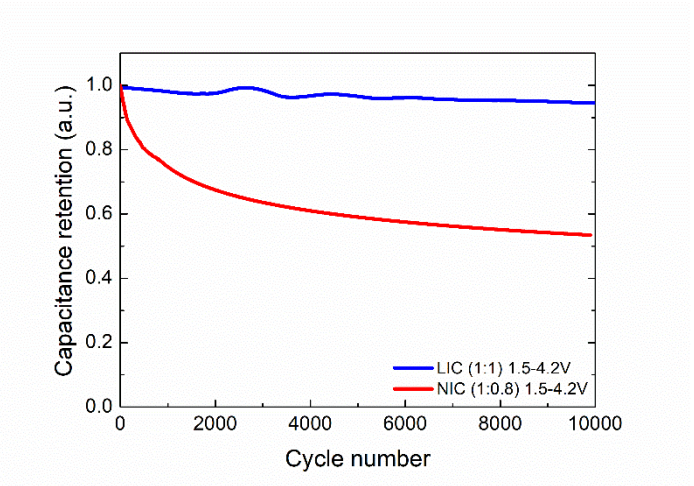

Figure 2.16. Capacitance retention of the best energy-to-power MICs: LIC (1:1) and NIC (1:0.8) both at 1.5 - 4.2 V cell voltage.

In the case of the LIC, excellent capacitance retention of 94% after 10000 cycles was obtained, while in NICs cycle life remains a challenge, with 30% loss of the initial capacitance after 2000 cycles, quite lower in comparison with its LIC counterpart.

2.5. Summary and conclusions

The fabrication of dual carbon LICs and NICs based on a high SSA (*i.e.* 2008 $m^2 g^{-1}$) and microporous olive pits derived AC as the ion adsorption/desorption positive electrode and on a disordered, reduced particle size, thin and high SSA (*i.e.* 480 $m^2 g^{-1}$) olive pits derived HC as the ion insertion/deinsertion negative electrode has allowed developing MICs with high energy and high power densities as well as long cycle life in organic electrolytes. Mass ratio and cell voltage studies were followed in order to obtain the best output from each device.

Fabricated MICs overcome their EDLC counterpart in terms of energy density throughout the whole power density range, exceeding the highly challenging energy density barrier of 100 Wh kg^{-1}_{AM}. Furthermore, LIC (1:1) equals the EDLC system in terms of power density (>10 kW kg^{-1}_{AM}), showing the ability to be charged and discharged within few seconds. It also shows high capacitance retention of 94% after 10000 cycles. In parallel, the developed NIC (1:0.8) is effectively limited to 2000 cycles keeping 70% of its initial capacitance. Overall, the fabrication of MICs all on the basis of the same precursor material opens new avenues for covering a large assortment of technological applications with different requirements.

2.6. Bibliography

[1] V. Khomenko, E. Raymundo-Piñero, F. Béguin, High-energy density graphite/AC capacitor in organic electrolyte, J. Power Sources. 177 (2008) 643–651. doi:10.1016/j.jpowsour.2007.11.101.

[2] C. Decaux, G. Lota, E. Raymundo-Piñero, E. Frackowiak, F. Béguin, Electrochemical performance of a hybrid lithium-ion capacitor with a graphite anode preloaded from lithium bis(trifluoromethane)sulfonimide-based electrolyte, Electrochimica Acta. 86 (2012) 282–286. doi:10.1016/j.electacta.2012.05.111.

[3] S.R. Sivakkumar, A.S. Milev, A.G. Pandolfo, Effect of ball-milling on the rate and cycle-life performance of graphite as negative electrodes in lithium-ion capacitors, Electrochimica Acta. 56 (2011) 9700–9706. doi:10.1016/j.electacta.2011.06.060.

[4] ULTIMO Lithium Ion Capacitor Laminate Cells - LIC | JSR Micro, Inc., (n.d.). https://www.jsrmicro.com/emerging-technologies/lithium-ion-capacitor/products/ultimo-lithium-ion-capacitor-laminate-cells-lic (accessed June 22, 2018).

[5] Li-ion Capacitors - Yunasko is the developer and licensor of high power ultracapacitors, (n.d.). http://yunasko.com/en/products/lithium-ion-capacitors (accessed January 15, 2019).

[6] M.T. Inc, Maxwell Technologies Delivers First Commercial Application of Lithium-Ion Capacitor Technology in China, (n.d.). https://www.prnewswire.com/news-releases/maxwell-technologies-delivers-first-commercial-application-of-lithium-ion-capacitor-technology-in-china-300354618.html (accessed December 2, 2017).

[7] M. Schroeder, M. Winter, S. Passerini, A. Balducci, On the Use of Soft Carbon and Propylene Carbonate-Based Electrolytes in Lithium-Ion Capacitors, J. Electrochem. Soc. 159 (2012) A1240–A1245. doi:10.1149/2.050208jes.

[8] M. Schroeder, S. Menne, J. Ségalini, D. Saurel, M. Casas-Cabanas, S. Passerini, M. Winter, A. Balducci, Considerations about the influence of the structural and electrochemical properties of carbonaceous materials on the behavior of lithium-ion capacitors, J. Power Sources. 266 (2014) 250–258. doi:10.1016/j.jpowsour.2014.05.024.

[9] J. Ajuria, E. Redondo, M. Arnaiz, R. Mysyk, T. Rojo, E. Goikolea, Lithium and sodium ion capacitors with high energy and power densities based on carbons from recycled olive pits, J. Power Sources. 359 (2017) 17–26. doi:10.1016/j.jpowsour.2017.04.107.

[10] J. Ding, H. Wang, Z. Li, K. Cui, D. Karpuzov, X. Tan, A. Kohandehghan, D. Mitlin, Peanut shell hybrid sodium ion capacitor with extreme energy–power rivals lithium ion capacitors, Energy Environ. Sci. 8 (2015) 941–955. doi:10.1039/C4EE02986K.

[11] H. Moriwake, A. Kuwabara, C.A.J. Fisher, Y. Ikuhara, Why is sodium-intercalated graphite unstable?, RSC Adv. 7 (2017) 36550–36554. doi:10.1039/C7RA06777A.

[12] Y. Liu, B.V. Merinov, W.A. Goddard, Origin of low sodium capacity in graphite and generally weak substrate binding of Na and Mg among alkali and alkaline earth metals, Proc. Natl. Acad. Sci. 113 (2016) 3735–3739. doi:10.1073/pnas.1602473113.

[13] B. Jache, P. Adelhelm, Use of Graphite as a Highly Reversible Electrode with Superior Cycle Life for Sodium-Ion Batteries by Making Use of Co-Intercalation Phenomena, Angew. Chem. Int. Ed. 53 (2014) 10169–10173. doi:10.1002/anie.201403734.

[14] Z.-L. Xu, G. Yoon, K.-Y. Park, H. Park, O. Tamwattana, S.J. Kim, W.M. Seong, K. Kang, Tailoring sodium intercalation in graphite for high energy and power sodium ion batteries, Nat. Commun. 10 (2019) 2598. doi:10.1038/s41467-019-10551-z.

[15] X. Dou, I. Hasa, D. Saurel, C. Vaalma, L. Wu, D. Buchholz, D. Bresser, S. Komaba, S. Passerini, Hard carbons for sodium-ion batteries: Structure, analysis, sustainability, and electrochemistry, Mater. Today. 23 (2019) 87–104. doi:10.1016/j.mattod.2018.12.040.

[16] E. Irisarri, A. Ponrouch, M.R. Palacin, Review—Hard Carbon Negative Electrode Materials for Sodium-Ion Batteries, J. Electrochem. Soc. 162 (2015) A2476–A2482. doi:10.1149/2.0091514jes.

[17] C. Liu, N. Xiao, Y. Wang, H. Li, G. Wang, Q. Dong, J. Bai, J. Xiao, J. Qiu, Carbon clusters decorated hard carbon nanofibers as high-rate anode material for lithium-ion batteries, Fuel Process. Technol. 180 (2018) 173–179. doi:10.1016/j.fuproc.2018.09.004.

[18] W.S.V. Lee, X. Huang, T.L. Tan, J.M. Xue, Low Li+ Insertion Barrier Carbon for High Energy Efficient Lithium-Ion Capacitor, ACS Appl. Mater. Interfaces. 10 (2018) 1690–1700. doi:10.1021/acsami.7b15473.

[19] C. Li, X. Zhang, K. Wang, X. Sun, Y. Ma, High-power lithium-ion hybrid supercapacitor enabled by holey carbon nanolayers with targeted porosity, J. Power Sources. 400 (2018) 468–477. doi:10.1016/j.jpowsour.2018.08.013.

[20] D.A. Stevens, J.R. Dahn, High Capacity Anode Materials for Rechargeable Sodium-Ion Batteries, J. Electrochem. Soc. 147 (2000) 1271–1273. doi:10.1149/1.1393348.

[21] C. Bommier, T.W. Surta, M. Dolgos, X. Ji, New Mechanistic Insights on Na-Ion Storage in Nongraphitizable Carbon, Nano Lett. 15 (2015) 5888–5892. doi:10.1021/acs.nanolett.5b01969.

[22] D. Saurel, B. Orayech, B. Xiao, D. Carriazo, X. Li, T. Rojo, From Charge Storage Mechanism to Performance: A Roadmap toward High Specific Energy Sodium-Ion Batteries through Carbon Anode Optimization, Adv. Energy Mater. 8 (2018) 1703268. doi:10.1002/aenm.201703268.

[23] S. Alvin, D. Yoon, C. Chandra, H.S. Cahyadi, J.-H. Park, W. Chang, K.Y. Chung, J. Kim, Revealing sodium ion storage mechanism in hard carbon, Carbon. 145 (2019) 67–81. doi:10.1016/j.carbon.2018.12.112.

[24] K. Kubota, S. Komaba, Review—Practical Issues and Future Perspective for Na-Ion Batteries, J. Electrochem. Soc. 162 (2015) A2538–A2550. doi:10.1149/2.0151514jes.

[25] W. Li, M. Chen, C. Wang, Spherical hard carbon prepared from potato starch using as anode material for Li-ion batteries, Mater. Lett. 65 (2011) 3368–3370. doi:10.1016/j.matlet.2011.07.072.

[26] L. Wang, Z. Schnepp, M.M. Titirici, Rice husk-derived carbon anodes for lithium ion batteries, J. Mater. Chem. A. 1 (2013) 5269–5273. doi:10.1039/C3TA10650K.

[27] J. Yang, X. Zhou, J. Li, Y. Zou, J. Tang, Study of nano-porous hard carbons as anode materials for lithium ion batteries, Mater. Chem. Phys. 135 (2012) 445–450. doi:10.1016/j.matchemphys.2012.05.006.

[28] J. Wang, J.-L. Liu, Y.-G. Wang, C.-X. Wang, Y.-Y. Xia, Pitch modified hard carbons as negative materials for lithium-ion batteries, Electrochimica Acta. 74 (2012) 1–7. doi:10.1016/j.electacta.2012.03.099.

[29] X. Zhang, S. Han, C. Fan, L. Li, W. Zhang, Hard carbon enveloped with graphene networks as lithium ion battery anode, Mater. Lett. 138 (2015) 259–261. doi:10.1016/j.matlet.2014.10.023.

[30] R. Väli, A. Jänes, T. Thomberg, E. Lust, D-Glucose Derived Nanospheric Hard Carbon Electrodes for Room-Temperature Sodium-Ion Batteries, J. Electrochem. Soc. 163 (2016) A1619–A1626. doi:10.1149/2.0771608jes.

[31] Y. Li, S. Xu, X. Wu, J. Yu, Y. Wang, Y.-S. Hu, H. Li, L. Chen, X. Huang, Amorphous monodispersed hard carbon micro-spherules derived from biomass as a high performance negative electrode material for sodium-ion batteries, J. Mater. Chem. A. 3 (2015) 71–77. doi:10.1039/C4TA05451B.

[32] V. Simone, A. Boulineau, A. de Geyer, D. Rouchon, L. Simonin, S. Martinet, Hard carbon derived from cellulose as anode for sodium ion batteries: Dependence of electrochemical properties on structure, J. Energy Chem. 25 (2016) 761–768. doi:10.1016/j.jechem.2016.04.016.

[33] L. Wu, D. Buchholz, C. Vaalma, G.A. Giffin, S. Passerini, Apple-Biowaste-Derived Hard Carbon as a Powerful Anode Material for Na-Ion Batteries, ChemElectroChem. 3 (2016) 292–298. doi:10.1002/celc.201500437.

[34] Y. Li, Y.-S. Hu, M.-M. Titirici, L. Chen, X. Huang, Hard Carbon Microtubes Made from Renewable Cotton as High-Performance Anode Material for Sodium-Ion Batteries, Adv. Energy Mater. 6 (2016). doi:10.1002/aenm.201600659.

[35] W. Lv, F. Wen, J. Xiang, J. Zhao, L. Li, L. Wang, Z. Liu, Y. Tian, Peanut shell derived hard carbon as ultralong cycling anodes for lithium and sodium batteries, Electrochimica Acta. 176 (2015) 533–541. doi:10.1016/j.electacta.2015.07.059.

[36] M. Dahbi, M. Kiso, K. Kubota, T. Horiba, T. Chafik, K. Hida, T. Matsuyama, S. Komaba, Synthesis of hard carbon from argan shells for Na-ion batteries, J. Mater. Chem. A. 5 (2017) 9917–9928. doi:10.1039/C7TA01394A.

[37] M.K. Rybarczyk, Y. Li, M. Qiao, Y.-S. Hu, M.-M. Titirici, M. Lieder, Hard carbon derived from rice husk as low cost negative electrodes in Na-ion batteries, J. Energy Chem. 29 (2019) 17–22. doi:10.1016/j.jechem.2018.01.025.

[38] J. Xiang, W. Lv, C. Mu, J. Zhao, B. Wang, Activated hard carbon from orange peel for lithium/sodium ion battery anode with long cycle life, J. Alloys Compd. 701 (2017) 870–874. doi:10.1016/j.jallcom.2017.01.206.

[39] S. Qiu, L. Xiao, M.L. Sushko, K.S. Han, Y. Shao, M. Yan, X. Liang, L. Mai, J. Feng, Y. Cao, X. Ai, H. Yang, J. Liu, Manipulating Adsorption–Insertion Mechanisms in Nanostructured Carbon Materials for High-Efficiency Sodium Ion Storage, Adv. Energy Mater. 7 (2017) 1700403. doi:10.1002/aenm.201700403.

[40] Z. Yuan, L. Si, X. Zhu, Three-dimensional hard carbon matrix for sodium-ion battery anode with superior-rate performance and ultralong cycle life, J. Mater. Chem. A. 3 (2015) 23403–23411. doi:10.1039/C5TA07223A.

[41] Y. Li, L. Mu, Y.-S. Hu, H. Li, L. Chen, X. Huang, Pitch-derived amorphous carbon as high performance anode for sodium-ion batteries, Energy Storage Mater. 2 (2016) 139–145. doi:10.1016/j.ensm.2015.10.003.

[42] M. Arnaiz, V. Nair, S. Mitra, J. Ajuria, Furfuryl alcohol derived high-end carbons for ultrafast dual carbon lithium ion capacitors, Electrochimica Acta. 304 (2019) 437–446. doi:10.1016/j.electacta.2019.03.029.

[43] H. Wang, Z. Shi, J. Jin, C. Chong, C. Wang, Properties and sodium insertion behavior of Phenolic Resin-based hard carbon microspheres obtained by a hydrothermal method, J. Electroanal. Chem. 755 (2015) 87–91. doi:10.1016/j.jelechem.2015.07.032.

[44] A. Beda, P.-L. Taberna, P. Simon, C. Matei Ghimbeu, Hard carbons derived from green phenolic resins for Na-ion batteries, Carbon. 139 (2018) 248–257. doi:10.1016/j.carbon.2018.06.036.

[45] D. Zhou, M. Peer, Z. Yang, V.G. Pol, F.D. Key, J. Jorne, H.C. Foley, C.S. Johnson, Long cycle life microporous spherical carbon anodes for sodium-ion batteries derived from furfuryl alcohol, J. Mater. Chem. A. 4 (2016) 6271–6275. doi:10.1039/C6TA00242K.

[46] Z. Yang, H. Guo, X. Li, Z. Wang, Z. Yan, Y. Wang, Natural sisal fibers derived hierarchical porous activated carbon as capacitive material in lithium ion capacitor, J. Power Sources. 329 (2016) 339–346. doi:10.1016/j.jpowsour.2016.08.088.

[47] S. Jayaraman, A. Jain, M. Ulaganathan, E. Edison, M.P. Srinivasan, R. Balasubramanian, V. Aravindan, S. Madhavi, Li-ion vs. Na-ion capacitors: A performance evaluation with coconut shell derived mesoporous carbon and natural plant based hard carbon, Chem. Eng. J. 316 (2017) 506–513. doi:10.1016/j.cej.2017.01.108.

[48] P. Sennu, N. Arun, S. Madhavi, V. Aravindan, Y.-S. Lee, All carbon based high energy lithium-ion capacitors from biomass: The role of crystallinity, J. Power Sources. 414 (2019) 96–102. doi:10.1016/j.jpowsour.2018.12.089.

[49] K. Kuratani, M. Yao, H. Senoh, N. Takeichi, T. Sakai, T. Kiyobayashi, Na-ion capacitor using sodium pre-doped hard carbon and activated carbon, Electrochimica Acta. 76 (2012) 320–325. doi:10.1016/j.electacta.2012.05.040.

[50] J. Ding, H. Wang, Z. Li, K. Cui, D. Karpuzov, X. Tan, A. Kohandehghan, D. Mitlin, Peanut shell hybrid sodium ion capacitor with extreme energy–power rivals lithium ion capacitors, Energy Environ. Sci. 8 (2015) 941–955. doi:10.1039/C4EE02986K.

[51] D. Li, C. Ye, X. Chen, S. Wang, H. Wang, A high energy and power sodium-ion hybrid capacitor based on nitrogen-doped hollow carbon nanowires anode, J. Power Sources. 382 (2018) 116–121. doi:10.1016/j.jpowsour.2018.02.036.

[52] M.E. Lee, H.W. Kwak, H. Kim, H.-J. Jin, All-Fibrous Pyroprotein-Based Monolithic Electrodes Containing Heteroatoms for Sodium-Ion Hybrid Capacitors, Macromol. Res. 27 (2019) 497–503. doi:10.1007/s13233-019-7073-9.

[53] C. Schütter, S. Pohlmann, A. Balducci, Industrial Requirements of Materials for Electrical Double Layer Capacitors: Impact on Current and Future Applications, Adv. Energy Mater. 0 (n.d.) 1900334. doi:10.1002/aenm.201900334.

[54] X. Wang, L. Liu, Z. Niu, Carbon-based materials for lithium-ion capacitors, Mater. Chem. Front. (2019). doi:10.1039/C9QM00062C.

[55] G. Rodríguez, A. Lama, R. Rodríguez, A. Jiménez, R. Guillén, J. Fernández-Bolaños, Olive stone an attractive source of bioactive and valuable compounds, Bioresour. Technol. 99 (2008) 5261–5269. doi:10.1016/j.biortech.2007.11.027.

[56] INNOLIVA convierte 45.000 toneladas de desecho de aceituna en biomasa, Innoliva. (2016). https://www.innoliva.com/es/innoliva-convierte-45-000-toneladas-de-desecho-de-aceituna-en-biomasa/ (accessed June 16, 2019).

[57] F. Rodríguez-Reinoso, M. Molina-Sabio, Activated carbons from lignocellulosic materials by chemical and/or physical activation: an overview, Carbon. 30 (1992) 1111–1118. doi:10.1016/0008-6223(92)90143-K.

[58] J. Jagiello, J.P. Olivier, A Simple Two-Dimensional NLDFT Model of Gas Adsorption in Finite Carbon Pores. Application to Pore Structure Analysis, J. Phys. Chem. C. 113 (2009) 19382–19385. doi:10.1021/jp9082147.

[59] M. Dahbi, N. Yabuuchi, K. Kubota, K. Tokiwa, S. Komaba, Negative electrodes for Na-ion batteries, Phys. Chem. Chem. Phys. 16 (2014) 15007–15028. doi:10.1039/C4CP00826J.

[60] Komaba Shinichi, Murata Wataru, Ishikawa Toru, Yabuuchi Naoaki, Ozeki Tomoaki, Nakayama Tetsuri, Ogata Atsushi, Gotoh Kazuma, Fujiwara Kazuya, Electrochemical Na Insertion and Solid Electrolyte Interphase for Hard-Carbon Electrodes and Application to Na-Ion Batteries, Adv. Funct. Mater. 21 (2011) 3859–3867. doi:10.1002/adfm.201100854.

[61] H. Lindström, S. Södergren, A. Solbrand, H. Rensmo, J. Hjelm, A. Hagfeldt, S.-E. Lindquist, Li+ Ion Insertion in TiO2 (Anatase). 2. Voltammetry on Nanoporous Films, J. Phys. Chem. B. 101 (1997) 7717–7722. doi:10.1021/jp970490q.

[62] V. Augustyn, P. Simon, B. Dunn, Pseudocapacitive oxide materials for high-rate electrochemical energy storage, Energy Environ. Sci. 7 (2014) 1597–1614. doi:10.1039/C3EE44164D.

[63] P. Simon, Y. Gogotsi, B. Dunn, Where Do Batteries End and Supercapacitors Begin?, Science. 343 (2014) 1210–1211. doi:10.1126/science.1249625.

[64] T. Brousse, D. Bélanger, J.W. Long, To Be or Not To Be Pseudocapacitive?, J. Electrochem. Soc. 162 (2015) A5185–A5189. doi:10.1149/2.0201505jes.

[65] M. Arnaiz, J.L. Gómez-Cámer, F. Mijangos, T. Rojo, E. Goikolea, J. Ajuria, Novel Lithium-Ion Capacitor Based on TiSb2 as Negative Electrode: The Role of Mass Ratio Towards High Energy-To-Power Densities and Long Cyclability, Batter. Supercaps. 0 (n.d.). doi:10.1002/batt.201800099.

[66] A. Laheäär, P. Przygocki, Q. Abbas, F. Béguin, Appropriate methods for evaluating the efficiency and capacitive behavior of different types of supercapacitors, Electrochem. Commun. 60 (2015) 21–25. doi:10.1016/j.elecom.2015.07.022.

[67] J. Ding, W. Hu, E. Paek, D. Mitlin, Review of Hybrid Ion Capacitors: From Aqueous to Lithium to Sodium, Chem. Rev. (2018). doi:10.1021/acs.chemrev.8b00116.

CHAPTER 3

Looking toward alternative electrolytes for dual carbon metal ion capacitors

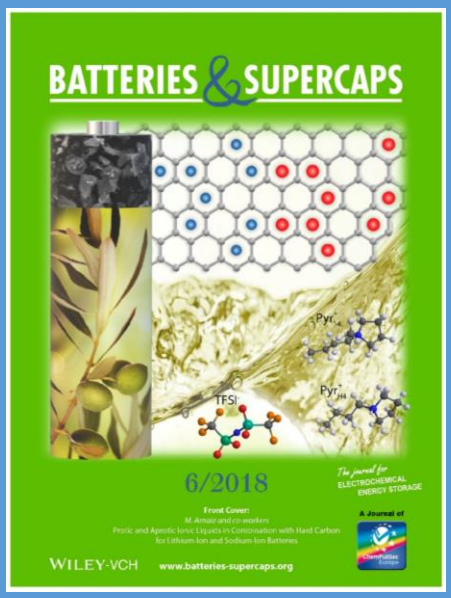

FRIEDRICH-SCHILLER-
UNIVERSITÄT
JENA

Looking toward alternative electrolytes for dual carbon metal ion capacitors

In continuation of the research reported in Chapter 2, different electrolytes were investigated in order to search for a higher electrochemical stability window that will enable to increase the energy density of dual carbon MICs. In this regard, pyrrolidinium-based ILs and an alternative solvent named 3-cyanopropionic acid methyl ester (CPAME) were tested. The lack of conductivity and high viscosity of ILs limited the behaviour of HC at high rates. Hence, it was abandoned concerning the dual carbon MIC development. Instead, CPAME shows to be a promising solvent in view of the development of high voltage LICs. Being able to operate in an extended voltage window of 1.5 - 4.5 V when the mass ratio is set to 1:0.5, when compared to the reference LIC based on 1 M $LiPF_6$ (EC:DMC) electrolyte, higher energy-to-power ratios have been achieved when discharge time is above 1 min. Moreover, it shows a capacitance retention of 70% after 5000 cycles.

Table of contents:

3.1. Introduction to alternative electrolytes for MICs

Same as for LIBs and EDLCs (as it was mentioned in **Chapter 1 - Section 1.3.3.2.** and **1.4.2.2.**, respectively) one of the strategies to increase the energy density of MICs goes through the selection of an electrolyte with high electrochemical stability window (ESW). In this sense, mainly different solvents and ILs have been studied for batteries and supercapacitors. Nevertheless, being MICs a novel technology, research was firstly focused on the search of materials able to give response to the high rates demanded. Thus, commonly used battery-type electrolytes such as 1 M $LiPF_6$ in EC:DMC in Li-ion and, 1 M $NaPF_6$ in EC:PC or 1 M $NaClO_4$ in EC:PC in Na-ion have been the preferable choices for LICs and NICs respectively. However, the technology has currently reached a maturity level in the field of materials that has allowed expanding the research focus to electrolytes.

Recently, Iwama *et al.* reported on the use of a different solvent for a LTO:AC based LIC, changing their previous 1 M $LiBF_4$ in PC by 1 M $LiBF_4$ in ethyl isopropyl sulfone (EiPS). Using PC as solvent and targeting high voltage LICs, oxidative decomposition of surface functional groups in the AC were taking place when the upper potential was set at 3.3 V. These reactions led to degradation of the negative electrode due to H_2O generation from the AC electrode that induced gas generation and SEI formation on the LTO electrode. Hence, the necessity of replacing PC by an alternative solvent less susceptible to hydrolysis was clear. Thus, being EiPS hydrolysis-resistant, those oxidative reactions were prevented and a high voltage operation LTO:AC based LIC without LTO degradation was achieved, exhibiting a 95% capacity retention after 1000 cycles [1].

Fleischmann *et al.* recently reported on the use of the IL 1-methyl-1-propylpyrrolidinium bis(trifluoromethylsulfonyl)imide (PMPyrr-TFSI) together with lithium bis(trifluoromethylsulfonyl)imide (LiTFSI) or sodium bis(trifluoromethylsulfonyl)imide (NaTFSI) salts in order to characterize an AC and a LTO as the positive and the negative

electrode respectively, and to develop both LICs and NICs. On the one side, the individual characterization of the AC showed a typical capacitive behaviour both within Li- and Na-based ILs. On the other side, LTO showed similar specific capacity values both in Li-ion (*i.e.* 143 mAh g^{-1} at 0.025 A g^{-1} and 108 mAh g^{-1} at 0.1 A g^{-1}) and Na-ion (*i.e.* 100 mAh g^{-1} at 0.001 A g^{-1} and 53 mAh g^{-1} at 0.1 A g^{-1}) in comparison with reported values in organic electrolytes [2,3]. Moreover, it was confirmed by XRD that the lithiation and sodiation mechanisms respectively did not change when ILs were used. This made both LTO-IL systems comparable with other works in literature. Motivated by these results, an LTO:AC based LIC and NIC were developed and characterized within a cell voltage of 1 – 4 V using its respective electrolyte. At low power densities (*i.e.* 25 W kg^{-1}), the LIC delivered 98 Wh kg^{-1} and the NIC 90 Wh kg^{-1}, while at their maximum power density (*i.e.* 1800 W kg^{-1}) the LIC showed an energy density of 10 Wh kg^{-1} and the NIC 5.5 Wh kg^{-1}. All the values were calculated respect the mass of both active and inactive materials. However, still the higher viscosity and lower conductivity of ILs limits the behaviour of MICs at high power demanding regions [4].

As alternative electrolytes mainly for Na-ion technology, ether-based electrolytes, also known as glymes, arose. These electrolytes were proposed owing to the impossibility of using graphite in Na-ion technology due to the thermodynamical instability of Na-GICs with ester-based electrolytes. Instead, glyme-based ones create stable ternary Na-GICs and expand the graphite layers allowing the successful insertion of Na^+. Following the research done in NIBs, the first NIC using a glyme-based electrolyte was reported in 2015. Han *et al.* developed a NIC using graphitic mesocarbon microbead as the negative electrode, and an AC as the positive electrode using 1 M $NaPF_6$ in diglyme as electrolyte. The graphitic mesocarbon microbead showed 130 mAh g^{-1} at 0.02 A g^{-1} and still kept 105 mAh g^{-1} at 1.5 A g^{-1}, demonstrating its good compatibility with the electrolyte. The AC also showed excellent capacitive behaviour in the potential range of 1 – 4 V *vs.* Na^+/Na. Thus, combining both materials a NIC able to deliver 93.5 Wh kg^{-1}_{AM} at 573 W kg^{-1}_{AM} and 86.5 Wh kg^{-1}_{AM} at 2832 W kg^{-1}_{AM} was obtained. However, the

capacitance retention of the device fade quite fast maintaining only the 60% of the initial capacitance after 1500 cycles. The latter was ascribed to the wide cell voltage. Although sacrificing energy, a more limited cell voltage of 1 – 3.3 V in the NIC allowed keeping 98% of its initial capacitance after more than 3000 cycles [5].

Recently, Park *et al.* reported on the use of 1 M $NaClO_4$ in combination with different ether-based solvents such as 1,2-dimethoxyethane (DME), diethylene glycol dimethyl ether (DEGDME) or tetraethylene glycol dimethyl ether (TEGME) in order to developed a NIC using AC as the negative electrode and $Na_3V_2(PO_4)_3$ (NVP) as the positive electrode. It was shown that among the above-mentioned electrolytes, the ionic conductivity was higher for 1 M $NaClO_4$ DME>DEGDME>TEGDME electrolytes, while the viscosity was higher for 1 M $NaClO_4$ TEGDME>DEGDME>DME. These ether-based and other typical ester-based electrolytes such as 1 M $NaClO_4$ in EC:DEC, EC:PC or PC were used to electrochemically characterized AC:NVP based NICs. It was shown that DEGDME and TEGDME-based ones maintained the ~67% of the initial capacitance after 1000 cycles, while those using ester-based electrolytes show at least ~85% retention [6]. Hence, as it is shown there is still room for research in electrolyte and MICs field.

In this regard, continuing with the olive pits derived dual carbon HC:AC hybrid system developed in **Chapter 2**, first, some ILs were studied and then an alternative solvent to replace the typical carbonates was also proposed.

3.2. Ionic liquids

ILs can be divided in two main groups, aprotic ionic liquids (AILs) and protic ionic liquids (PILs) [7]. The main difference between them is that PILs have an available proton on the cation. Up to now, the studies with negative electrode materials for both LIBs and NIBs have been focused on the use of AILs owing to their wider ESW compared to PILs. However, recent works suggest that PIL-based batteries can perform

better than their AIL-based counterparts at high rates. Moreover, taking into account the fact that PILs are a more affordable option, then, the use of these electrolytes becomes an even more attractive alternative in the search for next generation batteries [8–10]. Regarding NIBs, Fukunaga *et al.* studied the electrochemical performance of a HC in N-methyl-N-propylpyrrolidiniumbis(fluorosulfonyl)amide [C_3C_1pyrr][FSA], reporting a reversible capacity of 260 mAh g^{-1} at 0.05 A g^{-1} and 90 ºC [11]. Using the same IL, Ding *et al.* reported the behaviour of a HC at different temperature ranges and showed that this anodic material could deliver 230 mAh g^{-1} at 90 °C and 25 mAh g^{-1} at 25 °C [12]. Wang *et al.* reported the performance of a (HC:$Na_{044}MnO_2$) NIB containing N-propyl-N-methylpyrrolidinium (PMP)–FSI with 1 M NaFSI at room-temperature (RT). Surprisingly, the performance of this full cell in the IL-based electrolyte was even better than that observed in a conventional organic electrolyte. This improvement was ascribed to the low charge transfer resistance (R_{ct}) values of the interface between the electrode materials and the IL [13]. A recent study shows that a NIB containing HC:($Na_3V_2(PO_4)_3$/C) as electrodes and working in 1 M NaFSI dissolved in N-propyl-N-methyl pyrrolidinium bis(fluoromethanesulfonyl)imide (C_3mpyrFSI) can show a RT energy density of 368 Wh kg^{-1} [14]. In the case of LIBs, the best performance of a HC was reported by Zheng *et al.* who investigated the behaviour of this material in 1 M LiTFSI trimethyl-n-hexylammonium (TMHA) -bis(trifluoromethanesulfone)imide (TFSI) at different temperatures, reporting a capacity value as high as 675 mAh g^{-1} at 80 ºC [15]. As evidenced by this short literature overview, most of the studies dedicated to HCs in ILs have been carried out at high temperature. Furthermore, the behaviour of a HC in PILs has never been investigated. Against this background, the performance of a HC in AILs and PILs at RT for both Li- and Na-ion technologies is studied in this thesis.

For the investigations reported, two ILs have been considered, the AIL 1-butyl-1-methylpyrrolidinium bis(trifluoromethanesulfonyl)imide (Pyr_{14}TFSI) and the PIL 1-butylpyrrolidinium bis(trifluoromethanesulfonyl)imide (Pyr_{H4}TFSI) (**Figure 3.1**). As

salts, lithium bis(trifluoromethanesulfonyl)imide (LiTFSI) and sodium bis(trifluoromethanesulfonyl)imide (NaTFSI) have been used (**Figure 3.1**).

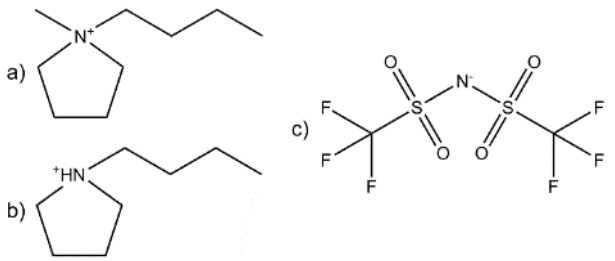

Figure 3.1. a) 1-butyl-1-methylpyrrolidinium (Pyr_{14}^{+}) cation, b) 1-butylpyrrolidinium cation (Pyr_{H4}^{+}) and c) bis(trifluoromethanesulfonyl)imide ($TFSI^{-}$) anion.

$Pyr_{14}TFSI$ has been largely used in the past owing to its air-stable, hydrophobic, thermal stability (up to 300 ºC) and high ESW (up to 5.5 V) features [16]. It shows a conductivity and a viscosity of 1.85 mS cm^{-1} and 95 Pa·s, respectively, at 20ºC, values that are comparable to conventional organic solvents of LIBs. Several authors investigated the use of this electrolyte in some cathode and anode materials in both Li- and Na-ion technologies [17–20]. More exactly, Menne *et al.* reported on the use of graphite with LiTFSI-$Pyr_{14}TFSI$ and LiTFSI-$Pyr_{H4}TFSI$ and on the use of soft carbon with LiTFSI-$Pyr_{14}TFSI$ [20]. Thereby, going from a perfectly ordered carbon (*i.e.* graphite) to a disordered but still graphitizable one (*i.e.* soft carbon), at this stage, the study in a disordered and non-graphitizable material such as HC became a challenge. While in the case of the Na-based electrolytes (NaTFSI-$Pyr_{14}TFSI$ and NaTFSI-$Pyr_{H4}TFSI$), it was not until very recently, in 2018, when Stettner *et al.* reported for the first time their use in an AC:AC EDLC system [21]. Hence, those Na-based electrolytes in a battery-type carbonaceous anode material are tested in this thesis for the first time.

3.2.1. Preparation of ILs and physicochemical characterization

Pyr_{14}TFSI has been purchased from Iolitec (99% purity), while Pyr_{H4}TFSI has been synthesized as previously reported [22]. It was synthesized using a metathesis method. First, 1-butylpyrrolidinium was freshly distilled in order to avoid further impurities and then introduced into a three-necked round-bottom flask immersed in an ice bath and topped by a reflux condenser. A dropping funnel was utilized to add the acid solution (37% HCl in water), and a thermometer to control the temperature. The solution was added dropwise to the imine under vigorous stirring (30 min). As the acid-base reaction was slightly exothermic, an ice bath was used to maintain the temperature below 25ºC. After the addition of all the acid to the imine, stirring was maintained for 2 h at room temperature. Then all the water was removed via rotary vapor to get the exact amount of 1-butylpyrrolidinium chloride (Pyr_{H4}Cl) and later add the same amount of LiTFSI.

Subsequently, Pyr_{H4}Cl was mixed with water, and maintained under stirring until total dissolution. The LiTFSI was also mixed in water. Then, those two solutions were mixed together and the stirring was continued for 2 h. This process enabled replacing the Cl^- by the $TFSI^-$. After the stirring period, the aqueous phase was placed at the top and the PIL one at the bottom. For a better separation of these two phases, a small amount of chloroform was added, and the product was introduced into a separating funnel. The PIL diluted in chloroform was separated from the aqueous phase, and then washed with small amounts of water, in order to eliminate the chloride, as LiCl, formed during the metathesis process. After being washed with water several times, tests were performed with $AgNO_3$ on the aqueous phase, in order to determine whether any chloride was remaining in the PIL. In fact, silver reacts with the chloride to form AgCl, which is a well-known white precipitate, which darkens upon exposure to light. Thus, the absence of this solid led to the supposition that almost all chloride had been removed from the PIL.

After the purification process, chloroform was evaporated under reduced pressure. Finally, the PIL was dried under a high vacuum using a liquid nitrogen trap, during two or three days. The PIL was analyzed for water content using coulometric Karl-Fisher titration, and was found to contain approximately 20 or 30 ppm, just after drying.

Regarding lithium and sodium salts, both of them, LiTFSI and NaTFSI, have been purchased from Solvionic (99.5% purity). Thus, in the end the prepared electrolytes were: 0.5M LiTFSI-Pyr_{14}TFSI, 0.5M LiTFSI-Pyr_{H4}TFSI, 0.5M NaTFSI-Pyr_{14}TFSI and 0.3M NaTFSI-Pyr_{H4}TFSI. This last concentration was selected based on the maximum solubility of NaTFSI in Pyr_{H4}TFSI. All of them were also characterized using 2 wt% of vinyl ethylene carbonate as additive and denoted with VEC. The water content of the ILs is measured using a Karl-Fisher coulometer, and is found to be lower than 30 ppm for all electrolytes. **Table 3.1** summarizes the conductivity and viscosity values at 30ºC and the ESW of the studied electrolytes reported elsewhere [20,21].

Table 3.1. Conductivity and viscosity at 30ºC of the used electrolytes.

Electrolyte	Conductivity ($mS \cdot cm^{-1}$)	Viscosity (mPa·s)	ESW (V vs. Ag)	Reference
0.5M LiTFSI-Pyr_{14}TFSI	1.9	136.7	-3 to 3V	[20]
0.5M LiTFSI-Pyr_{H4}TFSI	2.0	99.7	-1 to 3V	[20]
0.5M NaTFSI-Pyr_{14}TFSI	1.7	111	-3.3 to 2.5V	[21]
0.3M NaTFSI-Pyr_{H4}TFSI	2.8	70	-1 to 2.5V	[21]

As it is observed, all of them show similar conductivity values. While regarding the viscosity, it is shown that AIL are more viscous than their PIL counterparts. Concerning the ESW, PILs show a limited value at low potentials due to the instability of Pyr_{H4}^{+}, while AILs show a wider ESW.

3.2.2. Electrochemical characterization using HC electrode

All the electrochemical measurements were carried out in a three-electrode Swagelok® type cell, using glass fibre membrane as separator (Whattman GFB) and one lithium or sodium metal disc as counter electrode and another lithium or sodium metal disc as reference electrode in the case of $Pyr_{14}TFSI$-based electrolytes. In order to avoid the reaction between the alkali metals and the protons from $Pyr_{H4}TFSI$, in $Pyr_{H4}TFSI$-based electrolytes an oversized $LiFePO_4$ or $Na[Fe_{0.5}Mn_{0.5}]O_2$ was used as counter electrode and Ag wire as reference. In this latter case, for the sake of comparison, the potential values reported in the figures are referring to Li^+/Li or Na^+/Na.

Figure 3.2 shows a comparison of the CVs recorded using olive pits derived HC electrodes at RT and 0.1 mV s^{-1} between 0.005 and 2 V *vs.* Li^+/Li and Na^+/Na in 0.5 M LiTFSI-$Pyr_{14}TFSI$ (AIL-Li), 0.5 M LiTFSI-$Pyr_{H4}TFSI$ (PIL-Li), 0.5 M NaTFSI-$Pyr_{14}TFSI$ (AIL-Na) and 0.3 M NaTFSI-$Pyr_{H4}TFSI$ (PIL-Na) electrolytes. According to previous studies, vinyl ethylene carbonate (VEC) decomposes within the ESW of the prepared PIL, and thus, it can avoid the exfoliation of the carbon electrode and ultimately improve the electrochemical performance. Also, due to the limited cathodic stability of the Pyr_{H4}^+ cation (**Table 3.1**), the presence of a film-forming additive is always necessary when working with this PIL [20].

In order to test the effect of using this additive with HC electrodes, AIL-Li-VEC and PIL-Li-VEC electrolyte formulations were also studied. **Figure 3.2a** and **3.2b** show the behaviour of the HC in AIL-Li and AIL-Li-VEC, respectively. As shown, the CVs obtained in both electrolytes exhibit a peak at ~ 1 V *vs.* Li^+/Li, which can be ascribed to the SEI formation. These results show that in HC, contrary to graphite, the use of an additive is not always required when working in $Pyr_{14}TFSI$ [23]. Nevertheless, its use promotes a more stable and suitable SEI, which is reflected in the sharper cathodic peak observed below 1 V *vs.* Li^+/Li (**Figure 3.2b**), indicative of an improved Li^+ insertion in the microstructure of the HC [24]. Moreover, by using the additive the first cycle CE

calculated from the CVs rises from 48% to 54% in the case of the AIL-Li. In the following cycles the CE is stabilized at 96% independent of the addition of VEC. In the case of the HC cycled in PIL-Li-VEC (**Figure 3.2c**), the decomposition of VEC occurs at ~1.5 V *vs.* Li^+/Li, whereas the SEI formation and reversible Li^+ insertion/deinsertion peaks are observed at about 1 V and below 0.5 V *vs.* Li^+/Li, respectively. The first cycle CE of the HC in this electrolyte is as low as 34%, while in the following cycles it is stabilized at 88%. Formerly, Menne *et al*. reported the use of LiTFSI-Pyr_{H4}TFSI in combination with graphite and soft carbon-based electrodes. Now, these results show, that it is possible to use PIL-based electrolytes also in combination with HC electrodes.

Figure 3.2d and **3.2e** show the CVs of the HC in AIL-Na and AIL-Na-VEC electrolytes, respectively. Similar to the results obtained in Li-ion, a more pronounced and better resolved peak at ~1 V *vs.* Na^+/Na reveals an improved SEI formation owing to the use of a film-forming additive. This allows identifying better the typical HC profile indicative of the Na^+ insertion mechanism [25,26]. Furthermore, the use of the additive shows a major enhancement in the first cycle CE going from 44% to 58%. In the following cycles, the CE stabilizes at 90% and 99% for AIL-Na and AIL-Na-VEC, respectively. As in the Li-based PIL, also the limited cathodic stability of the Pyr_{H4}^+ cation in the Na-based PIL (**Table 3.1**), makes necessary the presence of a film-forming additive for the SEI formation. However, contrary to Li-based systems, after testing different additives and maintaining always the water content of the electrolyte below 30 ppm, PIL-Na-VEC electrolyte appears to be unstable below ~1.2 V *vs.* Na^+/Na, hindering its use with the studied carbonaceous material in Na-based electrolytes (**Figure 3.2f**).

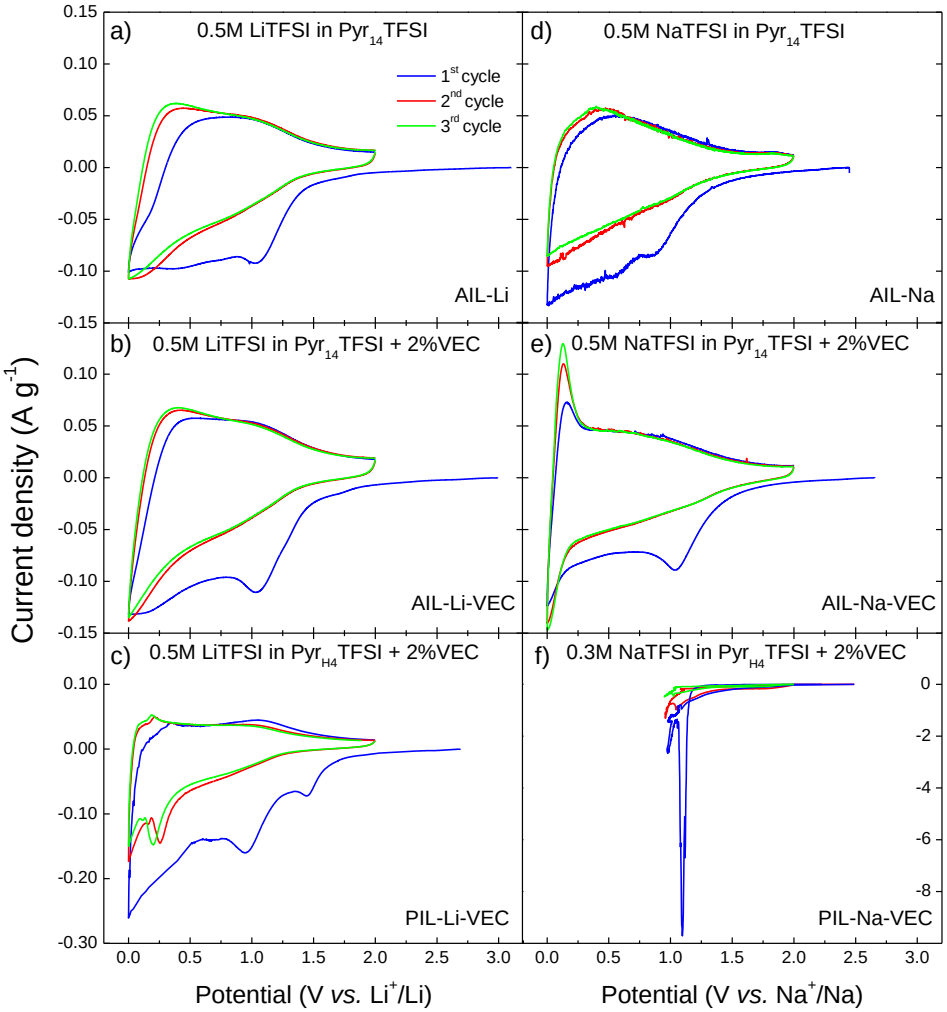

Figure 3.2. CVs recorded at 0.1 mV s^{-1} from 0.005 V to 2 V *vs.* Li^+/Li or Na^+/Na for HC-based electrodes in a) AIL-Li, b) AIL-Li-VEC, c) PIL-Li-VEC, d) AIL-Na, e) AIL-Na-VEC and f) PIL-Na-VEC.

Figure 3.3 shows GA charge/discharge measurements performed just after the CVs in a potential window of 0.005 - 2 V *vs.* Li^+/Li and *vs.* Na^+/Na. **Figure 3.3a** shows the charge/discharge profile of the HC in AIL-Li, AIL-Li-VEC and PIL-Li-VEC electrolytes at C/5. As shown in **Figure 3.3a**, all charge/discharge profiles are in good agreement with

the absence of sharp peaks observed in the CVs, and they are all displaying a sloping region from 1 V to 0.005 V *vs.* Li^+/Li, which can be assigned to the Li^+ insertion through the HC layers [27]. **Figure 3.3b** compares the specific capacities delivered by the HC at different C-rates in the investigated Li-based electrolytes. As shown, the HC electrode in combination with AIL-Li-VEC delivers a specific capacity of 242 mAh g^{-1} at C/5 and 102 mAh g^{-1} at 1C, while the system working in AIL-Li delivers 224 mAh g^{-1} at C/5 and 88 mAh g^{-1} at 1C. Taking into account these results, it appears that at low rates SEI features play an important role on the Li^+ deinsertion mechanism, while increasing the C-rate, the difference in the specific capacity due to the VEC addition is attenuated. The use of PIL-Li-VEC leads to a different behaviour. As shown, at C/5 the HC electrode displays a specific capacity of 185 mAh g^{-1} which is lower than those observed in AIL-based electrolytes (with and without VEC). At high rates, however, the use of the PIL appears to be more advantageous as indicated by the fact that the HC electrode displays a specific capacity of 122 mAh g^{-1} at 1C and 58 mAh g^{-1} at 5C. These higher values show that the unique lithium environment of PIL-based electrolytes [8,28] and their higher ionic conductivity (**Table 3.1**) have a positive effect on carbonaceous negative electrodes.

After the C-rate tests, the electrodes were cycled at C/5 to measure the stability of the investigated systems. As shown in **Figure 3.3c**, after 30 cycles both the capacity retention and the CE of the HC in AIL-Li-based electrolytes is still almost 100%. After the same number of cycles, the HC electrode cycled in PIL-Li electrolyte retains about 90% of the initial capacity. In the case of the latter system, some degradation processes were presumably taking place during cycling as evidenced by the CE values exceeding 100%. Nevertheless, taking into account that better CE values could be obtained through the electrolyte composition optimization, the main conclusion drawn from these results is that PIL-Li-based electrolytes can be successfully utilized in combination with a variety of carbonaceous negative electrodes for LIBs.

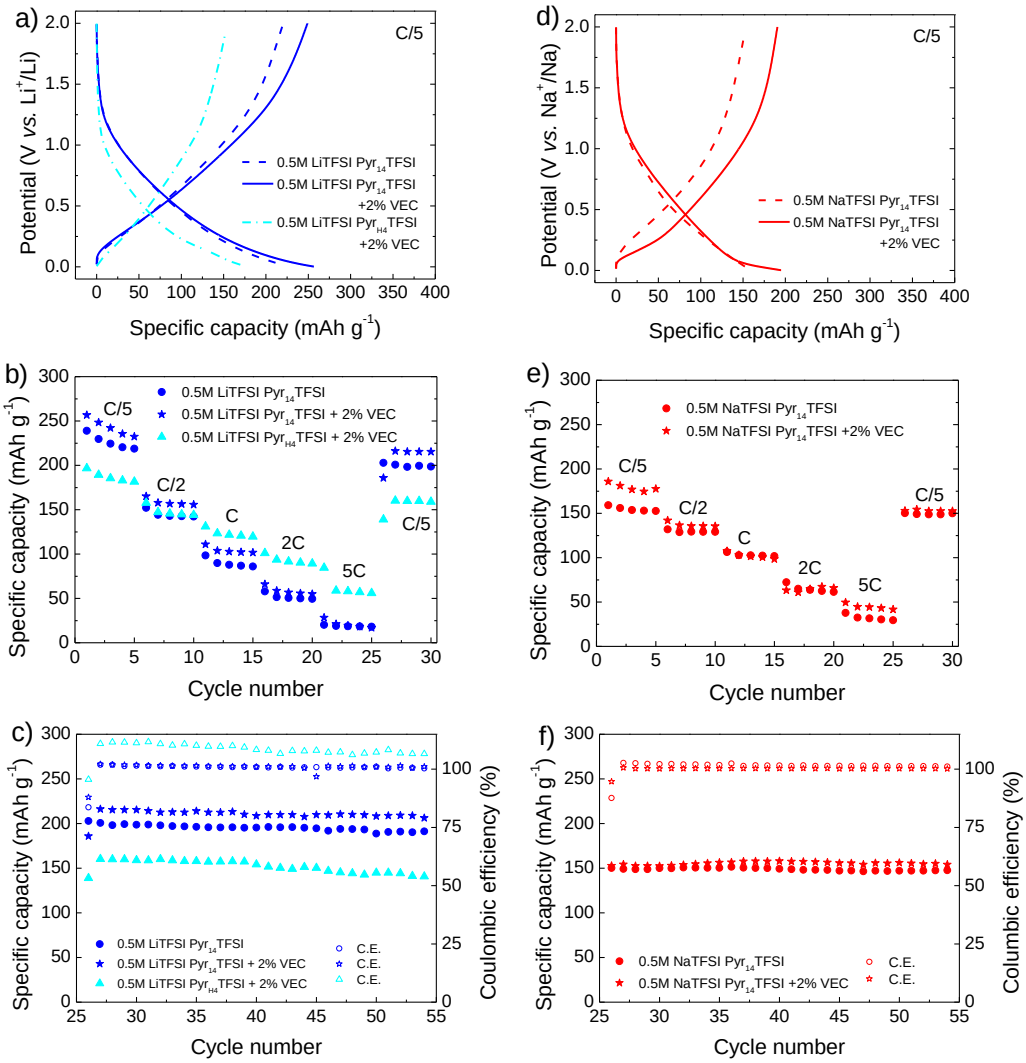

Figure 3.3. GA charge/discharge characterization of the HC electrodes between 0.005 V to 2 V *vs.* Li^+/Li (a, b, c) and Na^+/Na (d, e, f) in the investigated electrolyte: a),d) Charge/discharge profiles of the HC, b), e) Rate capability and c), f) Stability at C/5.

Figure 3.3d compares the GA charge/discharge profiles of HC electrodes in AIL-Na-based electrolytes. These profiles were obtained at C/5 and in the potential window comprise between 0.005 and 2 V *vs.* Na^+/Na. As shown in the figure, the sloping region

observed from *ca.* 1 V to 0.2 V *vs.* Na^+/Na, followed by a low potential plateau is in good agreement with the CV profiles (**Figure 3.2d and 3.2e**). As already discussed in the literature, the sloping region can be ascribed to the interlayer insertion of Na^+, while the plateau could be related to the Na^+ insertion into the micropores [25,26]. **Figure 3.3e** shows that when VEC is added, the initial capacity is slightly higher probably due to the decomposition of the additive. Then, in both AIL-Na and AIL-Na-VEC electrolytes, there is an initial capacity drop during the first 5 cycles at C/5 (stabilizing/conditioning stage) while the capacity seems to recover after the rate capability screening. Already at the 30^{th} cycle at C/5 the capacity is not dependent on the presence of VEC. As shown in **Figure 3.3e**, the HC electrode cycled in AIL-Na-VEC delivers 178 mAh g^{-1} at C/5 while in AIL-Na the capacity is 154 mAh g^{-1}. At an increased discharge rate of 2C both systems deliver a capacity of 64 mAh g^{-1}, whereas at 5C capacity values differ slightly, 44 mAh g^{-1} and 32 mAh g^{-1} for AIL-Na-VEC and AIL-Na systems, respectively. As shown in **Figure 3.3f**, the use of both electrolytes allows a very stable performance. In fact, after 30 cycles at C/5, HC electrodes are able to keep all their initial capacity and during cycling the CE is always close to 100%. Therefore, based on the high and stable specific capacity values achieved by HC electrodes, these results indicate that IL-based electrolytes can also be used in NIBs even at RT [11,12,15].

In summary, in this study the use of AIL and PIL based electrolytes at RT in view of its use together with a HC electrode was investigated. It is shown that $Pyr_{14}TFSI$ can be successfully utilized, with or without additive, when a HC is used as negative electrode. In combination with LiTFSI, the HC displays a RT capacity of *ca.* 200 mAh g^{-1} at C/5 and a good cycling stability when using this AIL. It is also shown for the first time that PIL-based electrolytes such as $Pyr_{H4}TFSI$ could be effectively used in LIBs built with olive pits derived HC electrodes. Particularly interesting appears to be the use of this PIL for high rate applications. Moreover, as shown in **Figure 3.4,** the studied HC overcomes elsewhere reported graphite in terms of specific capacity values in all the studied C-rate range [20], what encourages the replacement of graphite by HC when using these ILs.

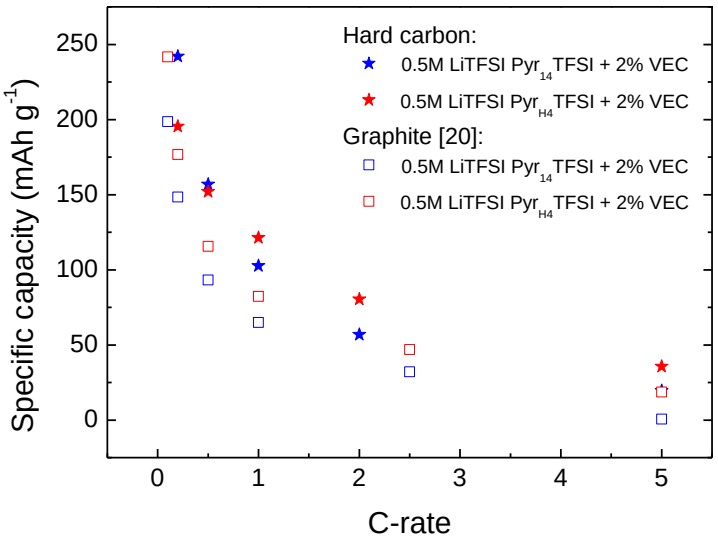

Figure 3.4. Specific capacity values at different C-rates for the studied HC and already reported graphite [20] in AIL-Li-VEC.

Finally, it has been shown that $Pyr_{14}TFSI$ is also a very promising candidate for the realization of Na-ion based systems. As a matter of fact, the use of this AIL in combination with NaTFSI guarantees high RT specific capacity and a good cycling stability. However, $Pyr_{H4}TFSI$ cannot be successfully used with HC electrodes in NIBs, most probably because the additive is not able to form a stable SEI that ensures reversible deprotonation/protonation of Pyr_{H4}^{+} and hence, it reacts at low potentials.

Moreover, as consequence of the low specific capacity values obtained at high rates, these electrolytes are still limited for high power applications and hence, they were left aside to be tested together with an AC for the realization of dual carbon MICs.

3.3. Alternative solvent: 3-cyanopropionic acid methyl ester

In view that the studied ILs did not fulfil power expectations, a new strategy was adopted in order to find potential electrolytes able to substitute the commonly used organic ones

and enhance the cell voltage of MICs. In order to facilitate the search for alternative solvents, Schütter *et al.* developed a fast prediction formula. Based on a computational screening method, it allows identifying the most promising solvent candidates for the realization of high voltage electrolytes for EDLC applications [29]. Among them, 3-cyanopropionic acid methyl ester, hereafter named as CPAME, was found to be one of the best alternatives, displaying operative voltages up to 3.5 V [30,31]. Later, Brox *et al.* investigated different cyanoester solvents, such as, methyl 2-cyano-2-methylpropanoate (MCMP), methyl 2-cyanoacetate (MCA), ethyl 2-cyano-2-methylpropanoate (ECMP) and methyl 3-cyanopropanoate (MCP, renamed in this work as CPAME), all with a certain amount of fluoroethylene carbonate (FEC) additive, to develop new electrolyte formulations based on $LiPF_6$ salt for the development of LIBs using $LiNi_{1/3}Mn_{1/3}Co_{1/3}O_2$ (NMC111) as the positive electrode and graphite as the negative electrode. CPAME-based electrolyte turned out to be the one that showed the most stable cycling performance and the highest capacity retention [32]. Despite the possibilities of CPAME as a solvent for both EDLC [31,33] and LIB [32,34] technologies, to the best of my knowledge, its use in LIC technology has never been explored before. Thereby, targeting high voltage LICs, the use of an electrochemically more stable electrolyte allows increasing the cell voltage and hence, to enhance the energy density of the overall device. Thus, in this work, the potential use of $LiPF_6$ in CPAME electrolyte is evaluated for the first time in LIC technology.

3.3.1. Preparation and physicochemical characterization of $LiPF_6$ (CPAME)

CPAME solvent is commercially available and has been purchased from ABCR (99% purity). It has been dried over 3 Å molecular sieves until its water content was below 25 ppm, as measured by Karl-Fischer technique. The $LiPF_6$ salt (Sigma-Aldrich, battery grade, >99.99% purity) was used as received to prepare different solutions in CPAME with concentrations of 0.5 M, 1 M and 1.5 M. The preparation was followed in a glove

box under argon atmosphere with H_2O and O_2 content below 0.1 ppm. Afterwards, viscosity and conductivity measurements were followed to select the most appropriate electrolyte concentration. In **Figure 3.5** viscosity and conductivity values of CPAME-based electrolytes with different concentrations (0.5 M, 1 M and 1.5 M) are reported and compared with commercial 1 M $LiPF_6$ (EC:DMC). Both the viscosity and the ionic conductivity are key parameters that determine the final performance of the electrolyte. On the one hand, viscosity defines the ion transport capability along the device. On the other hand, conductivity will determine the power performance of the overall system. **Figure 3.5a** shows that the viscosity of CPAME-based electrolytes increases depending on the salt concentration along the studied temperature range. The influence of temperature is very notorious: at low temperatures (*e.g.* -10ºC), the salt concentration plays a key role on the measured viscosity, increasing viscosity values up to 20.7 mPa·s, 52.5 mPa·s and 152.8 mPa·s for 0.5 M, 1 M and 1.5 M, respectively. However, when the temperature reaches 20ºC, the difference among viscosities tends to neutralize and the values go down to 5.6 mPa·s, 10.5 mPa·s and 21.3 mPa·s respectively. Finally, at 60ºC, similar viscosities of 2.4 mPa·s, 3.8 mPa·s and 6.12 mPa·s are obtained. On the contrary, 1 M $LiPF_6$ (EC:DMC) maintains its viscosity rather constant within the range of 5.6 - 1 mPa·s going from -10ºC to 60ºC. With regard to the conductivity, **Figure 3.5b** shows that very similar conductivity values are measured for CPAME-based systems until 20ºC independently of the electrolyte concentration, *i.e.* 2.5 mS cm^{-1}, 3 mS $cm^{-1}$and 2.3 mS cm^{-1} for 0.5 M, 1 M and 1.5 M, respectively. In contrast, when the temperature is increased, while 1 M and 1.5 M based electrolytes maintain similar values, 0.5 M shows lower conductivity. Instead, 1 M $LiPF_6$ (EC:DMC) shows a notable increase in the conductivity going from 4.64 to 19.45 mS cm^{-1} within the range of -10ºC to 60ºC, values twice as much for those obtained for CPAME-based systems. Taking these results into account, although 1 M $LiPF_6$ (EC:DMC) presents better transport properties, the investigated 1 M $LiPF_6$ (CPAME) electrolyte, which turns out to best balance viscosity and conductivity features among the different studied salt concentrations, appears to

display conductivity and viscosity values able to match the standards required for the assembly of powerful LICs.

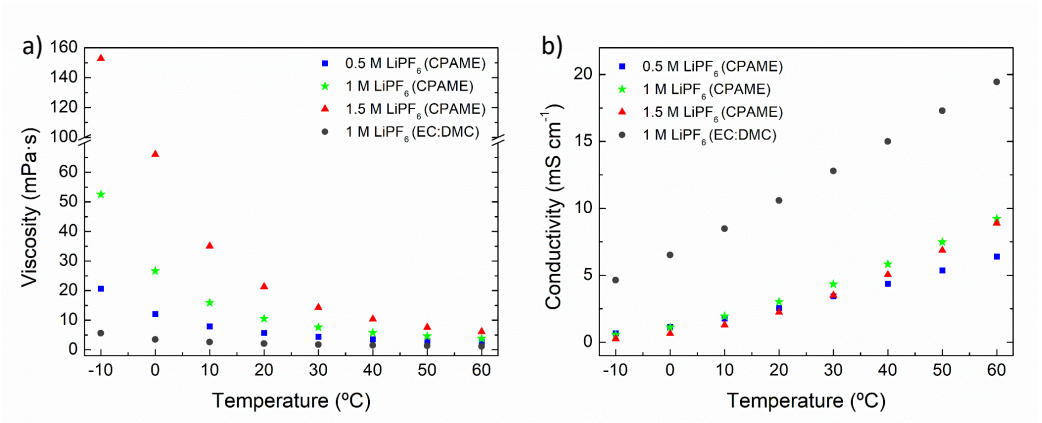

Figure 3.5. a) Viscosity and b) conductivity values for different salt concentration of $LiPF_6$ in CPAME compared to 1 M $LiPF_6$ (EC:DMC) in the temperature range from -10 to 60ºC.

Thermogravimetric analysis of the selected 1 M $LiPF_6$ (CPAME) is shown in **Figure 3.6**. An initial temperature scan carried out at 10ºC min^{-1} from RT to 175ºC reveals a decrease in weight of the electrolyte occurring at around 100ºC, ascribed to the electrolyte decomposition at high temperatures. More in depth analysis monitoring the weight percentage of the electrolyte along 5 steps of 25ºC measured during 2 h each in the range of 25 - 125ºC showed the detailed thermal behaviour of the electrolyte (inset **Figure 3.6**). At 25ºC the electrolyte is quite stable, while at 50ºC degradation starts to occur. Finally, after 2 h at 75ºC the electrolyte is completely decomposed. Thus, for the sake of stability, the studied CPAME-based electrolyte should be used at temperatures close to RT. In order to evaluate the electrochemical stability of the studied electrolyte, the ESW was determined in both anodic and cathodic ranges (**Figure 3.7**). For comparison, reported potential values are referred *vs.* Li^+/Li. The obtained results determined the ESW for 1 M $LiPF_6$ (CPAME) to be between 0 and 6 V vs. Li^+/Li. Out of this potential range, the specific current increases, indicating that the electrolyte is decomposing. Compared to commercial 1 M $LiPF_6$ (EC:DMC), the ESW is widen about 0.5 V at the high potential

range [35], allowing this electrolyte to be used in high voltage systems close to 5 V. However, the ESW results cannot be directly extrapolated to a full cell system due to the different cell conditions.

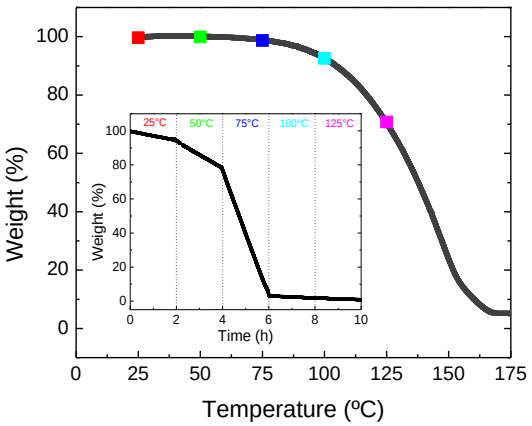

Figure 3.6. Thermogravimetric analysis of 1 M $LiPF_6$ (CPAME): temperature scan at 10 ºC min^{-1} and inset: weight percentage of the electrolyte along 5 steps measured during 2 h in the range of 25-125ºC.

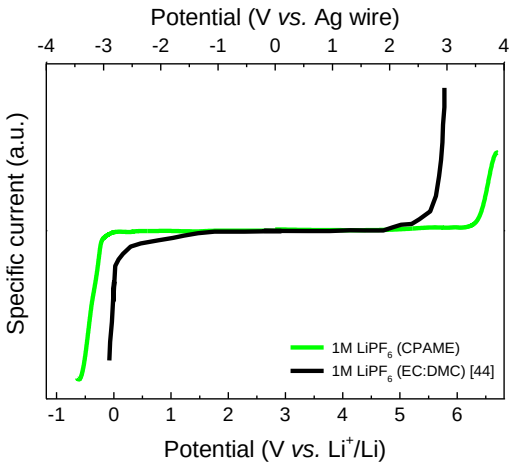

Figure 3.7. ESW of the studied 1 M $LiPF_6$ (CPAME) at 1 mV s^{-1} scan rate.

3.3.2. Electrochemical characterization of both HC and AC

Preliminary CV of the HC in 1 M $LiPF_6$ (CPAME) (**Figure 3.8a**) reveals its impossibility to create a suitable SEI hindering the ion insertion/deinsertion into the microstructure of the HC, consequently the use of an additive such as vinylene carbonate (VC) is required. Thus, electrochemical characterization of the HC electrode in 1 M $LiPF_6$ (CPAME) + 3 wt% VC, hereafter known as HC-CPAME was followed. **Figure 3.8b** shows the first three voltammograms recorded at 1 mV s^{-1} between 0.005 and 2 V *vs.* Li^+/Li. The first charge step of the HC-CPAME shows a reduction peak centered at ~1 V *vs.* Li^+/Li corresponding to the SEI formation through the decomposition of the carbonate additive [36,37]. The following oxidation peak appearing below 0.5 V *vs.* Li^+/Li describes the ion insertion into the microstructure. In the following cycles, same peaks are observed at low potentials confirming the reversible nature of the Li^+ insertion/deinsertion process taking place in the HC-CPAME system [38,39]. GA charge/discharge profiles shown in **Figure 3.8c** are in good agreement with previous voltammograms and the described mechanism. Rate capability performance of the HC-CPAME electrode compared to HC in 1 M $LiPF_6$ (EC:DMC), hereafter named as HC-EC:DMC, both in the potential window of 0.005 - 2 V *vs.* Li^+/Li is shown in **Figure 3.8d**. With regard to HC-CPAME, the first charge step recorded at C/10 delivers a total specific capacity of 650 mAh g^{-1} from which 342 mAh g^{-1} are reversible, setting a CE of 50%. In the case of HC-EC:DMC, first charge capacity is 1070 mAh g^{-1} from which 450 mAh g^{-1} are reversible (CE of 42%). After 5 stabilizing cycles at C/10, HC-CPAME delivers 322 mAh g^{-1}, while HC-EC:DMC delivers 400 mAh g^{-1}. Increasing the current density up to 5C and 10C, HC-CPAME delivers 100 mAh g^{-1} and 80 mAh g^{-1}, while HC-EC:DMC reaches 240 and 215 mAh g^{-1} respectively. The difference in the specific capacity can be directly attributed to the difference in viscosity and conductivity of each electrolyte (2.1 mPa·s *vs.* 10.5 mPa·s and 10 mS cm^{-1} *vs.* 3 mS cm^{-1}, for EC:DMC- and CPAME-based electrolytes, respectively). Overall, despite the HC-CPAME system cannot match the performance of HC-EC:DMC, still good

capacity values close to 100 mAh g^{-1} are achieved at 10C, what added to the possibility of increasing the operative voltage holds promise for the development of high energy and high power LICs.

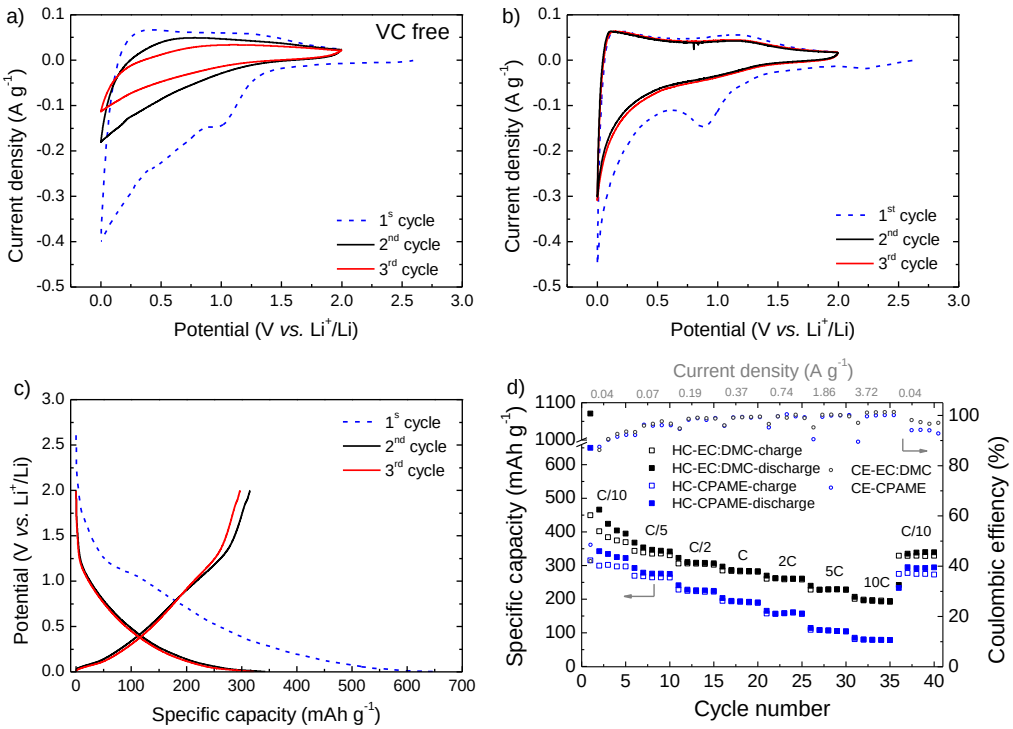

Figure 3.8. Electrochemical characterization of the HC between 0.005 – 2 V *vs.* Li^+/Li, CVs: a) in 1 M $LiPF_6$ (CPAME) without VC and b) with 3 wt% VC and GA charge/discharge measurement in 1 M $LiPF_6$ (CPAME) + 3 wt% VC: c) profiles at C/10 and d) rate capability.

With regard to the positive electrode, despite the ESW of 1 M $LiPF_6$ (CPAME) inferred good stability at high potentials, an accurate investigation of the operative potential of the AC in CPAME-based electrolyte is necessary in view of the realization of LICs. Consequently, CVs at different potential windows were run at 5 mV s^{-1} (**Figure 3.9a**). The lowest cut-off potential was set at 2 V *vs.* Li^+/Li while the highest cut-off potential was shifted from 4.2 to 5 V *vs.* Li^+/Li. The characteristic rectangular shape indicative of

the capacitive storage mechanism is maintained until 4.6 V *vs.* Li^+/Li, hereafter the voltammogram distorts showing what might be a porosity saturation effect, but still no evidence of electrolyte decomposition is observed [40]. Thus, when working with olive pits derived AC electrodes in 1 M $LiPF_6$ (CPAME) + 3 wt% VC electrolyte, a cut-off potential up to 4.6 V *vs.* Li^+/Li can be set. In order to evaluate the impact of widening the working potential window on the capacitance output of the AC, GA charge/discharge measurements were performed at different increasing potentials for the AC-CPAME system. In **Figure 3.9b**, specific capacitance values obtained for different high cut-off potential values at 3 A g^{-1} ($t_{discharge}\approx30$ s) are compared. With an initial value of 72 F g^{-1} at 4.2 V *vs.* Li^+/Li, it reaches its maximum at 4.5 V *vs.* Li^+/Li (*i.e.* 76 F g^{-1}) and maintains almost unvaried until 4.7 V *vs.* Li^+/Li, while beyond 4.8 V *vs.* Li^+/Li a severe decay is observed in good agreement with cyclic voltammetry results.

In order to evaluate the maximum capacity output that the AC can deliver in both electrolytes, rate capability at their widest operative potential window (AC-CPAME at 2 – 4.5 V *vs.* Li^+/Li and AC-EC:DMC at 2 - 4.2 V *vs.* Li^+/Li) is reported in **Figure 3.9c**. At low current densities (*e.g.* 0.1 A g^{-1}), the specific capacity of both systems is practically the same (96 mAh g^{-1} for AC-EC:DMC *vs.* 98 mAh g^{-1} for AC-CPAME). At higher current densities, *i.e.* above 1 A g^{-1}, conductivity becomes the overriding parameter, with the AC-CPAME system delivering 60 mAh g^{-1} and 34 mAh g^{-1} at 2 A g^{-1} and at 5 A g^{-1} respectively while its AC-EC:DMC counterpart delivers 85 mAh g^{-1} and 68 mAh g^{-1} at same current densities.

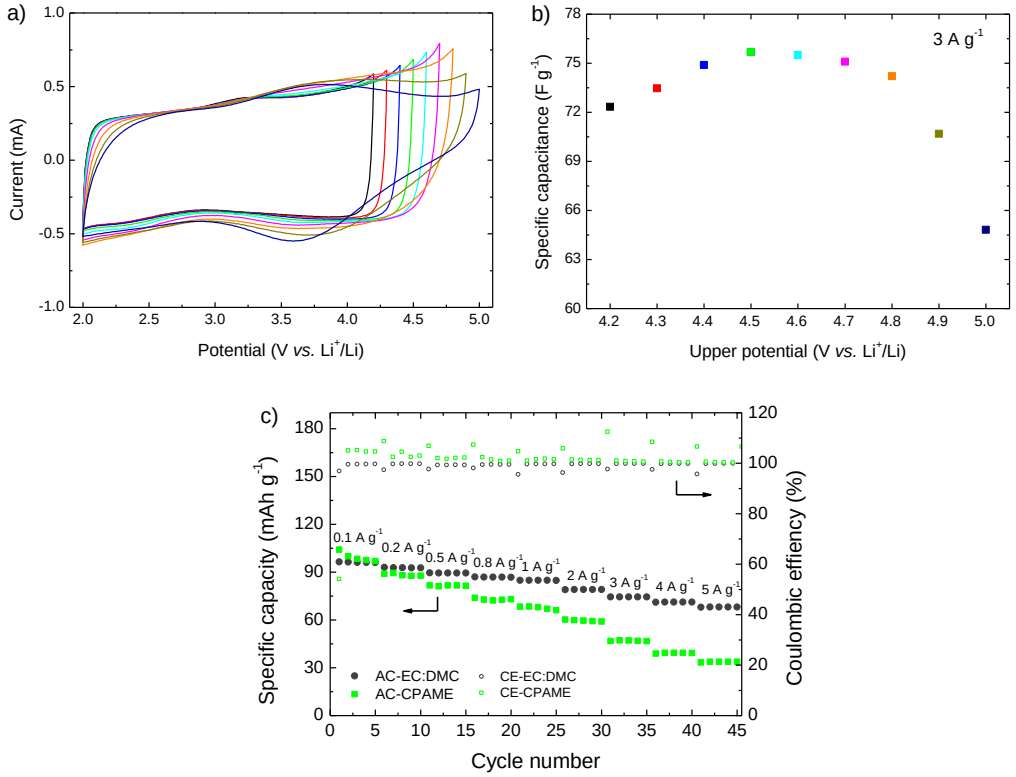

Figure 3.9. Electrochemical characterization of the AC: a) CV at 5 mV s^{-1} from 2 V to 4.2 - 5 V *vs.* Li^+/Li, b) Specific capacitance values for different potential windows at 3 A g^{-1} and c) Rate capability in 1 M $LiPF_6$ (CPAME) + 3 wt% VC between 2 – 4.5 V *vs.* Li^+/Li (green squares) in comparison with the same AC in 1 M $LiPF_6$ (EC:DMC) between 2 – 4.2 V *vs.* Li^+/Li (grey dots).

3.3.3. Development of high voltage LICs

As detailed in previous MICs, the balancing of the active mass of the negative and positive electrodes is crucial for the final performance of the device. In this case, owing to the similar specific capacity values of both electrodes in all the studied current density range (**Figure 3.10a**) a 1:1 (HC:AC) mass ratio was selected. After the pre-conditioning step, which was equal to previous MICs (**Figure 3.10b**), the LIC was characterized at different current densities. The initial operational cell voltage was set to 1.5 - 4.2 V and

was widen stepwise towards 5 V. Unfortunately, the HC cannot balance the increasing capacity output of the positive electrode when the voltage is raised and lithium plating occurs. Thus, the maximum cell voltage is limited to only 4.3 V, hindering the real expectation of the 1 M $LiFP_6$ (CPAME) system. In order to exploit the maximum potential of CPAME, the mass ratio was readjusted to make a lower use of the HC. Thus, a new 1:0.5 (HC:AC) mass ratio was set. Despite the expected reduction in the capacity output, this approach could allow a lower use of the HC, enabling to balance the higher capacity of the AC when the operating voltage goes beyond 4.2 V. Finally, both LICs with different mass ratio are compared.

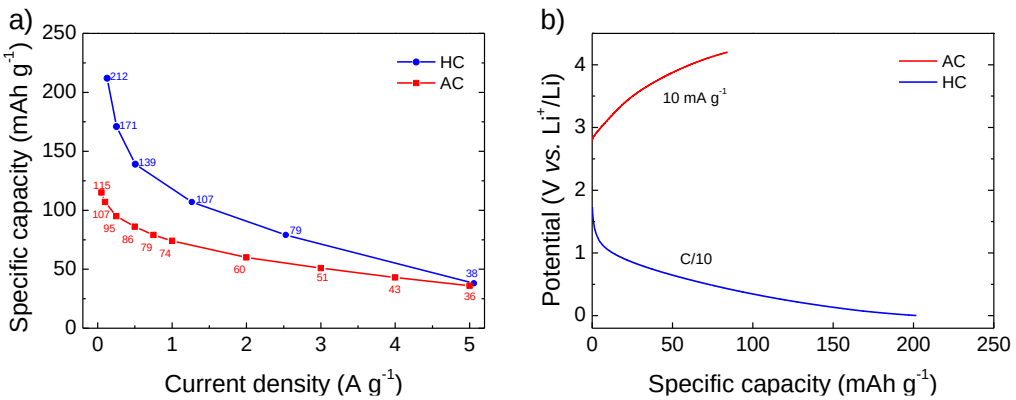

Figure 3.10. a) Summary of the specific capacities of the HC (0.005 - 2 V *vs.* Li^+/Li) and AC (2 - 4.3 V *vs.* Li^+/Li) at different current densities and b) Pre-conditioning step: AC set at a cut-off potential of 4.2 V *vs.* Li^+/Li and HC set at a cut-off potential of 0.1 V *vs.* Li^+/Li.

The evaluation of LIC (CPAME, 1:1) was done within the operational voltage range of 1.5 - 4.3 V, while for LIC (CPAME, 1:0.5) the range was extended until 4.5 V. For comparison purposes, a LIC using 1 M $LiFP_6$ (EC:DMC) in a 1:1 mass ratio was characterized in its standard voltage window of 1.5 - 4.2 V. **Figure 3.11** shows the different charge/discharge profiles of the AC (dash red line), the HC (dash-dot blue line) and the full LIC (straight black line) at different discharge times, going from the region affordable for batteries (*i.e.* 30 min) to discharge times usually restricted to EDLCs

(*i.e.* 50 s). In order to study the behaviour of all devices at similar discharge times, the current densities of **Figure 3.11** were adapted to each system.

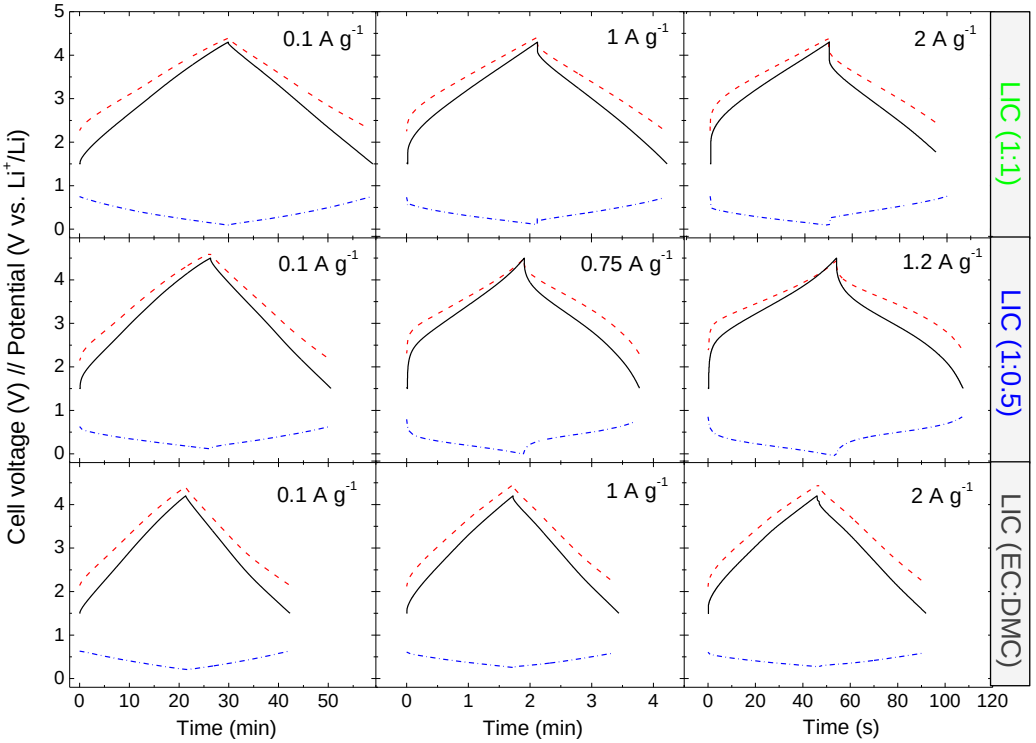

Figure 3.11. Charge/discharge profiles of the AC (red dash line), HC (blue dash-dot line) and LIC (black straight line) at different discharge times for both studied LICs (CPAME) and LIC (EC:DMC).

At a discharge time of 30 min, applying low current densities, the profiles of all LICs show a symmetric shape indicative of a capacitive storage mechanism. The AC from the reference LIC (EC:DMC) swings from 2.1 to 4.3 V *vs.* Li^+/Li while the upper potential is extended for LIC (CPAME, 1:1) to 4.4 V *vs.* Li^+/Li and for LIC (CPAME, 1:0.5) to 4.6 V *vs.* Li^+/Li. The opposite occurs for the HC, where in LIC (CPAME 1:1) it swings in a broader ~0.8 to 0.1 V *vs.* Li^+/Li potential compared to the narrower ~0.6 to 0.1 V *vs.* Li^+/Li in LIC (CPAME, 1:0.5) and the narrowest ~0.5 to 0.2 V *vs.* Li^+/Li in

LIC (EC:DMC). Going toward fast discharge times in the range of few minutes, the applied current density was increased, both CPAME based LICs show a small ohmic drop owing to the internal resistance of the system at these high rates while LIC (EC:DMC) remains unvaried. Further increase in the applied current density reduces the discharge time to *ca.* 50 s, a highly challenging discharge time that even few standard LICs based on commercial electrolyte reach [41,42]. At this low discharge time, in both LIC (CPAME) the ohmic drop is increased and the potential of HCs *vs.* Li^+/Li is lowered beyond 0.1 V *vs.* Li^+/Li. This is the lowest discharge time allowed for the system since at higher current densities lithium plating in the negative electrode occurs. Meanwhile, LIC (EC:DMC) shows only a slight increase in the internal resistance, owing to the better conductivity of $LiPF_6$ in the EC:DMC mixture over that in CPAME.

Specific capacitance values obtained for both systems at different discharge times are summarized in **Figure 3.12a**. LIC (CPAME, 1:1) shows the highest capacitance almost all over the whole discharge time range. Only at discharge times below 40 s LIC (EC:DMC) system is able to exhibit higher capacitance. The capacitance increase for LIC (CPAME, 1:1) can be attributed to the widening of the overall voltage window, which implies a lengthening of both the AC and the HC profiles. Instead, below 40 s, the lower conductivity of CPAME-based electrolyte in comparison with the EC:DMC-based one leads to limited charge storage. With regard to LIC (CPAME, 1:0.5), this system shows the lowest capacitance values all along the discharge time region as a consequence of the reduced AC mass loading.

Energy-to-power characteristics of all systems are shown in **Figure 3.12b** and values summarized in **Table 3.2**. At low power densities, *i.e.* < 1000 W kg^{-1}_{AM} , within discharge times ranging from 1 h to 10 min, LIC (CPAME, 1:1) performs the best followed by LIC (CPAME, 1:0.5) and LIC (EC:DMC). Its higher energy density in comparison with LIC (EC:DMC) is attributed to the widening in the operational voltage window (*i.e.* 1.5 - 4.3 V) and the increase in capacitance. Despite the lower capacitance of LIC (CPAME, 1:0.5), its wider operational voltage window (*i.e.* 1.5 - 4.5 V) makes it

competitive over LIC (EC:DMC). Entering at the medium-high power density region, *i.e.* 1000 - 5000 W kg^{-1}_{AM}, and discharge times between 10 and 1 min, LIC (CPAME, 1:1) still performs the best. In this region, both LIC (CPAME) systems exhibit a decreasing trend in energy density while LIC (EC:DMC) remains almost constant. This is attributed to the lower conductivity of the CPAME-based electrolyte compared to EC:DMC-based one. Even so, LIC (CPAME, 1:1) still shows higher energy density values than LIC (EC:DMC) up to the very challenging 1 min discharge time region. The higher energy density shown by LIC (CPAME, 1:1) is attributed to the best balance reached for the specific capacitance and the cell voltage, factors that determine the final energy output ($E=1/2 \cdot C \cdot \Delta V^2$). Beyond that discharge time, owing to the higher conductivity of the electrolyte, LIC (EC:DMC) becomes dominant, with the best energy-to-power characteristics. In fact, both LIC (CPAME) cannot go below discharge times of 40 s since lithium plating occurs (red dots in **Figure 3.12a** and **3.12b**).

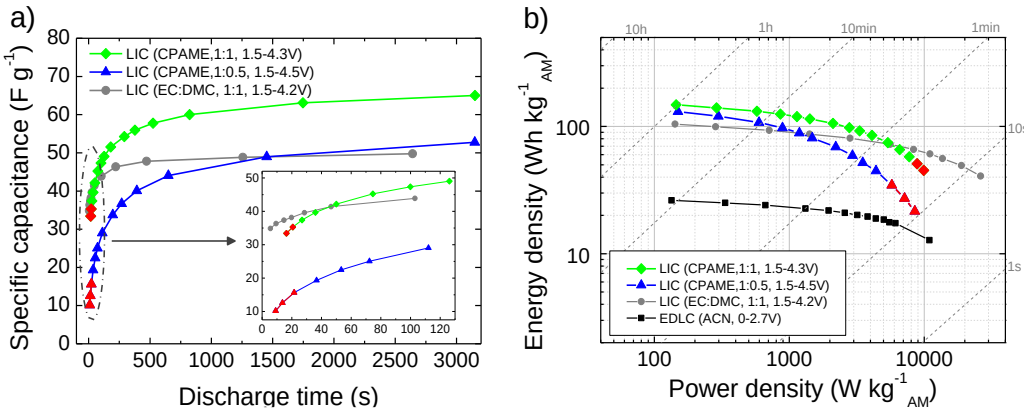

Figure 3.12. a) Specific capacitance of LICs at different discharge times, inset: zoom at lower discharge time region; b) Ragone plot with the studied LICs and their EDLC counterpart. Red points show where lithium plating occurs.

Table 3.2. Energy and power density values of all the studied LICs at different discharge times.

LICs	$t_{dischage}$					
	~30 min		~2 min		~50 s	
	Wh kg_{AM}^{-1}	W kg_{AM}^{-1}	Wh kg_{AM}^{-1}	W kg_{AM}^{-1}	Wh kg_{AM}^{-1}	W kg_{AM}^{-1}
CPAME 1:1	140	289	98	2789	75	5377
CPAME 1:0.5	121	299	69	2213	52	3511
EC:DMC 1:1	99	284	81	2824	72	5605

Overall, even that limited energy density is obtained within LIC (CPAME, 1:0.5) system, the possibility to increase the voltage window up to 4.5 V using 1 M $LiFP_6$ (CPAME) electrolyte is demonstrated. In the case of LIC (CPAME, 1:1), the increase of only 0.1 V in the cell voltage allows rising the energy density 50% at 150 W kg^{-1}_{AM} and 30 % at 2800 W kg^{-1}_{AM} compared to LIC (EC:DMC). One of the major concerns about extending the cell voltage is stability. Thus, a cyclability test at the constant current of 1 A g^{-1} was run for LIC (CPAME, 1:1) in order to check its reliability. Within a discharge time of 2 minutes, it shows a promising 70 % capacitance retention after 5000 cycles. Altogether, it is shown that CPAME can be a promising alternative solvent for high power density LICs. In this regard, the use of a more powerful negative electrode, *e.g.* alloying materials with higher capacity output [43], could unchained all the potential of the 1 M $LiFP_6$ (CPAME) system targeting for voltages close to 5 V.

3.4. Summary and conclusions

Once high energy and power dual carbon MICs were obtained in **Chapter 2**, the study on the electrolyte became attractive in order to select an electrolyte that might allow opening the cell voltage of the final MICs and hence, increase even more the energy density. In that scenario, first, Li- and Na-based (0.5 M LiTFSI and 0.5 M NaTFSI) aprotic ionic liquid (AIL, Pyr_{14}TFSI) and protic ionic liquids (PIL, Pyr_{H4}TFSI) were

investigated together with the negative electrode of the previously developed dual carbon MICs. It is shown that both Li- and Na-based $Pyr_{14}TFSI$ electrolytes can be used together with the HC electrode, while only Li-based $Pyr_{H4}TFSI$ can be tested due to the instability of Pyr_{H4}^{+} in Na-based electrolyte. However, as consequence of the low specific capacity values obtained at high rates, these electrolytes are still limited for high power applications as MICs and hence, were left aside to be tested in full HC:AC devices.

However, better results were obtained from the strategy of changing the typical carbonate solvents (*i.e.* EC:DMC). On the search of an alternative solvent that could increase the operational voltage window of LICs, 3-cyanopropionic acid methyl ester (CPAME) was selected owing to its wide electrochemical stability window together with its suitable viscosity and conductivity features. On the one hand, the combination of the AC (capacitor-type, positive electrode) and the 1 M $LiPF_6$ (CPAME) + 3 wt% VC electrolyte shows to be electrochemically stable up to 4.6 V *vs.* Li^{+}/Li. On the other hand, the HC (battery-type, negative electrode) shows promising specific capacities of 322 mAh g^{-1} at C/10 and 80 mAh g^{-1} at 10C. Finally, combining both materials, dual carbon-based LICs have been developed in the CPAME-based electrolyte capable to operate in a cell voltage of 1.5 - 4.3 V when a HC:AC 1:1 mass ratio is selected and in an extended voltage window of 1.5 - 4.5 V when the mass ratio is set to 1:0.5. Compared to the reference LIC based on 1 M $LiPF_6$ (EC:DMC) electrolyte, higher energy-to-power ratios were achieved when discharge time is above 1 min.

3.5. Bibliography

[1] E. Iwama, T. Ueda, Y. Ishihara, K. Ohshima, W. Naoi, M.T.H. Reid, K. Naoi, High-voltage operation of Li4Ti5O12/AC hybrid supercapacitor cell in carbonate and sulfone electrolytes: Gas generation and its characterization, Electrochimica Acta. 301 (2019) 312–318. doi:10.1016/j.electacta.2019.01.088.

[2] J. Huang, Z. Jiang, The preparation and characterization of Li4Ti5O12/carbon nano-tubes for lithium ion battery, Electrochimica Acta. 53 (2008) 7756–7759. doi:10.1016/j.electacta.2008.05.031.

[3] L.Y. Yang, H.Z. Li, J. Liu, S.S. Tang, Y.K. Lu, S.T. Li, J. Min, N. Yan, M. Lei, Li4Ti5O12 nanosheets as high-rate and long-life anode materials for sodium-ion batteries, J. Mater. Chem. A. 3 (2015) 24446–24452. doi:10.1039/C5TA07403G.

[4] S. Fleischmann, M. Widmaier, A. Schreiber, H. Shim, F.M. Stiemke, T.J.S. Schubert, V. Presser, High voltage asymmetric hybrid supercapacitors using lithium- and sodium-containing ionic liquids, Energy Storage Mater. 16 (2019) 391–399. doi:10.1016/j.ensm.2018.06.011.

[5] P. Han, X. Han, J. Yao, L. Zhang, X. Cao, C. Huang, G. Cui, High energy density sodium-ion capacitors through co-intercalation mechanism in diglyme-based electrolyte system, J. Power Sources. 297 (2015) 457–463. doi:10.1016/j.jpowsour.2015.08.011.

[6] M.-S. Park, G.K. Veerasubramani, R. Thangavel, Y.-S. Lee, D.-W. Kim, Effect of Organic Solvents on the Electrochemical Performance of Sodium-Ion Hybrid Capacitors, ChemElectroChem. 6 (2019) 653–660. doi:10.1002/celc.201801517.

[7] S. Menne, T. Vogl, A. Balducci, Lithium coordination in protic ionic liquids, Phys. Chem. Chem. Phys. 16 (2014) 5485–5489. doi:10.1039/C3CP55183K.

[8] T. Vogl, S. Menne, R.-S. Kühnel, A. Balducci, The beneficial effect of protic ionic liquids on the lithium environment in electrolytes for battery applications, J. Mater. Chem. A. 2 (2014) 8258–8265. doi:10.1039/C3TA15224C.

[9] T. Vogl, C. Vaalma, D. Buchholz, M. Secchiaroli, R. Marassi, S. Passerini, A. Balducci, The use of protic ionic liquids with cathodes for sodium-ion batteries, J Mater Chem A. 4 (2016) 10472–10478. doi:10.1039/C6TA02277D.

[10] A. Basile, S.A. Ferdousi, F. Makhlooghiazad, R. Yunis, M. Hilder, M. Forsyth, P.C. Howlett, Beneficial effect of added water on sodium metal cycling in super concentrated ionic liquid sodium electrolytes, J. Power Sources. 379 (2018) 344–349. doi:10.1016/j.jpowsour.2018.01.044.

[11] A. Fukunaga, T. Nohira, R. Hagiwara, K. Numata, E. Itani, S. Sakai, K. Nitta, S. Inazawa, A safe and high-rate negative electrode for sodium-ion batteries: Hard carbon in NaFSA-C1C3pyrFSA ionic liquid at 363 K, J. Power Sources. 246 (2014) 387–391. doi:10.1016/j.jpowsour.2013.07.112.

[12] C. Ding, T. Nohira, R. Hagiwara, A. Fukunaga, S. Sakai, K. Nitta, Electrochemical performance of hard carbon negative electrodes for ionic liquid-based sodium ion batteries over a wide temperature range, Electrochimica Acta. 176 (2015) 344–349. doi:10.1016/j.electacta.2015.07.024.

[13] C.-H. Wang, C.-H. Yang, J.-K. Chang, Suitability of ionic liquid electrolytes for room-temperature sodium-ion battery applications, Chem. Commun. 52 (2016) 10890–10893. doi:10.1039/C6CC04625H.

[14] C. V. Manohar, T. Correia Mendes, M. Kar, D. Wang, C. Xiao, M. Forsyth, S. Mitra, D. R. MacFarlane, Ionic liquid electrolytes supporting high energy density in sodium-ion batteries based on sodium vanadium phosphate composites, Chem. Commun. 54 (2018) 3500–3503. doi:10.1039/C8CC00365C.

[15] H. Zheng, Q. Qu, L. Zhang, G. Liu, V. S. Battaglia, Hard carbon: a promising lithium-ion battery anode for high temperature applications with ionic electrolyte, RSC Adv. 2 (2012) 4904–4912. doi:10.1039/C2RA20536J.

[16] A. Balducci, Ionic Liquids in Lithium-Ion Batteries, Top. Curr. Chem. 375 (2017) 20. doi:10.1007/s41061-017-0109-8.

[17] I. Hasa, S. Passerini, J. Hassoun, Characteristics of an ionic liquid electrolyte for sodium-ion batteries, J. Power Sources. 303 (2016) 203–207. doi:10.1016/j.jpowsour.2015.10.100.

[18] T. Vogl, C. Vaalma, D. Buchholz, M. Secchiaroli, R. Marassi, S. Passerini, A. Balducci, The use of protic ionic liquids with cathodes for sodium-ion batteries, J. Mater. Chem. A. 4 (2016) 10472–10478. doi:10.1039/C6TA02277D.

[19] S.F. Lux, M. Schmuck, S. Jeong, S. Passerini, M. Winter, A. Balducci, Li-ion anodes in air-stable and hydrophobic ionic liquid-based electrolyte for safer and greener batteries, Int. J. Energy Res. 34 (2010) 97–106. doi:10.1002/er.1557.

[20] S. Menne, M. Schroeder, T. Vogl, A. Balducci, Carbonaceous anodes for lithium-ion batteries in combination with protic ionic liquids-based electrolytes, J. Power Sources. 266 (2014) 208–212. doi:10.1016/j.jpowsour.2014.04.155.

[21] T. Stettner, P. Huang, M. Goktas, P. Adelhelm, A. Balducci, Mixtures of glyme and aprotic-protic ionic liquids as electrolytes for energy storage devices, J. Chem. Phys. 148 (2018) 193825. doi:10.1063/1.5013117.

[22] L. Timperman, P. Skowron, A. Boisset, H. Galiano, D. Lemordant, E. Frackowiak, F. Béguin, M. Anouti, Triethylammonium bis(tetrafluoromethylsulfonyl)amide protic ionic liquid as an electrolyte for electrical double-layer capacitors, Phys. Chem. Chem. Phys. PCCP. 14 (2012) 8199–8207. doi:10.1039/c2cp40315c.

[23] S.F. Lux, M. Schmuck, G.B. Appetecchi, S. Passerini, M. Winter, A. Balducci, Lithium insertion in graphite from ternary ionic liquid–lithium salt electrolytes: II. Evaluation of specific capacity and cycling efficiency and stability at room temperature, J. Power Sources. 192 (2009) 606–611. doi:10.1016/j.jpowsour.2009.02.066.

[24] M. Khasanov, E. Pazhetnov, W.C. Shin, Dicarboxylate-Substituted Ethylene Carbonate as an SEI-Forming Additive for Lithium-Ion Batteries, J. Electrochem. Soc. 162 (2015) A1892–A1898. doi:10.1149/2.0901509jes.

[25] D.A. Stevens, J.R. Dahn, High Capacity Anode Materials for Rechargeable Sodium-Ion Batteries, J. Electrochem. Soc. 147 (2000) 1271–1273. doi:10.1149/1.1393348.

[26] K. Kuratani, M. Yao, H. Senoh, N. Takeichi, T. Sakai, T. Kiyobayashi, Na-ion capacitor using sodium pre-doped hard carbon and activated carbon, Electrochimica Acta. 76 (2012) 320–325. doi:10.1016/j.electacta.2012.05.040.

[27] E. Irisarri, A. Ponrouch, M.R. Palacin, Review—Hard Carbon Negative Electrode Materials for Sodium-Ion Batteries, J. Electrochem. Soc. 162 (2015) A2476–A2482. doi:10.1149/2.0091514jes.

[28] P. Ray, T. Vogl, A. Balducci, B. Kirchner, Structural Investigations on Lithium-Doped Protic and Aprotic Ionic Liquids, J. Phys. Chem. B. 121 (2017) 5279–5292. doi:10.1021/acs.jpcb.7b02636.

[29] C. Schütter, T. Husch, M. Korth, A. Balducci, Toward New Solvents for EDLCs: From Computational Screening to Electrochemical Validation, J. Phys. Chem. C. 119 (2015) 13413–13424. doi:10.1021/acs.jpcc.5b02113.

[30] C. Schütter, T. Husch, V. Viswanathan, S. Passerini, A. Balducci, M. Korth, Rational design of new electrolyte materials for electrochemical double layer capacitors, J. Power Sources. 326 (2016) 541–548. doi:10.1016/j.jpowsour.2016.06.022.

[31] C. Schütter, S. Passerini, M. Korth, A. Balducci, Cyano Ester as Solvent for High Voltage Electrochemical Double Layer Capacitors, Electrochimica Acta. 224 (2017) 278–284. doi:10.1016/j.electacta.2016.12.063.

[32] S. Brox, S. Röser, T. Husch, S. Hildebrand, O. Fromm, M. Korth, M. Winter, I. Cekic-Laskovic, Alternative Single-Solvent Electrolytes Based on Cyanoesters for Safer Lithium-Ion Batteries, ChemSusChem. 9 (2016) 1704–1711. doi:10.1002/cssc.201600369.

[33] J. Krummacher, A. Balducci, Al(TFSI)3 as a Conducting Salt for High-Voltage Electrochemical Double-Layer Capacitors, Chem. Mater. 30 (2018) 4857–4863. doi:10.1021/acs.chemmater.8b02253.

[34] S. Brox, S. Röser, B. Streipert, S. Hildebrand, U. Rodehorst, X. Qi, R. Wagner, M. Winter, I. Cekic-Laskovic, Innovative, Non-Corrosive LiTFSI Cyanoester-Based Electrolyte for Safer 4 V Lithium-Ion Batteries, ChemElectroChem. 4 (2017) 304–309. doi:10.1002/celc.201600610.

[35] V. Sharova, A. Moretti, T. Diemant, A. Varzi, R.J. Behm, S. Passerini, Comparative study of imide-based Li salts as electrolyte additives for Li-ion batteries, J. Power Sources. 375 (2018) 43–52. doi:10.1016/j.jpowsour.2017.11.045.

[36] X. Zhang, C. Fan, P. Xiao, S. Han, Effect of vinylene carbonate on electrochemical performance and surface chemistry of hard carbon electrodes in lithium ion cells operated at different temperatures, Electrochimica Acta. 222 (2016) 221–231. doi:10.1016/j.electacta.2016.10.149.

[37] Y. Hu, W. Kong, H. Li, X. Huang, L. Chen, Experimental and theoretical studies on reduction mechanism of vinyl ethylene carbonate on graphite anode for lithium ion batteries, Electrochem. Commun. 6 (2004) 126–131. doi:10.1016/j.elecom.2003.10.024.

[38] J. Ajuria, E. Redondo, M. Arnaiz, R. Mysyk, T. Rojo, E. Goikolea, Lithium and sodium ion capacitors with high energy and power densities based on carbons from recycled olive pits, J. Power Sources. 359 (2017) 17–26. doi:10.1016/j.jpowsour.2017.04.107.

[39] M. Arnaiz, P. Huang, J. Ajuria, T. Rojo, E. Goikolea, A. Balducci, Protic and Aprotic Ionic Liquids in Combination with Hard Carbon for Lithium-Ion and Sodium-Ion Batteries, Batter. Supercaps. 1 (2018) 204–208. doi:10.1002/batt.201800073.

[40] R. Mysyk, E. Raymundo-Piñero, J. Pernak, F. Béguin, Confinement of Symmetric Tetraalkylammonium Ions in Nanoporous Carbon Electrodes of Electric Double-Layer Capacitors, J. Phys. Chem. C. 113 (2009) 13443–13449. doi:10.1021/jp901539h.

[41] C.-L. Hsieh, D.-S. Tsai, W.-W. Chiang, Y.-H. Liu, A composite electrode of tin dioxide and carbon nanotubes and its role as negative electrode in lithium ion hybrid capacitor, Electrochimica Acta. 209 (2016) 332–340. doi:10.1016/j.electacta.2016.05.090.

[42] V. Aravindan, W. Chuiling, S. Madhavi, High power lithium-ion hybrid electrochemical capacitors using spinel LiCrTiO4 as insertion electrode, J. Mater. Chem. 22 (2012) 16026–16031. doi:10.1039/C2JM32970K.

[43] M. Arnaiz, J.L. Gómez-Cámer, F. Mijangos, T. Rojo, E. Goikolea, J. Ajuria, Novel Lithium-Ion Capacitor Based on TiSb2 as Negative Electrode: The Role of Mass Ratio Towards High Energy-To-Power Densities and Long Cyclability, Batter. Supercaps. 0 (n.d.). doi:10.1002/batt.201800099.

CHAPTER 4

SnO_2-rGO as negative electrode for lithium ion capacitors

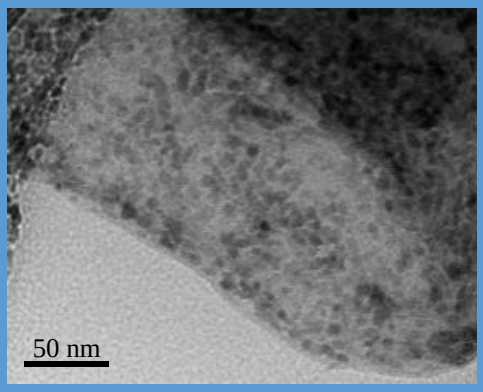

SnO_2-rGO as negative electrode for lithium ion capacitors

The effort to increase the energy density of conventional EDLCs and dual carbon LICs, could go through the use of alloying materials as negative electrode in order to develop higher energy density LICs. Herein, a self-standing, binder-free composite is studied as the battery-type negative electrode obtained by a low-cost and easily scalable method. Tin (IV) oxide nanoparticles (<10 nm) embedded in a reduced graphene oxide matrix (SnO_2-rGO) were prepared by an in-situ synthetic approach that involves the freeze/freeze-drying of a graphene oxide suspension in the presence of a tin precursor and its subsequent thermal reduction under argon atmosphere. Physicochemical and electrochemical characterization confirmed the optimum nano-structuring of the composite showing ultrafast response at high current densities. Coupled with a highly porous olive pits waste derived AC as the capacitor-type positive electrode a LIC with an excellent energy density output has been fabricated. The newly designed LIC is able to deliver 60 Wh kg^{-1}_{AM} at 2.9 kW kg^{-1}_{AM} ($t_{discharge} \approx 1$ min) and still 27 Wh kg^{-1}_{AM} at 11 kW kg^{-1}_{AM} ($t_{discharge} \approx 10$ s), what is 5 times more energy density than its EDLC counterpart. In addition, the system presents a highly promising 78% capacitance retention after 2000 cycles run at 3 A g^{-1} within a discharge time of 15 s.

Table of contents:

4.1. Introduction to Sn-based materials and graphene networks

High energy and high power density values as well as excellent cycle life were already demonstrated for dual carbon MICs in **Chapter 2** and **3**. Nevertheless, new emerging applications with an increasing demand on energy density have triggered the search of a new generation of more energetic anode materials in order to overcome the capacity limitation of carbons (**Figure 4.1**) [1]. In this search, materials that can electrochemically alloy with lithium have become one of the most studied alternatives in LIBs, owing to their high specific reversible capacities and low reduction potentials. Among them, elements such as silicon (Si) and tin (Sn) have been the most studied ones.

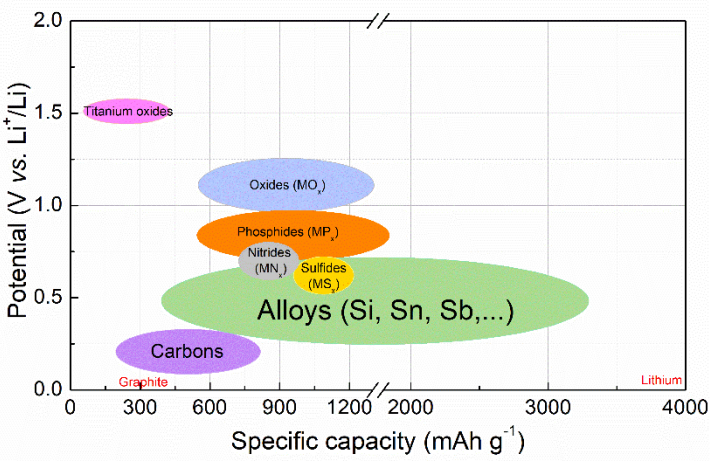

Figure 4.1. Anode materials classified by their reduction potential and specific capacity.

On one side, Si is considered one of the most promising materials to be used as negative electrode in future commercial LIBs owing to its high gravimetric and volumetric capacities (4200 mAh g^{-1} and 9786 mAh cm^{-3} lithiated to $Li_{4.4}Si$, respectively). Besides, it reacts with lithium at low potentials (~0.4 V *vs.* Li^+/Li), which allows increasing the cell voltage. Moreover, it is quite abundant and environmentally friendly. Nevertheless, expensive nanotechnology is needed to overcome volume changes. Instead, even that Sn shows similar issues, its nanostructuration processes are generally simpler and cheaper.

Hence, in this chapter, tin (IV) oxide (SnO_2) was selected as active material. Fuji *et al.* reported for the first time a Sn-based amorphous oxide composite that was able to deliver twice the reversible capacity of graphite, which triggered research in this direction [2,3]. In fact, currently Sn and SnO_2 have become two of the most promising materials owing to their low active reduction potential (~0.5 V *vs.* Li^+/Li) and high theoretical reversible specific capacities of 994 and 782 mAh g^{-1} respectively, making them superior to the vast majority of materials in terms of capacity [4]. Nevertheless, the large volume changes (up to 300%) that all alloying materials suffer during the lithiation/delithiation process leads to mechanical stress and consequently capacity fading and lack of sufficient cycling stability [5].

Thus, in order to overcome this mechanical drawback, different strategies have been explored. First, reducing the particle size and going to nanostructured materials allows increasing electrochemical behaviour owing to the larger surface area and abundant active sites. Moreover, in the case of alloys, nano-size features can also improve their performance as large free spaces that may relax their large volume expansions are created [6]. Lately, a carbon coating strategy has also been followed. Carbonaceous matrixes have been designed in order to accommodate the particles of active materials. Different type of carbonaceous matrixes such as carbon nanotubes [7], carbon nanofibres [8], MOFs [9] or graphene [10] have been reported in literature. These matrixes act as a support that allows buffering the large volume changes caused during cycling, preventing the agglomeration of the particles and providing a continuous path for the electrolyte propagation and Li^+ and e^- transport. Thereby, in order to develop high performance and durable alloying materials, well-dispersed nanoparticles should be accommodated into a carbon matrix. Among the different studied carbon matrixes, owing to its outstanding electrical conductivity, high flexibility and high SSA, graphene was selected as a carbon network to embed SnO_2 nanoparticles. Thus, a reduced graphene oxide matrix nanodecorated with SnO_2 nanoparticles (SnO_2-rGO) was prepared and used as negative electrode in LICs in this thesis.

4.1.1. Sn- and graphene-based materials

The use of a graphene network in combination with Sn-based materials was previously reported by different groups [10]. In 2009, Wang *et al.* reported on a Sn/graphene nanocomposite with a 3D architecture. This architecture, together with the good distribution of Sn nanoparticles (*i.e.* 5 nm) into the graphene matrix, effectively prevented the re-stacking of graphene nanosheets and circumvented the aggregation of Sn particles during cycling. Contrary to bare Sn powder -which failed after the first 10 cycles- the Sn/graphene composite enhanced the electrochemical performance of the material enabling to retain 508 mAh g^{-1} of specific capacity after 100 cycles at low rates [11]. Lian *et al.* developed not only a Sn material dispersed in a graphene matrix but Sn particles coated with carbon and then dispersed into graphene (Sn/C-graphene). This additional coating suppressed the aggregation of particles and avoided the exfoliation of Sn particles during cycling. Besides, its electrochemical test showed high specific capacities such as 600 mAh g^{-1} at 0.1 A g^{-1} and 320 mAh g^{-1} at 1 A g^{-1} [12]. Nevertheless, despite high specific capacity values were obtained with Sn-graphene based materials, Botas *et al.* demonstrated that using SnO_2 as pristine material instead of Sn permits to work with particles of lower size and consequently, volume expansions/contractions can be better controlled [13]. It was shown that while SnO_2 was irreversibly reduced to Sn in the first charge step, particles were pulverized and as consequence, higher electrochemical performance was achieved [13]. Following the previous double coating strategy, Yue *et al.* reported on a hollow SnO_2/C-graphene composite within a 70 wt% of SnO_2 loading, showing well-dispersed nanoparticles into the graphene matrix and excellent electrochemical performance delivering 700 mAh g^{-1} at 3 A g^{-1} [14]. Also Zhang *et al.* developed SnO_2 nanoparticles accommodated in a three-dimensional (3D) graphene network (SnO_2@3DG) within an outstanding 89.51 wt% SnO_2 content. After a solvothermal reaction and high-temperature annealing, a three-dimensional cross-linked monolithic graphene material was achieved. Microstructural analysis of the material showed an excellent dispersion of SnO_2 into the graphene matrix, translated into an

excellent electrochemical performance. Specific capacity values of 1000 mAh g^{-1} at 1 A g^{-1} and 600 mAh g^{-1} at 5 A g^{-1} were achieved. Moreover, an excellent capacity retention of almost 100% was obtained when the material was cycled at 1 A g^{-1} constant current for 150 charge/discharge cycles [15].

As a result of the good electrochemical response of Sn/SnO_2-graphene based materials at high current densities, these materials have emerged as promising candidates for MICs technology, where ultrafast response is of foremost importance.

4.1.2. State-of-the-art on Sn-based Lithium ion capacitors

In 2014 Qu *et al.* first reported on a combination of a SnO_2-C hybrid anode and a tubular mesoporous carbon positive electrode to be used in LICs. After different SnO_2 loadings were studied for the preparation of the negative electrode, in the end, owing to its better capacity response and cycling stability, the electrode with a 57 wt% material loading was selected. In combination with a mesoporous carbon-based positive electrode they developed a LIC that in the low power density region could achieve an energy density of 110 Wh kg^{-1}_{AM}, and 45 Wh kg^{-1}_{AM} at 3000 W kg^{-1}_{AM} power density [16]. Later, Sun *et al.* reported on a LIC assembled with a nitrogen (*i.e.* 14.51 atomic %) doped Sn-C negative electrode and a pomelo peel derived AC as the positive electrode. SEM images of the negative electrode confirmed highly porous carbon spheres with a 40 wt% of Sn loading. Half-cell electrochemical characterization revealed good rate capability showing almost 800 mAh g^{-1} at 1 A g^{-1} and 500 mAh g^{-1} at 4 A g^{-1}. The system built from the combination of this composite material as the negative electrode and the highly porous pomelo peel derived AC as the positive electrode, was able to get high energy densities of 196 Wh kg^{-1}_{AM} and 85 Wh kg^{-1}_{AM} at 731 W kg^{-1}_{AM} and 24375 W kg^{-1}_{AM}, respectively. Furthermore, owing to the good design of both materials a retention of 70% from the initial capacitance was achieved after 5000 cycles [17]. Lately, Xuan Tran *et al.* reported on an ultra-thin carbon layer-coated porous SnO_2 as negative electrode for LICs. SEM images showed that these were ~2 µm particles with 30 nm thick nano-leaves like extensions on the

surface. These leaves could withstand volumetric changes during cycling. Combining this anode material with a commercial YP-80F AC, the assembled LIC delivered 130 Wh kg^{-1}_{AM} and 45 Wh kg^{-1}_{AM} at 125 W kg^{-1}_{AM} and 1000 W kg^{-1}_{AM}, respectively. Nevertheless, the capacitance retention after 100 cycles was 90% [18].Nonetheless, even that promising results were obtained for Sn-based materials in half-cell configuration, only few were implemented in MICs. Moreover, none of them were graphene coated and most of them followed a non-scalable and complex preparation method. Thus, owing to the outstanding features of graphene -such as its excellent electronic conductivity- that can play a determinant role at high power values and looking toward an environmentally friendlier method, in this thesis a self-standing, binder-free, high loading nano-SnO_2 particles embedded into a rGO matrix was developed as the negative electrode of LICs. For the positive electrode, previously developed and optimized olive pits derived AC was used.

4.2. Fabrication and characterization of SnO_2-rGO

In order to overcome the issue of volume changes during cycling, an approach consisting on the encapsulation of Sn-based particles within a rGO environment [13] was followed in this thesis for the development of a Sn-based negative electrode toward its application in MICs. SnO_2 sub-micron particles were *in-situ* embedded within rGO layers, which acted as a support, buffering the volume changes undergone by the Sn composites and as a conductive additive. However, the relatively large particle size of SnO_2 still suffered significant volume changes during cycling. Consequently, the mechanical stress reduced the overall electrode cycle life, which was especially evident at high current rates. In order to circumvent this limitation, a modified synthesis method for the SnO_2-rGO composite was developed. By applying this synthetic procedure, first, it was possible to decrease the SnO_2 particle size below 10 nm, offering shorter paths for Li^+ diffusion and thus, enhancing the rate capability of the negative electrode material [19]. Second, a more homogeneous particle distribution within the carbon matrix was achieved, mitigating the

stress produced by the volume change and improving the long-term electrochemical performance [20]. Third, it was possible to increase the SnO_2 loading owing to the reduction in particle size.

4.2.1. Synthesis and electrode preparation of SnO_2-rGO

Graphene oxide (GO) was synthesized by a previously reported modified Hummer's method [21]. Following this method, graphite flakes and $NaNO_3$ were mixed in the same amount. Then the mixture was cooled down using an ice bath and $KnMnO_4$ was slowly added to maintain the temperature at 20ºC. Afterwards, the solution was heated up to 35ºC and stirred for 3 h. After this period, being an oxidation reaction which was taking place, reductive H_2O_2 was added in order to stop the reaction. The remaining solid material was washed with water and centrifuged several times. In the end, after 1 h sonication of the diluted graphite oxide suspension and its later centrifugation, a GO suspension of 5.2 mg ml^{-1} was obtained (**Scheme 4.1**).

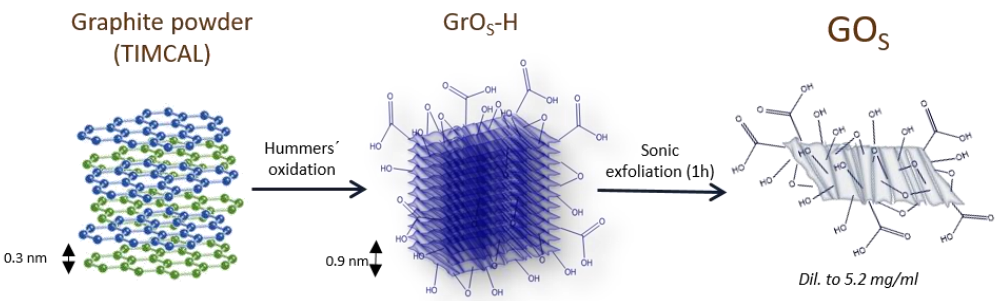

Scheme 4.1. Hummer's method to obtain graphene oxide dissolution (GO_S) from graphite and through graphite oxide dissolution (GrO_S-H).

To prepare the GO aerogel, 100 ml of the GO suspension (5.2 mg ml^{-1}) was freeze/freeze-dried and then thermally treated at 1ºC min^{-1} to 250ºC to avoid the thermal exfoliation of GO layers and at 2ºC min^{-1} to 650ºC for 1 h under argon atmosphere (100 ml min^{-1}) in

order to obtain rGO samples (**Scheme 4.2a**). To prepare SnO_2-rGO composites, first $SnSO_4$ (Sigma Aldrich) was slowly added to the GO suspension (5.2 mg ml^{-1}) and water dissolution at different SnO_2:rGO ratios (50:50, 75:25 and 90:10 wt%). Hereafter denoted as SnO_2-rGO-50, SnO_2-rGO-75 and SnO_2-rGO-90. All of them were stirred during 30 min at RT to obtain a homogeneous mixture and then some drops of 1 M NH_3 were added to increase the pH up to 9 to induce the precipitation of $Sn(OH)_2$ onto GO layers (**Scheme 4.2b**). After 30 minutes of additional stirring, the same procedure as for rGO was followed to obtain the composites. Foams were pressed and cut to obtain the desired electrode geometry before thermal reduction (**Figure 4.2**).

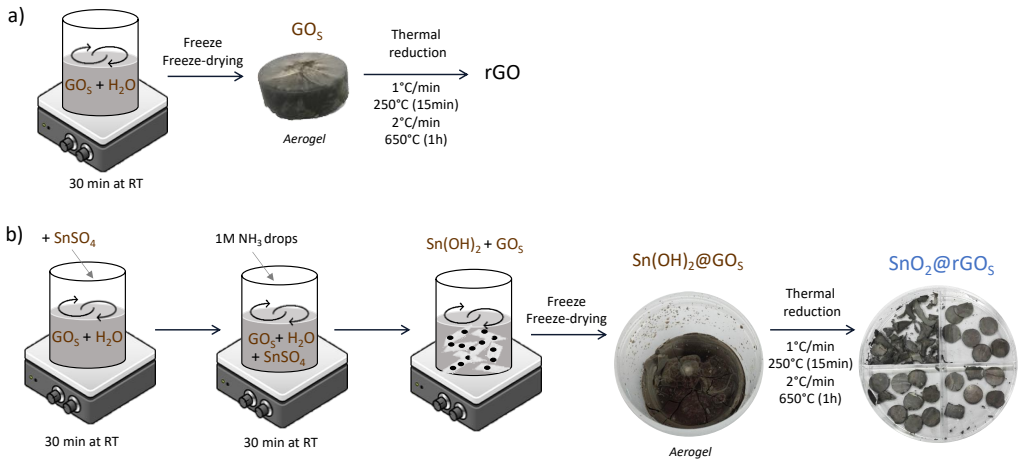

Scheme 4.2. a) rGO electrode preparation route and b) SnO_2-rGO preparation route.

Figure 4.2. a) SnO_2-rGO 3D foam and b) SnO_2-rGO self-standing and binder free electrode.

Aerogels with tin loadings of *ca.* 90 wt% were not able to be processed as self-standing electrodes due to their poor mechanical properties, thus, they were not further characterized. The final electrodes have a loading of ~2 mg cm^{-2} and thickness of ~70 µm.

4.2.2. Physicochemical characterization of SnO_2-rGO

XRD patterns of SnO_2-rGO-50 and SnO_2-rGO-75 are shown in **Figure 4.3a**. The three main peaks at 2θ angle of 26.7º, 34.2º and 51.9º assigned to the (110), (101) and (211) planes can be ascribed to the crystalline tetragonal rutile structure of SnO_2 (JCPDS card 41-1445). It is worth noticing that both diffraction patterns exhibit broad maxima, which is characteristic of nanosized compounds. The intensity of the diffraction maxima of the SnO_2-rGO-50 sample is lower due to its lower nanoparticle content. The characteristic diffraction peak corresponding to (002) planes from the rGO matrix is hidden by the broad (110) peak of the SnO_2 nanoparticles [13]. Structural properties were also studied by Raman spectroscopy (**Figure 4.3b**). Raman spectra of both SnO_2-rGO samples showed bands at 1350 and 1580 cm^{-1}, which correspond to the disordered (D) and graphitic (G) bands of carbon materials. The D band is generated by out of plane vibrations attributed to the presence of structural defects, whereas the G band is the result of in-plane vibrations of sp^2 bonded carbon atoms. The ratio between the integral of I_D and I_G bands (I_D/I_G = 1.7) shows that the SnO_2-rGO has a disordered morphology. This feature can be ascribed to the high porosity and the related large amount of defects of the graphene matrix [22]. Additionally, two peaks are observed at 450 and 610 cm^{-1}, corresponding to E_g and A_{1g} vibration modes of SnO_2 [23].

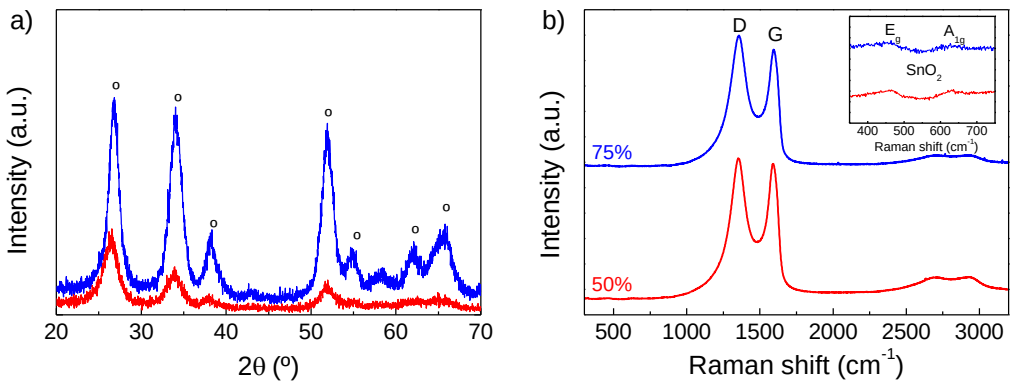

Figure 4.3. a) XRD pattern using CuK_{α} radiation for SnO_2-rGO-50 (red) and SnO_2-rGO-75 (blue) where (º) describes the peaks corresponding to the SnO_2 phase. b) Raman spectra of SnO_2-rGO-50 (red) and SnO_2-rGO-75 (blue). Inset: magnification for SnO_2 bands.

The amount of SnO_2 in each composite was quantified by means of thermogravimetric analysis (TGA) (**Figure 4.4**). TGA curves also show that in those samples containing SnO_2, rGO burns at lower temperature (*i.e.* 450ºC) compared with the SnO_2-free sample, which occurs at *ca.* 620ºC. This difference might be ascribed to the catalytic effect of SnO_2 nanoparticles.

Microstructural analysis carried out by different electron microscopy techniques clearly point out morphological differences between the original synthesis method where the suspension was mixed at 60ºC during 5 h [13] and the current modified synthesis route where the suspension was mixed at RT during 30 min. SEM analysis reveals a clear evolution from sub-micron to nanosized SnO_2 particles. As it can be observed in **Figure 4.5a**, sub-micron particles (approx. 250 nm in diameter) are deposited on rGO layers, while in **Figure 4.5b** only tiny dots (in the range of <10 nm) are visible lying on rGO sheets.

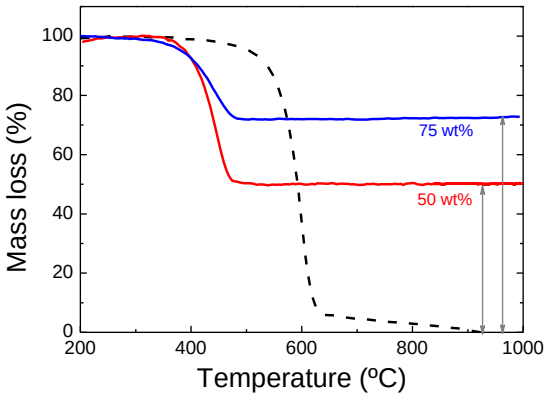

Figure 4.4. TGA of SnO_2-rGO-50 (red line) and SnO_2-rGO-75 (blue line) samples in comparison with the bare rGO (dash black line).

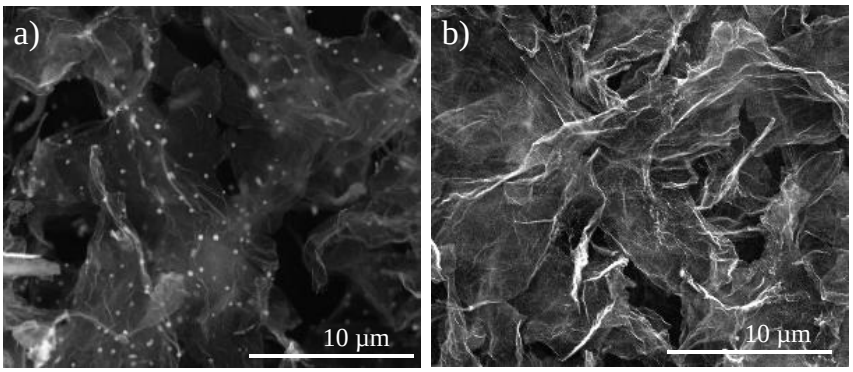

Figure 4.5. SEM images of: a) SnO_2-rGO sub-micron particles, b) SnO_2-rGO-75 nanoparticles.

New SnO_2-rGO samples were further studied by means of TEM. **Figures 4.6a** and **4.6b** show low resolution TEM micrographs of a single rGO layer decorated with SnO_2 nanoparticles of both SnO_2-rGO-50 and SnO_2-rGO-75 samples respectively. The nanoparticle distribution along the rGO sheet is highly homogeneous for both samples, although a higher population of nanoparticles can be inferred for the sample with the higher SnO_2 loading (SnO_2-rGO-75). This fact is confirmed by means of higher

resolution micrographs shown in **Figure 4.6c** and **4.6d** where, furthermore, it is evidenced that nanoparticles have a mean particle sizes of 8 and 7 nm respectively, with almost no particles larger than 12 nm in diameter (**Figure 4.6e** and **4.6f**).

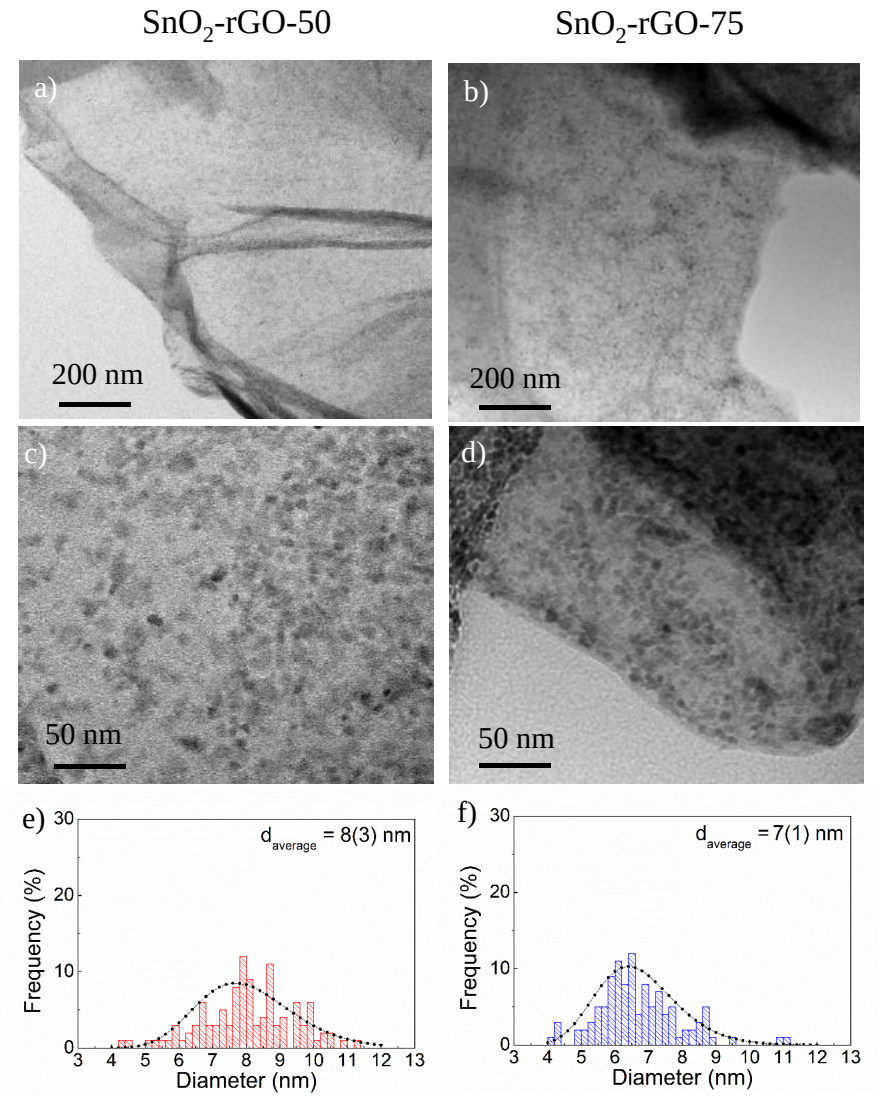

Figure 4.6. TEM images at different magnifications of SnO_2-rGO-50: a), c) and e) particle size distributions and SnO_2-rGO-75: b), d) and f) particle size distributions.

Textural properties of SnO_2-rGO composites were assessed by means of N_2 adsorption/desorption isotherms (**Figure 4.7a**). According to the IUPAC classification, these specific isotherms exhibit a Type II profile associated to a non-porous or macroporous material. The SSA and the average pore size values calculated by 2D NLFT model and SAIEUS software were 46 $m^2 g^{-1}$ and 12 nm for SnO_2-rGO-50 and 101 $m^2 g^{-1}$ and 14 nm for SnO_2-rGO-75 (**Figure 4.7b**). Thus, it is confirmed that the use of graphene as support provides an additional open structure which is favorable for electrolyte propagation towards pores and nanoparticles [10].

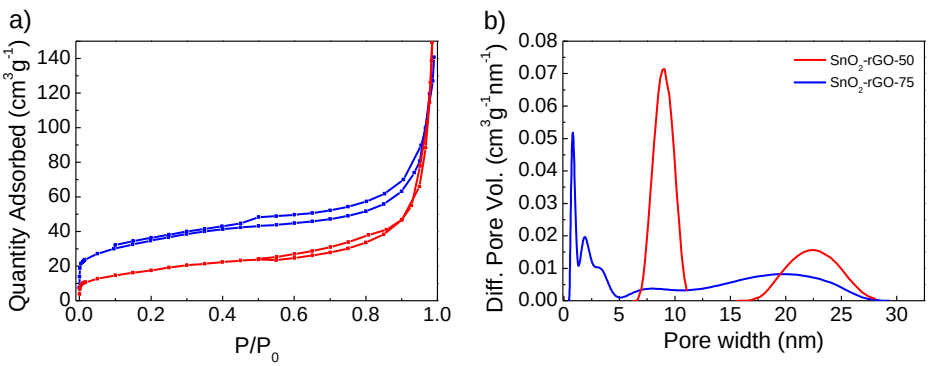

Figure 4.7. Isotherms of a) SnO_2-rGO-50 and -75 composites and b) their pore size distribution.

Furthermore, the high macroporosity of the graphene-based matrix might help to accommodate the SnO_2 volume changes and provide a more effective Li^+ diffusion path, contributing to increase the capacity as well as extending the cycling performance [15].

4.2.3. Electrochemical characterization of SnO_2-rGO

Electrochemical characterization of SnO_2-rGO-50 and SnO_2-rGO-75 composites consisted on CVs registered between 0.005 - 3 V at 0.1 mV s^{-1} sweep rate and, GA charge/discharges at different current densities between 0.05 - 5.0 A g^{-1} in the potential range of 0.005 - 2.0 V *vs.* Li^+/Li. Initially, the working potential was set up to 3 V *vs.* Li^+/Li for the CVs, however, after seeing that none reaction was given a more realistic upper potential of 2 V *vs.* Li^+/Li was set. In **Figure 4.8** the first two cycles of both CVs

and GA charge/discharge profiles for each composite are shown. On the one hand, voltammograms shown in **Figure 4.8a** reveal two main peaks at 0.88 and 0.10 V *vs.* Li^+/Li within the first charge step (cathodic sweep) which are associated to the irreversible conversion reaction of SnO_2 into metallic Sn (**Equation 4.I**) and to the SEI formation. Peaks below 0.1 V *vs.* Li^+/Li are ascribed to the alloying process of Li_xSn (**Equation 4.II**). This correlates well with the 1st GA charge/discharge profile shown in **Figure 4.8b**, where a charge plateau at around 1 V and a decreasing sloping profile region between 0.8 V and 0.3 V *vs.* Li^+/Li is observed for the SEI formation and conversion reaction respectively. On the other hand, in the 1st discharge step (anodic sweep), two main peaks appeared at 0.56 and 1.30 V *vs.* Li^+/Li. The peak observed at 0.56 V *vs.* Li^+/Li is assigned to the dealloying of Li_xSn, meanwhile at 1.30 V the reversible conversion of Sn into SnO_2 occurs [24–27]. The same potentials of the corresponding transformations are evident from the GA profiles (**Figure 4.8b**). It is also concluded that the composite with the highest Sn loading, should provide higher specific capacity values due to the higher area of the peaks.

$$SnO_2 + 4\ Li^+ + 4\ e^- \Rightarrow 2\ Li_2O + Sn \qquad \textbf{Equation 4.I}$$

$$Sn + x\ Li^+ + x\ e^- \Leftrightarrow Li_xSn\ (0 \leq x \leq 4.4) \qquad \textbf{Equation 4.II}$$

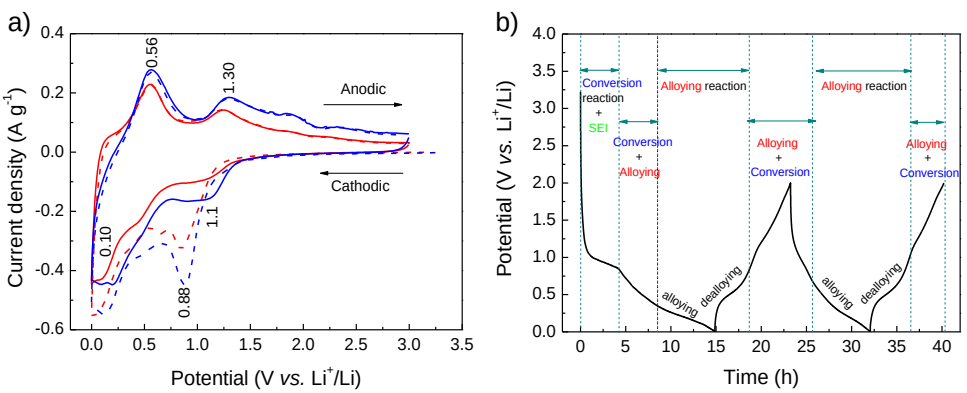

Figure 4.8. a) CV 1st (dash line) and 2nd (solid line) cycles of SnO_2-rGO-50 (red) and SnO_2-rGO-75 (blue) composites. b) 1st and 2nd charge/discharge profiles for SnO_2-rGO-75 composite.

Furthermore, *operando* recorded XRD has allowed validating the reaction mechanisms by following the structural changes upon cycling. **Figure 4.9** shows the evolution of the *operando* XRD patterns registered for the SnO_2-rGO-75 during the first cycle between 2.0 V and 0.005 V *vs.* Li^+/Li at C/40 ≈ *ca.* 0.02 A g^{-1}. First, the XRD pattern at the OCP shows two peaks at 35.8º and 37.5º assigned to the (101) and (211) planes, which correspond to the crystalline rutile tetragonal structure of SnO_2 (JCPDS card 41-1445). The additional peaks at 2θ angles of 28.6º, 29.9º, 40.6º and 42.1º come from the stainless steel of the in-house made electrochemical cell. The SEI formation occurs during the first irreversible charge above *ca.* 1.0 V *vs.* Li^+/Li. The XRD patterns recorded at those potential values (in green in **Figure 4.9**) show that the conversion reaction of SnO_2 into metallic Sn occurs in parallel to the growth of the SEI (**Equation 4.I**). Thus, the intensity of the diffraction maxima of the SnO_2 phase decreases until their complete disappearance at 2θ angle of 35.8º and 37.4º while the peaks corresponding to the tetragonal structure of metallic tin (JCPDS card 04-0673) start appearing and becoming sharper for the lower potentials. At 0.6 V *vs.* Li^+/Li the alloying reaction starts (**Equation 4.II**) and the peaks corresponding to metallic Sn are less intense. Both the alloying reaction (0.6 - 0.005 V, in red in **Figure 4.9**) and the reverse dealloying reaction (0.005 - 0.9 V, in light red in **Figure 4.9**) are not associated with any diffraction peak. Likely, this comes from the amorphous nature of the alloy and/or the small particle size. Above 0.9 V *vs.* Li^+/Li the peaks corresponding to metallic Sn are evident and maintained during charging and discharging until the second alloying reaction starts again at 0.6 V *vs.* Li^+/Li.

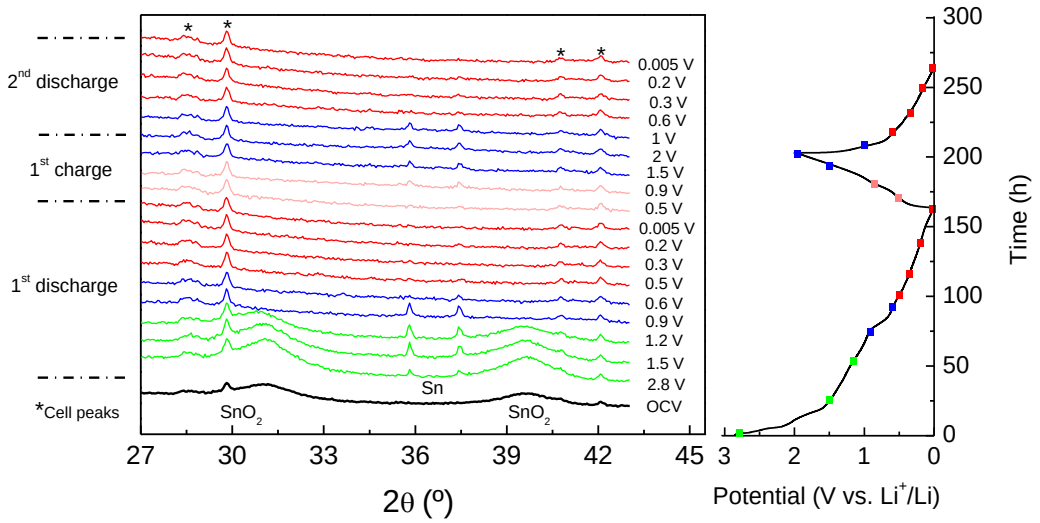

Figure 4.9. In situ XRD patterns using CuK_{α} radiation for SnO_2-rGO-75 and its electrochemical behaviour.

Due to the high content of SnO_2 within the composites, electrodes have higher mass loadings (*i.e.* ~2 mg cm^{-2}) compared to those previously reported when different synthetic route was followed (*i.e.* ~1 mg cm^{-2}) [13]. Therefore, **Figure 4.10** also includes areal capacity values in addition to specific capacity values, to allow a fair comparison with the already reported values [13]. First cycle CE of both SnO_2-rGO-75 and SnO_2-rGO-50 is 55%. This low value can be ascribed to the conversion reaction from SnO_2 to Sn taking place in the first charge step and to the large SSA of the rGO. During the rate capability test, where the capacity evolution *vs.* the current density is analyzed, 20 cycles were necessary to stabilize the alloying reaction and then higher current densities were applied. As can be observed in **Figure 10a**, high capacity values of 600 mAh g^{-1} and 450 mAh g^{-1} were obtained at lower current densities (*i.e.* 0.1 A g^{-1}) for SnO_2-rGO-75 and SnO_2-rGO-50, respectively. In order to quantify the contribution of rGO to the overall capacity, a blank sample formed only by rGO was also characterized showing a capacity value of 258 mAh g^{-1}. At higher current densities of 1 A g^{-1}, 2 A g^{-1} and 3 A g^{-1} (inset **Figure 4.10a** and **4.10b**), specific capacity values of 250 mAh g^{-1}, 165 mAh g^{-1} and

115 mAh g^{-1} were obtained for SnO_2-rGO-50 and 280 mAh g^{-1}, 175 mAh g^{-1} and 110 mAh g^{-1} for SnO_2-rGO-75, evidencing the slightly superior performance of the latter electrode. These good results at high current densities are ascribed to the importance of having an excellent conductive matrix made of rGO [28]. In terms of areal capacity, see **Figure 4.10b**, it is also confirmed that the higher SnO_2 loading provides the higher areal capacity values throughout the whole studied current density range. The capacity difference between SnO_2-rGO-50 and rGO is higher in terms of gravimetric values than in terms of areal values due to the different electrode weight. Also, the SnO_2 mass loading of the previously reported composite with sub-micron particles was lower [13], 1 mg cm^{-2} in the previous study *vs.* 2 mg cm^{-2} in this work, with all electrodes having the same area. Thus, specific areal capacity values of all of them are comparable.

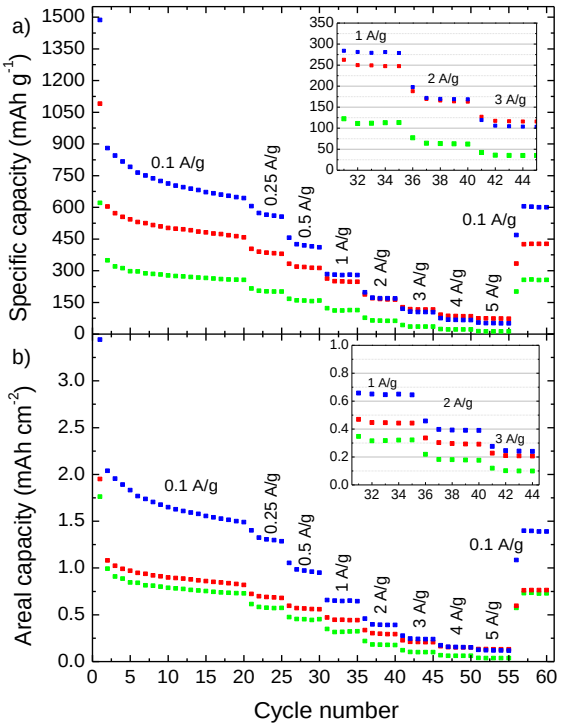

Figure 4.10. Rate capability of SnO_2-rGO-75 (blue), SnO_2-rGO-50 (red) and rGO (green). a) Specific gravimetric capacity values b) Specific areal capacity values. Inset: magnification for high current densities.

These results confirm the expected superior capacity performance achieved by nanosized composites when compared to the previous sub-micron composite since at high current densities (*i.e.* 1 A g^{-1}) higher capacity values (0.63 mAh cm^{-2} *vs.* 0.45 mAh cm^{-2}) were achieved (**Figure 4.11**). Thus, SnO_2-rGO-75 was selected as the battery-type negative electrode for the final LIC.

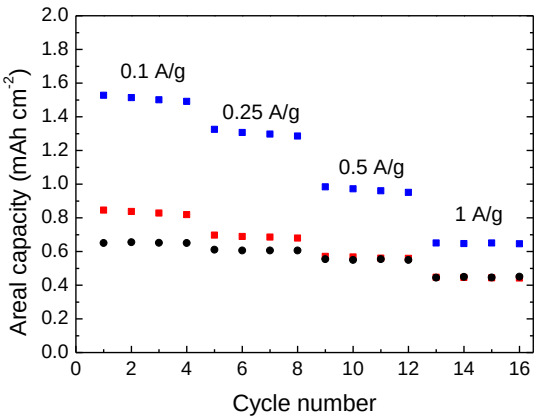

Figure 4.11. Rate capability of SnO_2-rGO-75 (blue) and SnO_2-rGO-50 (red) from this thesis, and SnO_2-rGO (black) used as reference from Ref. [13].

Additionally, SnO_2-rGO-75 nanocomposite was also tested in Na-ion technology. To this purpose, sodium metal was used as counter electrode and 1M $NaPF_6$ (EC:PC) as electrolyte in two electrode cell configuration. In order to make a fair comparison, a bare rGO sample was also characterized. **Figure 4.12** shows the rate capability of the as-prepared materials. As it can be observed, in terms of specific capacity, the SnO_2-rGO-75 nanocomposite only overcomes its rGO counterpart at very low current densities (*i.e.* 0.1 A g^{-1}). It is known that high SSA and disordered materials such as graphene show lower electrical conductivity than those non-porous and perfectly ordered ones. Hence, owing to the larger diffusion barrier of Na^+ in comparison with Li^+, the lower electrical conductivity of the nanocomposite does not allow obtaining as high specific capacity values as those obtained in Li-ion technology. Moreover, it was reported that the

sodiation speed in this material is approximately 20-times slower than the lithiation one [29].

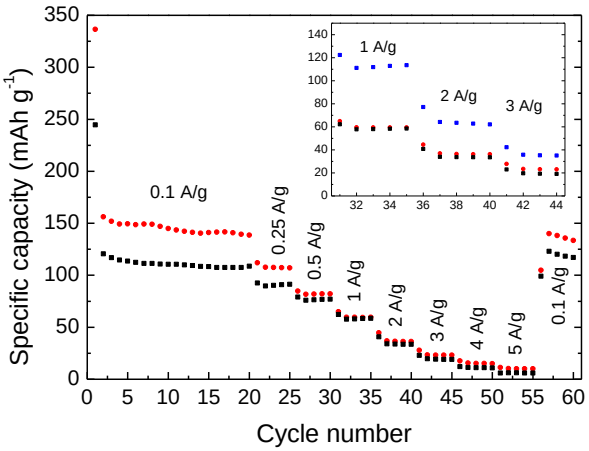

Figure 4.12. Rate capability of SnO_2-rGO-75 (red) and bare rGO (black) in Na-ion technology. Inset: magnification for high current densities comparing with SnO_2-rGO-75 in Li-ion chemistry (blue).

Thus, even that it shows good electrochemical performance at low currents densities, providing a reversible specific capacity of 150 mAh g^{-1} at 0.1 A g^{-1}, its limited behaviour at high rates limits its implementation in a NIC.

4.3. Development of a LIC based on SnO_2-rGO and AC

As stated before, SnO_2-rGO-75 nanocomposite was selected as the negative electrode material for LIC development since it outperforms its SnO_2-rGO-50 counterpart in terms of specific capacity. For the positive electrode, previously reported olive pits derived AC was selected, and a full LIC was assembled with both electrodes separated by a glass fibre membrane (Whatman GFB) in a three electrode Swagelok® cell using lithium metal as the reference electrode and 1 M $LiPF_6$ (EC:DMC) as the electrolyte. As detailed in **Chapter 2**, the balancing of the active mass of the negative and positive electrodes is

crucial for the final LIC performance. Hence, as can be observed in **Figure 4.13**, the capacity of both materials diverges along the applied current density values and, thus, it is not possible to define a suitable mass ratio for the whole range. Since LICs are designed to be used in low discharge time applications, typically below 2 min, a mass ratio of 1:1 was selected owing to the similar capacity values of both materials at high current densities. Then, in order to maximize the output voltage of the LIC, both electrodes were pre-conditioned (**Figure 4.13b**). Thus, SnO_2-rGO was cycled 10 times between 0.002 and 2 V *vs.* Li^+/Li at 50 mA g^{-1} in order to form the SEI and supply sufficient lithium to compensate for the first cycle irreversibility. Then, a cut-off potential of 0.2 V *vs.* Li^+/Li was set to avoid any safety issue due to lithium plating. AC was charged to a cut-off potential of 4.0 V *vs.* Li^+/Li at a current density of 10 mA g^{-1}.

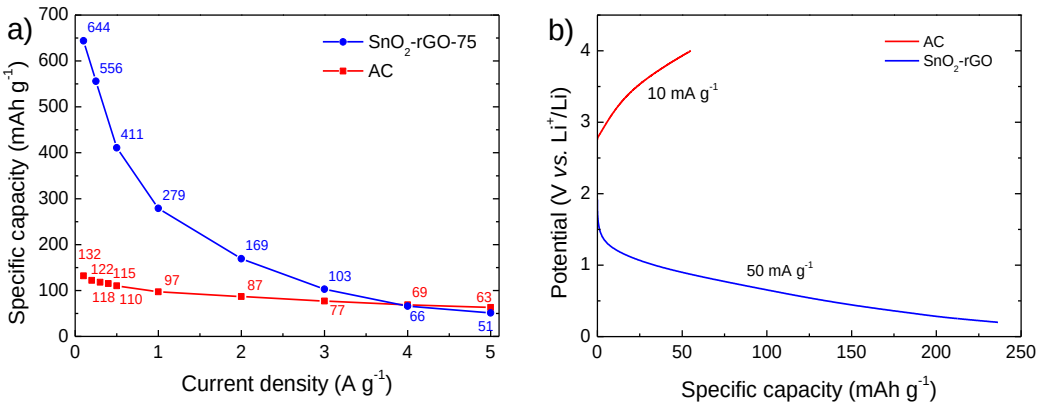

Figure 4.13. Specific capacity values for the AC cycled between 1.5 - 4.2V *vs.* Li^+/Li and the SnO_2-rGO-75 cycled between 0.005 - 2V *vs.* Li^+/Li at different current densities.

After the pre-conditioning step the GA charge/discharge characterization of the LIC was performed between 1.5 - 4.2 V *vs.* Li^+/Li at current densities between 0.05 and 5 A g^{-1}. In **Figure 4.14**, the profiles of both electrodes and the LIC are shown at 0.1 A g^{-1}, 1 A g^{-1} and 3 A g^{-1}. At low current densities, *i.e.* 0.1 A g^{-1}, within a discharge time of 26 min, the positive electrode (red dash line) swings from 2.2 to 4.2 V *vs.* Li^+/Li showing an ideal symmetric profile indicative of the capacitive storage mechanism, while the negative

electrode (dash-dot blue line) swings in a potential window from 0.8 to 0.1 V *vs.* Li^+/Li. A 10-fold increase in the applied current density, from 0.1 A g^{-1} to 1 A g^{-1}, decreases the discharge time to 29 s, a discharge time restricted to EDLCs, unattainable for batteries. Although potential profiles are slightly distorted from ideality, the increase in the ohmic resistance of the overall system is negligible and thus, the LIC charge/discharge profile is still determined by a capacitive charge storage mechanism. A further 30-fold increase in the current, from 0.1 A g^{-1} to 3 A g^{-1}, reduces the discharge time to 15 s. At this extremely challenging discharge time, the positive electrode still manages to work in a secure potential window, without going beyond the electrolytic decomposition potential, while the negative electrode is able to work in a potential window of 0.005 - 1.5 V *vs.* Li^+/Li, using its maximum capacity, and thus, confirming that the 1:1 mass ratio is ideally suitable and charge storage capacities of both electrode materials are well-balanced for the extremely rapid discharge times for hybrid supercapacitors.

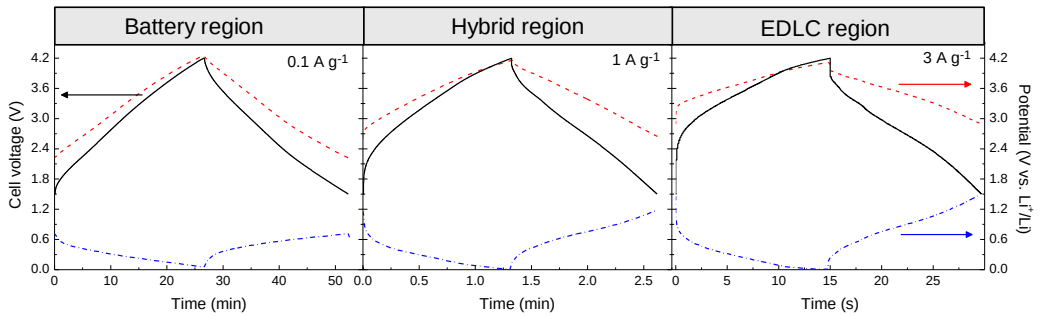

Figure 4.14. GA charge/discharge profiles of positive (AC, dash red line) and negative (SnO_2-rGO-75, dash-dot blue line) electrodes and full cell (LIC, straight black line).

However, some ESR is observed in the profiles of **Figure 4.14** when going to discharge times in the range of seconds, hence, energy efficiency should be considered. In the battery and hybrid region, the studied LIC shows 87% and 82% energy efficiency respectively, while going to the EDLC region, where ultrafast response is required, the energy efficiency decreases, being about 75%. This lower value is mostly ascribed to the higher applied current density. However, some other factors, previously mentioned for

dual carbon MICs, should be also considered and optimized in order to reduce the ESR and increase the energy efficiency of LICs.

For comparison purposes, a symmetric EDLC using the same AC and working in 1.5 M Et_4NBF_4 (ACN) was also built. **Figure 4.15** shows a comparison among the energy-to-power density ratios both in gravimetric and volumetric terms for the developed LIC with its EDLC counterpart. The reported results show that the LIC is able to store and deliver between 5- and 3-times more gravimetric and volumetric energy density than the olive pits derived AC based EDLC counterpart. At the low power density range, within a discharge time of ~1 h, as high as 140 Wh kg^{-1}_{AM} (57 Wh dm^{-3}) energy is delivered, while reducing the discharge time to 10 min, 101 Wh kg^{-1}_{AM} (42 Wh dm^{-3}) energy is delivered. As it is shown in **Figure 4.15**, from discharge times of 1 h to 1 min, the stored energy density is importantly higher than its EDLC counterpart, showing 5- and 4-times higher values. However, reducing the discharge time to the very challenging and normally limited discharge time region for supercapacitors (*i.e.* 10 s), the developed LIC is still able to provide, both in gravimetric and volumetric terms, double the energy density than its EDLC counterpart.

These results show that higher energy density values are possible to obtain in the same power density range of an EDLC when the device is hybridized. Furthermore, one of the main challenges of hybrid supercapacitors is also to maintain a cycle life similar to that of EDLCs. However, in this study only 78% capacitance retention was obtained after 2000 cycles at a constant current of 3 A g^{-1} ($t_{discharge}$ = 15 s). Despite the encouraging cycle life, is far to be comparable to that of EDLCs. This might be related to the 100% used of the negative electrode while cycling at 3 A g^{-1}. A less favorable mass ratio allows using a lower percentage of the negative electrode -thus implying a reduction on the energy output- will definitively extend the cycle life of the LIC. In order to gain some more insights on the low cyclability, a post-mortem analysis was carried out.

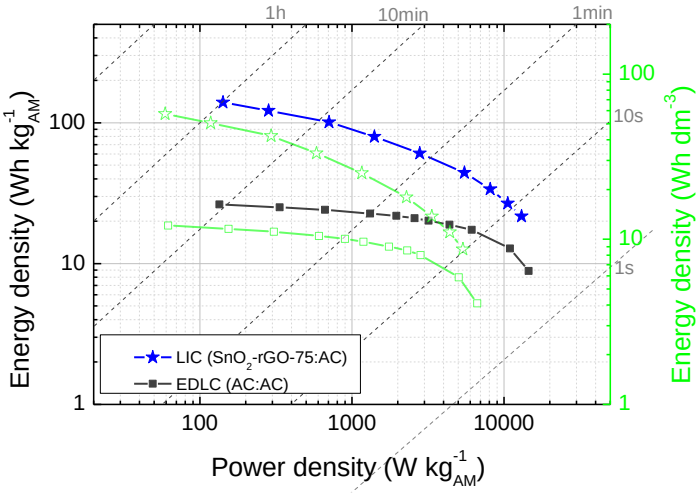

Figure 4.15. Gravimetric and volumetric Ragone plots comparing the olive pits derived EDLC.

In **Table 4.1** the obtained results are compared to other state-of-the-art reported Sn-based LICs. As it is observed, similar energy-to-power density and cyclability values were achieved in comparison with other groups.

Table 4.1. Summary of already reported Sn-based LICs.

Anode	Sn wt.% loading	**Cathode**	**Energy (Wh kg$^{-1}_{AM}$)**	**Power (Wh kg$^{-1}_{AM}$)**	**Stability**	**Ref.**
SnO_2-C	57	Tubular mesoporous carbon	110 75 47	180 1000 3000	80% after 2000 cycle	[16]
Sn-C	40	Pomelo peel AC	196 85	731 24375	70% after 5000 cycle	[17]
SnO_2-C	-	YP-80F	130 45	125 1000	90% after 100 cycle	[18]
SnO_2-rGO	75	Olive pits AC	140 80 61	142 1407 2788	78% after 2000 cycle 55% after 10000 cycle	**This work**

4.4. Post-mortem analysis

SEM image from the cycled SnO_2-rGO-75 electrode (**Figure 4.16**) reveals a remarkable SEI and no evidence of graphene sheets in comparison with the pristine material (inset **Figure 4.16**). Moreover, the cycled electrode presents some cracks caused by the mechanical stress suffered upon cycling. Hence, these results can give some insights on the low cycle life of the developed LIC.

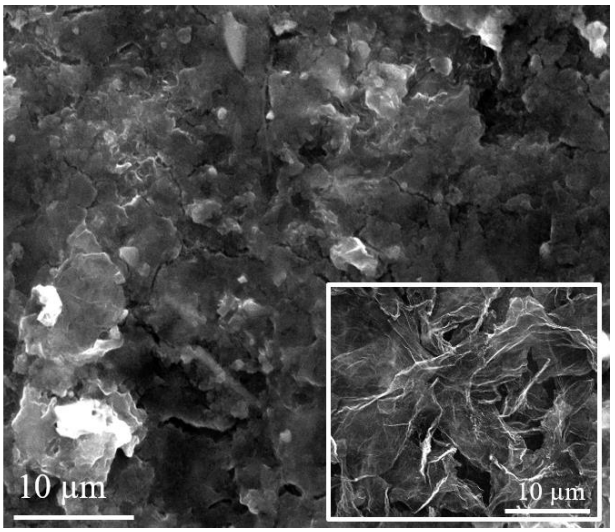

Figure 4.16. Post-mortem SEM image of the SnO_2-rGO-75 negative electrode after long-term cycling in comparison with the pristine material (inset).

4.5. Summary and conclusions

In this work, based on the previous work done by Botas *et al*., the synthetic route that consists on an *in-situ* synthetic approach that involves the freeze/freeze-drying of a graphene oxide suspension in the presence of a Sn precursor and its subsequent thermal reduction under argon atmosphere has been modified in order to improve the electrochemical performance of SnO_2-rGO with the intended use in LICs. Reducing the mixing time and working at RT conditions have allowed to obtain nanosized SnO_2

particles (<10 nm) instead of the previously reported sub-micron SnO_2 particles (≈250 nm), which allowed for higher SnO_2 loading -up to 75 wt%- onto graphene layers without increasing the mechanical stress. The high SnO_2 content translates into a remarkable electrochemical performance, especially at medium and high current densities, a highly appealing feature for ultrafast LICs. Contrary, in Na-ion chemistry, due to the hindered Na^+ diffusion and the larger volume expansions that Na-based alloying materials might suffer in comparison with their Li-based counterparts, the specific capacity output is limited. Hence, more effort should be focused on tailoring the composite in order to enhance its performance in Na-ion technology. While in Li-ion technology, the combination of a 75 wt% Sn loading SnO_2-rGO composite with recycled olive pits derived AC enables targeting high energy density LICs with excellent gravimetric and volumetric characteristics. Altogether, this coupling gives the opportunity to assemble an encouraging hybrid device which stores/delivers high energy density at high power density. In fact, at low power densities, a 5-fold -gravimetric- and a 6-fold -volumetric- increase has been achieved in terms of energy density, while at the high power region the energy density is still between double and triple that of the EDLC using the same porous carbon. In addition, the system presents a highly promising 78% capacitance retention after 2000 cycles run at a constant current of 3 A g^{-1} within a discharge time of 15 s.

4.6. Bibliography

[1] N. Nitta, F. Wu, J.T. Lee, G. Yushin, Li-ion battery materials: present and future, Mater. Today. 18 (2015) 252–264. doi:10.1016/j.mattod.2014.10.040.

[2] M.V. Reddy, T.T. Linh, D.T. Hien, B.V.R. Chowdari, SnO2 Based Materials and Their Energy Storage Studies, ACS Sustain. Chem. Eng. 4 (2016) 6268–6276. doi:10.1021/acssuschemeng.6b00445.

[3] J. Ajuria, M. Arnaiz, C. Botas, D. Carriazo, R. Mysyk, T. Rojo, A.V. Talyzin, E. Goikolea, Graphene-based lithium ion capacitor with high gravimetric energy and power densities, J. Power Sources. 363 (2017) 422–427. doi:10.1016/j.jpowsour.2017.07.096.

[4] X.-T. Chen, K.-X. Wang, Y.-B. Zhai, H.-J. Zhang, X.-Y. Wu, X. Wei, J.-S. Chen, A facile one-pot reduction method for the preparation of a SnO/SnO2/GNS composite for high

performance lithium ion batteries, Dalton Trans. 43 (2014) 3137–3143. doi:10.1039/C3DT52661E.

[5] H. Li, L. Shi, W. Lu, X. Huang, L. Chen, Studies on Capacity Loss and Capacity Fading of Nanosized SnSb Alloy Anode for Li-Ion Batteries, J. Electrochem. Soc. 148 (2001) A915–A922. doi:10.1149/1.1383070.

[6] L. Ji, Z. Lin, M. Alcoutlabi, X. Zhang, Recent developments in nanostructured anode materials for rechargeable lithium-ion batteries, Energy Environ. Sci. 4 (2011) 2682–2699. doi:10.1039/C0EE00699H.

[7] Z. Favors, W. Wang, H.H. Bay, A. George, M. Ozkan, C.S. Ozkan, Stable Cycling of SiO2 Nanotubes as High-Performance Anodes for Lithium-Ion Batteries, Sci. Rep. 4 (2014) 4605. doi:10.1038/srep04605.

[8] Y. Yu, L. Gu, C. Wang, A. Dhanabalan, P.A. van Aken, J. Maier, Encapsulation of Sn@carbon Nanoparticles in Bamboo-like Hollow Carbon Nanofibers as an Anode Material in Lithium-Based Batteries, Angew. Chem. Int. Ed. 48 (2009) 6485–6489. doi:10.1002/anie.200901723.

[9] R. Dai, W. Sun, Y. Wang, Ultrasmall Tin Nanodots Embedded in Nitrogen-Doped Mesoporous Carbon: Metal-Organic-Framework Derivation and Electrochemical Application as Highly Stable Anode for Lithium Ion Batteries, Electrochimica Acta. 217 (2016) 123–131. doi:10.1016/j.electacta.2016.08.051.

[10] Y. Deng, C. Fang, G. Chen, The developments of SnO2/graphene nanocomposites as anode materials for high performance lithium ion batteries: A review, J. Power Sources. 304 (2016) 81–101. doi:10.1016/j.jpowsour.2015.11.017.

[11] G. Wang, B. Wang, X. Wang, J. Park, S. Dou, H. Ahn, K. Kim, Sn/ graphene nanocomposite with 3D architecture for enhanced reversible lithium storage in lithium ion batteries, J. Mater. Chem. 19 (2009) 8378–8384. doi:10.1039/B914650D.

[12] P. Lian, J. Wang, D. Cai, G. Liu, Y. Wang, H. Wang, Design and synthesis of porous nano-sized Sn@C/graphene electrode material with 3D carbon network for high-performance lithium-ion batteries, J. Alloys Compd. 604 (2014) 188–195. doi:10.1016/j.jallcom.2014.03.116.

[13] C. Botas, D. Carriazo, G. Singh, T. Rojo, Sn– and SnO2–graphene flexible foams suitable as binder-free anodes for lithium ion batteries, J. Mater. Chem. A. 3 (2015) 13402–13410. doi:10.1039/C5TA03265B.

[14] L. Yue, C. Xue, B. Huang, N. Xu, R. Guan, Q. Zhang, W. Zhang, High performance hollow carbon@SnO2@graphene composite based on internal-external double protection strategy for lithium ion battery, Electrochimica Acta. 220 (2016) 222–230. doi:10.1016/j.electacta.2016.10.110.

[15] M. Zhang, Z. Sun, T. Zhang, D. Sui, Y. Ma, Y. Chen, Excellent cycling stability with high SnO2 loading on a three-dimensional graphene network for lithium ion batteries, Carbon. 102 (2016) 32–38. doi:10.1016/j.carbon.2016.02.032.

[16] W.-H. Qu, F. Han, A.-H. Lu, C. Xing, M. Qiao, W.-C. Li, Combination of a SnO2–C hybrid anode and a tubular mesoporous carbon cathode in a high energy density non-

aqueous lithium ion capacitor: preparation and characterisation, J. Mater. Chem. A. 2 (2014) 6549–6557. doi:10.1039/C4TA00670D.

[17] F. Sun, J. Gao, Y. Zhu, X. Pi, L. Wang, X. Liu, Y. Qin, A high performance lithium ion capacitor achieved by the integration of a Sn-C anode and a biomass-derived microporous activated carbon cathode, Sci. Rep. 7 (2017) srep40990. doi:10.1038/srep40990.

[18] M. Xuan Tran, A.-Y. Kim, J.K. Lee, Employment of ultra-thin carbon layer-coated porous tin oxide as anode in lithium-ion capacitor, Appl. Surf. Sci. 461 (2018) 161–170. doi:10.1016/j.apsusc.2018.04.259.

[19] Y. Wang, H. Li, P. He, E. Hosono, H. Zhou, Nano active materials for lithium -ion batteries, Nanoscale. 2 (2010) 1294–1305. doi:10.1039/C0NR00068J.

[20] Y. Xu, Q. Liu, Y. Zhu, Y. Liu, A. Langrock, M.R. Zachariah, C. Wang, Uniform Nano-Sn/C Composite Anodes for Lithium Ion Batteries, Nano Lett. 13 (2013) 470–474. doi:10.1021/nl303823k.

[21] C. Botas, P. Álvarez, C. Blanco, R. Santamaría, M. Granda, P. Ares, F. Rodríguez-Reinoso, R. Menéndez, The effect of the parent graphite on the structure of graphene oxide, Carbon. 50 (2012) 275–282. doi:10.1016/j.carbon.2011.08.045.

[22] J. Shan, Y. Liu, P. Liu, Y. Huang, Y. Su, D. Wu, X. Feng, Nitrogen-doped carbon-encapsulated SnO 2 –SnS/graphene sheets with improved anodic performance in lithium ion batteries, J. Mater. Chem. A. 3 (2015) 24148–24154. doi:10.1039/C5TA06617D.

[23] J. Cheng, H. Xin, H. Zheng, B. Wang, One-pot synthesis of carbon coated-SnO2/graphene-sheet nanocomposite with highly reversible lithium storage capability, J. Power Sources. 232 (2013) 152–158. doi:10.1016/j.jpowsour.2013.01.025.

[24] C.-L. Hsieh, D.-S. Tsai, W.-W. Chiang, Y.-H. Liu, A composite electrode of tin dioxide and carbon nanotubes and its role as negative electrode in lithium ion hybrid capacitor, Electrochimica Acta. 209 (2016) 332–340. doi:10.1016/j.electacta.2016.05.090.

[25] J. Sun, L. Xiao, S. Jiang, G. Li, Y. Huang, J. Geng, Fluorine-Doped SnO2@Graphene Porous Composite for High Capacity Lithium-Ion Batteries, (2015). doi:10.1021/acs.chemmater.5b00885.

[26] X. Zhou, L.-J. Wan, Y.-G. Guo, Binding SnO2 Nanocrystals in Nitrogen-Doped Graphene Sheets as Anode Materials for Lithium-Ion Batteries, Adv. Mater. 25 (2013) 2152–2157. doi:10.1002/adma.201300071.

[27] L. Noerochim, J.-Z. Wang, S.-L. Chou, H.-J. Li, H.-K. Liu, SnO2-coated multiwall carbon nanotube composite anode materials for rechargeable lithium-ion batteries, Electrochimica Acta. 56 (2010) 314–320. doi:10.1016/j.electacta.2010.08.078.

[28] A. González, E. Goikolea, J.A. Barrena, R. Mysyk, Review on supercapacitors: Technologies and materials, Renew. Sustain. Energy Rev. 58 (2016) 1189–1206. doi:10.1016/j.rser.2015.12.249.

[29] M. Gu, A. Kushima, Y. Shao, J.-G. Zhang, J. Liu, N.D. Browning, J. Li, C. Wang, Probing the Failure Mechanism of SnO 2 Nanowires for Sodium-Ion Batteries, Nano Lett. 13 (2013) 5203–5211. doi:10.1021/nl402633n.

CHAPTER 5

$TiSb_2$ as negative electrode for lithium and sodium ion capacitors

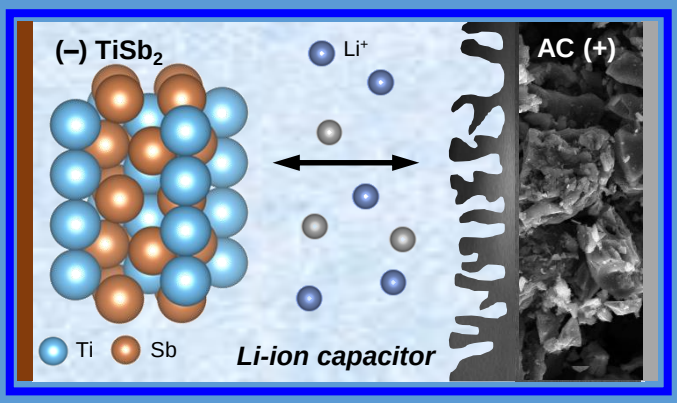

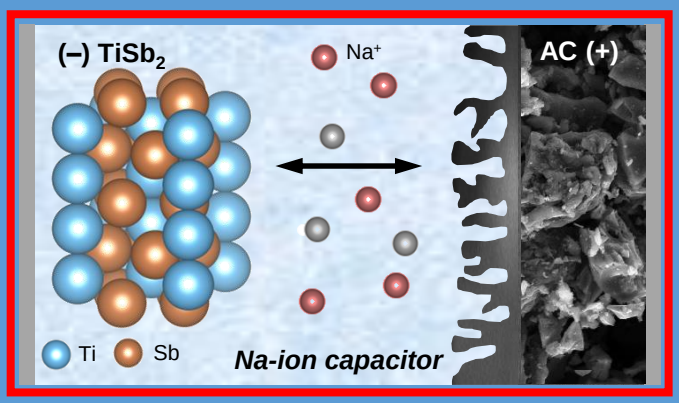

$TiSb_2$ as negative electrode for LICs and NICs

Negative electrodes based on alloying materials show excellent balance between low reduction potentials and high specific capacity values, but suffer large volume expansion that hinders their implementation in real devices. In order to address this problematic, a promising intermetallic compound was synthetized: $TiSb_2$. Owing to the obtained excellent set of characteristics, its viability has been explored for the development of high performing lithium ion capacitors (LICs) and sodium ion capacitors (NICs).

In Li-ion technology, $TiSb_2$ shows high specific capacity (360 mAh g^{-1} at 10C) and an excellent rate capability performance together with exceptional volumetric features, enabling its use as a promising candidate for high power requiring technologies. In order to maximize the LIC performance, the influence of the mass ratio between active materials ($TiSb_2$:AC) has been studied. The best $TiSb_2$-based LIC is able to deliver an energy density as high as 167 Wh kg^{-1}_{AM} at 115 W kg^{-1}_{AM} and 90 Wh kg^{-1}_{AM} at 11 kW kg^{-1}_{AM} which are among the best reported values for LICs. In addition, an encouraging 80% retention of the initial capacitance after 10000 cycles at 10 A g^{-1} constant current ($t_{discharge}$=11 s) is obtained.

With regard to the Na-ion technology, the electrochemical performance of $TiSb_2$ shows a capacity of about 225 mAh g^{-1} for 200 cycles at C/10. Discrepancies with the expected theoretical capacity are discussed by means of operando XRD and ex-situ TEM analysis. Nevertheless, the good capacity values at high rates (i.e. 100 mAh g^{-1} at 10C) enables the use of $TiSb_2$ in NICs, achieving promising high energy densities of 132 Wh kg^{-1}_{AM} at 114 W kg^{-1}_{AM} and 65 Wh kg^{-1}_{AM} at 11 kW kg^{-1}_{AM}. However, due to the large volume expansion, the capacitance retention is affected. The study of different cross-linked functional binders allowed improving cyclability from 10% to 63% after 1000 cycles at 5 A g^{-1} constant current, paving the way to develop new high-performance anodes for NICs.

Table of contents:

5.1. Introduction to intermetallic compounds

Following the goal of replacing graphite as the negative electrode in MIC technology and moving toward anode materials that enable the achievement of higher energy density values, stable materials with good rate capabilities below ~1 V *vs.* Li^+/Li or Na^+/Na are needed [1–3]. For that reason, alloying materials such as Li_xA or Na_xA (where A = Si, Sn, Sb…) became a good alternative since the reduction potential of all of them is around ~0.3 - 1 V *vs.* Li^+/Li or Na^+/Na. Moreover, high specific capacity values, *i.e.* 992 mAh g^{-1} for $Li_{4.4}Sn$, 4200 mAh g^{-1} for $Li_{22}Si_5$, and 660 mAh g^{-1} for Li_3Sb, while 800 mAh g^{-1} for $Na_{15}Sn_4$, 900 mAh g^{-1} for NaSi, and 660 mAh g^{-1} for Na_3Sb, have been demonstrated [3–6]. Compared to the specific capacity of graphite (LiC_6: 372 mAh g^{-1}), they all show much higher specific capacities. Nevertheless, the large volume changes that these alloying materials suffer results in a large internal mechanical stress and directly impacts on their cycle life. Thus, many efforts are centered on buffering the large volume expansions. The main strategies to overcome this problem are focused on reducing the particle size and/or coating the active material with a conductive material such as carbon or graphene, as it was explored in the previous **Chapter 4** [7,8], or even with a non-conductive material such as metal oxides [9,10]. A novel strategy lately in vogue is to synthetize intermetallic compounds such as MA_y, (where M=Ti, In, Cu, Mn, Co, Zn; A=Si, Sn, Sb and y=1, 2, 3) based on an inactive phase that does not react with lithium or sodium, and an active phase that does [11,12]. The inactive phase allows a fine dispersion of the active element during cycling (**Figure 5.1**). This not only avoids the agglomeration of particles and the above-mentioned volume changes, but it also provides better conductivity to the material and longer cycle life [3,9].

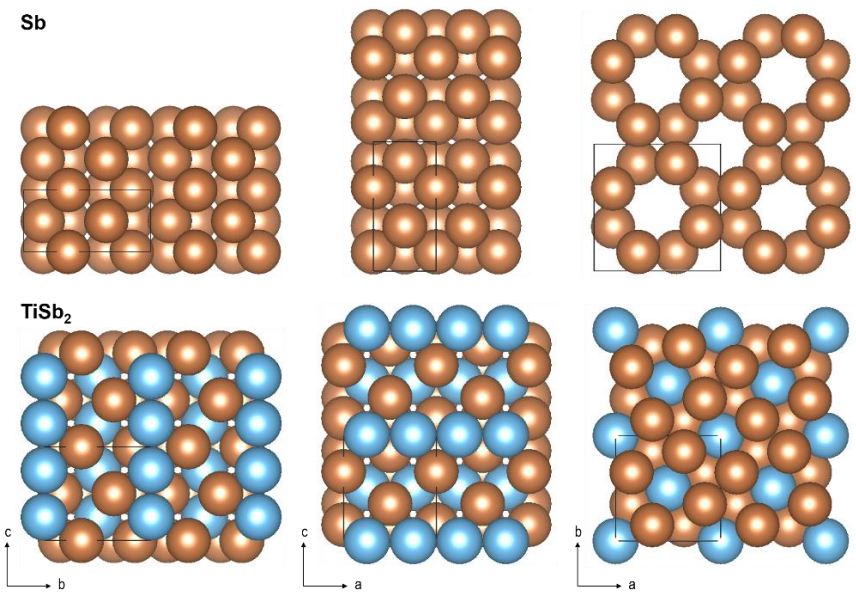

Figure 5.1. Sb and the intermetallic compound $TiSb_2$.

A large amount of different intermetallic compounds have been studied in the literature during the last decades. Moreover, tremendous efforts have been done in order to find the most appropriate inactive metal to improve their cycle life and stability. In this thesis, moving from the already studied Sn-based material and encouraged by its high gravimetric capacity values, Sb was selected as the active material for the development of an intermetallic compound: $TiSb_2$.

5.2. Sb-based intermetallic compounds for Li-ion technology

In order to solve the aforementioned problems, research has been focused on Sb-based intermetallic compounds (MSb_y). The reaction mechanism of these materials is normally defined by two parallel reactions. Simultaneously, a Li ternary phase is created owing to the Li insertion within MSb_y, while a Li_3Sb phase is generated together with a nanocrystalline metal owing to a conversion/alloying reaction [3]. These reactions are described as follows:

Insertion reaction: $MSb_y + z\ Li^+ + xe^- \rightarrow Li_zMSb_y$

Conversion/alloying reaction: $MSb_y + 3\ Li + 3e^- \rightarrow y\ Li_3Sb + M$

The formation of Li_zMSb_y results in fast rate capability and stable cycling behaviour owing to its stable crystalline structure. Besides, nanocrystalline metal and Li_3Sb produced by the conversion reaction helps to afford less structural stress [3].

Among the different Sb-based intermetallic compounds found in literature, Co-Sb, Cu_2Sb, Zn_4Sb_3, and $TiSb_2$ can be highlighted. Park *et al.* reported on different Co-Sb compounds such as CoSb, $CoSb_2$, and $CoSb_3$. In order to improve their mechanical performance, nanostructured composites of these compounds were carbon coated by a high-energy mechanical milling technique. Among them, $CoSb_2$/C showed the best electrochemical performance with a high charge capacity of 578 mAh g^{-1}, an initial CE of 78.1%, and an excellent rate capability showing a retention of 82% and 72% of the initial capacity at 1C and 3C, rate respectively [13]. Morcrette *et al.* investigated on the use of Cu_2Sb, which delivered a specific capacity of 290 mAh g^{-1} below 1 V *vs.* Li^+/Li. In order to better understand the reaction mechanisms, *operando* XRD measurements were performed concluding that Cu_2Sb could offer electrochemical and structural reversibility if particles were in the nanometer range and carbon coated [14]. Zn_4Sb_3 was also studied as a potential anode material for LIBs. In this case, it was also shown that an appropriate carbon coating (Zn_4Sb_3/C) could not only increase the first cycle specific capacity from 507 mAh g^{-1} to 580 mAh g^{-1} at C/10 but could also maintain a 67% of the initial capacity after 10 cycles, while the non-carbon coated material showed almost null capacity after 5 cycles [15].

Among the different studied materials in literature, research of this thesis is focused on the use of $TiSb_2$ as a potential candidate for its implementation as negative electrode in MIC technology. Park *et al.* first showed the potential use of this intermetallic compound as anode for LIBs. Its electrochemical performance was compared with bare Sb metal

and it was shown that while Sb showed a large reaction plateau at 0.8 V *vs.* Li^+/Li, $TiSb_2$ showed a sloppy profile from 0.8 V *vs.* Li^+/Li up to 0 V. It was demonstrated that the absence of a volume buffering matrix in Sb material led to a huge capacity decay only in the first 10 cycles, while the capacity of $TiSb_2$ showed to be more stable [16]. Later, Gómez-Cámer *et al.* investigated on its reaction mechanism by *operando* XRD [17]. The authors showed that $TiSb_2$ was able to accept lithium in its structure and led to a new ternary phase (Li_xTiSb_2) which crystallized in the tetragonal system with the same space group as $TiSb_2$ (*I4/mcm*). During lithiation, the intensity of the reflections of this ternary phase decreased, while a new phase appeared and increased with the lithium content. This conversion process led to the formation of cubic Li_3Sb phase and extruded Ti nanoparticles. During delithiation process, a direct conversion from Li_3Sb to Sb happened, whereas Ti nanoparticles were increasingly disengaged from the electrode, and thus, became electrochemically inactive. In order to improve the electrochemical behaviour, the same group later focused on the electrode engineering [18]. It was shown that the rate capability, CE, and cycle life could be improved when $TiSb_2$-based electrodes were prepared with lithium polyacrylate (LiPAA) binder instead of the typical polyvinylidene difluoride (PVdF). The better ability of LiPAA to homogeneously disperse active materials, led in the end to a better volume expansion control whereas rate capability was enhanced by reducing the particle size and creating shorter diffusion paths.

Despite the outstanding capacity values shown by $TiSb_2$ at high C-rates (*i.e.* 400 mAh g^{-1} at 12C), its potential use for power applications has gone unnoticed. Thereby, in this thesis, $TiSb_2$ was selected as a potential candidate to substitute graphite as the negative electrode in MICs technology, owing to i) the high specific capacity of Li_3Sb and ii) the lightness of titanium, its non-toxicity and good conductive properties as inactive material. Furthermore, its use in NICs was also explored.

5.2.1. Material and electrode preparation of $TiSb_2$

$TiSb_2$ was prepared by placing a stoichiometric mixture of Sb (ABCR, 100 mesh, 99.5% purity) and Ti (ABCR, 325 mesh, 98.7% purity) in a tubular furnace and heated at 5 ºC min^{-1} to 900 ºC for 12 h under argon atmosphere (100 ml min^{-1}). After the heat treatment, the sample was first grounded in a mortar and then particle size was reduced by wet (*i.e.* isopropanol) ball milling in a Fritsch Pulverisette 7 at 500 rpm during 2 h (**Scheme 5.1**).

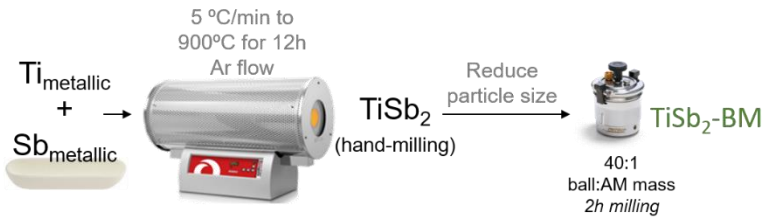

Scheme 5.1. Synthesis route for the $TiSb_2$ intermetallic compound.

The preparation of the AC used for the final device as the positive electrode was described in **Chapter 2 – Section 2.3.1.**

In order to prepare the laminates for further electrochemical characterization, the $TiSb_2$ slurry was prepared by a mixture of the active material, Super P C65 (Imerys Graphite & Carbon) as conductive material and carboxymethyl cellulose (CMC) as binder in 80:10:10 mass ratio dispersed in ethanol/water solvent using an IKA®T25 digital Ultra Turrax ® homogenizer. In order to make a fair electrochemical comparison an Sb-based laminate was also prepared following the same procedure. While the AC slurry was prepared as previously explained. Then both slurries were laminated, $TiSb_2$-based one onto copper current collector foil and AC-based slurry onto aluminum foil. Laminates were transferred into a vacuum oven and dried at 80 ºC under constant vacuum for 12 h before 1.13 cm^2 circular electrodes were cut out. The weight and thickness of the

electrodes were around 1 mg and 30 µm for $TiSb_2$, and from 1 to 3 mg cm^{-2} and from 33 to 87 µm for AC, respectively.

5.2.2. Physicochemical characterization of $TiSb_2$

In order to confirm the crystalline structure of the synthesized antimony intermetallic compound, XRD patterns from the pristine $TiSb_2$ and the ball milled $TiSb_2$ ($TiSb_2$-BM) are shown in **Figure 5.2**. While all the diffraction maxima presented in the pristine $TiSb_2$ can be ascribed to the intermetallic compound [18], the ball milled sample shows an additional small peak at a 2θ angle of 28º and a wide peak at 40º that could be attributed to small amounts of Sb and Ti respectively generated during the ball milling process. The broader peaks observed for this last sample also suggest a particle size reduction. This fact is further confirmed by calculating the crystallite size of each sample by using the Scherrer equation (**Equation AI.II**) [19], obtaining *ca.* 268 nm size for the pristine sample and *ca.* 16 nm particle size for the ball milled one. This is in good agreement with the particle size observed by SEM, where the microstructural analysis reflects a particle size of ~10 µm for the pristine material (**Figure 5.2a**) and about 0.4 µm for the ball milled sample (**Figure 5.2b**).

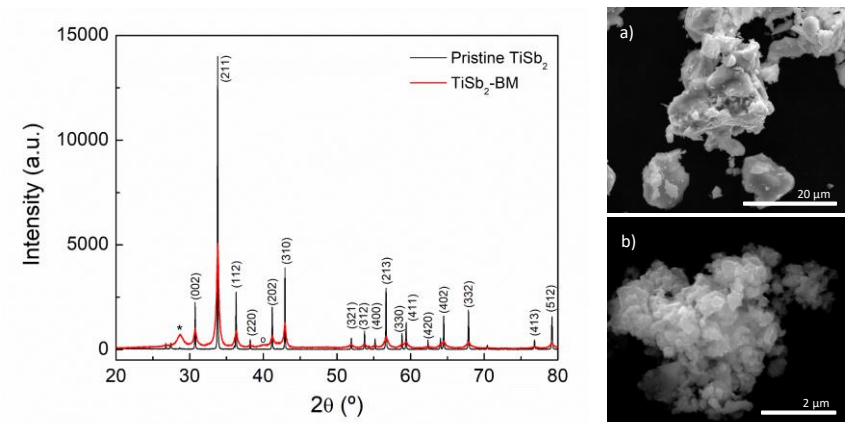

Figure 5.2. XRD pattern of pristine $TiSb_2$ (black) and $TiSb_2$-BM (red). (*) and (º) peaks correspond to Sb and Ti metal respectively. SEM images of a) Pristine $TiSb_2$ and b) $TiSb_2$-BM.

5.2.3. Electrochemical characterization of $TiSb_2$

The electrochemical characterization of the $TiSb_2$ composite was carried out by CV recorded at 0.1 mV s^{-1} and GA charge/discharge measurements at different C-rates between C/10 and 100C, all in the potential range of 0.05 - 1.5 V *vs.* Li^+/Li. Three-electrode Swagelok® cells using lithium metal both as counter and reference electrodes and 1 M $LiPF_6$ (EC:DMC) as the electrolyte were used. In **Figure 5.3** the first two CV curves are shown. On the one hand, within the first charge step (cathodic sweep) two main peaks appear at 0.75 and 0.20 V *vs.* Li^+/Li, which are associated to the SEI formation and to the Li_3Sb and Ti^0 -generated after the irreversible conversion reaction of $TiSb_2$- formation respectively. In the first discharge step (anodic sweep), one major peak appears at 1.1 V *vs.* Li^+/Li which is assigned to the lithium extraction from Li_3Sb. On the other hand, in the second scan, the main cathodic peak is shifted to 0.8 V *vs.* Li^+/Li owing to the Sb alloying reaction with lithium. This allows to conclude that the final product after the first cycle was mainly Sb, instead of $TiSb_2$. As a result, Ti becomes to work as an inactive element which acts as a matrix that buffers the volume changes of Sb [17,18].

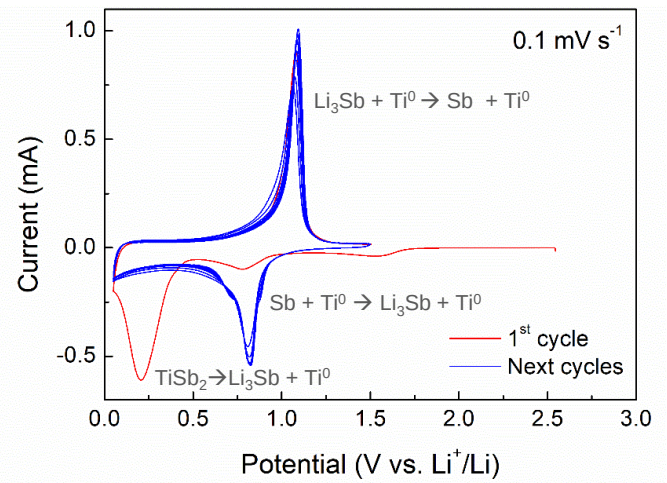

Figure 5.3. CV of $TiSb_2$ recorded at 0.1 mV s^{-1} between 0.05 - 1.5 V *vs.* Li^+/Li in 1M $LiPF_6$ (EC:DMC).

In order to evaluate the possible electrochemical influence of the Sb metal traces observed by XRD for the $TiSb_2$-BM sample, GA charge/discharge measurements were carried out for both Sb and $TiSb_2$-BM based electrodes. **Figure 5.4a** and **5.4b** show the first and second discharge profiles measured for both materials. In **Figure 5.4a**, two different regions are distinguished for Sb, while three are observed for $TiSb_2$-BM. In both cases the first sloping region (region I) can be associated to the SEI formation. The plateau at 0.8 V *vs.* Li^+/Li (region II) observed in the discharge profile of Sb is indicative of the alloying reaction to form Li_3Sb. Whereas in the case of $TiSb_2$-BM, the sloppier profile is a consequence of the lower amount of initial Sb and the less homogeneous particle-size distribution. Moreover, in the case of $TiSb_2$-BM, around 0.4 V *vs.* Li^+/Li, the irreversible reaction from $TiSb_2$ to Sb occurs (region III). After the first charge/discharge cycle, the plateau at 0.8 V *vs.* Li^+/Li is still observed for Sb (**Figure 5.4b**), while for $TiSb_2$-BM a unique sloping region starting at the same potential appears, which also corresponds to the alloying reaction.

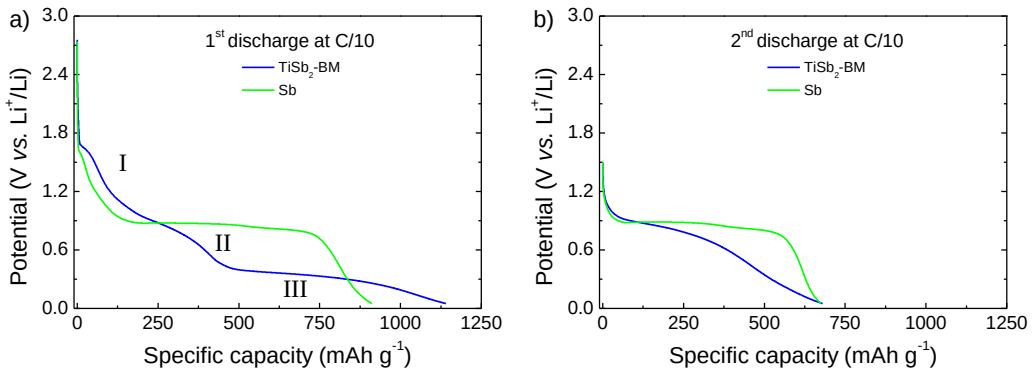

Figure 5.4. GA charge/discharge measurement for $TiSb_2$ and Sb between 0.05 - 1.5 V *vs.* Li^+/Li: a) 1st discharge profile at C/10, b) 2nd discharge profile at C/10.

In **Figure 5.5a** the rate capability of both materials is reported. For $TiSb_2$ the theoretical capacity is 552 mA g^{-1} [17] and 660 mA g^{-1} for Sb [3]. Initial charge and discharge capacities of $TiSb_2$ at C/10 are 1140.8 mAh g^{-1} and 483.3 mAh g^{-1}, respectively,

corresponding to a CE of ~42%. This discrepancy between charge and discharge capacities is attributed to the SEI formation and the irreversible conversion reaction from $TiSb_2$ to Sb. However, $TiSb_2$ shows excellent reversible capacities in the following cycles onward, with a CE close to 98%. In contrast, owing to the absence of any irreversible conversion reaction, Sb shows a higher first cycle CE of 71%. At low C-rates both materials deliver a specific capacity as high as 600 mAh g^{-1}. However, in the following cycles, the specific capacity of Sb decreases faster than that of $TiSb_2$-BM. This rapid capacity fading is attributed to the higher internal mechanical stress caused by the large volume changes undergone by Sb over cycling. The rise of the internal resistance is clearly visible in the Nyquist Plot (**Figure 5.6**).

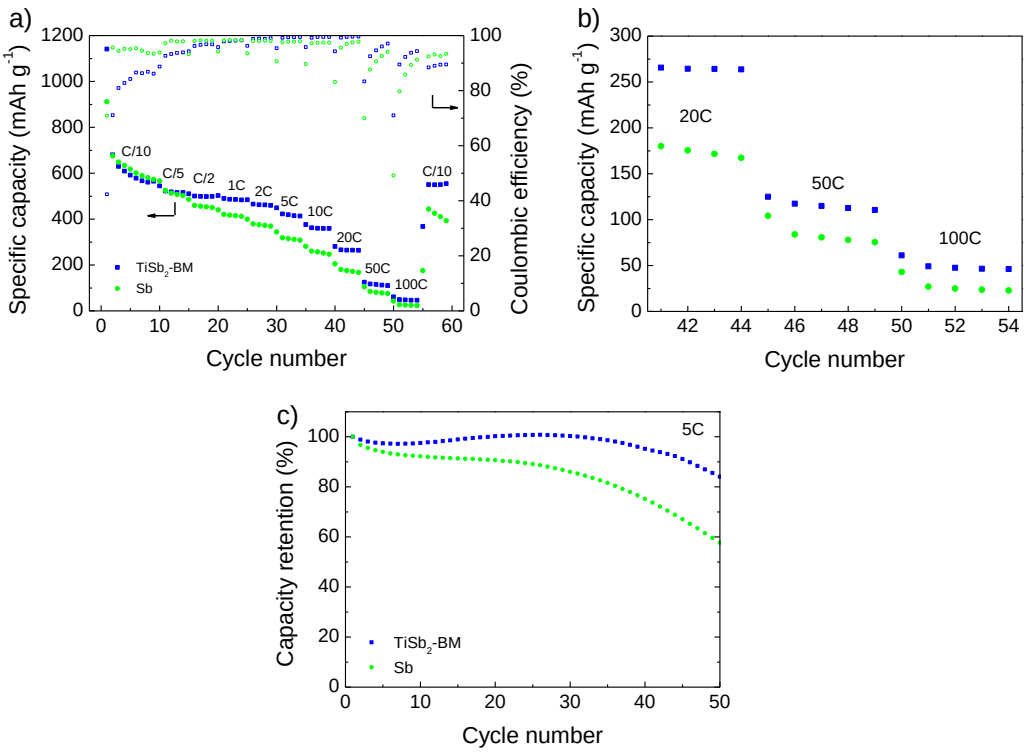

Figure 5.5. Electrochemical characterization of $TiSb_2$ and Sb between 0.05 - 1.5 V *vs.* Li^+/Li: a) Rate capability and b) Zoom of rate capability at high rates and c) Capacity retention.

In order to evaluate the impact of the volume changes on the overall electrode resistance EIS measurements were carried out for both Sb- and TiSb$_2$-based electrodes. Measurements were performed in a two-electrode Swagelok® airtight system using lithium metal as both counter and reference electrode and applying a low sinusoidal amplitude alternating voltage of 10 mV over the OCP and 50 mV at frequencies from 1 MHz to 10 mHz. As it is shown in **Figure 5.6**, in all the stages the resistance of the Sb-based cell is higher compared to that of TiSb$_2$-BM. Moreover, in the course of the cycles, the difference between the resistances of both samples becomes higher. Overall, higher resistance is obtained when Sb material is not embedded in a Ti matrix as it suffers large volume changes during cycling. Thus, it is evident that this mechanical stress directly affects the electrochemical performance of the material owing to the increase of the internal electrode resistance.

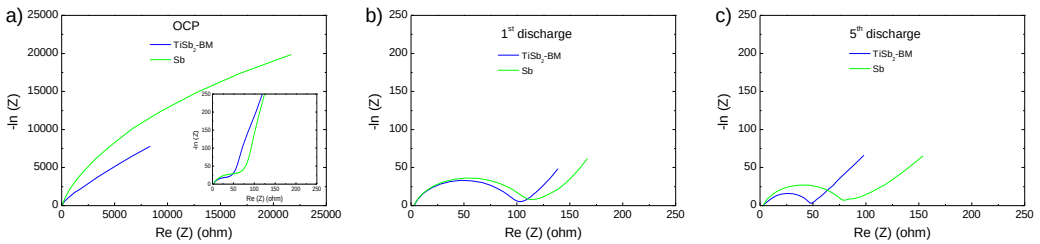

Figure 5.6. EIS measurements at a) OCP, b) 1st discharge and c) 2nd discharge at 0.05 V *vs.* Li$^+$/Li for TiSb$_2$-BM and Sb.

In contrast, owing to the titanium matrix, the aforementioned volume expansion and contractions are buffered in TiSb$_2$-BM and, consequently, it presents improved capacity retention (see **Figure 5.5c**). Overall, TiSb$_2$-BM is capable to deliver high specific capacity values such as 463 mAh g^{-1}, 419 mAh g^{-1}, 360 mAh g^{-1}, 264 mAh g^{-1} and 115 mAh g^{-1} at 2C, 5C, 10C, 20C and 50C, respectively. Moreover, as it is shown in **Figure 5.7**, the charge/discharge profile features observed at low C-rates remain undistorted even at 20C ($t_{discharge} \approx 2$ min). This figure of merit might boost its use as a negative electrode in LICs.

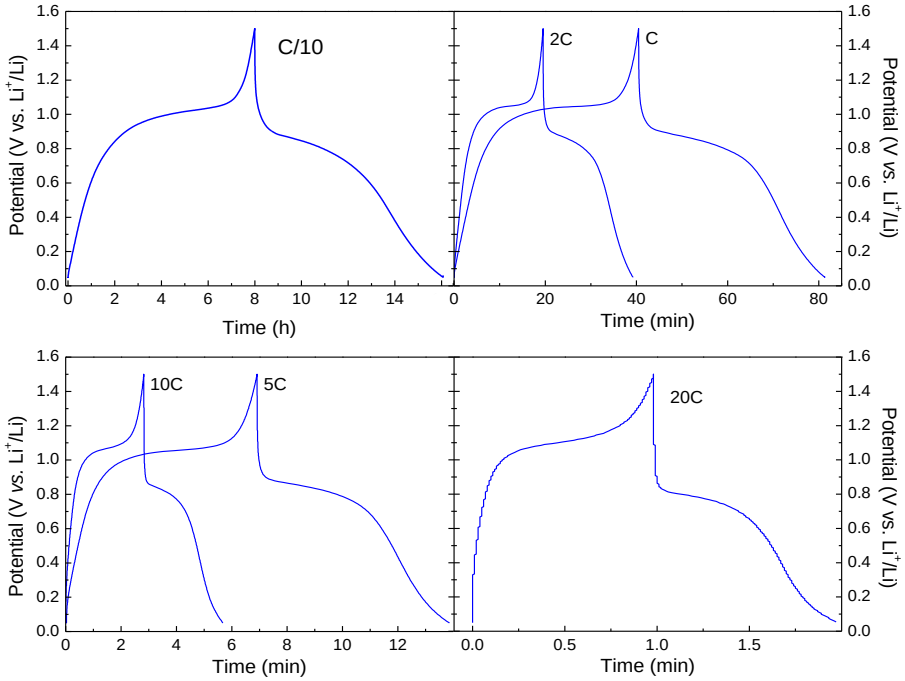

Figure 5.7. GA charge/discharge profiles for $TiSb_2$ at different C-rates between 0.05 - 1.5 V *vs.* Li^+/Li.

5.2.4. Development of LICs

LIC assembly was carried out using $TiSb_2$ as the negative electrode and the previously reported AC derived from olive pits as the positive electrode. They were all assembled in three-electrode Swagelok ® cells under argon atmosphere using 1 M $LiPF_6$ (EC:DMC) as the electrolyte, lithium metal as the reference electrode and fibre glass as separator (Whatman GFB). A key factor for the assembly of a high performing LIC, as mentioned in previous chapters, is an accurate balance of the mass ratio ($TiSb_2$:AC) between electrodes in order to get the maximum capacity output from both materials [20]. As it is shown in **Figure 5.8**, the capacities of both materials diverge along the applied current density range and it is not possible to define a suitable mass ratio which could be valid for all the applied range.

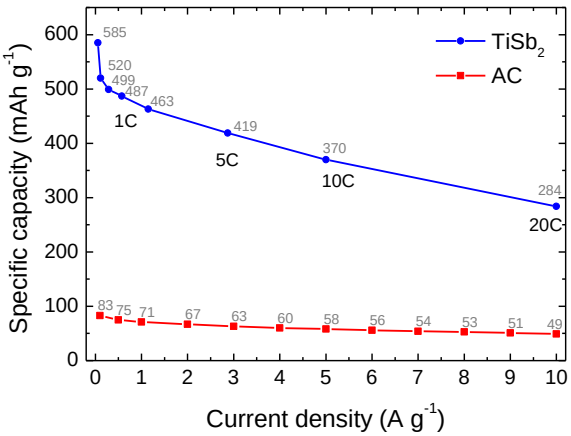

Figure 5.8. Specific capacity values of AC derived from olive pits obtained for the potential range 2 - 4.2 V *vs.* Li$^+$/Li (red) and TiSb$_2$ obtained in the potential range of 0.05 - 1.5 V *vs.* Li$^+$/Li (blue).

Thus, a detailed electrochemical study of various TiSb$_2$:AC mass ratios was carried out in order to find out the best combination. In view of the experimental specific capacities of the electrode materials, 1:1, 1:2 and 1:3 mass ratios were selected, herein denoted as LIC (1:1), LIC (1:2) and LIC (1:3). It was decided not to go beyond 1:3 mass ratio in order not to overuse the negative electrode. Otherwise, it will lead to a fast degradation of the system.

5.2.4.1. Mass ratio study

In order to maximize the output voltage of all studied LICs, both electrodes were pre-conditioned (**Figure 5.9**). TiSb$_2$ was cycled 5 times between 0.05 and 1.5 V *vs.* Li$^+$/Li at 50 mA g^{-1} in order to form the SEI and supply sufficient lithium to compensate for the first cycle irreversibility and then, a cut-off potential of 0.4 V *vs.* Li$^+$/Li was set. For the AC, it was charged to a cut-off potential of 4.2 V *vs.* Li$^+$/Li at 10 mA g^{-1}. After the pre-conditioning step, GA charge/discharge measurements were run for all LICs between 1 - 3.6 V *vs.* Li$^+$/Li at different current densities between 0.05 and 10 A g^{-1} considering

the active mass of both positive and negative electrodes. The voltage window was set owing to the active potential of $TiSb_2$ (~0.6 V *vs.* Li^+/Li) in Li-ion chemistry.

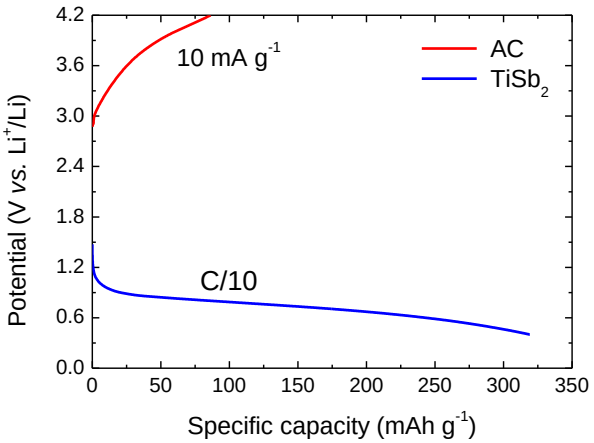

Figure 5.9. Pre-conditioning step for the $TiSb_2$ and AC with a cut-off potential set at 0.4 V and at 4.2 V *vs.* Li^+/Li respectively.

Since the capacity of the negative electrode is much higher than that of the positive electrode through all the applied current density range, as a first approach, a conservative LIC (1:1) was studied. **Figure 5.10** shows the GA charge/discharge profiles of each electrode together with the profile of the LIC system at different applied current densities. At low current densities, *i.e.* 0.1 A g^{-1}, within a discharge time of 30 min, the positive electrode swings from 2 to 4 V *vs.* Li^+/Li showing an ideal symmetric profile indicative of a capacitive storage mechanism. Concurrently, the negative electrode swings in a potential window from 1 to 0.5 V *vs.* Li^+/Li, where the alloying reaction of Li_3Sb occurs during the charge of the LIC and the dealloying reaction of Sb during the discharge of the device. Thus, the storage mechanism of the LIC is given by both non-faradaic and faradaic mechanisms. Increasing the current density from 0.1 A g^{-1} to 1 A g^{-1} decreases the discharge time to 2.5 min while the potential windows of both positive and negative electrodes remain constant. A further 10-fold increase from 1 A g^{-1} to 10 A g^{-1} reduces the discharge time to 9 s. This is a very short discharge-time mainly limited to the EDLC

technology, but this newly developed LIC presents also an excellent performance under these conditions. Although voltage profiles are slightly distorted, ohmic resistance of the overall system remains almost unvaried, the key reason why the LIC performs so well. Still, the potential window of the negative electrode is far too narrow compared to that of the positive electrode, indicative of the capacity limiting nature of the AC electrode. Thus, with the aim of improving the capacity output from the system, an increase in the weight of the AC mass is envisaged while the mass of $TiSb_2$ will be maintained constant.

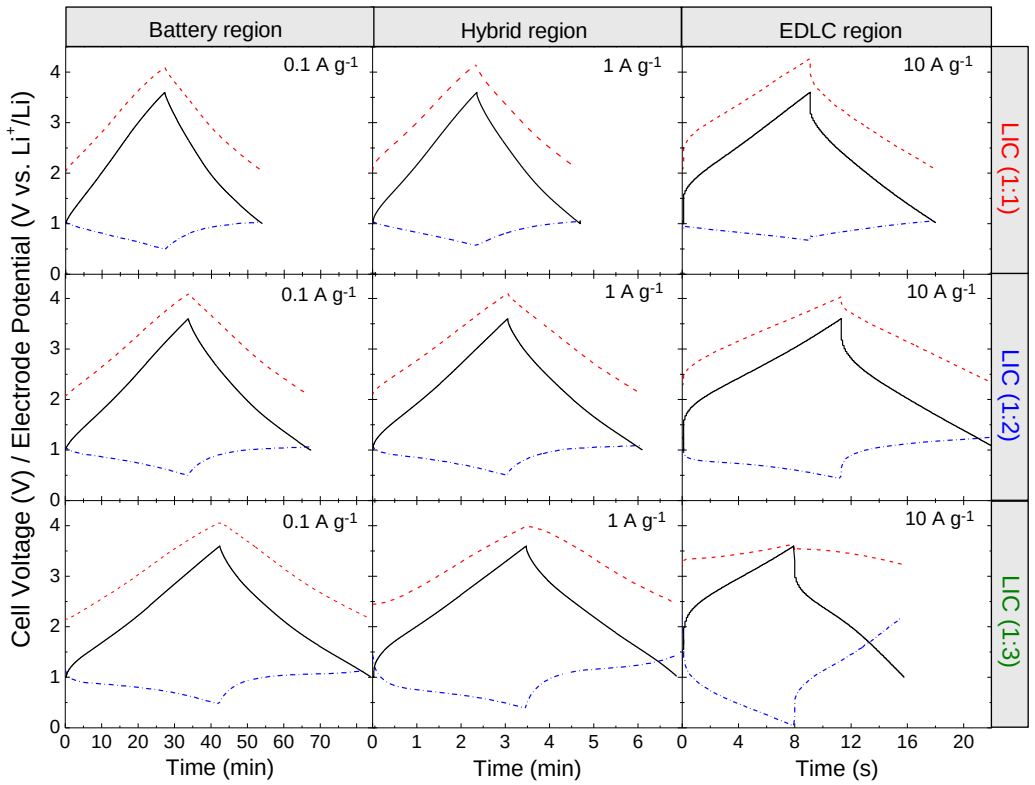

Figure 5.10. GA charge/discharge profiles for full LICs (black straight line), positive (AC, red dash line) and negative ($TiSb_2$, blue dash-dot line) electrodes at different discharge regions.

At first sight, the new LIC (1:2), with double the AC mass relative to the negative electrode, does not infer remarkable changes in the potential window of each electrode and at low current densities these remain similar to those measured in the initial LIC (1:1). However, the AC mass-increase in the positive electrode allows the negative electrode to lengthen its discharge profile and, therefore, to increase its capacity output in all the applied current density range. Thus, in LIC (1:2) a 31% specific capacitance gain, *e.g.* from 55 to 72 F g^{-1} at 1 A g^{-1}, is achieved through all the applied current densities owing to the mass increase of the AC electrode (**Figure 5.10**).

Challenging the limits, a further AC mass loading turned out in LIC (1:3). Similar to LIC (1:2), at low and medium current densities (*i.e.* 0.1 A g^{-1} and 1 A g^{-1}), a gain in the capacitance output of the system is also obtained. Thus, this cell keeps the characteristic linear profile of capacitive systems while increasing the overall capacitance by 49% with respect to the initial LIC (1:1) (**Figure 5.11**). However, at high current densities (*i.e.* 10 A g^{-1}) the negative electrode works within a discharge time of *ca.* 8 s and a potential window that goes from 2.21 to 0.04 V *vs.* Li^+/Li. Moreover, the low minimum potential of the negative electrode can result in lithium plating and further cell short circuit, which makes LIC (1:3) unsafe in this discharge-time region. In addition, due to the poor performance of the negative electrode, the operational potential window of the AC electrode is reduced to 0.4 V (*i.e.* 3.6 - 3.2 V *vs.* Li^+/Li). As a result, at high current densities the intermetallic compound limits the operation of the device, and thus, LIC (1:3) shows worsen electrochemical performance.

As consequence of the higher ESR observed in the profiles of **Figure 5.10** when going to discharge times in the range of seconds, the energy efficiency of LICs should be considered. All $TiSb_2$-based LICs show about 86% and 84% energy efficiency in the battery and hybrid region, respectively, while going to the EDLC region, where ultrafast response is required, the energy efficiency decreases, being about 73% for the LIC (1:1), 71% for the LIC (1:2) and 68% for the LIC (1:3). This lower values are ascribed to the

higher current density applied and in the case of the LIC (1:3), also to the overuse of the negative electrode.

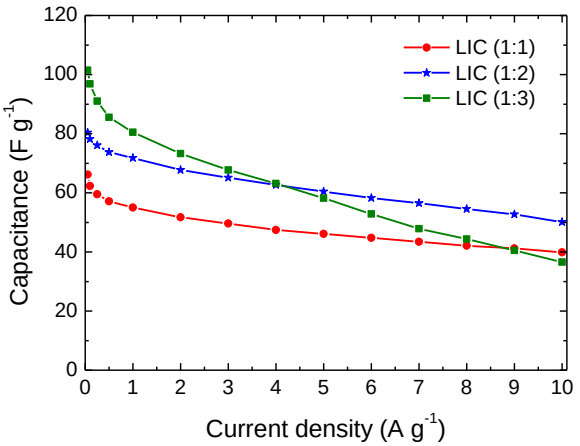

Figure 5.11. Specific capacitance values for each LIC.

Both gravimetric and volumetric energy and power densities of the studied different LICs are reported in **Figure 5.12** respect the total active mass and volume of both electrodes, respectively. For comparison purposes, a symmetric EDLC using the same olive pits derived AC and working in 1.5 M Et_4NBF_4 (ACN) was built. For all the studied LICs a ~5-fold and ~4-fold increase in gravimetric and volumetric energy density terms respectively were obtained. At low power densities, where the discharge time is about 30 min, the higher the AC loading, the higher the specific capacitance output of the system. Thus, while in LIC (1:1) system the energy density is 103 Wh kg^{-1}_{AM}, in the case of LIC (1:2) the energy reaches 129 Wh kg^{-1}_{AM} (an increase of 30%) and 159 Wh kg^{-1}_{AM} (an increase of 60%) in LIC (1:3) (**Figure 5.12a**). This is in good agreement with the previously observed specific capacitance gain, which translates in a higher energy density output (**Equation AI.XXI**).

At medium power densities, where the discharge time is *ca.* 3 min, LIC (1:1) and LIC (1:2) show an excellent gravimetric energy density retention of ~88%, while

LIC (1:3) presents a slightly reduced retention of ~81%. Despite this fact, the overall energy density output of LIC (1:3) is superior to LIC (1:1) and (1:2). Instead, as shown in the Ragone plot, at high power densities, when the discharge time is ~9 s, the mass overloading of the AC electrode limits the overall performance of LIC (1:3). At this point, while LIC (1:1) and LIC (1:2) exhibit energy density values of 52 Wh kg^{-1}_{AM} and 66 Wh kg^{-1}_{AM} respectively, the energy density of LIC (1:3) drops to 45 Wh kg^{-1}_{AM}, limited by the overuse of the negative electrode. The volumetric energy density values, shown in **Figure 5.12b**, follow the same aforementioned trend. Overall, owing to its excellent behaviour at all power density regions in both gravimetric and volumetric terms and its safe performance avoiding any lithium plating or electrolyte decomposition, 1:2 turned out to be the best mass ratio for this $TiSb_2$:AC based LIC. In fact, the energy-to-power performance of LIC (1:2) compares very well with the state-of-the-art as shown in **Figure 5.13** [21–32]. Moreover, it shows a 5-fold increase respect its EDLC counterpart.

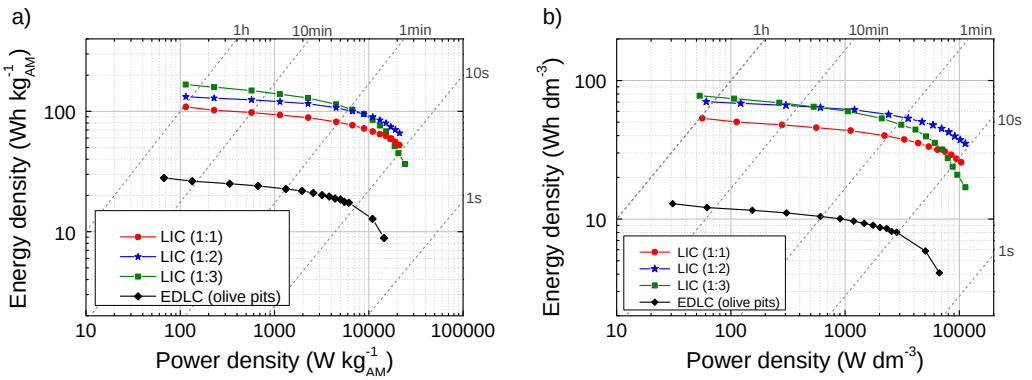

Figure 5.12. a) Gravimetric and b) volumetric Ragone plots comparing all studied LICs to their EDLC counterpart.

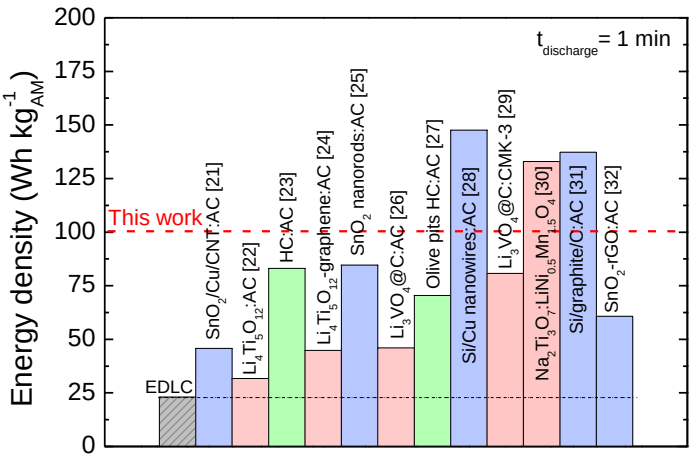

Figure 5.13. Summary of the energy density values of the latest and more challenging LICs at the discharge time of 1 minute. In red alloy-based, in blue oxide-based and in green carbon-based LICs.

Furthermore, the great challenge of LICs is to keep cycle life as close as possible to that of EDLCs. In this sense, when LIC (1:2) is galvanostatically cycled at 10 A g^{-1} constant current ($t_{discharge}$ ≈ 11 s) the system shows a promising capacitance retention of 80% after 10000 cycles (**Figure 5.14**).

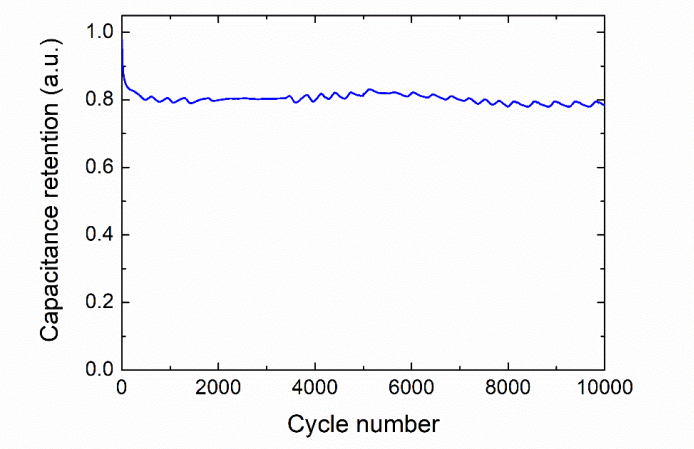

Figure 5.14. Stability test for LIC (1:2) at 10 A g^{-1} within a discharge time of 11 s.

Moreover, if the first 50 cycles are considered as stabilizing cycles, the capacitance retention of the device rises up to 91% after 10000 cycles. In order to gain some insight into the degradation mechanism behind this capacity fading, a post-mortem analysis was carried out.

5.2.4.2. Post-mortem analysis

The XRD pattern in **Figure 5.15** shows the $TiSb_2$-BM material in its discharge stage after cycling where two small broad maxima at 2θ values of 38º and 45º can be ascribed to Li_3Sb. The presence of the alloy demonstrates that the charge storage mechanism of the negative electrode is still governed by the alloying/dealloying reaction.

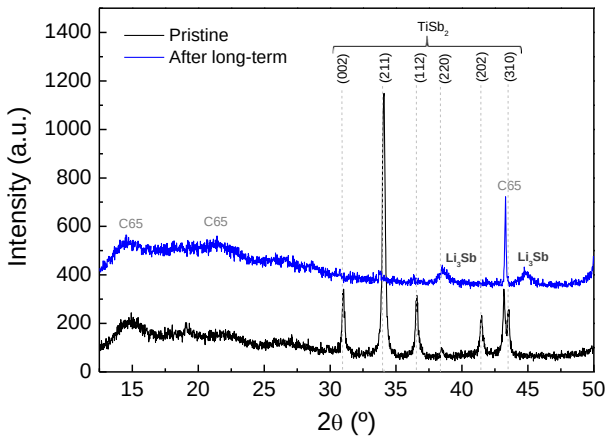

Figure 5.15. Post-mortem analysis of $TiSb_2$ negative electrode after long-term cycling in comparison with the pristine material: XRD patterns.

In addition, SEM images (**Figure 5.16a** and **5.16b**) show that the surface of the cycled electrode presents some cracks due to the mechanical stress suffered upon cycling. Moreover, a relatively thick SEI can also be observed (inset **Figure 5.16b**). Even so, these results highlight the good mechanical properties of the studied $TiSb_2$-BM negative electrode, and thus, the excellent performance of the LIC.

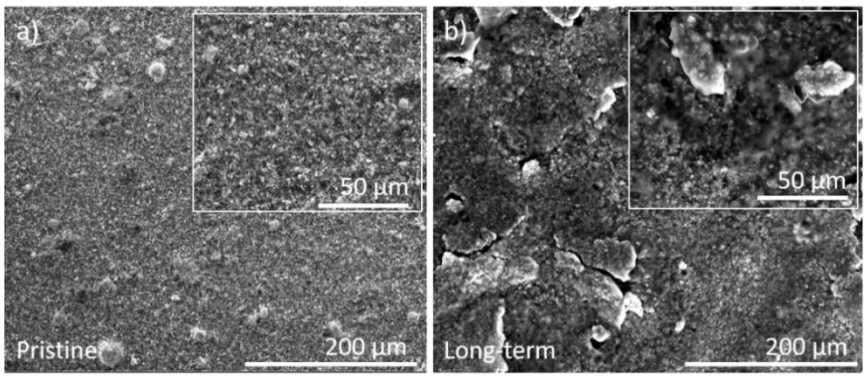

Figure 5.16. Post-mortem analysis of $TiSb_2$ negative electrode after long-term cycling in comparison with the pristine material. SEM images: a) Pristine and b) After long-term electrodes (inset: magnifications).

5.3. Sb-based intermetallic compounds for Na-ion technology

Even that the charge storage reaction mechanism usually changes when moving from Li- to Na-ion chemistry, the electrode engineering issues are mostly equal for both technologies. Thereby, same strategies could be followed. In that context, different Sb-based intermetallic compounds have been also investigated for Na-ion technology. Some of them such as Cu_2Sb and ZnSb were already investigated in Li-ion, while Fe_2Sb was only studied for Na-ion [33].

Nam *et al.* reported on a three-dimensional porous Sb/Cu_2Sb electrode as anode for NIBs. The composite showed good rate capability and cycle life delivering a stable 485 mAh g^{-1} specific capacity over 120 cycles with a CE of 97%. Besides, the capacity retention at 3C was ~70% of the initial one at C/10. Moreover, the reaction mechanism of the compound with Na^+ was proposed by the investigation of *ex-situ* XRD, which confirmed that Cu_2Sb reversibly reacted with sodium [34]. Three-dimensional ZnSb balls composed of ultra-thin nanowire were also proposed as anode material for NIBs. Owing to its small size and unique 3D configuration, ZnSb was able to deliver 400 mAh g^{-1} and 205 mAh g^{-1} at 0.02 A g^{-1} and 0.65 A g^{-1}, respectively [35]. Later, Bagetto *et al.* reported for the first

time on $FeSb_2$ for both Li- and Na-ion technologies. However in order to elucidate the lower reversible capacity obtained in Na-ion (*ca.* 360 mAh g^{-1} *vs.* theoretical 537 mAh g^{-1}) the work was mainly focused on the sodiation reaction mechanism by XRD and ^{57}Fe Mössbauer spectroscopy [33].

Nonetheless, similar to intermetallic compounds studied for Li-ion technology, none of the above-mentioned materials have been utilized as negative electrode in NICs. However, materials such as antimony oxides and sulfides (*i.e.* Sb_2O_3 and Sb_2S_3) have already been successfully implemented. Even that they are not intermetallic compounds, their charge storage mechanism consists also on conversion and alloying reactions (defined below). This is the only reported research done in regard with alloying materials for MICs.

Conversion reaction: $Sb_2O_3 + 6\ Na^+ + 6\ e^- \rightarrow 2\ Sb + 3\ Na_2O$

$Sb_2S_3 + 6\ Na^+ + 6\ e^- \rightarrow 2\ Sb + 3\ Na_2S$

Alloying reaction: $2\ Sb + 6\ Na^+ + 6\ e^- \rightarrow 2\ Na_3Sb$

In view of the high specific capacity values at high current densities, such as 509 mAh g^{-1} at 0.01 A g^{-1} and 265 mA g^{-1} at 5 A g^{-1} for Sb_2O_3 [36], or 750 mAh g^{-1} at 0.01 A g^{-1} and 200 mA g^{-1} at 3.2 A g^{-1} for Sb_2S_3 [37], these compounds were selected to be used as negative electrode in the development of NICs. Unfortunately, similar to other metal oxides and alloying materials, they suffered from capacity fading due to their poor conductivity and large volume expansions. In order to circumvent this limitation authors applied a carbon coating to these materials. This coating made possible the improvement of the electrochemical performance of both materials obtaining capacity values as high as 350 mAh g^{-1} and 591 mAh g^{-1} at 5 A g^{-1} for Sb_2O_3/CFC and Sb_2S_3/CFC, respectively. In order to develop the NICs, carbon fibres (CFs) prepared by an electrospinning method were used as the positive electrode. Once the most appropriate mass ratio was chosen -1:5.9 for Sb_2O_3/CFC:CFs and 1:8.5 for Sb_2S_3/CFC:CFs- NICs were

characterized in 1.5 – 4.3 V cell voltage at different current densities. Energy density values of about 120 Wh kg^{-1}_{AM} at 580 W kg^{-1}_{AM} power density and 65 Wh kg^{-1}_{AM} at 5800 W kg^{-1}_{AM} were obtained with both Sb_2O_3/CFC:CFs and Sb_2S_3/CFC:CFs devices. Moreover, both systems showed a capacitance retention of 90% after 4000 cycles in the case of Sb_2O_3-based NIC and after 3500 cycles in the case of the Sb_2S_3-based one [38].

Motivated by these work on NICs together with the outstanding results obtained with $TiSb_2$ intermetallic compound in Li-ion technology, its potential use in Na-ion chemistry has also been explored.

5.3.1. Material and electrode preparation of $TiSb_2$ samples

Scheme 5.2 shows the preparation route for the samples studied in Na-ion. $TiSb_2$ alloy was prepared by placing a mixture of the stoichiometric amounts of Sb (ABCR, 100 mesh, 99.5% purity) and Ti (ABCR, 325 mesh, 98.7% purity) in a tubular oven and heating it at 900° C during 12 h under an argon flow. The pristine $TiSb_2$ was milled in a Pulverisette 7 within some isopropanol and using 5 mm ZrO_2 balls in the 40:1 weight ratio during 2h ($TiSb_2$-BM sample). In a following step, the $TiSb_2$-BM was carbon coated by ball milling with 7 wt% C-nergy™ Super C65 carbon black (Imerys Graphite & Carbon) in a Fritsch Pulverisette 5 using ZrO_2 jars and balls in the 30:1 weight ratio ($TiSb_2$-C sample). Two different ball-milling times, *i.e.* 30 min ($TiSb_2$-C30min) and 20 h ($TiSb_2$-C20h), were set in order to study the effect of the milling time on the preparation of an appropriate carbon coating as well as on the purity of the $TiSb_2$ phase.

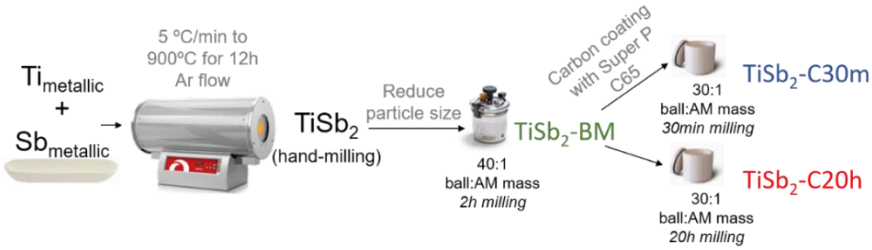

Scheme 5.2. Synthesis route for the $TiSb_2$ intermetallic compounds.

The olive pits derived AC already explained in **Chapter 2** – **Section 2.3.1** was used as the positive electrode in final NICs.

In order to prepare the laminates for further electrochemical characterization, $TiSb_2$-based samples were prepared following the same procedure as for the $TiSb_2$ electrode for LICs, using a $TiSb_2$:binder:C65 mass ratio of 80:10:10. In order to make a fair electrochemical comparison a Sb-based electrode was also prepared following the same procedure. While the AC was prepared by 95:5 AC:binder mass ratio as previously explained. Then, all slurries were laminated, in this case, all onto aluminum foil, and were transferred into a vacuum oven and dried at 80 ºC under constant vacuum for 12 h before 1.13 cm^2 circular electrodes were cut out. The weight of the electrodes was around 1 mg cm^{-2} for all of them.

5.3.2. Physicochemical characterization of $TiSb_2$ samples

Figure 5.17a shows the XRD corresponding to each of the $TiSb_2$ based material. All of them can be indexed in a tetragonal system *I4/mcm* [39]. At 2θ value of 28º a secondary crystalline phase that corresponds to Sb appears after the first ball milling process. The amount of crystalline Sb, calculated from Rietveld refinement, was 18 wt% for $TiSb_2$-BM and 8 wt% and 21 wt% for the $TiSb_2$ samples carbon coated during 30 min and 20h, respectively ($TiSb_2$-C30m and $TiSb_2$-C20h, respectively). The calculations are based on the observed XRD peaks, thus, possible contributions from amorphous phases are not considered. In any case, while $TiSb_2$-C30m is an almost pure material, $TiSb_2$-C20h has an important amount of Sb that later might impact in the electrochemical behaviour. In order to avoid this additional Sb amount in the sample, a different carbon coating technique was also explored. The $TiSb_2$-BM material was hand-mixed with malic acid and then carbonized up to 265ºC. However, the XRD pattern in **Figure 5.17b** still reveals the presence of the Sb phase. With the aim of removing that Sb content, the sample was washed with acetic acid. Although it is confirmed by XRD ($TiSb_2$-Cmalic-w) that the main diffraction maxima of Sb at 2θ values of 28º and 43º disappeared, when the sample

was electrochemically characterized, secondary phases appeared as a result of parallel reactions. Hence, due to its more difficult preparation method and the need to better understand its electrochemistry, this sample was discarded and the work was focused on the sample with the carbon coating obtained by commonly used Super C65 conductive carbon and a mechanical ball milling process.

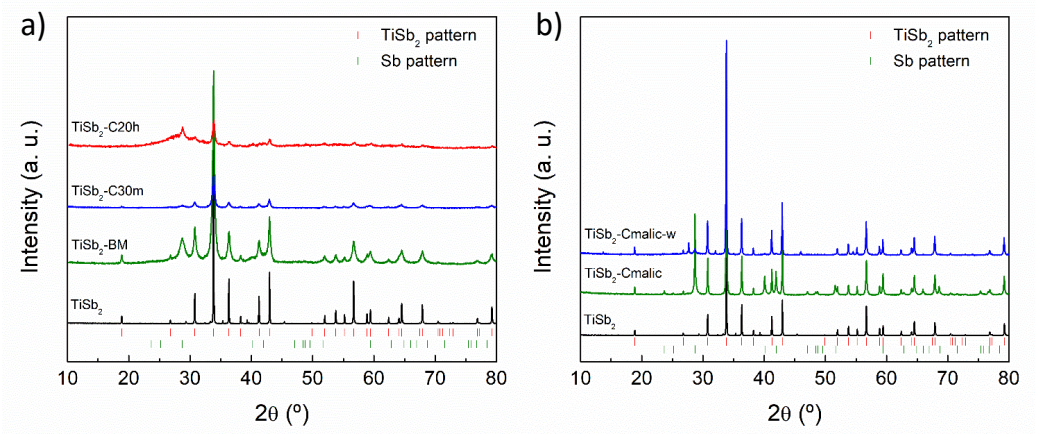

Figure 5.17. XRD patterns of the $TiSb_2$ based samples studied: a) $TiSb_2$, $TiSb_2$-BM, $TiSb_2$-C30m, and $TiSb_2$-C20h. Pristine $TiSb_2$ and the $TiSb_2$ and Sb patterns have been added for comparison. b) $TiSb_2$ samples coated with carbonized malic acid.

SEM images of the different materials are shown in **Figure 5.18.** The solid-state synthesis leads to large particles with sizes between a few and several tenths of microns fused in large agglomerates (**Figure 5.18a**). Meanwhile, after the ball milling processes, particle sizes are reduced to the sub-micrometer range, between approximately 100 and 800 nm, and agglomerated in few microns sized grains (**Figure 5.18b, 5.18c**, and **5.18d**). Crystallite sizes, calculated from Scherrer equation (**Equation AI.1.1**), decrease from almost 690 nm in the pristine $TiSb_2$ to around 17 nm after milling.

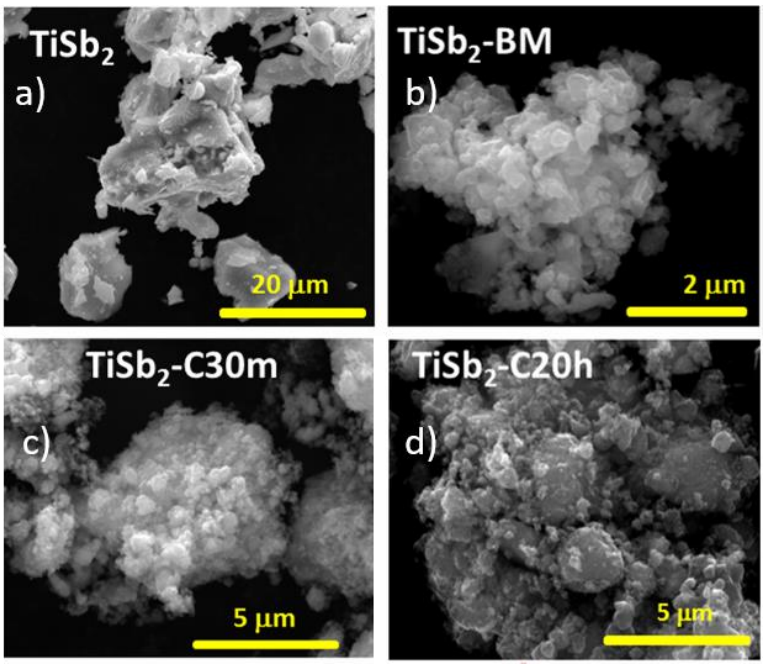

Figure 5.18. SEM images of the studied $TiSb_2$ based samples: a) $TiSb_2$, b) $TiSb_2$-BM, c) $TiSb_2$-C30m, and d) $TiSb_2$-C20h.

TEM images of $TiSb_2$-C30m (**Figure 5.19a**) and $TiSb_2$-C20h (**Figure 5.19b**) samples confirmed the presence of nanometer sized crystalline domains after ball milling and carbon coating processes. In the case of $TiSb_2$-C20h sample, the distance observed between lattice fringes corresponds to the (200) plane of $TiSb_2$ structure (**Figure 5.19c**). Moreover, TEM images revealed that both larger and smaller particles have a continuous carbon coating with thicknesses ranging from around 2 to 20 nm (**Figure 5.19c** and **5.19d**).

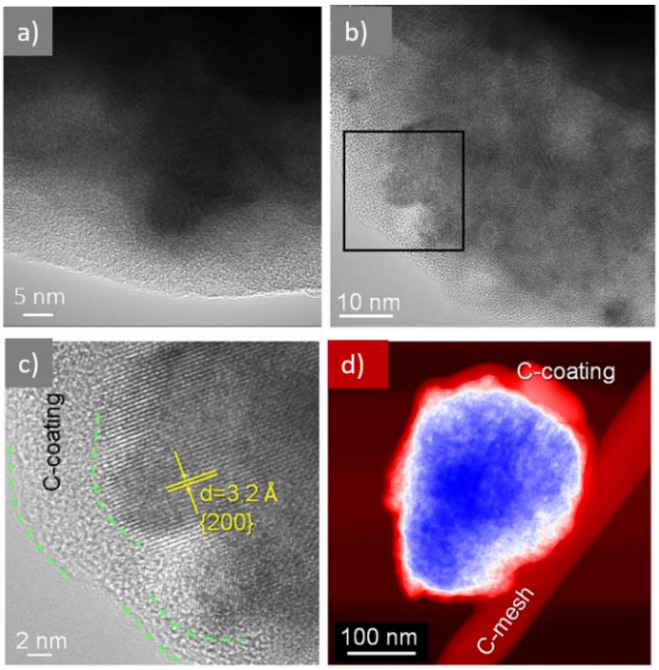

Figure 5.19. TEM images showing carbon coated a) $TiSb_2$-C30m, b) and c) $TiSb_2$-C20h particles with crystalline nanodomains and continuous carbon coating, and d) Colored STEM image of a representative $TiSb_2$-C20h carbon coated particle. The carbon mesh corresponds to the sample holder. The $TiSb_2$ is blue and carbon in red.

5.3.3. Electrochemical characterization of $TiSb_2$ samples

In order to electrochemically characterize all the studied materials (*i.e.* $TiSb_2$-BM, $TiSb_2$-C30m and $TiSb_2$-C20h) GA charge/discharge measurements were first performed at low rates (*i.e.* C/10) using sodium metal as counter electrode in a CR2032 coin cell configuration and 1 M $NaClO_4$ (EC:PC) + 5 wt% FEC as the electrolyte. As expected, **Figure 5.20** reveals a huge capacity fading for the $TiSb_2$-BM sample, the reason why additional carbon coated samples were also prepared. As previously shown by XRD refinement, the milling time has a strong impact on the composition. After coating $TiSb_2$ with 7 wt% of carbon during 30 minutes, the $TiSb_2$ structure remained as the main component with only a small crystalline Sb fraction (8 wt%). The $TiSb_2$-C30m sample

exhibited slightly better electrochemical behaviour than that of the bare ball milled sample, starting at 276 and 176 mAh g^{-1} in the initial cycle and showing good cycling stability, with a slight increase up to 220 mAh g^{-1} at the 100th cycle. The CE was improved from 53% to 64% in the first cycle and after 10 cycles it remained constant at 99%, slightly over the 98% of the CE obtained by $TiSb_2$-BM. $TiSb_2$-C30m sample was able to retain about 50% of the initial discharge (desodiation) capacity after 285 cycles.

Likewise, the sample coated with 7 wt% carbon during 20h, $TiSb_2$-C20h, increases its Sb initial fraction to 21 wt% and exhibited improved electrochemical behaviour. This sample delivered higher specific capacity in the first charge and discharge cycle, 405 and 198 mAh g^{-1} respectively, and reached 225 mAh g^{-1} after 20 cycles. Improved capacity retention was also observed, maintaining more than 80% of its initial discharge capacity for about 285 cycles. The initial CE was of only 49%, indicating that a larger amount of sodium is trapped in the electrode, but after 20 cycles it reaches a CE of 99%. Since the relative amount of carbon used in the milling process is the same for both $TiSb_2$-C30m and $TiSb_2$-C20h samples, the contribution coming from the amorphous carbon coating should be similar. The higher irreversible charge loss in the initial cycles could be a result of the smaller particle size, therefore larger area and larger extent of SEI formation.

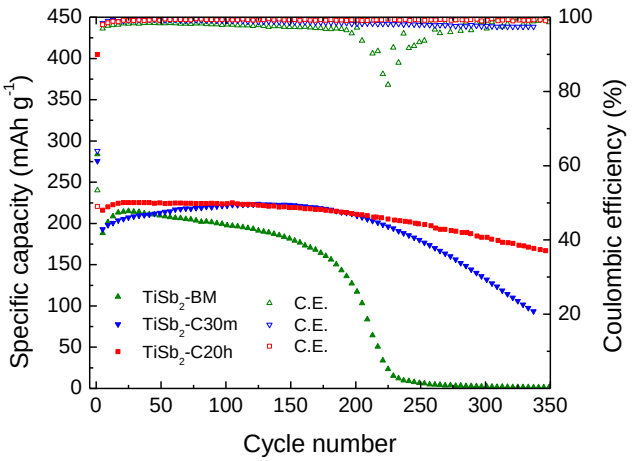

Figure 5.20. Specific capacity and CE of $TiSb_2$-BM, $TiSb_2$-C30m, and $TiSb_2$-C20h samples.

In spite of the improved cycling stability resulting from a long time carbon coating, the specific capacity is still lower than the expected. To better understand the reasons why a complete reaction is not achieved, the first charge/discharge cycle of $TiSb_2$-C20h at C/30 was studied by *operando* XRD in an in-house fabricated cell (**Figure 5.21**).

At the beginning of the charge, all peaks correspond to crystalline $TiSb_2$ and Sb phases. No peak shift is observed for both phases and the intensities remain virtually constant until the beginning of the plateau at *ca.* 0.5 V. The Sb phase clearly disappears (see maxima at 2θ values of 33.2°, 46.5° and 48.8°) as new peaks corresponding to the hexagonal Na_3Sb phase appear at 2θ values of 24.7°, 38.9° and 39.9°. The last two diffraction maxima overlap with the most intense $TiSb_2$ peak at 39.6º, which does not seem to disappear during cycling.

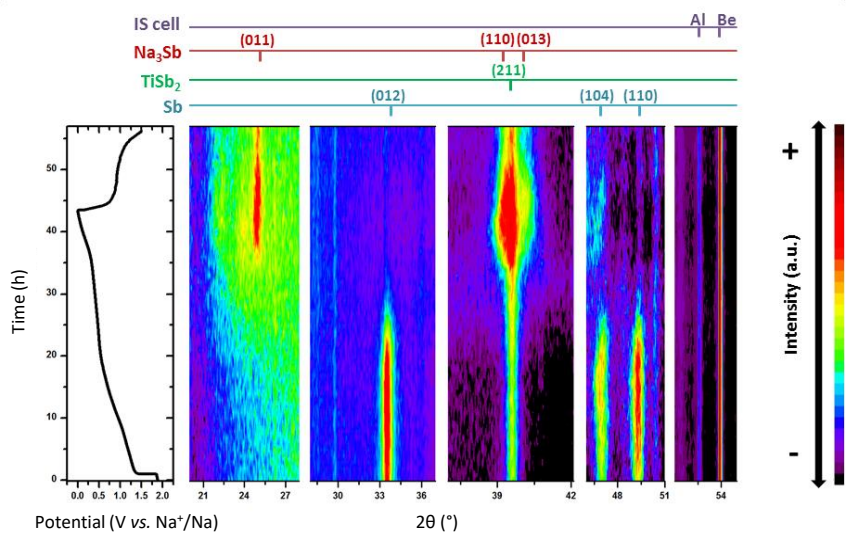

Figure 5.21. *Operando* evolution of the XRD pattern recorded at C/30 rate (right), and the corresponding voltage profile (left).

During this *operando* measurement unreacted $TiSb_2$ remains even after the first cycle. According to Baggetto *et al.,* the lack of a full reaction observed for a η-Cu_6Sn_5 intermetallic compound, which shows around a 32% of its theoretical capacity, is

attributed to the steric hindrance of Na^+ diffusion inside the structure. Moreover, an optimum particle size of about 10 nm was estimated to fully utilize its capacity. A mixture of η-Cu_6Sn_5 and Sn in 66:34 wt% ratio was also proposed to increase the reversible stored capacity [40]. Similarly, a lower capacity than that expected for $TiSb_2$ is also observed, around 40% of the theoretical value, and persistent unreacted cores. Local *ex-situ* STEM and semi quantitative energy dispersive X-ray (EDX) analysis performed on charged electrodes confirmed that the highest Na^+ concentration is located on the outer shell of the particles, whereas in the core the concentration is much lower (**Figure 5.22**). During discharge, Na_3Sb is transformed to amorphous Sb. Since part of the $TiSb_2$ phase remained unreacted, it is difficult to confirm whether the reverse reaction forms crystalline $TiSb_2$ from Ti and Na_3Sb upon desodiation. Nanometer sized $TiSb_2$ particles should achieve specific capacities closer to the theoretical values, however, finding the proper precursors and synthetic route might be an issue.

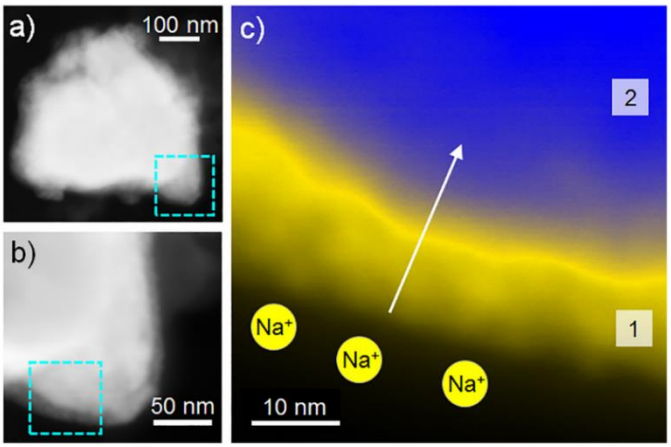

Figure 5.22. a) STEM image of a representative $TiSb_2$ particle in the charged state (sodiated), b) zoom in on the edge of the particle in a), c) zoom in on the edge of the particle in b), the image has been colored according to the Na^+ concentrations found by EDX, ranging from yellow (more Na) to blue (less Na). Local EDX quantification results: point 1, (Na:Ti:Sb)=0.6:1:1.3 and point 2, (Na:Ti:Sb)=0.3:1:1.8, where the concentrations have been normalized with respect to the Ti atomic %.

With that aim, $TiSb_2$-based carbon coated samples ($TiSb_2$-C30m and $TiSb_2$-C20h) and bare Sb electrodes were fabricated and electrochemically characterized. The latter was prepared in order to make a fair comparison owing to the 21 wt% of crystalline Sb content in the $TiSb_2$-C20h sample. This way, it would be possible to compare $TiSb_2$ ($TiSb_2$-C30m), $TiSb_2$+Sb ($TiSb_2$-C20h) and Sb electrode materials. **Figure 5.23** shows the rate capability of the three different materials assembled in three-electrode Swagelok® cells using oversized AC as counter electrode, sodium metal as reference and 1 M $NaClO_4$ (EC:PC) + 5% FEC as the electrolyte. $TiSb_2$-C20h shows a CE of 55%, while $TiSb_2$-C30m shows a CE of 66% and Sb of 74%. The lower CE of $TiSb_2$ samples respect Sb is ascribed to their lower particle size and first conversion reaction from $TiSb_2$ to Sb metal. In the case of the ball milled $TiSb_2$, $TiSb_2$-C20h shows the lowest CE owing to its reduced particle size. In the following charge/discharge cycles, similar capacity values are obtained for $TiSb_2$-C20h and Sb electrodes, while at high current densities (*i.e.* >2C), Sb electrode shows a huge capacity fading. This can be attributed to the larger particle size and hence less buffered volume expansions. Meanwhile, $TiSb_2$-C30m shows significantly lower capacity values in all the studied C-rates.

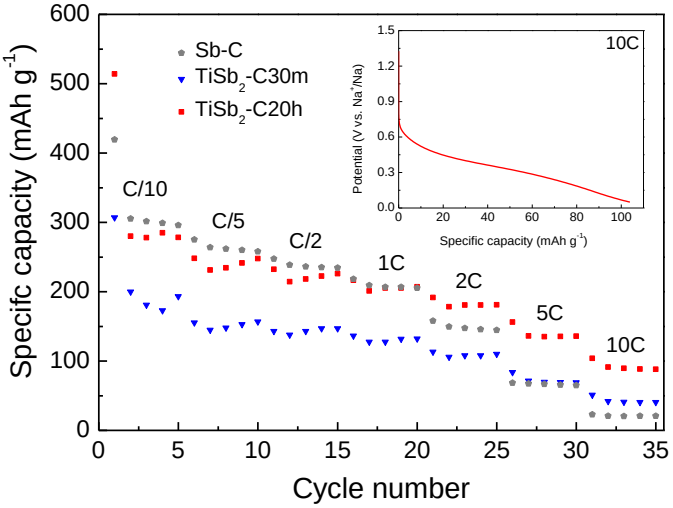

Figure 5.23. Rate capability between 0.05 - 1.5 V *vs.* Na^+/Na for the Sb-C, $TiSb_2$-C30m and $TiSb_2$-C20h samples. Inset: charge profile of $TiSb_2$-C20h at 10C.

Thus, these results show that the Sb content in the $TiSb_2$-C20h sample benefits the material in terms of specific capacity, while the titanium matrix is compulsory when long cycle life and fast response are needed. Thereby, the high capacity at high current densities (*i.e.* 100 mAh g^{-1} at 10C) and the low working sloping type potential (<0.4 V *vs.* Na^+/Na) are encouraging to test $TiSb_2$-C20h as negative electrode in NICs.

5.3.4. Development of NICs: the role of the binder towards enhancing cycle life

One of the main challenges of hybrid capacitors is to match the excellent cycle life of EDLCs. Thus, an accurate electrode design is needed to obtain a NIC that performs as good as an EDLC in the high power region. It has been previously demonstrated that stability of NICs is affected by the binder selection and so it is necessary to use a material not only for holding the active material particles within the electrode but also that buffers the mechanical stress during cycling [42].

PVdF has been widely used in commercial batteries owing to its good chemical, electrochemical and thermal stability [43]. Nevertheless, it is relatively expensive and needs the use of volatile organic solvents to prepare the slurries, such as NMP, that are toxic and expensive [44]. Moreover, the poor flexibility of PVdF is not sufficient to face the large volume changes of alloying reactions [45]. In contrast, alternative water-soluble, environmentally friendly and low-cost natural polymers, such as carboxymethyl cellulose (CMC), sodium alginate (Na-Alg) or poly(acrylic acid) (PAA), have been recently introduced as binders [46,47]. All these binders are characterized by their high cross-linking nature derived from the hydrogen bonds created between the carboxyl groups of the binder and the hydroxyl groups of the surface of the active material [48]. All the three above-mentioned binders are defined by a 1D linear chain nature. CMC is based on a cellulose backbone, whereas PAA on a polyethylene one. It determines the higher rigidity of CMC in comparison with both Na-Alg and PAA, which their nature

makes them much more flexible [49]. The higher concentration of carboxylic functional groups of PAA allows creating a higher cross-linkage network, while Na-Alg -being more polar than CMC- can ensure better interfacial interaction between the binder and the active material [42]. It is known that the combination of CMC with Na-Alg or PAA creates a 3D polymeric network owing to the condensation reaction between the polymers. At this point, the higher rigidity of CMC plays a key role in the formation of a suitable 3D network [50]. This matrix allows uniformly accommodating the active material and mitigate the mechanical stress induced by the large volume changes, thus, increasing the capacity retention of the active material and providing an overall better electrochemical performance [44,48,51,52]. For that reason, CMC, Na-Alg and combinations between CMC-Alg and CMC-PAA were selected to set these different $TiSb_2$-C20h battery-type electrodes for NICs.

Figure 5.24 shows the rate capability study of $TiSb_2$-C20h electrodes prepared using the above-mentioned binder formulations, between 0.05 and 1.5 V *vs.* Na^+/Na from C/5 to 20C. It is shown that for all the studied C-rates the electrodes prepared with Na-Alg are the ones that perform the worst, delivering 185 mAh g^{-1} at 1C and 55 mAh g^{-1} at 10C, while the electrodes prepared with CMC exhibit 205 mAh g^{-1} at 1C and 88 mAh g^{-1} at 10C. Instead, the electrodes prepared with the combination of CMC-Alg and CMC-PAA, show better electrochemical performance providing 248 mAh g^{-1} and 235 mAh g^{-1} at 1C and 81 mAh g^{-1} and 88 mAh g^{-1} at 10C respectively owing to their higher cross-linkage network. Despite the better suitability of CMC-Alg and CMC-PAA based formulations at low rates, at higher rates there are no significant differences among the studied binders. Thus, three different NICs were assembled in three electrode airtight Swagelok® cells, hereafter denoted as NIC (CMC), NIC (CMC-Alg) and NIC (CMC-PAA), where the negative electrode was $TiSb_2$-C20h in the corresponding formulation, the positive electrode an AC derived from olive pits and the reference electrode a sodium metal disc. The AC was prepared by casting onto aluminum foil a slurry with an AC:PVdF composition ratio of 95:5.

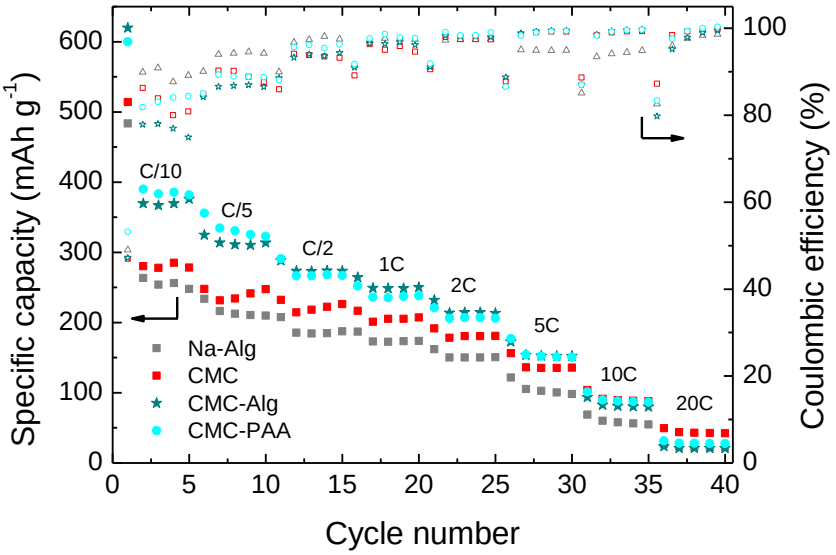

Figure 5.24. $TiSb_2$-C20h rate capability between 0.05 - 1.5 V *vs.* Na^+/Na using different binders.

In order to set the correct mass ratio between the active material of the negative and positive electrodes ($TiSb_2$:AC), the specific capacities of all materials at different current densities are summarized in **Figure 5.25**. As it is shown, capacity diverges along the applied current density and, thus, it is not possible to define a suitable mass ratio for the whole range. Following the same criteria as for $TiSb_2$-based LICs, a mass ratio of 1:1 was set, partially limiting the usage of the $TiSb_2$-C20h negative electrode in order to increase the durability of the system.

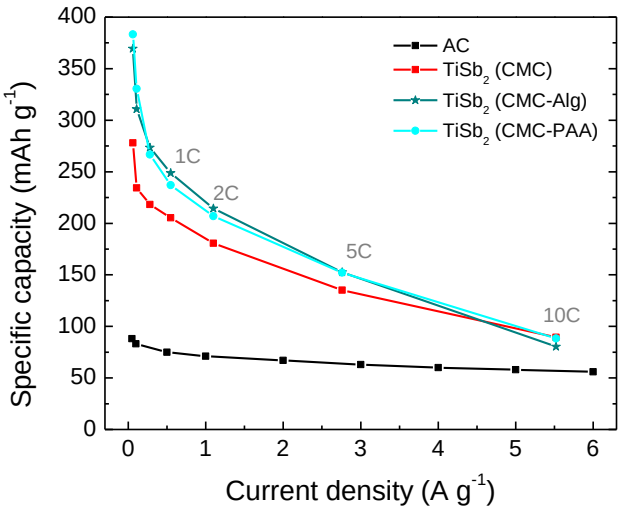

Figure 5.25. Specific capacity values of activated carbon derived from olive pits obtained in the potential range of 2 - 4.2 V *vs.* Na^+/Na (black) and $TiSb_2$-C20h values obtained in the potential range of 0.05 - 1.5 V *vs.* Na^+/Na (red-square for CMC, dark blue-stars for CMC-Alg, light blue-dots for CMC-PAA).

With the aim of maximizing the output voltage of all studied NICs, each electrode was pre-conditioned in order to form the SEI and supply sufficient sodium to compensate the first cycle irreversibility. $TiSb_2$-C20h (CMC), $TiSb_2$-C20h (CMC-Alg) and $TiSb_2$-C20h (CMC-PAA) were cycled 5 times between 0.05 and 1.5 V *vs.* Na^+/Na at C/10 and a cut-off potential of 0.4 *vs.* Na^+/Na was set. In the case of the AC, it was charged to a cut-off potential of 4.2 V *vs.* Na^+/Na at 10 mA g^{-1}. After the pre-conditioning of the electrodes, NICs were GA charged/discharged between 1 and 3.6 V at different current densities between 0.05 - 8 A g^{-1}. **Figure 5.26** shows the galvanostatic profiles of both positive and negative electrodes as well as the profile of the overall NIC. At low current densities, *i.e.* 0.1 A g^{-1}, within a discharge time of *ca.* 30 min, the three NICs show very low ESR, thus, very low voltage drop. In all cases, the AC shows an ideal symmetric profile owing to its capacitive storage mechanism that swings from about 2.0 to almost 4.2 V *vs.* Na^+/Na, while $TiSb_2$-C20h (CMC) works in a narrow potential window from

ca. 1.0 to 0.6 V *vs.* Na^+/Na. A 10-fold increase in the applied current density (*i.e.* 1 A g^{-1}), reduces the discharge time to ~2 min, while the ESR increase is negligible and the profiles of each of the electrodes do not suffer remarkable changes. At high current densities, differences among the various systems are more noticeable. Regarding negative electrodes, $TiSb_2$-C20h (CMC-Alg) presents much lower polarization than its $TiSb_2$-C20h (CMC) and $TiSb_2$-C20h (CMC-PAA) counterparts due to the lower ohmic resistance. Thus, while the discharge time of NIC (CMC-Alg) at 8 A g^{-1} is 12 s, the discharge time of NIC (CMC) and NIC (CMC-PAA) are 7 and 9 s, respectively.

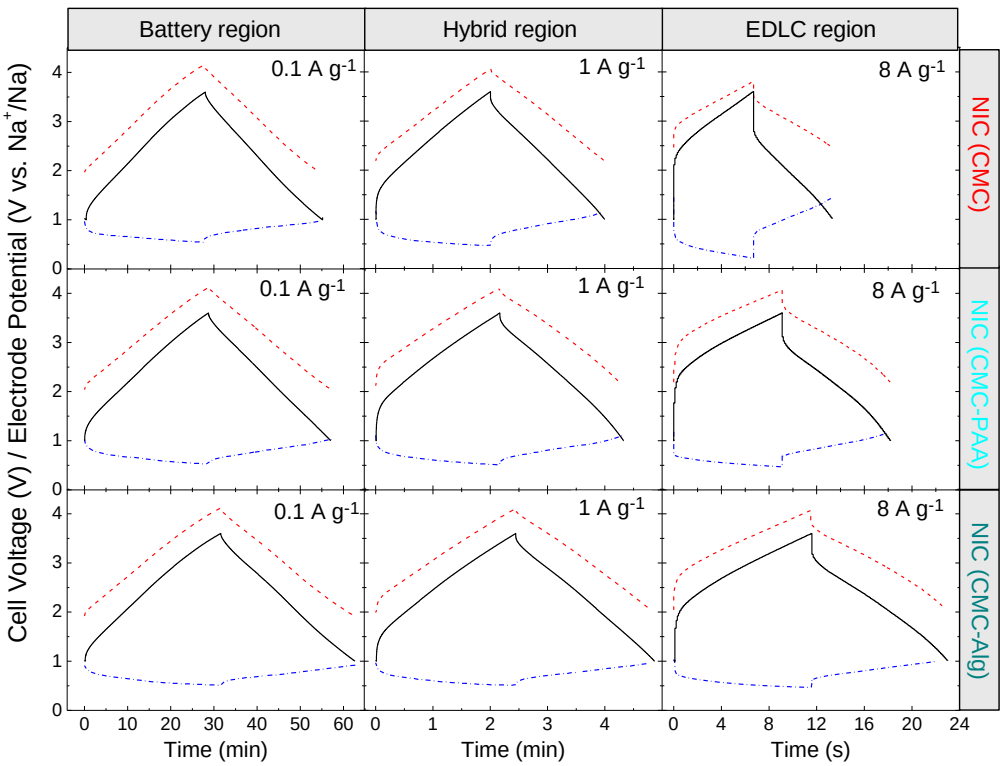

Figure 5.26. Galvanostatic charge/discharge profiles of the positive electrode (AC, dash red line), the negative electrode ($TiSb_2$-C20h, dash-dot blue line) and the full cell (straight black line) of each NIC.

Nevertheless, some ESR is observed in **Figure 5.26** for all the studied NICs, thus, energy efficiency should also be mentioned. All the $TiSb_2$-based NICs show about 88% and 86% energy efficiency in the battery and hybrid region, respectively, while going to the EDLC region, where ultrafast response is required, the energy efficiency is about 72 - 78%. This lower value is ascribed to the higher current density applied and engineering issues already mentioned also for LICs. Nonetheless, it is clearly observed that the selection of the binder in the preparation of the negative electrode plays a key role at the EDLC discharge time region. The ESR is notoriously reduced when CMC is combined with PAA or Alg and hence, the energy efficiency is enhanced, going from 72% for NIC (CMC) to 76% and 78% for NIC (CMC-PAA) and NIC (CMC-Alg), respectively.

From the above described NIC profiles, energy and power density values were calculated and represented in a Ragone plot (**Figure 5.27a**). Numeric values for energy-to-power ratios respect to the discharge time are summarized in **Table 5.1**. As it can be seen, at the low power density region, *i.e.* 114 W kg^{-1}_{AM}, where the discharge time is ~1 h, the difference in terms of energy density is negligible, ranging from 115 Wh kg^{-1}_{AM} to 132Wh kg^{-1}_{AM} for all the different systems. When increasing the applied current density and discharge time decreases to few minutes, differences start to arise, but it is at the highest power density region (*i.e.* ~20 kW kg^{-1}_{AM}), within discharge times of few seconds, where the binder effect is clearly notorious. In the latter regime, NIC (CMC-Alg) delivers the highest energy density value, 49 Wh kg^{-1}_{AM}, while NIC (CMC) and NIC (CMC-PAA) deliver 27 Wh kg^{-1}_{AM} and 37 Wh kg^{-1}_{AM}, respectively. Thus, the NIC prepared by the mixture of CMC and Na-Alg binder gives the best energy-to-power values: more than 6-times the energy density given by its EDLC counterpart -built using the same AC in both positive and negative electrodes in 1.5 M Et_4NBF_4 (ACN) electrolyte– for the entire studied power density region. Nevertheless, to develop a competitive NIC, apart from excellent energy-to-power ratios, a cycle life approaching that of EDLCs is needed. For that purpose, the selection of an appropriate binder is crucial. **Figure 5.27b** shows a comparison of the capacitance

retention of the hybrid systems built using different binder formulations. After 1000 cycles at a current density of 5 A g^{-1} ($t_{discharge}$ = ~20 s) the systems using CMC-Alg and CMC can only retain 23% and 10%, respectively, of their initial capacitance while CMC-PAA based system is able to keep up to 63% of the initial capacitance. Thus, the cross-linking nature of PAA, which provides higher flexibility, allows –in combination with CMC– increasing the capacitance retention of the overall NIC up to 53% compared to its NIC (CMC) counterpart.

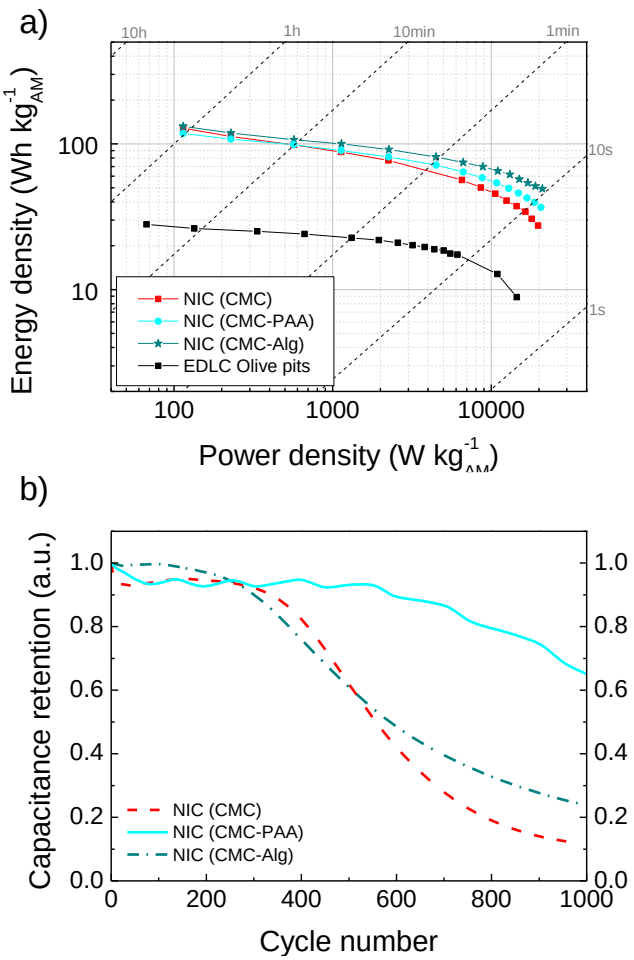

Figure 5.27. a) Ragone plot with all studied NICs and their EDLC counterpart based on olive pits derived ACs. b) Capacitance retention of each NIC at constant current of 5 A g^{-1}.

Table 5.1. Energy-to-power density values of the studied NICs at different discharge times.

	$t_{discharge}$					
	~1 h		~2 min		~10 s	
NICs	**Wh kg_{AM}^{-1}**	**W kg_{AM}^{-1}**	**Wh kg_{AM}^{-1}**	**W kg_{AM}^{-1}**	**Wh kg_{AM}^{-1}**	**W kg_{AM}^{-1}**
NIC (CMC)	128	114	67	4401	27	19760
NIC (CMC-Alg)	132	114	81	4486	49	21052
NIC (CMC-PAA)	118	114	72	4500	37	20625

In summary a NIC using $TiSb_2$ intermetallic compound as negative electrode that is able to store energy densities as high as 72 Wh kg^{-1}_{AM} and 37 Wh kg^{-1}_{AM} at 4500 W kg^{-1}_{AM} and 20625 W kg^{-1}_{AM} power densities, respectively, combined with a good capacitance retention of 63% after 1000 cycles at constant current of 5 A g^{-1} has been developed.

5.4. Comparative evaluation between $TiSb_2$-based LIC & NIC

In order to make a comparison between $TiSb_2$-based LIC and NIC devices, the systems showing the best overall performance are summarized in the Ragone plot of **Figure 5.28**. The best LIC is the one within a mass ratio of 1:2 and in the case of NICs the system which the negative electrode is formulated with CMC-PAA binder. The energy-to-power values show that at low current densities, despite the higher charge storage capacity of the material in Li-ion chemistry (see **Figure 5.5c** and **Figure 5.24**), in the final device the difference is not that remarkable due to the limited potential window of the negative electrode at low rates. At high power densities, as a consequence of the outstanding rate capability of $TiSb_2$ in Li-ion chemistry, the energy density values achieved by the LIC are higher than those obtained by the NIC. Moreover, the LIC is able to maintain a capacitance retention of 80% after 10000 cycles at constant current of 10 A g^{-1} ($t_{discharge}$ ≈ 11 s), whereas the best NIC is not able to keep more than 63% after 1000 cycles at 5 A g^{-1} current density. This can be attributed to the difficulty of Na^+ to diffuse through the crystal lattice and to the larger volume expansion of Na_3Sb (293%) respect Li_3Sb (135%) counterpart [53]. Thus, even if the selection of the appropriate binder has been

crucial to achieve higher cycle life in NICs, still further work should be carried out in order to make NICs as competitive as LICs.

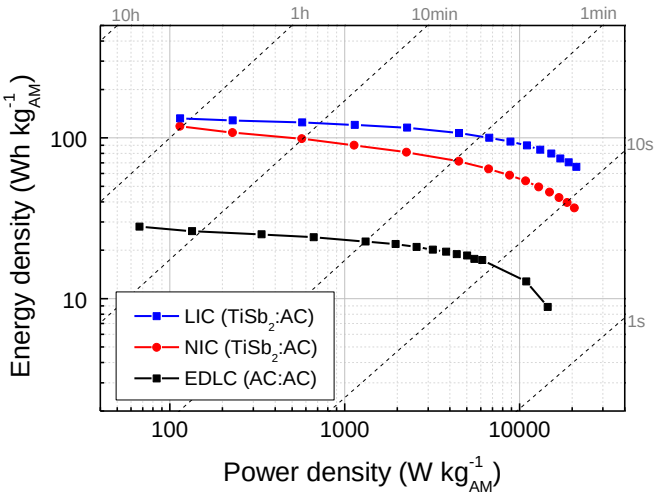

Figure 5.28. a) Ragone plot with LIC (1:2) and NIC (CMC-PAA) and their EDLC counterpart.

Overall, it can be concluded that excellent energy-to-power ratios as well as large cycle life have been achieved when $TiSb_2$ has been used as negative electrode. Thus, a new avenue for alloying based MICs has been opened.

5.5. Summary and conclusions

$TiSb_2$ intermetallic compound with reduced particle size was explored for its potential use as the negative electrode in LICs owing to its high specific capacity values and its excellent capacity retention at high C-rates (*i.e.* 360 mAh g^{-1} at 10C). Thus, novel LICs using $TiSb_2$ as the negative electrode and olive pits derived AC as the positive electrode were developed. Different applications have different energy and power requirements, and in general a unique positive-to-negative electrode mass ratio does not work for a broad power region. Thus, the effect of the electrode mass ratio in the energy delivery was studied. Considering high power applications and also bearing in mind the

importance of a safe operation, LIC (1:2) (*i.e.* an AC with double the mass of the $TiSb_2$) was found to be the best performing system. This system is able to deliver 132 Wh kg_{AM}^{-1} at 115 W kg_{AM}^{-1} (70 Wh dm^{-3} at 61 W dm^{-3}) and 90 Wh kg_{AM}^{-1} at 11053 W kg_{AM}^{-1} (48 Wh dm^{-3} at 5880 W dm^{-3}). Furthermore, it shows an outstanding capacitance retention of 80% after 10000 cycles at 10 A g^{-1} within a discharge time of 11 s. XRD and SEM post-mortem analysis confirm the improved mechanical properties of this novel LIC.

In view of the excellent results obtained in Li-ion technology, the challenge of trying to extend it to Na-ion technology was highly motivating. Even though the research was hindered owing to the major chemical difficulties that arise in this technology, in the end, several high performing NICs were developed despite the limited cyclability. $TiSb_2$-based electrodes made from sub-micron sized, carbon coated alloy particles, delivered a reversible specific capacity of about 225 mAh g^{-1} over 200 cycles, what was about half of the theoretical value. *Operando* XRD measurement revealed, that the reaction mechanism was similar to that exhibited by analogous transition metal antimonides. However, hindered Na^+ diffusion in the relatively large $TiSb_2$ particles limits the specific capacity output. Nevertheless, the specific capacity values observed for the ball milled and carbon coated $TiSb_2$-C20h at high rates make it a suitable candidate to be used as negative electrode in NICs. In order to increase the durability of this device a detailed study on the $TiSb_2$ electrode fabrication process was carried out studying the effect of different binders such as carboximethyl cellulose (CMC), sodium alginate (Na-Alg), the mixture of both (CMC-Alg) and the mixture of CMC with polyacrilic acid (CMC-PAA). Through the achieved energy-to-power values and mainly based on cyclability tests, the combination of CMC-PAA was found to be the most appropriate binder for this material. The developed NIC (CMC-PAA), with a positive-to-negative electrode mass ratio of 1 to 1, is able to deliver 118 Wh kg^{-1}_{AM} at 114 W kg^{-1}_{AM} and 54 Wh kg^{-1}_{AM} at 11 kW kg^{-1}_{AM}, while the capacitance retention after 1000 cycles is 63%, much larger than the 10% of retention measured for the NIC (CMC) counterpart.

5.6. Bibliography

[1] V. Aravindan, J. Gnanaraj, Y.-S. Lee, S. Madhavi, Insertion-Type Electrodes for Nonaqueous Li-Ion Capacitors, Chem. Rev. 114 (2014) 11619–11635. doi:10.1021/cr5000915.

[2] D. Cericola, R. Kötz, Hybridization of rechargeable batteries and electrochemical capacitors: Principles and limits, Electrochimica Acta. 72 (2012) 1–17. doi:10.1016/j.electacta.2012.03.151.

[3] C.-M. Park, J.-H. Kim, H. Kim, H.-J. Sohn, Li-alloy based anode materials for Li secondary batteries, Chem. Soc. Rev. 39 (2010) 3115–3141. doi:10.1039/B919877F.

[4] C. Wang, Y. Li, Y.-S. Chui, Q.-H. Wu, X. Chen, W. Zhang, Three-dimensional Sn–graphene anode for high-performance lithium-ion batteries, Nanoscale. 5 (2013) 10599–10604. doi:10.1039/C3NR02872K.

[5] H. Shang, Z. Zuo, L. Yu, F. Wang, F. He, Y. Li, Low-Temperature Growth of All-Carbon Graphdiyne on a Silicon Anode for High-Performance Lithium-Ion Batteries, Adv. Mater. 30 (2018) 1801459. doi:10.1002/adma.201801459.

[6] N. Yabuuchi, Y. Matsuura, T. Ishikawa, S. Kuze, J.-Y. Son, Y.-T. Cui, H. Oji, S. Komaba, Phosphorus Electrodes in Sodium Cells: Small Volume Expansion by Sodiation and the Surface-Stabilization Mechanism in Aprotic Solvent, ChemElectroChem. 1 (2014) 580–589. doi:10.1002/celc.201300149.

[7] H. Lv, S. Qiu, G. Lu, Y. Fu, X. Li, C. Hu, J. Liu, Nanostructured Antimony/carbon Composite Fibers as Anode Material for Lithium-ion Battery, Electrochimica Acta. 151 (2015) 214–221. doi:10.1016/j.electacta.2014.11.013.

[8] Z. Yi, Q. Han, P. Zan, Y. Wu, Y. Cheng, L. Wang, Sb nanoparticles encapsulated into porous carbon matrixes for high-performance lithium-ion battery anodes, J. Power Sources. 331 (2016) 16–21. doi:10.1016/j.jpowsour.2016.09.027.

[9] S. Goriparti, E. Miele, F. De Angelis, E. Di Fabrizio, R. Proietti Zaccaria, C. Capiglia, Review on recent progress of nanostructured anode materials for Li-ion batteries, J. Power Sources. 257 (2014) 421–443. doi:10.1016/j.jpowsour.2013.11.103.

[10] U. Kasavajjula, C. Wang, A.J. Appleby, Nano- and bulk-silicon-based insertion anodes for lithium-ion secondary cells, J. Power Sources. 163 (2007) 1003–1039. doi:10.1016/j.jpowsour.2006.09.084.

[11] M. Dahbi, N. Yabuuchi, K. Kubota, K. Tokiwa, S. Komaba, Negative electrodes for Na-ion batteries, Phys. Chem. Chem. Phys. 16 (2014) 15007–15028. doi:10.1039/C4CP00826J.

[12] D. Larcher, L.Y. Beaulieu, O. Mao, A.E. George, J.R. Dahn, Study of the Reaction of Lithium with Isostructural A 2 B and Various Al x B Alloys, J. Electrochem. Soc. 147 (2000) 1703–1708. doi:10.1149/1.1393421.

[13] M.-G. Park, J.H. Song, J.-S. Sohn, C.K. Lee, C.-M. Park, Co–Sb intermetallic compounds and their disproportionated nanocomposites as high-performance anodes for rechargeable Li-ion batteries, J. Mater. Chem. A. 2 (2014) 11391–11399. doi:10.1039/C4TA00968A.

[14] M. Morcrette, D. Larcher, J.M. Tarascon, K. Edström, J.T. Vaughey, M.M. Thackeray, Influence of electrode microstructure on the reactivity of Cu2Sb with lithium, Electrochimica Acta. 52 (2007) 5339–5345. doi:10.1016/j.electacta.2007.01.083.

[15] X.B. Zhao, G.S. Cao, A study of Zn4Sb3 as a negative electrode for secondary lithium cells, Electrochimica Acta. 46 (2001) 891–896. doi:10.1016/S0013-4686(00)00669-1.

[16] C.-M. Park, H.-J. Sohn, Electrochemical Characteristics of TiSb2 and Sb/TiC/C Nanocomposites as Anodes for Rechargeable Li-Ion Batteries, J. Electrochem. Soc. 157 (2010) A46–A49. doi:10.1149/1.3254161.

[17] J.L. Gómez-Cámer, C. Villevieille, P. Novák, Antimony based negative electrodes for next generation Li-ion batteries, J. Mater. Chem. A. 1 (2013) 13011–13016. doi:10.1039/C3TA12762A.

[18] J.L. Gómez-Cámer, P. Novák, Polyacrylate bound TiSb2 electrodes for Li-ion batteries, J. Power Sources. 273 (2015) 174–179. doi:10.1016/j.jpowsour.2014.09.087.

[19] P. Scherrer, Bestimmung der Größe und der inneren Struktur von Kolloidteilchen mittels Röntgenstrahlen, Nachrichten Von Ges. Wiss. Zu Gött. Math.-Phys. Kl. 1918 (1918) 98–100.

[20] S. Dsoke, B. Fuchs, E. Gucciardi, M. Wohlfahrt-Mehrens, The importance of the electrode mass ratio in a Li-ion capacitor based on activated carbon and Li4Ti5O12, J. Power Sources. 282 (2015) 385–393. doi:10.1016/j.jpowsour.2015.02.079.

[21] C.-L. Hsieh, D.-S. Tsai, W.-W. Chiang, Y.-H. Liu, A composite electrode of tin dioxide and carbon nanotubes and its role as negative electrode in lithium ion hybrid capacitor, Electrochimica Acta. 209 (2016) 332–340. doi:10.1016/j.electacta.2016.05.090.

[22] B. Babu, P.G. Lashmi, M.M. Shaijumon, Li-ion capacitor based on activated rice husk derived porous carbon with improved electrochemical performance, Electrochimica Acta. 211 (2016) 289–296. doi:10.1016/j.electacta.2016.06.055.

[23] S. Jayaraman, A. Jain, M. Ulaganathan, E. Edison, M.P. Srinivasan, R. Balasubramanian, V. Aravindan, S. Madhavi, Li-ion vs. Na-ion capacitors: A performance evaluation with coconut shell derived mesoporous carbon and natural plant based hard carbon, Chem. Eng. J. 316 (2017) 506–513. doi:10.1016/j.cej.2017.01.108.

[24] G. Wang, C. Lu, X. Zhang, B. Wan, H. Liu, M. Xia, H. Gou, G. Xin, J. Lian, Y. Zhang, Toward ultrafast lithium ion capacitors: A novel atomic layer deposition seeded preparation of Li4Ti5O12/graphene anode, Nano Energy. 36 (2017) 46–57. doi:10.1016/j.nanoen.2017.04.020.

[25] P. Sennu, V. Aravindan, Y.-S. Lee, Marine algae inspired pre-treated SnO2 nanorods bundle as negative electrode for Li-ion capacitor and battery: An approach beyond intercalation, Chem. Eng. J. 324 (2017) 26–34. doi:10.1016/j.cej.2017.05.003.

[26] E. Lim, W.-G. Lim, C. Jo, J. Chun, M.-H. Kim, K.C. Roh, J. Lee, Rational design of Li3VO4@carbon core–shell nanoparticles as Li-ion hybrid supercapacitor anode materials, J. Mater. Chem. A. 5 (2017) 20969–20977. doi:10.1039/C7TA05863B.

[27] J. Ajuria, E. Redondo, M. Arnaiz, R. Mysyk, T. Rojo, E. Goikolea, Lithium and sodium ion capacitors with high energy and power densities based on carbons from recycled olive pits, J. Power Sources. 359 (2017) 17–26. doi:10.1016/j.jpowsour.2017.04.107.

[28] C.-M. Lai, T.-L. Kao, H.-Y. Tuan, Si nanowires/Cu nanowires bilayer fabric as a lithium ion capacitor anode with excellent performance, J. Power Sources. 379 (2018) 261–269. doi:10.1016/j.jpowsour.2018.01.046.

[29] X. Xu, F. Niu, D. Zhang, C. Chu, C. Wang, J. Yang, Y. Qian, Hierarchically porous Li3VO4/C nanocomposite as an advanced anode material for high-performance lithium-ion capacitors, J. Power Sources. 384 (2018) 240–248. doi:10.1016/j.jpowsour.2018.03.007.

[30] X. Zhu, D. Sun, B. Luo, Y. Hu, L. Wang, A stable high-power Na2Ti3O7/LiNi0.5Mn1.5O4 Li-ion hybrid energy storage device, Electrochimica Acta. 284 (2018) 30–37. doi:10.1016/j.electacta.2018.07.153.

[31] Q. Lu, B. Lu, M. Chen, X. Wang, T. Xing, M. Liu, X. Wang, Porous activated carbon derived from Chinese-chive for high energy hybrid lithium-ion capacitor, J. Power Sources. 398 (2018) 128–136. doi:10.1016/j.jpowsour.2018.07.062.

[32] M. Arnaiz, C. Botas, D. Carriazo, R. Mysyk, F. Mijangos, T. Rojo, J. Ajuria, E. Goikolea, Reduced graphene oxide decorated with SnO2 nanoparticles as negative electrode for lithium ion capacitors, Electrochimica Acta. 284 (2018) 542–550. doi:10.1016/j.electacta.2018.07.189.

[33] L. Baggetto, H.-Y. Hah, C.E. Johnson, C.A. Bridges, J.A. Johnson, G.M. Veith, The reaction mechanism of FeSb2 as anode for sodium-ion batteries, Phys. Chem. Chem. Phys. 16 (2014) 9538–9545. doi:10.1039/C4CP00738G.

[34] D.-H. Nam, K.-S. Hong, S.-J. Lim, H.-S. Kwon, Electrochemical synthesis of a three-dimensional porous Sb/Cu2Sb anode for Na-ion batteries, J. Power Sources. 247 (2014) 423–427. doi:10.1016/j.jpowsour.2013.08.095.

[35] S. Liao, Y. Sun, J. Wang, H. Cui, C. Wang, Three dimensional self-assembly ZnSb nanowire balls with good performance as sodium ions battery anode, Electrochimica Acta. 211 (2016) 11–17. doi:10.1016/j.electacta.2016.06.018.

[36] M. Hu, Y. Jiang, W. Sun, H. Wang, C. Jin, M. Yan, Reversible Conversion-Alloying of Sb2O3 as a High-Capacity, High-Rate, and Durable Anode for Sodium Ion Batteries, ACS Appl. Mater. Interfaces. 6 (2014) 19449–19455. doi:10.1021/am505505m.

[37] H. Hou, M. Jing, Z. Huang, Y. Yang, Y. Zhang, J. Chen, Z. Wu, X. Ji, One-Dimensional Rod-Like Sb2S3-Based Anode for High-Performance Sodium-Ion Batteries, ACS Appl. Mater. Interfaces. 7 (2015) 19362–19369. doi:10.1021/acsami.5b05509.

[38] S. Liu, Z. Cai, J. Zhou, M. Zhu, A. Pan, S. Liang, High-performance sodium-ion batteries and flexible sodium-ion capacitors based on Sb 2 X 3 (X = O, S)/carbon fiber cloth, J. Mater. Chem. A. 5 (2017) 9169–9176. doi:10.1039/C7TA01895A.

[39] M. Armbrüster, W. Schnelle, U. Schwarz, Y. Grin, Chemical Bonding in TiSb2 and VSb2: A Quantum Chemical and Experimental Study, Inorg. Chem. 46 (2007) 6319–6328. doi:10.1021/ic070284p.

[40] L. Baggetto, K.J. Carroll, H.-Y. Hah, C.E. Johnson, D.R. Mullins, R.R. Unocic, J.A. Johnson, Y.S. Meng, G.M. Veith, Probing the Mechanism of Sodium Ion Insertion into Copper Antimony Cu2Sb Anodes, J. Phys. Chem. C. 118 (2014) 7856–7864. doi:10.1021/jp501032d.

[41] J. Qian, Y. Chen, L. Wu, Y. Cao, X. Ai, H. Yang, High capacity Na-storage and superior cyclability of nanocomposite Sb/C anode for Na-ion batteries, Chem. Commun. 48 (2012) 7070–7072. doi:10.1039/C2CC32730A.

[42] J.-Y. Hwang, S.-T. Myung, Y.-K. Sun, Sodium-ion batteries: present and future, Chem. Soc. Rev. 46 (2017) 3529–3614. doi:10.1039/C6CS00776G.

[43] G. Kang, Y. Cao, Application and modification of poly(vinylidene fluoride) (PVDF) membranes – A review, J. Membr. Sci. 463 (2014) 145–165. doi:10.1016/j.memsci.2014.03.055.

[44] M. Dahbi, T. Nakano, N. Yabuuchi, T. Ishikawa, K. Kubota, M. Fukunishi, S. Shibahara, J.-Y. Son, Y.-T. Cui, H. Oji, S. Komaba, Sodium carboxymethyl cellulose as a potential binder for hard-carbon negative electrodes in sodium-ion batteries, Electrochem. Commun. 44 (2014) 66–69. doi:10.1016/j.elecom.2014.04.014.

[45] Z. Zhang, T. Zeng, Y. Lai, M. Jia, J. Li, A comparative study of different binders and their effects on electrochemical properties of LiMn2O4 cathode in lithium ion batteries, J. Power Sources. 247 (2014) 1–8. doi:10.1016/j.jpowsour.2013.08.051.

[46] S.-L. Chou, J.-Z. Wang, H.-K. Liu, S.-X. Dou, Rapid Synthesis of Li4Ti5O12 Microspheres as Anode Materials and Its Binder Effect for Lithium-Ion Battery, J. Phys. Chem. C. 115 (2011) 16220–16227. doi:10.1021/jp2039256.

[47] L. Wei, C. Chen, Z. Hou, H. Wei, Poly (acrylic acid sodium) grafted carboxymethyl cellulose as a high performance polymer binder for silicon anode in lithium ion batteries, Sci. Rep. 6 (2016) 19583. doi:10.1038/srep19583.

[48] D. Mazouzi, Z. Karkar, C. Reale Hernandez, P. Jimenez Manero, D. Guyomard, L. Roué, B. Lestriez, Critical roles of binders and formulation at multiscales of silicon-based composite electrodes, J. Power Sources. 280 (2015) 533–549. doi:10.1016/j.jpowsour.2015.01.140.

[49] Z. Karkar, D. Guyomard, L. Roué, B. Lestriez, A comparative study of polyacrylic acid (PAA) and carboxymethyl cellulose (CMC) binders for Si-based electrodes, Electrochimica Acta. 258 (2017) 453–466. doi:10.1016/j.electacta.2017.11.082.

[50] T. Kwon, J.W. Choi, A. Coskun, The emerging era of supramolecular polymeric binders in silicon anodes, Chem. Soc. Rev. 47 (2018) 2145–2164. doi:10.1039/C7CS00858A.

[51] M.-H. Ryou, J. Kim, I. Lee, S. Kim, Y.K. Jeong, S. Hong, J.H. Ryu, T.-S. Kim, J.-K. Park, H. Lee, J.W. Choi, Mussel-Inspired Adhesive Binders for High-Performance Silicon Nanoparticle Anodes in Lithium-Ion Batteries, Adv. Mater. 25 (2013) 1571–1576. doi:10.1002/adma.201203981.

[52] N. Yabuuchi, K. Kubota, M. Dahbi, S. Komaba, Research Development on Sodium-Ion Batteries, Chem. Rev. 114 (2014) 11636–11682. doi:10.1021/cr500192f.

[53] E. Edison, S. Sreejith, C.T. Lim, S. Madhavi, Beyond intercalation based sodium-ion batteries: the role of alloying anodes, efficient sodiation mechanisms and recent progress, Sustain. Energy Fuels. 2 (2018) 2567–2582. doi:10.1039/C8SE00381E.

CHAPTER 6

General discussion, conclusions and future perspectives

General discussion

Looking toward more energetic, more powerful and more stable LICs and NICs, an olive pits derived AC has been the material of choice for the capacitor-type positive electrode, while the selection of the battery-type negative electrode has been under depth research. In this thesis, different MICs (being M = L for Li and N for Na) based on HC, SnO_2-rGO and $TiSb_2$ as the negative electrode have been developed and optimized.

Fabricated **dual carbon** LICs and NICs are based on low-cost recycled bio-waste derived carbons. The preparation of HC electrodes was optimized by a ball milling step reducing the typical particle size of 10 - 20 microns to 1 - 5 microns and by a mass loading adjustment obtaining 1 - 2 mg cm^{-2} electrodes. These parameters showed to be crucial on MICs development as they facilitate the ion insertion/deinsertion and electrolyte propagation at high rates, allowing to achieve high specific capacity values up to ultrafast C-rates, *e.g.* 100C, both for Li- and Na-ion technologies. Besides, it has also been observed that this ultrafast response comes not only from the faradaic process but also from a capacitive contribution of the as-prepared HC. Moreover, the fabricated MICs showed the necessity to adapt their mass ratio and cell voltage in order to obtain the maximum energy output. However, it was concluded that it is not possible to obtain maximum energy, at maximum power, while keeping long cycle life. Hence, in order to obtain a well-balanced device, equilibrium between these specifications should be achieved. In this thesis, the dual carbon MICs that show the best energy-to-power performance considering the above-mentioned specifications are the LIC with a 1:1 (HC:AC) and the NIC with a 1:0.8 mass ratio, both characterized in the 1.5 – 4.2 V cell voltage window and showing over 10000 and 1000 cycles respectively.

On the search for **alternative electrolytes** that could increase the operational voltage window and hence, the energy density output, two strategies have been followed: i) the use of pyrrolidonium-based aprotic and protic ionic liquids and ii) the use of an

alternative solvent named 3-cyanopropionic acid methyl ester (CPAME). On the one hand, Li- and Na-based $Pyr_{14}TFSI$ electrolytes have shown to work together with HC electrodes, while $Pyr_{H4}TFSI$ was only possible to test in Li-ion technology due to the high reactivity of Pyr_{H4}^{+} at low potentials. However, their low performance at high rates limited their use in high power applications and hence, their utilization together with an AC or in a MIC was left aside. On the other hand, CPAME has been selected to replace the typical carbonate solvents of LICs owing to its electrochemical stability, which allowed developing LICs with a cell voltage of 4.5 V, showing superior energy-to-power ratios when discharge time was above 1 min. At lower discharge times, the higher viscosity and lower conductivity of CPAME compared to traditional EC:DMC solvents limited the energy density output.

Beyond dual carbon devices, alternative materials such as **SnO_2-rGO** have also been studied as battery-type negative electrode. Different tin loading electrodes have been formulated (*i.e.* 50%, 75% and 90%), however, electrodes with tin loadings of *ca.* 90 wt% were not possible to process as self-standing electrodes due to their poor mechanical properties. SEM and TEM revealed particle size being below 10 nm in diameter which allowed for a maximum tin loading of 75 wt% onto graphene layers. Moreover, following the structural changes upon cycling by *operando* XRD allowed us to validate the reaction mechanism of SnO_2-rGO in Li-ion chemistry. However, the combination of SnO_2-rGO with an olive pits derived AC could not outperform previous dual carbon based LICs at high power densities, showing a remarkable energy density decay, most probably due to uncomplete Li-Sn alloying reactions. Nevertheless, 78% capacitance retention after 2000 cycles was achieved, what demonstrates that embedding SnO_2 nanoparticles on a rGO matrix is a valid strategy to overcome volume induced degradation.

Same as insertion and Sn-based alloying materials, Sb-based materials also show potential to be used as battery-type negative electrode in MICs. This way, an **intermetallic compound -$TiSb_2$-** has been studied for the first time in hybrid capacitors under the framework of this thesis. Both the material and the electrode have been

engineered in order to adapt them to the final chemistry (*i.e.* Li- or Na-ion) used. In Li-ion technology a simple particle reduction was enough to obtain high specific capacity values and excellent capacity retention at high rates. An accurate study on the mass ratio ($TiSb_2$:AC) revealed that LIC (1:2), *i.e.* an AC with double the mass of the $TiSb_2$, was found to be the best performing system. After showing promising capacitance retention of 80% after 10000 cycles, post-mortem XRD and SEM of $TiSb_2$ electrode showed that the initial structure and the surface of the material remained unvaried without any structural change or remarkable mechanical stress. Hence, the fabricated intermetallic compound was found to successfully buffer the volume changes minimizing the degradation of this novel LIC.

In view of the excellent results obtained in Li-ion, the challenge of trying to extend it to Na-ion technology has been highly motivating. Nevertheless, technology transfer has not been straightforward and plenty of efforts have been necessary to make $TiSb_2$ work in Na-ion chemistry. *Operando* XRD measurement revealed that the reaction mechanism is similar to that exhibited by analogous transition metal antimonies. However, hindered Na^+ diffusion in the relatively large $TiSb_2$ particles limited the specific capacity output. Thus, in order to obtain better performance, an additional carbon coating step was necessary. However, still the specific capacity values were quite limited. TEM images of a charged electrode revealed that Na^+ could not diffuse through all the particle and the reactions were limited to the surface of the material. Hence, the specific capacity output was much lower than in Li-ion technology. Moreover, the cycle life of the final NIC was also limited in comparison with its LIC counterpart. Hence, in order to increase the durability of final devices, a detailed study in the $TiSb_2$ electrode fabrication process was carried out studying the effect of different binders. It was found that the high rigidity of CMC, which facilitates the formation of a 3D network, together with the high cross-linking nature and flexibility of PAA, showed CMC-PAA to be the most appropriate binder for $TiSb_2$. Resulting on a 63% capacitance retention after 1000 cycles, much larger than the 10% of retention measured for the NIC (CMC) counterpart.

To conclude, all the work done in commonly used organic electrolytes has been summarized in the following two figures: i) **Figure 6.1** shows the half-cell characterization of all studied battery-type materials in Li- and Na-ion technologies and ii) **Figure 6.2** shows two Ragone plots for the developed LICs and NICs.

Despite Li- and Na-ion technologies are supposed to exhibit similar chemistries, **Figure 6.1** clearly shows that switching from one to the other is not at all straightforward and there is a negative impact on the electrochemical behaviour in Na-ion technology. The difference is less notorious in the case of the HC, probably owing to the easier or less problematic ion insertion/deinsertion mechanism. However, in $TiSb_2$ and SnO_2-rGO electrodes, where conversion and alloying reactions take place, the decrease on specific capacity when the chemistry is changed is quite remarkable. This is directly attributed to the major difficulties of Na^+ to diffuse through the bulk of the materials and the larger volume changes that Sn- and Sb-based sodium alloys suffer in comparison with their Li-alloy counterparts. In the case of $TiSb_2$, an additional carbon coating step enables its use in Na-ion, while the activity of SnO_2-rGO is mainly limited to Li-ion.

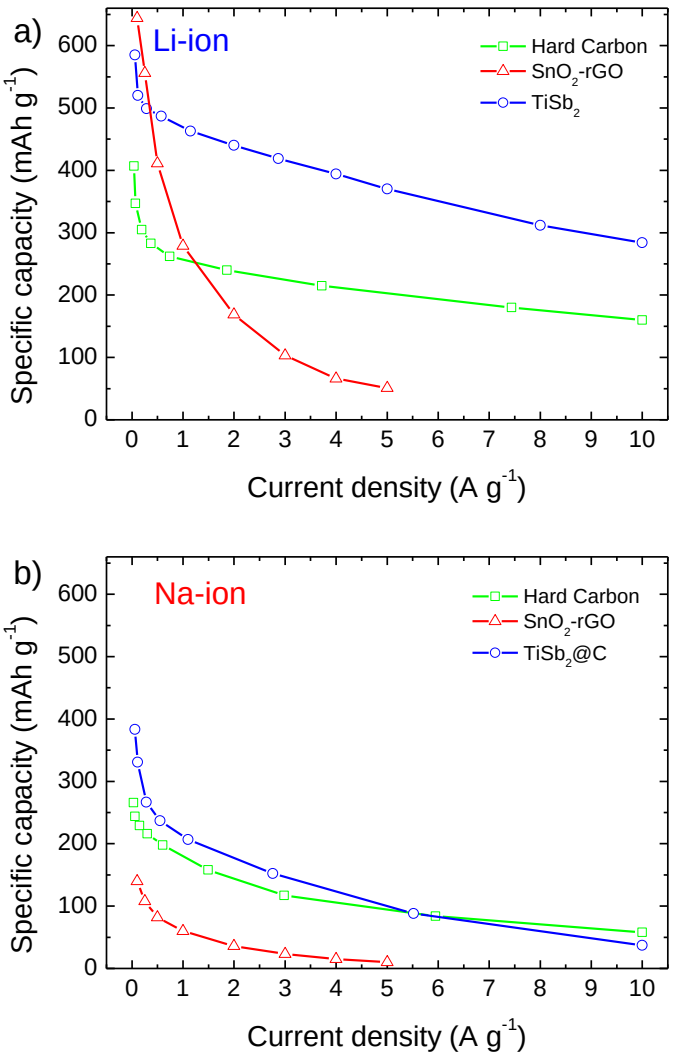

Figure 6.1. Half-cell characterization of all studied battery-type materials in a) Li- and b) Na-ion technologies.

Figure 6.2a shows the energy-to-power density ratios of all studied LICs. It is shown that the dual carbon and $TiSb_2$-based LICs show best energy retention among all the studied power density range. Moreover, the mass ratio study of these systems revealed that an increase on the weight of the AC enabled to obtain the maximum energy density

output. However, it was observed that the increase on energy density might lead to a reduction in power and/or cycle life. Thereby, looking for a balanced performance, the mass ratios of the studied LICs that best fulfil the more energetic, more powerful and more stable features are the 1:1 mass ratio for the HC-based and the 1:2 for the $TiSb_2$-based LICs, showing 94% and 80% capacitance retention after 10000 cycles respectively. Despite the high energy densities of SnO_2-rGO based LIC at low discharge times, faster energy decay occurs at high power densities showing power performance not comparable to the rest of the studied technologies.

Regarding NICs (**Figure 6.2b**), both HC- and $TiSb_2$-based systems showed very similar energy-to-power ratios up to the discharge time of about 3 min. However, due to the lower specific capacity output of the HC in comparison with $TiSb_2$, the 1:1 mass ratio device presented sodium plating when high current densities were applied and consequently, it cannot pass the barrier of 2000 W kg^{-1}_{AM}. In order to develop a NIC (HC:AC) able to work at higher power densities, the mass ratio was tuned to 1:0.8 what allowed us to gain on power but at the expenses of energy. Hence, regarding the final application, mass balance should be tailored accordingly. With regard to the $TiSb_2$-based NIC, the study of different binders with flexible features allowed to well-buffer the volume changes caused by alloying reactions and hence, to develop a promising NIC with power density output comparable to its LIC counterpart. However, similar to NIC (HC:AC), NIC ($TiSb_2$:AC) shows cyclability limited to 1000-2000 cycles, consequently more effort should be focused on enhancing the cycle life of Na-ion devices.

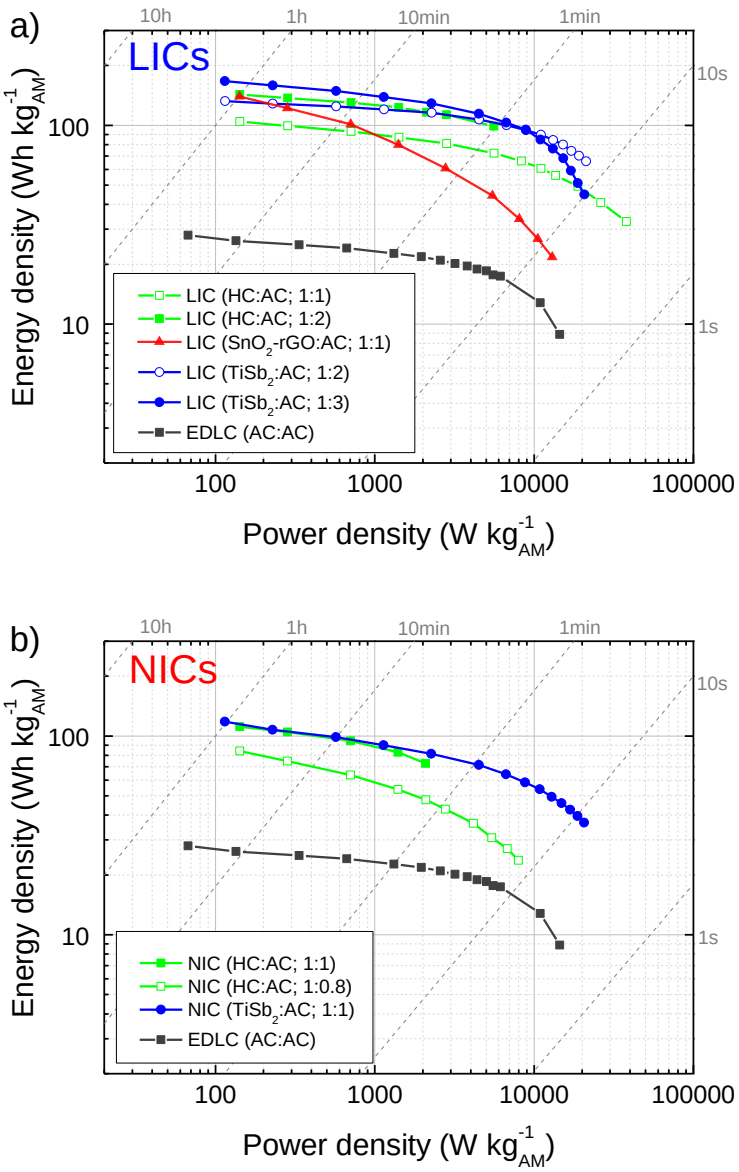

Figure 6.2. Ragone plot for all studied a) LICs and b) NICs.

Overall, $TiSb_2$-based MICs showed the best energy-to-power density output. However, considering costs as well as stability and reproducibility, dual carbon MICs turned out to be the best choice to continue developing the technology.

Conclusions

Carbons

1. Olive pits biomass waste showed to be an effective green source to prepare carbonaceous materials for energy storage.
2. The optimization of olive pits derived hard carbon electrodes by reducing the particle size and mass loading showed to be crucial on metal ion capacitors development.
3. The ultrafast response of olive pits derived hard carbons came not only from the faradaic process but also from a capacitive contribution of the as-prepared material.
4. Developed olive pits derived dual carbon metal ion capacitors needed to adapt their mass ratio and cell voltage in order to obtain the maximum energy output. However, a single mass ratio cannot provide maximum energy at maximum power while keeping long cycle life. Mass ratio needs to be tailored to target specific performance.

Electrolytes

5. Li- and Na-based $Pyr_{14}TFSI$ electrolytes demonstrated to work together with olive pits derived hard carbon electrodes, while $Pyr_{H4}TFSI$ was only possible to test in Li-ion technology due to the high reactivity of Pyr_{H4}^{+} at low potentials. Observed rate capacity performance discarded their use for metal ion capacitors.
6. Olive pits derived activated carbon in 1 M $LiPF_6$ (CPAME) does not show any distortion from the capacitive rectangular shape until 4.6 V *vs.* Li^+/Li, then, porosity saturation might occur. However, still no evidence of electrolyte decomposition was observed.
7. The larger electrochemical stability window of the selected CPAME solvent respect conventional carbonate solvents allows developing olive pits derived dual carbon lithium ion capacitors with a cell voltage of 4.5 V.

Alloys

8. The nanostructured SnO_2-rGO composite allows a maximum Sn loading of 75 wt% onto graphene layers.
9. The 78% capacitance retention after 2000 cycles achieved by the lithium ion capacitor assembled with SnO_2-rGO demonstrates that embedding SnO_2 nanoparticles on a rGO matrix is a valid strategy to overcome volume induced degradation.
10. The development of an intermetallic compound such as $TiSb_2$ showed to be a good strategy to buffer the volume changes of Sb-based alloying reactions.
11. A simple particle reduction of $TiSb_2$ was enough to obtain high specific capacity values and excellent capacity retention at high C-rates in Li-ion technology.
12. An accurate study on the mass ratio of $TiSb_2$:AC electrodes revealed that the lithium ion capacitor with double the mass of the AC respect the $TiSb_2$ exhibited the best energy-to-power values.
13. Initial structure and surface of $TiSb_2$ were kept without structural change and remarkable mechanical stress after 10000 cycles of the lithium ion capacitor.
14. $TiSb_2$ revealed similar reaction mechanism to analogous transition metal antimonies in Na-ion technology; however, hindered Na^+ diffusion in the relatively large $TiSb_2$ particles limited the specific capacity output.
15. The high cross-linking nature and flexibility of the studied binders for $TiSb_2$ electrode fabrication significantly reduce the mechanical stress of the as-prepared material.
16. The combination of carboximethyl cellulose with poly(acrylic) acid shows to be the most appropriate binder for $TiSb_2$ electrode fabrication as the capacitance retention of the final sodium ion capacitor was increased from 10% to 63% after 1000 cycles.

Future perspectives

Based on the results obtained in this thesis some future work is proposed.

The future success of metal ion capacitors will be definitively linked to the achievement of a particular set of assets that will differentiate this technology from batteries and supercapacitors. To this aim, new electrolytes enabling a new class of 5 V energy storage devices as well as novel electrode materials with increased capacity, rate performance and cyclability will need to be developed. In this regard, the outcome of this PhD thesis can serve as a good basis for further research and technology development.

With regard to novel electrolytes, 1 M $LiPF_6$ in CPAME showed potential to reach the so desired 5 V operational voltage, however, it was limited by AC's porosity saturation. Thus, the design of new carbons with tailored porosity to this specific solvent might unchain all the potential of this new electrolyte.

Regarding the results achieved for the different alloying materials, $TiSb_2$ showed most promising results for both Li- and Na-ion technology. Looking toward lower particle size precursors (*i.e.* nanosize) might reduce diffusion limits, increasing not only the capacity output of the material and hence the energy, but also the stability of the device.

Nevertheless, the flagship of the technology is the dual carbon metal ion capacitor, and the major technological barrier that still remains unresolved is the pre-lithiation/sodiation step. Actually it is a major drawback towards market entry of metal ion capacitors and it is a topical matter in the field. Without any doubt, it is going to be a hot topic within the next years too. With this regard, none of the studied materials along the thesis are a natural source of either lithium or sodium, thus they lack of an internal source to compensate for the first cycle irreversibility. Therefore, in order to compensate it and avoid malfunctioning of the overall device, chemical pre-lithiation/sodiation followed by a lithium/sodium reference electrode was used in all cases in order not to starve the

electrolyte and compromise posterior performance and cycle life. Nevertheless, this is a lab-scale confined strategy that cannot be used in industrial processes.

Despite not reported, research on different lithium/sodium sources has been carried out along this thesis. The obtained results were very interesting and were compiled in an invention disclosure that is currently being evaluated by the European patent attorney for patent protection. Coming publications will provide some more insight to the scientific community in this topic.

Appendices

Table of contents:

Appendix I: Experimental

AI.1. Physicochemical characterization techniques

Physicochemical characterization techniques have been used to characterize the structure, morphology and surface of the studied materials in this thesis.

AI.1.1. X-Ray Diffraction (XRD)

X-ray diffraction (XRD) is a technique that allows to know the nature of the molecular structure of a material. X-rays are electromagnetic radiations of the same nature of light but with much shorter wavelength (0.5-2.5 Å for X-ray *vs.* 4000 - 6000 Å for visible light).

To carry out XRD experiments a X-ray source, the investigated sample and a detector to gather the diffracted X-rays are needed. The latter are generated in a cathode tube by heating a filament to produce electrons, accelerating them toward the sample by applying a voltage (*i.e.* 30 kV) and bombarding the target material. When electrons have sufficient energy to dislocate inner shell electrons, X-rays are produced. These are collimated and directed to the sample. The intensity of reflected X-rays is recorded while the sample and the detector rotate. The interaction of the incident rays with the sample produces constructive interference when Bragg equation (**Equation AI.I**) is satisfied. Bragg's equation relates the wavelength of electromagnetic radiation, λ, to the diffraction angle, θ, and the lattice spacing in a crystalline sample, d. The intensity *vs.* 2θ (º) pattern obtained from this technique generates a fingerprint of the crystals in the sample that allows to know the structure, phase and crystallinity of the studied material [1].

$$n\lambda = 2d \cdot sen\ \theta \qquad \textbf{Equation AI.I}$$

In order to get to know the above mentioned features, a Rietveld refinement is normally followed by the FullProf software. This refinement adjust different characteristics such as cell parameters, atomic positions and strains from a benchmark pattern. When refining the experimental pattern, different phases can be added to the process. This way it is possible to obtain a detailed information about the crystalline features of the sample.

Furthermore, in order to determine the average crystallite size of a sample from an XRD pattern, Scherrer equation is used (**Equation AI.II**).Where *K*, is a constant value that describes the particle shape (*e.g.* for spherical particles $K = 0.9$), λ is the X-ray wavelength (nm), β the full width of the Bragg peak at half maximum (FWHM in nm) and θ is the Bragg peak (rad).

$$D = \frac{0.9\,\lambda}{\beta \cos\theta} \qquad \textbf{Equation AI.II}$$

In order to calculate β value, Gaussian equation is used (**Equation AI.III**), where *w* defines the FWHM of each peak.

$$y = y_0 + \frac{A\, e^{\frac{-4\,ln(2)\,(x-x_C)^2}{w^2}}}{w\sqrt{\frac{\pi}{4\,ln(2)}}} \qquad \textbf{Equation AI.III}$$

Moreover, in this thesis, *operando* XRD experiments have also been followed in order to understand the reaction mechanism of some materials (*i.e.* SnO_2-rGO in Li-ion and $TiSb_2$ in Na-ion). They were performed in a homemade electrochemical cell (**Figure AI.1**), where an aluminium transparent to X-ray covered by a beryllium window was used as the current collector for the working electrode, which is the material of interest, and lithium or sodium metal as the counter electrode.

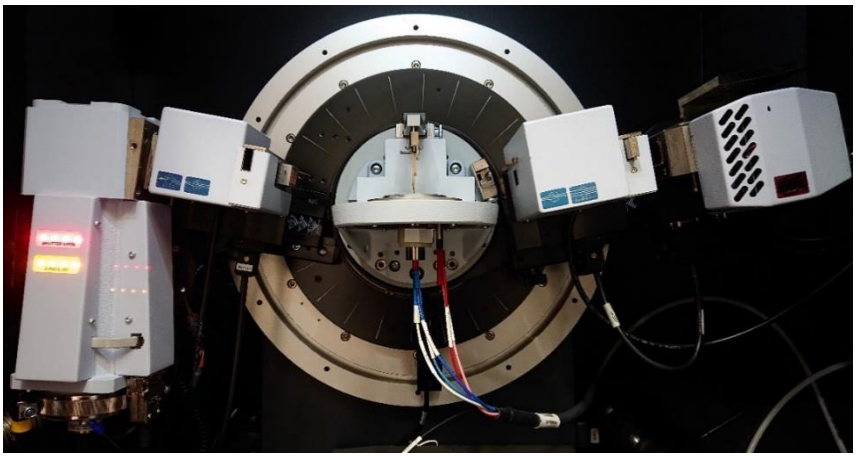

Figure AI.1. Bruker D8 Advance X-ray diffractometer while measuring operando XRD.

XRD patterns for *operando* electrode samples were recorded in a Bruker Advance X-ray diffractometer; data was collected at 40 kV and 30 mA using CoKα radiation over a fixed 2θ range for each sample. Electrochemical experiments were carried out with a VMP3 potentiostat (Bio-Logic), whereas XRD patterns for *ex-situ* materials were recorded in a Bruker D8 Discover X-ray diffractometer; data was collected at 40 kV and 30 mA using CuKα radiation over a fixed 2θ range for each studied material.

AI.1.2. Raman Spectroscopy

The basic equipment of Raman spectroscopy consists on a single frequency light source that irradiates the sample, a spectrometer that disperses the scattered light, and a detector that detects it [2]. The radiation is normally characterized by its wavelength, λ, however, in spectroscopy the interaction of the radiation with states of the molecule is usually discussed in energy terms. Hence, it is useful to use frequency, v, or wavenumber scales, which are linearly related to energy [3].

Much of the scattered radiation, E, has the same frequency of the incident radiation, E_0, and describes the Rayleigh scattering (**Figure AI.2**). Only a small amount of scattered radiation has a different frequency from the irradiated one, this constitutes the Raman

scattering. The Raman scattering process leads to absorption of energy by the molecule and its promotion to a higher energy excited vibrational state, *m.* This is called Stokes scattering. In contrast, due to thermal energy, some molecules might be presented in an excited state (*i.e. m* state). Scattering from this state to the initial state, *0*, is called anti-Stokes scattering and in this process energy is transferred to the scattered photon [4].

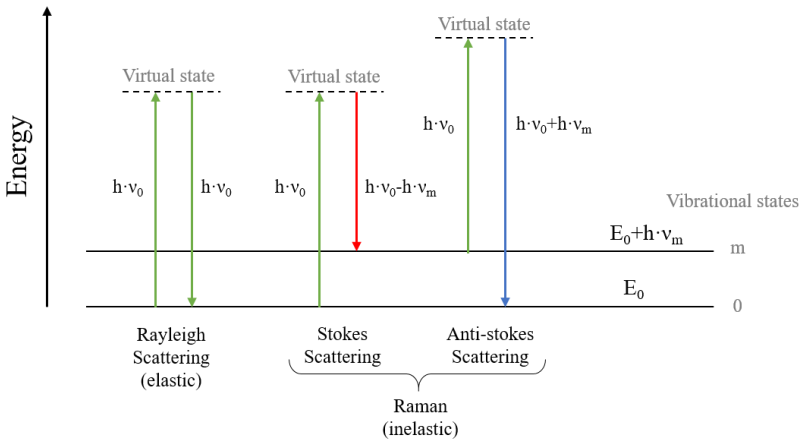

Figure AI.2. Jablonski Diagram representing quantum energy transitions for Rayleigh and Raman scattering.

All spectres were recorded with a Renishaw spectrometer (Nanonics Multiview 2000) operating at an excitation wavelength of 532 nm. The spectres were acquired after 10 s of exposition time of the laser beam into the sample.

In order to know the disordered/ordered nature of the studied materials, G- (in-plane C-C vibrations) and D-bands (a breathing mode only active when there is disorder in the structure) were in depth study. The ratio between the integral of D and G peaks was calculated by fitting the experimental curve with Gaussian and Lorentz equations (from **Equation AI.IV** to **AI.VI.**), where A is the height of the peak, w defines the full width of the Bragg's peak at half maximum, y_0 is related to the background, x_c described the wavelength number of each peak, while m_u defines the percentage of each type of curve.

$$y_{\mathrm{D}} = A_1\left(\left(m_{u,1}\frac{2}{\pi}\cdot\frac{w_1}{4\left(x-x_{c,1}\right)^2+{w_1}^2}\right)+\left(1-m_{u,1}\right)\sqrt{\frac{4\ln(2)}{\pi\, w_1}}e^{\frac{-4\,ln(2)}{{w_1}^2}\left(x-x_{c,1}\right)^2}\right)$$

Equation AI.IV

$$y_{\mathrm{G}} = A_2\left(\left(m_{u,2}\frac{2}{\pi}\cdot\frac{w_2}{4\left(x-x_{c,2}\right)^2+{w_2}^2}\right)+\left(1-m_{u,2}\right)\sqrt{\frac{4\ln(2)}{\pi\, w_2}}e^{\frac{-4\,ln(2)}{{w_2}^2}\left(x-x_{c,2}\right)^2}\right)$$

Equation AI.V

$$y = y_0 + y_1\cdot \mathrm{x} + y_{\mathrm{D}} + y_{\mathrm{G}}$$

Equation AI.VI

AI.1.3. X-ray Photoelectron Spectroscopy (XPS)

X-ray photoelectron spectroscopy (XPS) is a surface characterization technique able to analyse a sample of a depth of 2 to 5 nm. XPS measurements are carried out in ultrahigh vacuum (UHV) conditions, at around 10^{-9} mbar. These low pressures are necessary in order to count the real number of electrons during the acquisition of a spectrum with a minimum error since electron counting detectors are normally far from the material irradiated with X-rays. In a XPS experiment, a sample is irradiated with X-rays in order to excite the electrons that are in a specific bound state. This energy input is to break the photoelectron away from the nuclear attraction force of an element [5]. In a typical XPS spectrum, photo-ejected electrons inelastically scatter through the sample to the surface and are collected by an electron analyser that measures the kinetic energy. The electron analyser plots the number of electrons detected (*vs.* time) *vs.* the binding energy (which is the energy that electrons had before they left the atom) [6]. These energy peaks correspond to specific elements existing in the surface of the analysed material. The intensity of peaks can also provide information about the quantity of the element present in the sample. Besides, the area of each peak is proportional to the number of atoms available in each element.

XPS measurements were carried out in an UHV spectrometer chamber with base pressure below 10^{-10} mbar. The chamber features a hemispherical analyzer PHOIBOS 150 with a 2D-DLD detector (SPECS) and monochromatic X-ray source FOCUS500 (SPECS) with two anodes: Al Ka (hn ¼ 1486.74 eV) and Ag La (hn ¼ 2984.3 eV).

AI.1.4. Scanning Electron Microscopy (SEM)

Scanning Electron Microscopy (SEM) is used in order to get information about the microstructure of the surface of a material from electron-matter interactions created by an electron beam. Electron microscopes use electrons for imaging, in a similar way that light microscopes use visible light. Since the wavelength of electrons is much smaller than the wavelength of light, the resolution of SEMs is superior to the one in a light microscope.

The obtained images are created from the secondary electrons that arise from the sample and are attracted to the sample holder (reflective) through a positive potential (*i.e.* 30 kV). Thus, when electrons cross the sample and impact on the sample holder, a light that is converted by a photomultiplier in a voltage signal is generated and converted into an image.

Besides, energy dispersive X-ray analysis (EDX) can be also used in a scanning electron microscopy to identify the elemental composition of studied materials. Using an energy-dispersive spectrometer, EDX measures the number and energy of the X-rays emitted from a sample.

In this thesis a SEM (Quanta 200 FEG-FEI model) operated at 30 kV was used to acquired SEM images and EDAX data.

AI.1.5. Transmission Electron Microscopy (TEM)

Transmission Electron Microscopy (TEM) uses transmitted electrons, which pass through the sample, to create an image. Hence, TEM can also provide information on the inner structure of the sample, such as the crystal structure and the morphology.

TEM uses high energy electrons (*i.e.* up to 300 kV accelerating voltage) which are accelerated to nearly the speed of light. The beam of electrons is focused into a small and thin beam by the use of the condenser lens. High angle electrons will be excluded by the condenser aperture. The beam then strikes the sample and the transmitted electrons are focused by the objective lens into a phosphor screen to convert the electron image information to a visible form.

To perform TEM measurements in this thesis, all samples were ground with acetone and the resulting sample dispersions of the powder samples were transferred onto a holey carbon film fixed on a 3 mm copper grid (200 mesh). Tecnai F20 microscope from FEI was used.

AI.1.6. Thermogravimetric analysis (TGA)

Thermogravimetry (TG) is a technique that monitors the mass of a sample, measured by a microbalance, against the time or temperature in a specific atmosphere.

In this thesis, on one side, TGA has been used to determine the Sn wt% loading into SnO_2-rGO composites. Measurements were conducted from RT to 1000 ºC at a heating rate of 10ºC min^{-1} in synthetic air in Netzsch-STA 449 F3 Jupiter® equipment. On the other side, thermal analysis of 1 M $LiPF_6$ (CPAME) electrolyte was performed with a PerkinElmer STA 6000 using N_2 as carrier gas with a total flow rate of 60 ml min^{-1}. The heating rate for ramp experiments was 10ºC min^{-1}. While isothermal analysis was carried out between 25 and 125ºC utilizing isothermal steps of 2 hours.

AI.1.7. Gas adsorption/desorption

The adsorption/desorption of molecules from a certain gas into a solid surface is followed to get information about the specific surface area (SSA) and pore size distribution (PSD) of a material. N_2 adsorption at -195.8ºC (77 K) is the most commonly used technique owing to the large pore range that can cover and its weak interaction with most solids. However, when materials with pore size lower than 1 nm are studied, due to the larger size of N_2 molecules (4 Å) in comparison with CO_2 (2.8 Å) should be used as analyser gas [7].

N_2 adsorption/desorption isotherms were obtained at -195.8ºC using a Micromeritics ASAP 2020 instrument with relative pressure values (P/P_0) between 10^{-8} and 0.995, while CO_2 isotherms were obtained at 0ºC with P/P_0 between 0.05 and 0.25. Before the analysis samples were outgassed for 12 h at 250ºC. SSA and PSD values were calculated using the recently developed 2D Non-Local Density Functional Theory (2D NLDFT) treatment to the adsorption branch isotherm using the data reduction software SAIEUS [8].

The 2D NLDFT model describes a carbon slit pore model based on parallel circular graphene sheets as walls. This way, owing to its circular symmetry, the model is finite in all directions and can be treated using only two dimensions. This assumption introduces heterogeneity to the adsorption process. In this model, the equilibrium fluid densities in the pores and theoretical adsorption isotherms as a function of pressure and pore size are calculated [9].

AI.1.8. Rheology

Rheology measures the resistance from a relative motion between a fluid and a surface. Using a MCR 102 (Anton Paar) rheometer in the temperature range comprised between -10 and 60ºC, the viscosity of $LiPF_6$ (CPAME) electrolytes was measured.

AI.2. Electrochemical characterization techniques

In this thesis, two main electrochemical characterization techniques have been used: cyclic voltammetry (CV) and galvanostatic charge/discharges. Besides, punctually electrochemical impedance spectroscopy (EIS) has also been used. Electrochemical data was recorded with a VMP3 potentiostat (Bio-Logic).

AI.2.1. Electrode preparation

Olive pits derived activated carbons (ACs) were prepared by two different methods: self-standing or laminated. When self-standing electrodes were prepared AC was mixed with polytetrafluoroethylene (PTFE, 60 wt% dispersion in H_2O, Sigma Aldrich) as the binder in a mass ratio of 95:5. The slurry was worked out until plasticity, rolled to obtain a film and transferred into a vacuum oven and dried at 80ºC under constant vacuum for 12 h before 0.95 cm^2 circular electrodes were cut out. When AC laminates were used, the slurry was prepared by mixing the AC and polyvinylidene fluoride (PVdF) as the binder, in a mass ratio of 95:5 in N-methyl-2-pyrrolidone (NMP) by vigorous stirring for 1 h using a magnetic stirrer. The AC slurry was laminated onto an aluminum current collector sheet by a minicoater. Laminates were transferred into a vacuum oven and dried at 80 ºC under constant vacuum for 12 h, before 0.95 cm^2 circular individual electrodes were cut out. In order to perfectly control all the parameters when laminate fabrication and due to the high hygroscopic feature of the NMP, laminates were prepared inside a glove box in argon atmosphere where H_2O and O_2 content has been maintained under 0.1 ppm. The thickness of the self-standing ACs used in the LIC (SnO_2-rGO:AC) was around 70 µm, which correspond to 3.1 mg in weight of active mass. While the AC laminated electrodes for dual carbon MICs had a thickness of around 50 µm and a weight of 1 - 1.5 mg, while AC electrodes from $TiSb_2$-based MICs had a thickness from 33 to 87 µm and a weight from 1 to 3 mg.

The electrode slurry for the HC was prepared by a mixture of olive pits derived HC, Super P C65 (Imerys Graphite & Carbon) as conductive material, and PVdF as the binder in the mass ratio of 90:5:5 in NMP followed by vigorous stirring for 1 h. The HC slurry was deposited onto a copper current collector sheet. Laminates were immediately transferred into a vacuum oven and dried at 80ºC under constant vacuum for 12 h before 0.95 cm^2 circular individual electrodes were cut out. All electrodes weighed between 1 – 1.5 mg with a thickness of 30 – 40 µm.

Self-standing SnO_2-rGO electrodes were fabricated with no need of additive, neither binder nor conductive carbon.

The $TiSb_2$ slurry for Li-ion technology was prepared by a mixture of the $TiSb_2$, Super P C65 and carboxymethyl cellulose (CMC) as the binder in 80:10:10 mass ratio dispersed in ethanol/water solvent using an IKA®T25 digital Ultra Turrax® homogenizer. The slurry was deposited onto a copper current collector sheet. While the slurry for Na-ion technology was prepared by a mixture of $TiSb_2$@C, Super P C65 and different binders such as CMC, sodium alginate (Na-Alg), poly(acrylic acid) (PAA), or a combination between CMC-Alg or CMC-PAA, all in a 80:10:10 mass ratio dispersed in ethanol/water solvent using an IKA®T25 digital Ultra Turrax® homogenizer. $TiSb_2$@C slurry was deposited onto an aluminum current collector sheet. All laminates were immediately transferred into a vacuum oven and dried at 80ºC under constant vacuum for 12 h before 0.95 cm^2 circular individual electrodes were cut out. Before cell assembly all electrodes were dried at 120ºC overnight in a vacuum oven.

AI.2. Cell assembly

Cell assembly was carried out in CR2032 coin cell configuration (**Figure AI.3a**) or Swagelok® three-electrode configuration (**Figure AI.3b**). Coin cell configuration was used when slow CVs or EIS measurements were carried out. While Swagelok® cells were used for the rest of experiments.

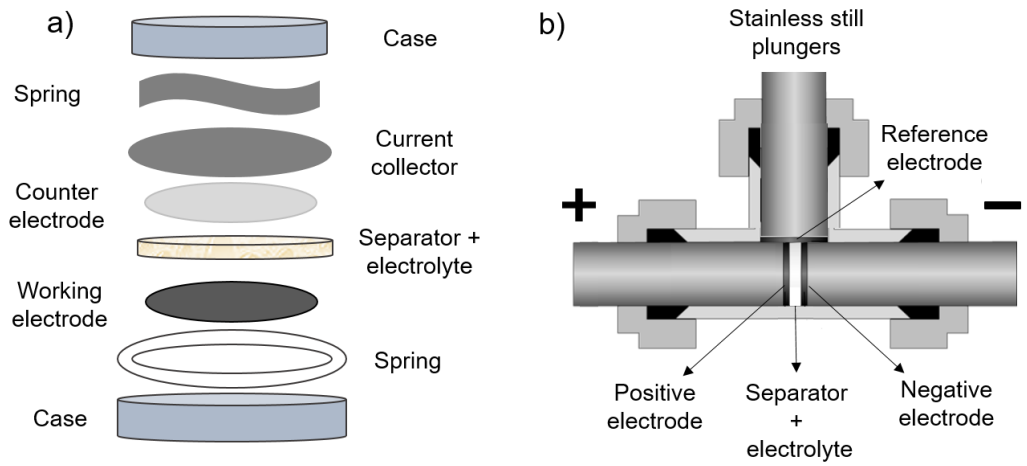

Figure AI.3. Type of used cells: a) Coin cell CR2032 and b) Three-electrode Swagelok® cell.

The electrochemical measurements of AC electrodes were carried out in a three-electrode Swagelok® airtight system using an oversized (thicker) commercial activated carbon (YP-80F, Kuraray, Japan) as counter electrode to ensure its higher surface area not to limit the current being supplied to the working electrode and a lithium or sodium metal as reference electrode. The electrolyte was chosen depending on the technology. In Li-ion chemistry 1M $LiPF_6$ in ethylene carbonate and dimethyl carbonate 1:1 (EC:DMC, v/v) and 1 M $LiPF_6$ in 3-cyano propionic acid methyl ester (CPAME) + 3 wt% vinylene carbonate (VC) were used, whereas, in Na-ion 1 M $NaPF_6$ (EC:DMC) and 1 M $NaClO_4$ in EC and propylene carbonate (PC) + 5 wt% fluoroethylene carbonate (FEC). All cells utilized a glass fibre membrane (Whatman GFB) as the separator and were assembled inside a glove box under argon atmosphere.

HC electrodes were characterized in three-electrode Swagelok® cells using lithium metal as counter and reference electrodes in 1 M $LiPF_6$ (EC:DMC) and 1 M $LiPF_6$ (CPAME) + 3 wt% and also using sodium metal as counter and reference electrodes in 1 M $NaPF_6$ (EC:DMC).

SnO_2-rGO electrodes were characterized in coin cell configuration using on one side lithium metal as the reference electrode in 1 M $LiPF_6$ (EC:DMC) electrolyte and on the other side using sodium metal as the reference electrode in 1 M $NaPF_6$ (EC:DMC) electrolyte.

$TiSb_2$ electrodes were characterized in three-electrode Swagelok® cells using lithium metal as counter and reference electrodes in 1M $LiPF_6$ (EC:DMC) and using an oversized AC as counter and sodium metal as reference electrodes in 1 M $NaClO_4$ (EC:PC) + 5 wt% FEC.

Final LICs and NICs were all assembled in three-electrode Swagelok® cells using HC, SnO_2-rGO or $TiSb_2$ as the negative electrode, an olive pits derived AC as the positive electrode and always using lithium or sodium metal as the reference and metal source of the device. The electrolyte was chosen depending on the system, being always the one use in the negative electrode characterization.

AI.2.3. Cyclic voltammetry (CV)

The cyclic voltammetry (CV) technique is one of the main techniques in electrochemistry, especially to qualitatively identify redox reactions, reaction mechanisms or intermediate reactions occurring on a material. This technique is based on the application of an electrical potential disturbance in the form of a linear variation as a function of time (dV dt^{-1}) between two voltage limits while the potentiostat measures the resulting current response. The applied voltage can be described as **Equation AI.VII**, where v is the scan-rate (V s^{-1}) and V_1 and V_2 are the two voltage boundaries.

$$V(t) = V_0 + vt \qquad \text{for } V \leq V_1 \qquad \textbf{Equation AI.VII}$$

$$V(t) = V_0 - vt \qquad \text{for } V \leq V_2$$

The resulting current response over time allows calculating the local capacity, Q_i, obtained for $V=V_i$, as shown in **Equation AI.VIII.**

$$Q_i = |\int i\, dt|_{V_i} \qquad \textbf{Equation AI.VIII}$$

As the calculation is done between V_1 and V_2, **Equation AI.IX** can be obtained, where C defines de capacitance and V the voltage, and from the slope of this curve the capacitance can be obtained.

$$Q = C \cdot V \qquad \textbf{Equation AI.IX}$$

However, when the charge/discharge deviates from the ideal triangular shape, due to surface parasitic reactions or redox processes, the capacitance should be calculated from **Equation AI.X.**

$$C = \frac{1}{\Delta V\, v}\int_{V_1}^{V_2} i\, dV \qquad \textbf{Equation AI.X}$$

Thus, the shape of the voltammogram gives an idea of the charge storage mechanism. A voltammogram with an ideal rectangular shape describes a capacitive storage mechanism, while the presence of peaks describes that some redox reactions are taken place. **Figure AI.4** summarizes the different CV shapes that can be obtained depending on the charge storage mechanism of the measured material [10].

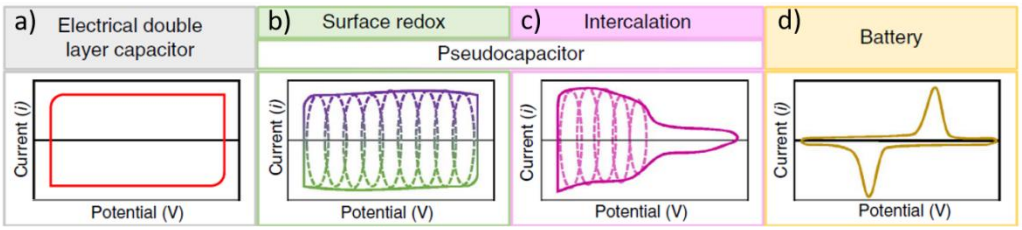

Figure AI.4. Cyclic voltammetries describing faradaic and capacitive energy storage mechanisms.

However, in order to calculate the percentage of diffusion- and capacitive-control processes, the Power-law can be utilized (**Equation AI.XI**) [11]. Hence, in order to study the diffusive and capacitive contribution of a material, CVs at different scan rates need to be followed. This way, kinetic information is obtained, where *i* is the current and *v* the scan rate. For an analytical purpose, **Equation AI.XI** needs to be rearranged to **Equation AI.XII**.

$$i = av^b \qquad \textbf{Equation AI.XI}$$

$$log\ (i) = log(a) + b \cdot log(\nu) \qquad \textbf{Equation AI.XII}$$

The slope of the linear curve obtained when plotting *log (i) vs. log (v)* gives the *b*-value, which will determine the nature of the current. In case *b*=0.5 the kinetic is controlled by diffusion, while if *b*=1 the capacitive charge storage mechanism is the dominant [12].

Further calculations to determine the diffusion and capacitive contributions to the total capacity can be followed using **Equation AI.XIII**, where k_1v defines the capacitive- and $k_2v^{1/2}$ the diffusion-controlled currents. For an analytical purpose, **Equation AI.XIII** has been rearranged to **Equation AI.XIV**, from which k_1 and k_2 values can be obtained in all the studied potential window, by the slope and the y-intercept, respectively.

$$i(V) = k_1\nu + k_2\nu^{1/2} \qquad \textbf{Equation AI.XIII}$$

$$\frac{i(V)}{\nu^{1/2}} = k_1\nu^{1/2} + k_2 \qquad \textbf{Equation AI.XIV}$$

Thereby, these calculations allow to know the diffusion and/or capacitive nature of the studied material.

AI.2.4. Galvanostatic (GA) charge/discharge

Galvanostatic (GA) charge/discharge measurements have been followed using a fix current with some potential limitations. In this technique a current is applied to the working electrode and the resulting potential is measured against a reference electrode as a function of time. GA charge/discharge measurements have been carried out in half-cell configuration for both positive and negative electrodes, and for final hybrid devices. Curves describing the variation of the potential *vs.* time allow to calculate the stored charge, the capacity, the capacitance, the equivalent series resistance (ESR), the specific energy and power from the working electrode or the overall device.

The charge stored by a certain material can be calculated by the integral of the applied constant current density and the charge/discharge time consumed (**Equation 1.XV**). However, batteries are normally defined by their specific capacity value, *c*, measured in milliampere hour per gram (mAh g^{-1}) in which as the charge stored per mass of active material (**Equation 1.XVI**) is defined.

$$Q = \int_0^t I(t)\, dt \qquad \textbf{Equation AI.XV}$$

$$c = \frac{Q}{m} \qquad \textbf{Equation AI.XVI}$$

Moreover, during charge/discharge cycling, electrode-electrolyte reactions, electrode decomposition or changes in electrode volume can cause irreversible loss of capacity. This is measured by the Coulombic Efficiency (CE), defined in **Equation AI.XVII.**

$$CE = \frac{Q_{discharge}}{Q_{charge}} \qquad \textbf{Equation AI.XVII}$$

The capacitance of hybrid capacitors studied in this thesis is calculated by the slope of the discharge curve, as shown in **Equation AI.XVIII**, where *I* is the applied current (mA) and m_{AM} (mg) the mass of the active material (AM). Meanwhile the capacity, as shown

in **Equation AI.XIX**, is calculated from the discharge time, $t_{discharge}$, and the applied current, *I*.

$$C\ (F\ g^{-1}) = \frac{I/m_{AM}}{dV\ /dt} = \frac{I}{slope_{discharge} \cdot m_{AM}} \qquad \textbf{Equation AI.XVIII}$$

$$c\ (mAh\ g^{-1}) = \frac{I}{t_2 - t_1} \qquad \textbf{Equation AI.XIX}$$

While the ESR is calculated from the potential or voltage drop during the current inversion as shown in **Equation AI.XX**.

$$ESR\ (\Omega) = \frac{\Delta V_{drop}}{\Delta I} \qquad \textbf{Equation AI.XX}$$

In capacitors, resistance is described as the ESR including interfacial, ionic diffusion and electrolyte ionic resistances. This number of resistances introduces a voltage drop which is ideally the same on charge or discharge steps. In contrast, a battery presents a close-to-constant voltage ($E_{equilibrium}$) during charge or discharge except when the state of charge approaches 100% charge (top of charge, TOC) or close to 0% (end of discharge, EOD). The potential difference between charge and discharge is described as polarization. This polarization is mainly affected by mass- and charge-transfer over potentials and by the resistance of the solution.

In view of the governing capacitive storage mechanism for hybrid capacitors, energy is calculated following the same formula as for EDLCs (see **Equation AI.XXI**), in which the specific capacitance, *C*, and the square of the voltage window, ΔV^2, of the device will determine the amount of stored energy. Moreover, data has also been contrasted and validated with integral calculation of the area below the capacity *vs.* time results (**Equation AI.XXII**).

$$E = \frac{1}{2}\ C\ \Delta V^2 \qquad \textbf{Equation AI.XXI}$$

$$E\ (Wh\ kg^{-1}) = \frac{I}{m_{AM}} \int_{t1}^{t2} V\ dt$$ **Equation AI.XXII**

When metal-ion capacitors are characterized at high current densities and hence going to discharge times in the range of seconds, due to the existing ESR, the stored and delivered energy is not the same. Hence the term of energy efficiency needs to be defined. In metal-ion capacitors it can be calculated by the ratio of the areas under the GA discharge/charge curves, multiplied by the current [13]. Thus, the ratio between the charged and delivered energy (**Equation AI.XXIII**).

$$Energy\ efficiency = \frac{I \int_{t1}^{t2} V\ dt_{charged}}{I \int_{t1}^{t2} V\ dt_{discharged}} = \frac{E_{charged}}{E_{discharged}}$$ **Equation AI.XXIII**

Power density of hybrid devices has been calculated by the energy and the time needed to be delivered (**Equation AI.XXIV**).

$$P\ (W\ kg^{-1}) = \frac{E}{\Delta t}$$ **Equation AI.XXIV**

In this thesis, GA charge/discharge measurements have been carried out to all the studied materials and to all final hybrid capacitors at different current densities.

AI.2.5. Electrochemical Impedance Spectroscopy (EIS)

Electrochemical impedance spectroscopy (EIS), measuring the ability of a circuit to resist to an electric current flow, can give an accurate information about the transport properties in an energy storage device. Electrochemical impedance is usually measured by applying an alternating current potential to an electrochemical cell and then measuring the current through the cell. It is usually measured using a sinusoidal potential excitation. The response to this potential is also an alternating current signal. Hence, the potential and current are defined as frequency dependence. This way, an analogous expression to Ohm's law enables to calculate the impedance of a system (**Equation AI.XXV**).

$$Z = \frac{E_t}{I_t} = \frac{E_0 \sin(wt)}{I_0 (\sin wt + \varphi)} = Z_0 \frac{\sin(wt)}{(\sin wt + \varphi)}$$ **Equation AI.XXV**

Hence, the impedance is expressed in terms of a magnitude, Z_0, and a phase shift, φ. It can also be expressed in two parts, the real part, Z', and the imaginary part, Z''. The real part describes the resistance, whereas the imaginary part defines the capacitance and inductance. The impedance is represented in a Nyquist plot (**Figure AI.5**) [14], where Z' is represented in the X-axis, Z'' in the Y-axis and each point of the graph represents one frequency. Moreover, EIS results are usually analysed by fitting to an equivalent circuit where elements such as capacitors, resistors, or inductors are described [15].

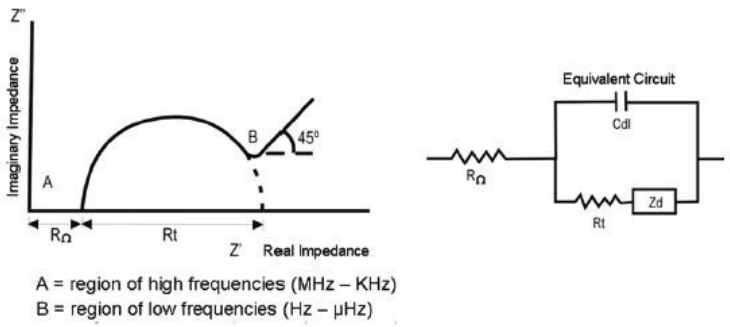

Figure AI.5. Nyquist diagram and its equivalent circuit.

In the framework of this thesis, EIS measurements have been carried out in order to better understand the diffusion limitation of Na^+ into the HC and AC and to evaluate the influence of the volume changes of $TiSb_2$- and Sb-based electrodes. Furthermore, conductivity values of $LiPF_6$ (CPAME) electrolytes were also acquired by EIS measurements.

AI.2.6. Linear sweep voltammetry (LSV)

Linear sweep voltammetry (LSV) has been used in order to measure the electrochemical stability window of the as-prepared $LiPF_6$ (CPAME) electrolytes. In this technique, unlike the CV, no backward scan is done, only the forward scan is applied. This leads to

the determination of the redox potential and the kinetic parameters. Measurements were carried out in a three-electrode Swagelok® cell using platinum as the working microelectrode (embedded in PEEK; active area of 0.79 mm^2), an oversized (thicker) YP-80F carbon electrode as the counter electrode and a silver electrode as the reference. After a 12 h rest at OCP to reach equilibrium, cells were swept from OCP either to positive or negatively direction at 1 mV s^{-1} until potentials of -4 V *vs.* OCP and 4 V *vs.* OCP were reached respectively.

AI.3. Bibliography

[1] C.D. Igwebike-Ossi, X-Ray Techniques, Fail. Anal. Prev. (2017). doi:10.5772/intechopen.72447.

[2] Introduction, Basic Theory and Principles, in: Mod. Raman Spectrosc. – Pract. Approach, John Wiley & Sons, Ltd, 2005: pp. 1–21. doi:10.1002/0470011831.ch1.

[3] G.S. Bumbrah, R.M. Sharma, Raman spectroscopy – Basic principle, instrumentation and selected applications for the characterization of drugs of abuse, Egypt. J. Forensic Sci. 6 (2016) 209–215. doi:10.1016/j.ejfs.2015.06.001.

[4] The Theory of Raman Spectroscopy, in: Mod. Raman Spectrosc. – Pract. Approach, John Wiley & Sons, Ltd, 2005: pp. 71–92. doi:10.1002/0470011831.ch3.

[5] Introduction, in: X-Ray Photoelectron Spectrosc., John Wiley & Sons, Ltd, 2011: pp. 1–12. doi:10.1002/9781118162897.ch1.

[6] Spectral Interpretation, in: X-Ray Photoelectron Spectrosc., John Wiley & Sons, Ltd, 2011: pp. 101–140. doi:10.1002/9781118162897.ch5.

[7] J. Garrido, A. Linares-Solano, J.M. Martin-Martinez, M. Molina-Sabio, Francisco. Rodriguez-Reinoso, R. Torregrosa, Use of nitrogen vs. carbon dioxide in the characterization of activated carbons, Langmuir. 3 (1987) 76–81. doi:10.1021/la00073a013.

[8] J. Jagiello, J.P. Olivier, 2D-NLDFT adsorption models for carbon slit-shaped pores with surface energetical heterogeneity and geometrical corrugation, Carbon. 55 (2013) 70–80. doi:10.1016/j.carbon.2012.12.011.

[9] J. Jagiello, J.P. Olivier, A Simple Two-Dimensional NLDFT Model of Gas Adsorption in Finite Carbon Pores. Application to Pore Structure Analysis, J. Phys. Chem. C. 113 (2009) 19382–19385. doi:10.1021/jp9082147.

[10] M. Lukatskaya, B. Dunn, Y. Gogotsi, Multidimensional materials and device architectures for future hybrid energy storage, Nat. Commun. 7 (2016) 12647. doi:10.1038/ncomms12647.

[11] H. Lindström, S. Södergren, A. Solbrand, H. Rensmo, J. Hjelm, A. Hagfeldt, S.-E. Lindquist, Li+ Ion Insertion in TiO2 (Anatase). 2. Voltammetry on Nanoporous Films, J. Phys. Chem. B. 101 (1997) 7717–7722. doi:10.1021/jp970490q.

[12] V. Augustyn, P. Simon, B. Dunn, Pseudocapacitive oxide materials for high-rate electrochemical energy storage, Energy Environ. Sci. 7 (2014) 1597–1614. doi:10.1039/C3EE44164D.

[13] A. Laheäär, P. Przygocki, Q. Abbas, F. Béguin, Appropriate methods for evaluating the efficiency and capacitive behavior of different types of supercapacitors, Electrochem. Commun. 60 (2015) 21–25. doi:10.1016/j.elecom.2015.07.022.

[14] D.V. Ribeiro, C. a. C. Souza, J.C.C. Abrantes, D.V. Ribeiro, C. a. C. Souza, J.C.C. Abrantes, Use of Electrochemical Impedance Spectroscopy (EIS) to monitoring the corrosion of reinforced concrete, Rev. IBRACON Estrut. E Mater. 8 (2015) 529–546. doi:10.1590/S1983-41952015000400007.

[15] A. Zheltikov, Impedance Spectroscopy: Theory, Experiment, and Applications Second Edition. Evgenij Barsoukov and J. Ross Macdonald (eds). John Wiley & Sons, Inc., Hoboken, New Jersey, 2005, pp. 595, J. Raman Spectrosc. 38 (2007) 122–122. doi:10.1002/jrs.1558.

Appendix II: List of abbreviations

2D NLDFT	Non-Local Density Functional Theory
AC	Activated carbon
ACN	Acetonitrile
AIL	Aprotic ionic liquid
AM	Active mass
BM	Ball milled
BMS	Battery management system
CAES	Compressed air energy storage
CDC	Carbide derived carbon
CE	Coulombic efficiency
CNT	Carbon nanotubes
CMC	Carboxyl methyl cellulose
CPAME	3-cyanopropionic acid methyl ester
CV	Cyclic voltammetry
DEC	Diethyl carbonate
DFT	Density functional theory
DMC	Dimethyl carbonate
EC	Ethylene carbonate

EDLC	Electrical double layer capacitor
EDX	Energy dispersive X-ray
EIS	Electrochemical impedance spectroscopy
EMC	Ethyl methyl carbonate
ESW	Electrochemical stability window
EV	Electric vehicle
FEC	Fluoroethylene carbonate
FES	Flywheel energy storage
GA	Galvanostatic
GF	Glass fibre
GHG	Greenhouse gasses
GIC	Graphite intermediate compounds
GITT	Galvanostatic intermittent titration
GO	Graphene oxide
GrO	Graphite oxide
HC	Hard carbon
HEV	Hybrid electric vehicle
HOMO	Highest occupied molecular orbital
IL	Ionic liquid
IUPAC	International Union of Pure and Applied Chemistry

KIB	Potassium ion battery
LCO	Li_2CoO_2
LFP	$LiFeO_4$
LIB	Lithium ion battery
LIC	Lithium ion capacitor
LMO	$LiMn_2O_4$
LTO	$Li_4Ti_5O_{12}$
LSW	Linear sweep voltammetry
LUMO	Lowes unoccupied molecular orbital
MIC	Metal ion capacitor
MOF	Metal organic framework
Na-Alg	Sodium alginate
NIB	Sodium ion battery
NIC	Sodium ion capacitor
NMP	N-methyl-2-pyrrolidone
OCP	Open circuit potential
PAA	Poly(acrylic acid)
PC	Propylene carbonate
PHS	Pumped hydro storage
PIL	Protic ionic liquid

PSD	Pore size distribution
PVdF	Polyvinylidene fluoride
R_{ct}	Charge transfer resistance
rGO	Reduced graphene oxide
RT	Room temperature
SEI	Solid electrolyte interphase
SEM	Scanning electron microscopy
SSA	Specific surface area
TEM	Transmission electron microscopy
TGA	Thermogravimetric analysis
VC	Vinylene carbonate
VEC	Vinyl ethylene carbonate
XRD	X-ray diffraction

Appendix III: List of contributions

PUBLICATIONS IN INTERNATIONAL JOURNALS

Arnaiz M., Bothe A., Dsoke S., Balducci A. and Ajuria J., Aprotic and protic ionic liquids combined with olive pits derived hard carbon for potassium-ion batteries, *Journal of Electrochemical Society, 166 (14), A3504–A3510, 2019.*

Ajuria J., Zarrabeitia M., **Arnaiz M.**, Urra O., Rojo T., Goikolea E., Graphene as Vehicle for Ultrafast Lithium Ion Capacitor Development Based on Recycled Olive Pit Derived Carbons, *Journal of Electrochemical Society 166, A2840–A2848, 2019*.

Gómez-Cámer J.L., **Arnaiz M.**, Rojo T., and Ajuria J., Novel lithium-ion capacitor based on tin phosphide and olive pit derived activated carbon. *Journal of Power Sources 434, 226695, 2019.*

Arnaiz M., Goikolea E., Rojo T., Wittscher L., Balducci A., and Ajuria J., On the use of 3-cyanopropionic acid methyl ester as alternative solvent for high voltage dual carbon lithium ion capacitors. *Journal of Power Sources 434, 226757, 2019*.

Arnaiz M., Nair V., Mitra S., and Ajuria J., Furfuryl alcohol derived high-end carbons for ultrafast dual carbon lithium ion capacitors. *Electrochimica Acta 304, 437–446, 2019.*

Arnaiz M., Gómez-Cámer J.L., Mijangos F., Rojo T., Goikolea E., and Ajuria J., Novel Lithium-Ion Capacitor Based on $TiSb_2$ as Negative Electrode: The Role of Mass Ratio towards High Energy-to-Power Densities and Long Cyclability. *Batteries & Supercaps 2, 153–159, 2019.*

Arnaiz M., Huang P., Ajuria J., Rojo T., Goikolea E., and Balducci A., Protic and Aprotic Ionic Liquids in Combination with Hard Carbon for Lithium-Ion and Sodium-Ion Batteries. *Batteries & Supercaps 1, 204–208, 2018.*

Arnaiz M., Gómez-Cámer J.L., Ajuria J., Bonilla F., Acebedo B., Jáuregui M., Goikolea E., Galceran M., and Rojo T., High Performance Titanium Antimonide $TiSb_2$ Alloy for Na-Ion Batteries and Capacitors. *Chem. Mater. 30, 8155–8163, 2018.*

Arnaiz M., Botas C., Carriazo D., Mysyk R., Mijangos F., Rojo T., Ajuria J., and Goikolea E., Reduced graphene oxide decorated with SnO_2 nanoparticles as negative electrode for lithium ion capacitors. *Electrochimica Acta, 284, 542–550, 2018.*

Ajuria J., **Arnaiz M**., Botas C., Carriazo D., Mysyk R., Rojo T., Talyzin A.V., and Goikolea E., Graphene-based lithium ion capacitor with high gravimetric energy and power densities. *Journal of Power Sources, 363, 422–427, 2017.*

Ajuria J., Redondo E., **Arnaiz M**., Mysyk R., Rojo T., and Goikolea E., Lithium and sodium ion capacitors with high energy and power densities based on carbons from recycled olive pits. *Journal of Power Sources, 359, 17–26, 2017.*

ORAL PRESENTATIONS

Arnaiz M., Gómez-Cámer J.L., Ajuria J., Goikolea E., Galceran M. and Rojo T., Na-ion capacitors based on $TiSb_2$ alloy negative electrode: the role of the binder towards enhancing cycle life. *International Symposium on Enhanced Electrochemical Capacitors (ISEECap) Meeting 2019, Nantes, France*.

Arnaiz M., Gómez-Cámer J.L., Rojo T., Goikolea E. and Ajuria J., Novel Lithium ion capacitor based on $TiSb_2$ alloy negative electrode with outstanding gravivolumetric energy-to-power densities. *69th Annual International Society of Electrochemistry Meeting 2018, Bologna, Italy*.

Arnaiz M., Gómez-Cámer J.L., Goikolea E. and Ajuria J., Energia-dentsitate altuko Na-ioi kondentsadoreak: $TiSb_2$ aleazioaren elektrodo ingeniaritza. *Materialen Zientzia eta Teknologia 2018, San-Sebastian, Gipuzkoa, Basque Country.*

Arnaiz M., Ajuria J., Botas C., Carriazo D., Mysyk R., Rojo T., Talyzin A.V., and Goikolea E., Graphene-based lithium ion capacitor with high gravimetric energy and power densities. *IkerGazte 2017, Iruñea, Navarra.*

POSTER PRESENTATIONS

Arnaiz M., Goikolea E., Rojo T., Wittscher L., Balducci A., and Ajuria J., On the use of 3-cyanopropionic acid methyl ester as alternative solvent for high voltage dual carbon lithium ion capacitors. *Power Our Future (POF) 2019, Vitoria-Gasteiz, Basque Country.*

Arnaiz M., Ajuria J., Botas C., Carriazo D., Mysyk R., Rojo T., Talyzin A.V., and Goikolea E., Graphene-based lithium ion capacitor with high gravimetric energy and power densities. *Graphene Week 2017, Athens, Greece.*

Arnaiz M., Ajuria J., Redondo E., Mysyk R., Rojo T., and Goikolea E., Lithium and sodium ion capacitors with high energy and power densities based on carbons from recycled olive pits. *ISEECap 2017, Jena, Germany.*

OTHER CONTRIBUTIONS

Arnaiz M., Huang P., Ajuria J., Rojo T., Goikolea E., and Balducci A., Cover picture from *Batteries & Supercaps Journal.*

DIPARTIMENTO DI CHIMICA "GIACOMO CIAMICIAN"

Bologna 10/10/2019

OBJECT: Evaluation of PhD Thesis "Development of Lithium and Sodium ion capacitors with high energy-to-power ratios" by María Arnaiz González, CIC energiGUNE

It is my great pleasure to support the PhD Thesis work "Development of Lithium and Sodium ion capacitors with high energy-to-power ratios" by María Arnaiz González, CIC energiGUNE.

This is an excellent work that addresses a very challenging research on the development of stable lithium and sodium ion capacitors

The experimental results are of high significance and might pave the way towards new next generation supercacoitros based on battery-like materials and addressing high specific energy perfomance.

The work is excellently described and the dissertation very well organized. The introduction chapters are exhaustive and review the recent research works on battteries and supercapacitors, including the metal-ion capacitors.

The challenges in these fields are deeply discussed, which clearly proves high familiarity of the candidate with the field of research in question.

Research approaches and results are original and innovative and rely on different activities, from the preparation of materials to their physical-chemical characterization and full supercapacitor cell test.

Novel electrode ($TiSb_2$, HC) and electrolyte (1 M LiPF6 in CPAME) components are proposed, with the target of enabling a new class of 5 V energy storage devices with increased capacitance, rate performance and cyclability. This is a very interesting approach that can have a high impact on the development of high-voltage supercapacitors making use of compounds based on not-critical elements, which is an urgent need in the battery and supercapacitor manufacturing industry.

The conclusive part of the dissertation demonstrates that the candidate has an outstanding ability to critically examine and compare with literature the achieved research results. This skills also permit to the candidate to delineate and suggest directions for future work in this topic.

The research work has been published in high impact-factor, peer reviewed Journals, therefore supporting the interest of the international scientific community to this work. Furthermore, it has been carried out in an international framework, by visiting periods of the candidate to laboratories worldwide recognized for the challenging reserachactivities on

ALMA MATER STUDIORUM • UNIVERSITÀ DI BOLOGNA
VIA SELMI, 2 - 40126 BOLOGNA - ITALIA - TEL. 0512099797 - FAX 0512099365 francesca.soavi@unibo.it

DIPARTIMENTO DI CHIMICA "GIACOMO CIAMICIAN"

supercapacitors.

I, therefore, believe that the proposed thesis fulfills the requirement of a doctoral dissertation to be awarded.

Sincerely,

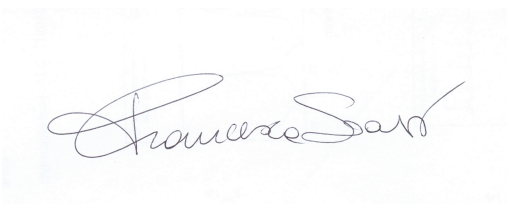

Francesca Soavi

ALMA MATER STUDIORUM • UNIVERSITÀ DI BOLOGNA
VIA SELMI, 2 - 40126 BOLOGNA - ITALIA - TEL. 0512099797 - FAX 0512099365 francesca.soavi@unibo.it

FRIEDRICH-SCHILLER-
UNIVERSITÄT
JENA

Institute for Technical Chemistry and Environmental Chemistry
Center for Energy and Environmental Chemistry Jena (CEEC Jena)

Universität Jena · Einrichtung · 07737 Jena

Prof. Dr. Andrea Balducci
PROF. für Angewandte Elektrochemie

Philosophenweg 7A
07743 Jena

Telefon: +49 (0) 3641 948464
Telefax: +49 (0) 3641 948402
E-Mail: andrea.balducci@uni-jena.de

Jena, 25. September 2019

To Whom It May Concern:

Report about the PhD thesis of Ms. Maria Arnaiz entitled "Development of Lithium and Sodium ion capacitors with high energy-to-power ratios"

The thesis of Ms. Maria Arnaiz is dedicated to the development of innovative and high performance lithium and sodium ion capacitors (LIC and SIC). These devices are presently regarded with high interested by the scientific and industrial communities due to their favorable combination of high power, relative high energy and large cycle life.
During her thesis, Ms. Arnaiz investigated several innovative active materials (based on carbons, SnO_2-rGO and $TiSb_2$) and innovative electrolytes (based on aprotic and protic ionic liquids and on the solvent CPAME) suitable for the realization of LIC and SIC with improved performance compared to the state-of-the art. The results of these studies are clearly reported and analyzed on her PhD thesis. Furthermore, they have been reported in several articles which have been published in high impact factor peer-reviewed papers.
I do believe that Ms. Arnaiz carried out an excellent work during her PhD, and that her PhD thesis is of very high quality. For this reason, I have no doubt to recommend the publication of her PhD thesis.

Prof. Andrea Balducci

Metal ion capacitor (MIC, being M = L for Li and N for Na) technology was first developed in the early 2000's as a novel approach based on the internal hybridization of lithium ion batteries (LIBs) and electrical double layer capacitors (EDLCs). These systems hold promise to merge the best features of each technology, achieving high energy densities, thanks to the battery-type electrode, at high power densities, owing to the capacitor-type electrode, while maintaining long cycle life. Since the first lithium ion capacitor reached the market in 2008, research on this field has notoriously increased. However, most of the developed systems gain energy at the expenses of power and/or cycle life. Hence, the aim of this thesis is to develop more energetic, more powerful and more stable lithium and sodium ion capacitors (LICs and NICs) than the existing ones.

In this scenario, the activated carbon (AC) has been the material of choice for the capacitor-type positive electrode owing to its fast response, stability and low-cost, while for the battery-type negative electrode three different faradaic materials with their own particular set of assets have been investigated. Hard carbon (HC), SnO_2 embedded in a reduce graphene oxide matrix (SnO_2-rGO) and $TiSb_2$ intermetallic compound have been the selected materials. LICs and NICs have been developed with HC and $TiSb_2$ while the use of SnO_2-rGO has been limited to Li-ion technology.